UNIVERSITA' DI PISA

Dipartimento di Ingegneria Civile e Industriale

Tesi di Laurea Magistrale

NONLINEAR AEROELASTIC ANALYSIS OF HIGHLY DEFORMABLE JOINED-WING CONFIGURATIONS

RELATORI

Prof. Aldo Frediani
Prof. Luciano Demasi
Dott. Ing. Rauno Cavallaro

ALLIEVO

Andrea Iannelli

Anno accademico 2012-2013

Ai miei genitori

Acknowledgements

L'opportunità di poter compiere quest'esperienza emerse quasi per caso durante un colloquio con il Prof. Frediani, il quale mi riferì che nel caso fossi stato interessato ad approfondire argomenti di natura aeroelastica nell'ambito della mia tesi, a San Diego c'era un team molto qualificato che si occupava di queste tematiche. Il primo ringraziamento va quindi a lui, non solo per avermi indicato questa possibilità, ma soprattutto per la convinzione e la tenacia che emergono dai numerosi progetti che ha intrapreso e tutt'ora porta avanti con successo, valori di indubbio insegnamento.

Se questo contributo ha qualche speranza di essere apprezzato, il merito va in buona parte riconosciuto al qualificato team di San Diego. Il Prof. Luciano Demasi e il Dott.Ing. Rauno Cavallaro hanno avuto la pazienza di seguirmi in questo processo di apprendimento, dandomi incessantemente fiducia e sostegno. In particolare vorrei ringraziare Rauno per i preziosi suggerimenti e stimoli dati quotidianamente, che mi hanno aperto punti di vista prima ignorati, e soprattutto per il clima di serenità e comprensione che non ha mai fatto mancare a noi tesisti. Un ringraziamento va poi sicuramente a tutto il Lab, per le preziose conoscenze scambiate vicendevolmente e per la compagnia nelle pause pranzo sotto il sole dell' inverno californiano.

Questi cinque anni mi hanno dato tanto, umanamente e come studente. Ringraziare ogni compagno di viaggio è per fortuna impresa ardua e vana. Non sarei mai riuscito ad arrivare qui senza l'appoggio dei molti amici che ho trovato lungo il percorso, la maggior parte dei quali mi ha mostrato come ogni difficoltà possa rivelarsi meno insormontabile del previsto affrontando tutto con una buona dose di spensieratezza e dando ad ogni cosa il giusto peso. Questi ed altri insegnamenti di vita, difficilmente acquisibili a lezione o sopra a un libro, sono stati decisivi nello smussare il mio carattere aiutandomi a farcela.

L'ultimo pensiero, ma probabilmente il più importante, va ai miei genitori. Vorrei ringraziarli di aver sempre creduto in me, facendomi sentire il loro appoggio e il loro entusiasmo verso ciò che facevo anche quando le scelte che prendevo mi avrebbero portato inevitabilmente lontano da loro. Spero di averli in qualche modo ripagati.

Grazie.

"L'anima dinamica ama levare le tende,
spegnere il fuoco, spargere le ceneri
e mettersi in viaggio;
più del luogo che lascia o raggiunge,
ama lo spostamento, il trasferimento,
lo stato intermedio, stare in mezzo."
Michael Onfray, Estetica del Polo Nord

Abstract

There is currently great interest in innovative aircraft configurations. Among them, Joined-Wing concept has captured the attention as a possible candidate layout for the airplane of the future.

However it is reasonable to wonder about the importance of their inherent structural nonlinearities that may invalidate the results obtained with fast lower-fidelity tools, necessary when exploring the large amount of parameters in the conceptual/preliminary design stage. In addition these nonlinearities are thought to be more concerning when the deformation of the wing is significant. This is a feature of modern aircrafts, where weight reduction has brought to an increase of flexibility, and in particular of certain classes as the unmanned aerial vehicles (UAV).

In the present work, dynamic (time-domain) solvers with different degrees of accuracy are developed and later employed to describe the aeroelastic behaviour of three different Joined-Wing configurations. Static and flutter (frequency-domain) solvers are employed as well in the analyses in order to provide both a general description of the response and a comparison between the predictions of linear and nonlinear tools.

The fluid-structure interaction problem is firstly presented, along with the aerodynamic models adopted (vortex lattice method with rigid or free wake) and the algorithms used for the interface (Infinite Plate Spline and Moving Least Square shape functions). For the structure, a geometrically nonlinear finite element is employed. Since the goal is the study of critical and postcritical conditions, an overview of stability and bifurcations of a generical nonlinear dynamical system is presented.

Results are then shown, focusing on the flutter occurrence and analyzing postcritical phenomena: Limit Cycle Oscillations (LCOs) are observed followed sometimes by a lost of periodicity of the solution as speed is further increased. Differences between flutter speed prediction with linear and nonlinear analyses are discussed, in order to understand if a less computationally intense approach may be used with confidence; furthermore both frequency and time-domain approaches are compared. In a perspective aimed to reduce the computational cost, but always staying within nonlinear tools, it is assessed in what measure the use of more sophisticated aerodynamic and interface models impacts the aeroelastic predictions.

These differences range from the algorithms adopted for the fluid-structure coupling to the models employed to describe the wake. When the tools give different results, a physical interpretation of the leading mechanism generating the mismatch is attempted.
The complex scenario arising from the aeroelastic response of Joined-Wings is particularly evident in the inception of topologically different bifurcations leading to multistability when a meaningful parameter (for example the speed in this analysis) is varied.

Finally, it is presented a possible method to perform the evaluation of the aerodynamic tangent matrix when un unsteady panel method (UPM) is used. This effort is meant as a tool for future aeroelastic studies involving the UPM for analyses on wing box models.

Contents

Chapter 1

Overview of the Joined-Wing concept

1.1 New challenges for the future aviation

A new attention has been recently devoted to sustainable growth in air transport. In 2002 the European Community indicated the next challenges and goals to be reached in the future in a document [1] titled "Vision 2020: strategic research agenda". Future aviation will need to supply to restrictive commitments in terms of costs, environments, safety and security. While at the advent of commercial aviation the aim was to fly as fast and high as possible, now different requirements have to be satisfied. Environmental concerns, for example, will become more restrictive: a 50% cut in CO_2 emissions per passenger kilometer and 80% cut in NO_x emissions are required in the next years. Another objective is to eliminate excessive noise outside the airport boundaries by day and night with a 50% reduction on perceived external noise. Other aspects are ambitious too, as the air transport system efficiency, which passes through a time reduction for boarding and disembarkation of passengers and luggage, and a 30% cut in Direct Operating Costs.

The improvement of the aerodynamic design is essential in the attempt to satisfy the previous requirements, in that a decrease of the drag would reduce operating costs together with pollution and noise emissions. During cruise, friction drag of large aircrafts is about the 45-50% of the total drag, while induced drag accounts for 40-45%, as depicted in Fig.1.1. Possible ways of reducing friction drag (e.g. boundary layer suction, turbulent flow control and others) are studied and applicable to all the aircraft configurations, even the innovative ones. The induced drag, on the other side, depends on the lift distribution over the wing span and thus it is fundamental the aircraft layout. Furthermore, the fraction of induced drag increases in take-off and landing, leading to a big influence over the low speed perfor-

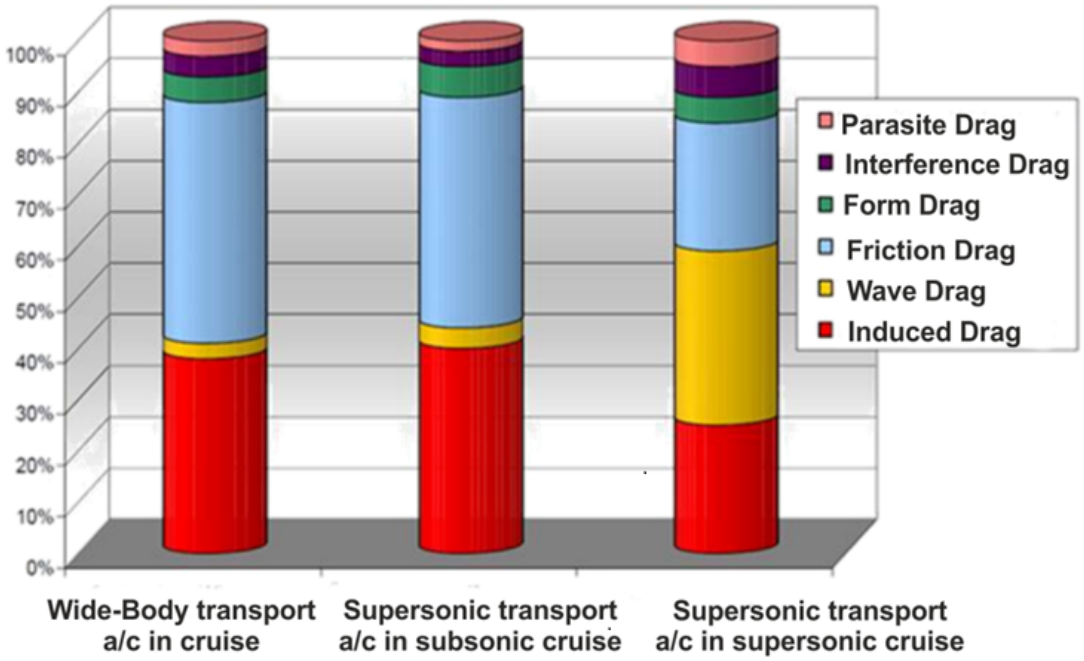

Fig. 1.1: Subdivision of aerodynamic drag in cruise for different classes of aircrafts

mances.

Unfortunately, the lift distribution of today transport aircraft is so optimized due to the large amount of CFD simulations, tunnel and flight tests and long service experience, that significant reduction of induced drag cannot be easily obtained. Due to limitations of conventional designs, new concepts have thus been conceived. An example of significant departure from these layouts is represented by the Joined-Wing configurations [39, 114].

1.2 Advantages of Joined-Wing layout

The Joined-Wing concept takes the cue from the studies of Prandtl [92] about the minimum induced drag when multiplane layouts are considered. He showed that a particular configuration exists, called"Best Wing System", that minimizes the induced drag for a given span and total lift; an exact solution of the Prandtl's problem can be found in [40].

This system is made of a box in the front view, with the two horizontal wings carrying the same lift, which has a distribution made of the superposition of an elliptical part and a constant one; the induced velocity is constant with a value depending on the total lift. The vertical wing (*bulk*) has a symmetric and butterfly shaped lift distribution with an induced

velocity identically zero. This geometry is depicted in Fig.1.2.

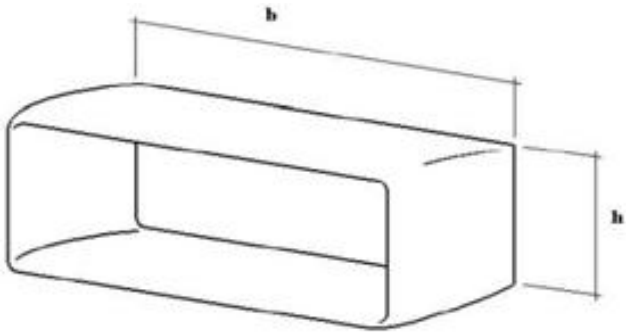

Fig. 1.2: Geometry of the Prandtl's Best Wing System

The efficiency of the wing system e, defined as the ratio of the induced drag of the multiplane layout with the optimal lift distribution to the induced drag of the monoplane with same span and total lift and elliptical lift distribution, results to be dependent on the *gap-to-span* ratio $\frac{h}{b}$. As this ratio increases, the efficiency of the wing system increases correspondingly. In particular, in the range $0.1 < \frac{h}{b} < 0.2$, it is achieved a 30% reduction in induced drag with respect to the equivalent monoplane, see Fig.1.3.
Making use of the fact that, due to Munk theorems, the induced drag is independent of the sweep angle and thus these results have a broad validity, this idea was recovered and developed, with proposals in the seventies for both commercial transport and supersonic fighters [71, 75] and several patents taken out [38, 82].
Rearrangements led to a variation of the original concept, with the introduction of layouts as the Strut-Braced Wings (SBW) [44] and the Truss-Braced Wings (TBW) [50]. Moreover in the recent years the Joined-Wing configuration found applications in the study of relatively new concepts as UAV [99] and HALE in particular [26].

Apart from the previously discussed high aerodynamic efficiency, many advantages on the basic layout fuselage-wing-tail are claimed. For example it is more attractive a solution in composites for the main structures (lifting systems). In fact: the chance to collocate the propulsion system into the rear fuselage leaves the wings free of concentrated loads due to the engines; the possibility to consistently reduce the chord length compared to cantilever wings, leading to higher thickness of the skins, makes attractive the layout of a wing box without stringers. The latter feature earns also significant technological and manufacturing advantages [41].
The shape of the wings enables to think about unconventional controls, like for example for

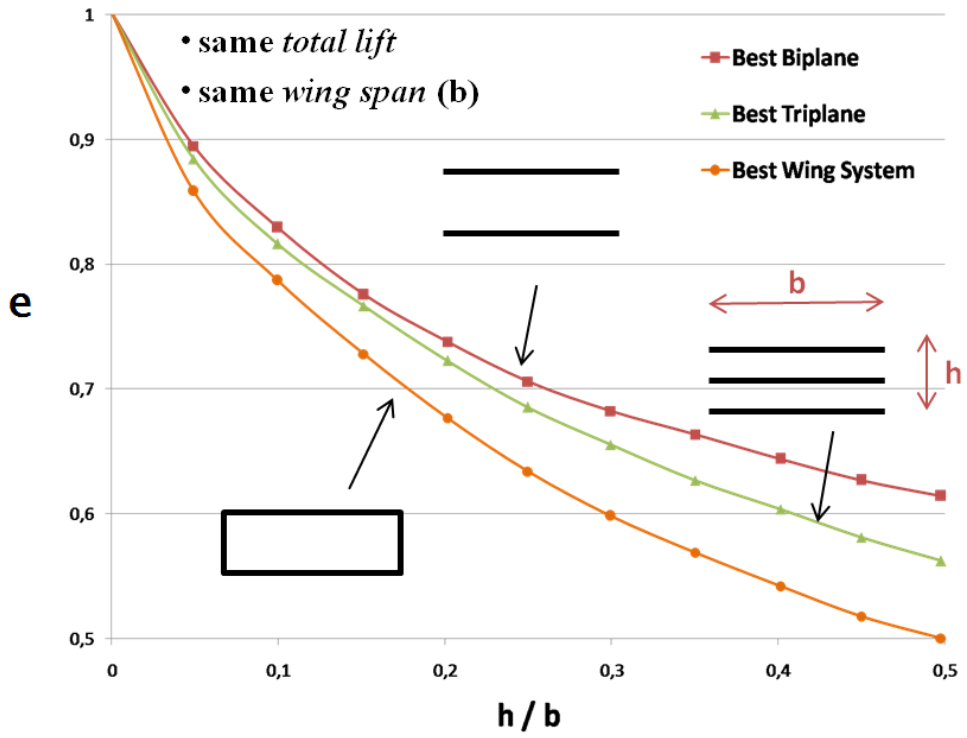

Fig. 1.3: Efficiency of the wing system with respect to the *gap-to-span* ratio, from [92]

the pitch control that could be obtained by means of two elevators located on both front and rear wing roots moved in phase opposition (pure couple without a variation in total lift is produced).

An example of application of the Joined-Wing concept is the *PrandtlPlane* [39], shown in Fig.1.4.

1.3 Issues of a preliminary design

Attracted by these advantages, many works have been devoted in the last decades to the analysis of Joined-Wings, both numerically and experimentally [96]. A design which could realistically assess their behaviour is much more challenging than the one corresponding to traditional configurations. Two of the main problems are the overconstrained layout and the presence of strong structural nonlinearities [65]; this brings the necessity to wonder if it is still adequate to rely on old, though consolidated, design strategies and used nowadays by the industry [24].

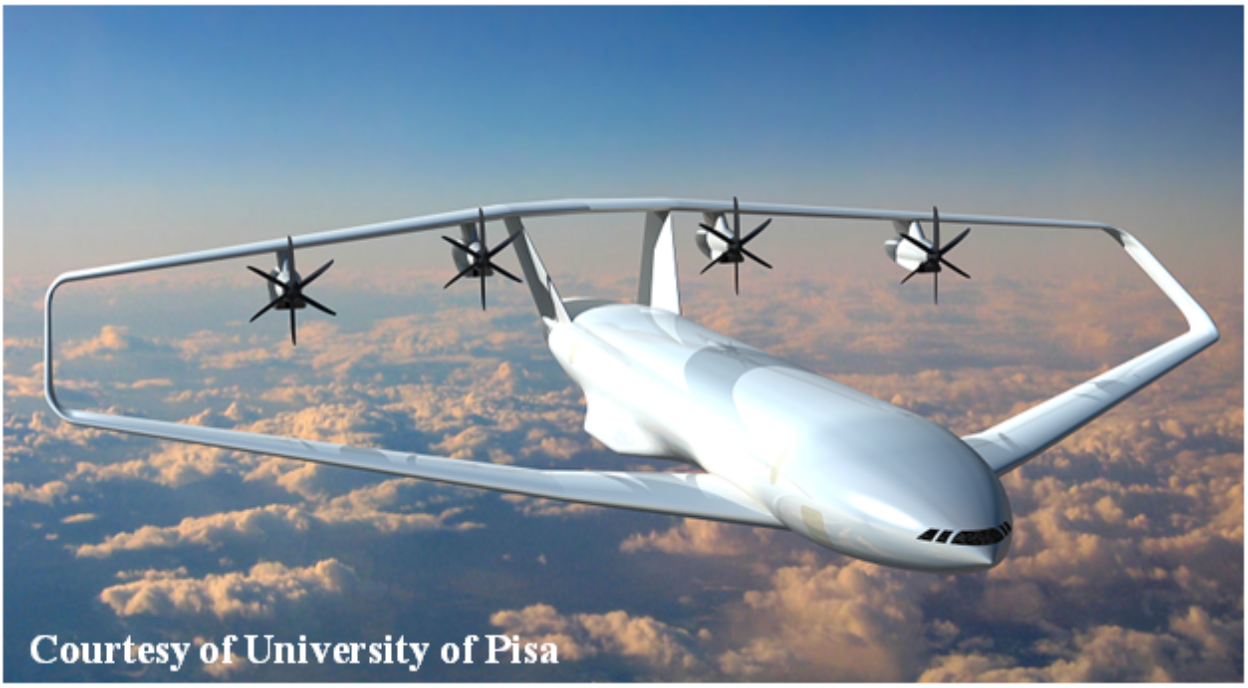

Fig. 1.4: PrandtlPlane layout for a civil aircraft

The results in fact could be misleading, as shown in [30] where has been demonstrated via full post-buckling investigations than the linear buckling analysis is not very reliable. Such evidences seems to suggest the importance to retain these nonlinearities early in the design stage. However, the adoption of fully-nonlinear structural models is impractical for design purposes especially if several alternative configurations are explored (for example in an optimization perspective). This has pushed the research toward computational efficient reduced order models [33], but outcomes in this direction have not been too encouraging.
The effort of the present paper is in the direction of showing, studying and gaining insight into the dynamic aeroelastic phenomena inherent to these configurations, and which have potential impact on the design stage. In a previous work [34], focus was devoted to the differences arising in the detection of divergence speed through eigenvalue analysis about particular configurations (usually the undeformed one) and nonlinear analysis, revealing substantial discrepancies with an overprediction of the critical speed with the traditional approach. It is then expected a mismatch also between flutter speed evaluated by means of linear and nonlinear flutter analyses.

Finally, once the flutter speed is determined, the postcritical dynamic response deserves a careful study. In fact, while flutter represents a critical condition for the design since a

disturbance can quickly grow unbounded, this forthcoming failure may be attenuated ending up in self-sustained Limit Cycle Oscillations (LCOs) if nonlinearities present in the dynamics of the system limit the exponential growth in amplitude predicted by the linear flutter analysis. This response actually is not desirable since has as main consequences a shortening of the aircraft service life (speeding up failure by fatigue) and the risk to induce other critical instabilities making available new couplings among the flexible aircraft components.

Chapter 2

Aeroelastic model

2.1 Introduction to the FSI analysis

The aeroelastic analysis of a wing, here pursued, is a particular application of a broader discipline, called Fluid-Structure Interaction (FSI), which studies the interaction of one or more solid flexible structures with an internal or surrounding fluid flow. A big variety of problems fall under this subject; just to cite a few examples: the behaviour of heavy particles falling under their own weight through a fluid (sedimentation) [16]; turbulent and transitional flows with dynamically moving boundaries [117]; dynamic of conducting fluids immersed in magnetic fluids, also known as magneto-hydrodynamic flows [48]; biofluid [4] and biomechanic, as blood-heart interaction; response of bridges and tall buildings to wind [109]; vibration of turbomachinery [17].

Despite the big variety of topics covered by these analyses, the numerical procedures to solve a generical FSI problem can be classified into two approaches: *monolithic* and *partitioned*. The brief description given here has just the aim to give an introduction to the subject; for a thorough review, see for example [56].
The monolithic approach [81] considers the fluid and structure dynamics in the same framework, such that they form a single system of equations for the entire problem, which is solved *simultaneously* by a unified algorithm. This implies that the interface, needed to pass the informations between the two fields, is implicit in the solution procedure. While this choice surely offers robustness to the method since domain splitting errors are not introduced, its major drawbacks are that the matrix for the full system may be ill-conditioned because of the difference in stiffness of the fluid and the structure [22] and it may not be a simple task to develop such a specialized code starting from structural and fluid solvers, especially for

large scale problems.
The partitioned approach [51], in contrast, solves separately the fluid and the structure fields, with their respective mesh discretizations and, mainly, numerical algorithms: these *disciplinary algorithms* are converted into subroutines called alternatively from a master program. The interfacial conditions, driven from this master, are used here explicitly to transfer the informations between fluid and structure solutions. The obvious advantage, due to its modularity, is the possibility to take advantage of single-disciplinary codes, just validated in the solution of fluid or structural problems, enabling the solution of the FSI problem with a possibly more sophisticated fluid and structural physic modelizations, since the best-suited solution strategy can be selected for each field independently; moreover, the resulting equations systems are smaller and generally better conditioned than the one dealt with in the monolithic approach. The difficulties of this approach are related to the effort in performing an efficient and accurate coordination of the disciplinary algorithms without a substantial modification of themselves. In this perspective, challenges can arise in the explicit definition of the interface location as it is often not known a priori and it changes with time; in some cases this can bring stability and convergence issues [102].

In the present investigation the former method is adopted, relying both on the simple aerodynamic model adopted and on the relatively small size of the problems, which make possible to avoid the difficulties concerning the latter approach.

2.2 Dynamic Solver

2.2.1 Newton's Law and Definition of the Residual

According to the second Newton's law, at each time dynamic equilibrium has to be obtained. Let consider at first a system with a single degree of freedom consisting of a point mass

$$F = M\ddot{x} \tag{2.1}$$

where M represents the mass of the point, x is the generic coordinate, and F is the net force acting on the mass. The residual of the system could be defined as

$$\mathcal{R} = M\ddot{x} - F \tag{2.2}$$

This approach can be extended to systems with multiple degrees of freedom like the one under investigation; let $\boldsymbol{s}$ be the generalized coordinate array (arising from the FE discretization) and $\dot{\boldsymbol{s}}$, $\ddot{\boldsymbol{s}}$ its time derivatives. Let assume $\boldsymbol{M}$ to be the mass matrix, and that the damping forces, related to the structural damping, are proportional to $\dot{\boldsymbol{s}}$ through the damping matrix $\boldsymbol{C}_d$, constant with time; the internal structural forces are indicated with $\boldsymbol{F}_{\text{int}}$ and, since only elastic materials are considered, they are functions of the deformation only. Their evaluation is performed by mean of the in-house structural capability, consisting in a finite element method.
The nonlinear finite element [42, 43, 76, 77] is based on the linear membrane constant strain triangle (CST) and the flat plate discrete Kirchhoff triangle (DKT). The here considered nonlinearity is then relative to the large displacement of the configuration only (geometric nonlinearity). The code has also embedded the calculation of the structural tangent matrix $\boldsymbol{K}_{ST}$, which is the sum of two contributions: the elastic stiffness matrix, $\boldsymbol{K}_E$, and the geometric stiffness matrix, $\boldsymbol{K}_G$. A corotational approach is used, thus rigid body motion is eliminated from the elements and the pure elastic deformations are found. For previous works based on this in-house structural capability, reader is referenced to [19, 34].

The external loads may be generic ones in this treatise, however, they are specialized to be the aerodynamic forces acting on the body, and are a generical function of t, $\boldsymbol{s}$, $\dot{\boldsymbol{s}}$ and $\ddot{\boldsymbol{s}}$; these dependencies are related to the history (wake evolution), current configuration (steady production of aerodynamic forces), velocity of deformation (which changes the local speed) and acceleration of deformation, respectively. The dynamic equilibrium law, with the previous assumptions, reads

$$\boldsymbol{M}\,\ddot{\boldsymbol{s}} + \boldsymbol{C}_d\,\dot{\boldsymbol{s}} = \boldsymbol{P}_{\text{ext}}(\boldsymbol{s}, \dot{\boldsymbol{s}}, \ddot{\boldsymbol{s}}, t) - \boldsymbol{F}_{\text{int}}(\boldsymbol{s}) \tag{2.3}$$

In analogy with eq.(2.2), the residual is then defined as

$$\boldsymbol{\mathcal{R}}(\boldsymbol{s}, \dot{\boldsymbol{s}}, \ddot{\boldsymbol{s}}, t) = \boldsymbol{M}\ddot{\boldsymbol{s}} + \boldsymbol{C}_d\dot{\boldsymbol{s}} - (\boldsymbol{P}_{\text{ext}}(\boldsymbol{s}, \dot{\boldsymbol{s}}, \ddot{\boldsymbol{s}}, t) - \boldsymbol{F}_{\text{int}}(\boldsymbol{s})) \tag{2.4}$$

In order to obtain the dynamic equilibrium the residual has to be zero at each generic time t. However, when the problem is discretized in respect of the time, it is possible to enforce the dynamic equilibrium only at some temporal points. In literature several methods exist for the time discretization of dynamic structural problems, see for example [11,28,57]. In the present study the framework of Newmark's $\beta-$Method is considered, with its successive improvements leading to the *Generalized α-Method* (GAM). The reasons that led to the introduction of the so called *Generalized Energy-Momentuum Method* (GEMM) and its implementation will be shortly presented.

2.2.2 Newmark's $\beta-$Method

Before further proceeding, the notation by which is meant the evaluation of the quantity $\boldsymbol{A}$ at the generic time t is introduced

$$^{t}\boldsymbol{A} = \boldsymbol{A}|_{t} \tag{2.5}$$

If the generic quantity $\boldsymbol{A}$ has both a direct and indirect dependence on time, for example $\boldsymbol{A}(\boldsymbol{s}(t), t)$, then

$$^{t}\boldsymbol{A} = \boldsymbol{A}_{(\,\boldsymbol{s}|_{t}, t)} \tag{2.6}$$

At first [88] a generic multivariate Taylor expansion on the velocity array is considered

$$^{t+\Delta t}\dot{\boldsymbol{s}} = {}^{t}\dot{\boldsymbol{s}} + \Delta t\, {}^{t}\ddot{\boldsymbol{s}} + o(\Delta t^2) \tag{2.7}$$

The mean value theorem assures the existence of a time $\hat{t}$ in the interval $[t, t+\Delta t]$ such that eq.(2.7) is exactly satisfied when the second derivative is there evaluated, that is

$$^{t+\Delta t}\dot{\boldsymbol{s}} = {}^{t}\dot{\boldsymbol{s}} + \Delta t\, {}^{\hat{t}}\ddot{\boldsymbol{s}} \tag{2.8}$$

Now the value of the acceleration array at $\hat{t}$ could be expressed as a linear combination of the values of the acceleration at times t and $t+\Delta t$, leading from eq.(2.7) to

$$^{t+\Delta t}\dot{\boldsymbol{s}} = {}^{t}\dot{\boldsymbol{s}} + (1-\gamma)\Delta t\, {}^{t}\ddot{\boldsymbol{s}} + \gamma\Delta t\, {}^{t+\Delta t}\ddot{\boldsymbol{s}} \tag{2.9}$$

With the same line of reasoning, the mean value theorem could be used for the Taylor expansion of $\boldsymbol{p}$

$$^{t+\Delta t}\boldsymbol{s} = {}^{t}\boldsymbol{s} + \Delta t\, {}^{t}\dot{\boldsymbol{s}} + (1-2\beta)\frac{\Delta t^2}{2}\, {}^{t}\ddot{\boldsymbol{s}} + \beta\Delta t^2\, {}^{t+\Delta t}\ddot{\boldsymbol{s}} \tag{2.10}$$

where for the linear combination of the values of the acceleration at the two different times the parameter 2β is used for commodity. The choice of γ and β determines important characteristics as accuracy, rate of convergence, stability and the alternatively explicit or implicit nature of the scheme [57]. Common choice is to take

$$\gamma = \frac{1}{2} \qquad \beta = \frac{1}{4} \tag{2.11}$$

which gives an unconditionally stable (irrespective of the size of the timestep) and quadratic convergent scheme (this applies for linear problems [59]); no numerical damping is added to the system. Adopting this values and rearranging eq.(2.9) and eq.(2.10), the following equations are obtained

$$\begin{aligned} {}^{t+\Delta t}\dot{\boldsymbol{s}} &= {}^{t}\dot{\boldsymbol{s}} + \frac{\Delta t}{2}\left({}^{t+\Delta t}\ddot{\boldsymbol{s}} + {}^{t}\ddot{\boldsymbol{s}}\right) \\ {}^{t+\Delta t}\boldsymbol{s} &= {}^{t}\boldsymbol{s} + \frac{\Delta t}{2}\left({}^{t+\Delta t}\dot{\boldsymbol{s}} + {}^{t}\dot{\boldsymbol{s}}\right) \end{aligned} \tag{2.12}$$

which define the scheme to discretized eq.(2.3) with respect to time and show why it is called the *average acceleration method* or the *trapezoidal rule*.

2.2.3 Enforcing convergence with Newton's method and Bathe predictor

Once the time scheme has been chosen, the dynamic equilibrium has to be enforced. A first problem comes out in the choice of the time when the solution has to be dynamically in equilibrium, or mathematically, the residual has to vanish. Considering Newmark's method, where all the quantities are expressed in terms of the values assumed at times t and $t + \Delta t$, and assuming the former to be known, a natural choice is to drive to convergence of the system at the end of the timestep, that is at time $t + \Delta t$. In this perspective, eq.(2.4) becomes

$${}^{t+\Delta t}\boldsymbol{\mathcal{R}} = \boldsymbol{M}\,{}^{t+\Delta t}\ddot{\boldsymbol{s}} + \boldsymbol{C}_d\,{}^{t+\Delta t}\dot{\boldsymbol{s}} - \left({}^{t+\Delta t}\boldsymbol{P}_{\text{ext}} - {}^{t+\Delta t}\boldsymbol{F}_{\text{int}}\right) = \boldsymbol{0} \tag{2.13}$$

The problem is then set, because eq.(2.13) can be recast in terms of ${}^{t+\Delta t}\boldsymbol{s}$ thanks to eq.(2.12) which relates the unknowns and enables to stress out the dependance from one only, for example ${}^{t+\Delta t}\boldsymbol{s}$. The system to be solved is nonlinear and so an iterative process is established to advance the solution at time $t + \Delta t$, once the status is known at t, driving to zero ${}^{t+\Delta t}\boldsymbol{\mathcal{R}}$. Since the Newton's method is used to perform this task, a predictor approach should be employed, that is at the beginning of each timestep an esteem of the values of the unknown

${}^{t+\Delta t}\boldsymbol{s}$ and of their two derivatives is given, such that the residual expression is recast in terms of a fixed part (predictor) and an iterative contribution (corrector). The choice adopted is the one presented in [9], which consists in the following assumptions (Bathe predictor)

$$\begin{cases} {}^{t+\Delta t}\boldsymbol{s}_{\text{pred}} = {}^{t}\boldsymbol{s} \\ {}^{t+\Delta t}\dot{\boldsymbol{s}}_{\text{pred}} = \left(1 - \dfrac{\gamma}{\beta}\right) {}^{t}\dot{\boldsymbol{s}} + \left(1 - \dfrac{\gamma}{2\beta}\right) \Delta t \, {}^{t}\ddot{\boldsymbol{s}} \\ {}^{t+\Delta t}\ddot{\boldsymbol{s}}_{\text{pred}} = -\dfrac{1}{\beta \Delta t} {}^{t}\dot{\boldsymbol{s}} - \left(\dfrac{1}{2\beta} - 1\right) {}^{t}\ddot{\boldsymbol{s}} \end{cases} \tag{2.14}$$

The predicted quantities on the l.h.s. of eq.(2.14) are totally defined once the status at time t is known and the superscript $t + \Delta t$ is reported just to point out that they can be used to predict the dynamic status at time $t + \Delta t$; it's now possible to give another expression of the relationships between the three unknowns of the problem, rearranging eq.(2.10)

$${}^{t+\Delta t}\ddot{\boldsymbol{s}} = \frac{1}{\beta \Delta t^2} \left({}^{t+\Delta t}\boldsymbol{s} - {}^{t+\Delta t}\boldsymbol{s}_{\text{pred}}\right) + {}^{t+\Delta t}\ddot{\boldsymbol{s}}_{\text{pred}} \tag{2.15}$$

and eq.(2.9)

$${}^{t+\Delta t}\dot{\boldsymbol{s}} = \frac{\gamma}{\beta \Delta t} \left({}^{t+\Delta t}\boldsymbol{s} - {}^{t+\Delta t}\boldsymbol{s}_{\text{pred}}\right) + {}^{t+\Delta t}\dot{\boldsymbol{s}}_{\text{pred}} \tag{2.16}$$

The residual expression in terms of the predictor is as follows

$$\begin{aligned} {}^{t+\Delta t}\boldsymbol{\mathcal{R}} = \frac{1}{\beta \Delta t} \left(\frac{1}{\Delta t}\boldsymbol{M} + \gamma \boldsymbol{C}_d\right) \left({}^{t+\Delta t}\boldsymbol{s} - {}^{t+\Delta t}\boldsymbol{s}_{\text{pred}}\right) + \\ \boldsymbol{M} \, {}^{t+\Delta t}\ddot{\boldsymbol{s}}_{\text{pred}} + \boldsymbol{C}_d \, {}^{t+\Delta t}\dot{\boldsymbol{s}}_{\text{pred}} - {}^{t+\Delta t}\boldsymbol{P}_{\text{ext}} + {}^{t+\Delta t}\boldsymbol{F}_{\text{int}} \end{aligned} \tag{2.17}$$

Introducing ${}^{t}\boldsymbol{\mathcal{R}}^{\text{iter } n}$ to indicate the value of the residual at time t during the n-th iteration, in a Newton's method the residual is locally approximated with an affine model and the new linearly predicted is enforced to zero, leading to the the single Newton iteration

$$\boldsymbol{0} = {}^{t+\Delta t}\boldsymbol{\mathcal{R}}^{\text{iter } n} + {}^{t+\Delta t}\left[\frac{\mathrm{d}\boldsymbol{\mathcal{R}}}{\mathrm{d}\boldsymbol{s}}\right]^{\text{iter } n} \left({}^{t+\Delta t}\boldsymbol{s}^{\text{iter } n+1} - {}^{t+\Delta t}\boldsymbol{s}^{\text{iter } n}\right) \tag{2.18}$$

where the symbolism

$${}^{t+\Delta t}\left[\frac{\mathrm{d}\boldsymbol{\mathcal{R}}}{\mathrm{d}\boldsymbol{s}}\right]^{\text{iter } n} \tag{2.19}$$

indicates the *system* tangent matrix evaluated at ${}^{t+\Delta t}\boldsymbol{s}^{\text{iter } n}$, and it holds

$${}^{t+\Delta t}\boldsymbol{s}^{\text{iter } n+1} - {}^{t+\Delta t}\boldsymbol{s}^{\text{iter } n} = {}^{t+\Delta t}\boldsymbol{u}^{\text{iter } n} \tag{2.20}$$

where ${}^{t+\Delta t}\boldsymbol{u}^{\mathrm{iter}\,n}$ is used to define the increments at the n-th iteration of the coordinates of ${}^{t+\Delta t}\boldsymbol{s}$. To enable the iterative procedure to be carried on, a key point is the definition of the *system* tangent matrix. With the previously discussed assumptions that the mass matrix $\boldsymbol{M}$ and the damping matrix $\boldsymbol{C}_{\mathrm{d}}$ are constant throughout the iteration, it has the following expression, according to eq.(2.17)

$$ {}^{t+\Delta t}\boldsymbol{K}_T{}^{\mathrm{iter}\,n} = {}^{t+\Delta t}\left[\frac{\mathrm{d}\boldsymbol{\mathcal{R}}}{\mathrm{d}\boldsymbol{s}}\right]^{\mathrm{iter}\,n} = \frac{1}{\beta\Delta t}\left(\frac{1}{\Delta t}\boldsymbol{M} + \gamma\boldsymbol{C}_d\right) - \left(\frac{\mathrm{d}\,{}^{t+\Delta t}\boldsymbol{P}_{\mathrm{ext}}}{\mathrm{d}\,{}^{t+\Delta t}\boldsymbol{s}} + \frac{\mathrm{d}\,{}^{t+\Delta t}\boldsymbol{F}_{\mathrm{int}}}{\mathrm{d}\,{}^{t+\Delta t}\boldsymbol{s}}\right) \quad (2.21) $$

Notice that eq.(2.35) changes during iterations only if the internal structural forces $\boldsymbol{F}_{\mathrm{int}}$ or the external (aerodynamic) loads $\boldsymbol{P}_{\mathrm{ext}}$ are nonlinear with ${}^{t+\Delta t}\boldsymbol{s}$. The resolution of the following linear system is finally required

$$ {}^{t+\Delta t}\boldsymbol{K}_T{}^{\mathrm{iter}\,n}{}^{t+\Delta t}\boldsymbol{u}^{\mathrm{iter}\,n} = -{}^{t+\Delta t}\boldsymbol{\mathcal{R}}^{\mathrm{iter}\,n} \quad (2.22) $$

With eqs.(2.17) and (2.21) the iterative process shown in eq.(2.22) can be initialized evaluating ${}^{t+\Delta t}\boldsymbol{u}^{\mathrm{iter}\,n}$; the residual is then re-evaluated and, if it does not satisfy the convergence criterion, this evaluation is repeated.

An approach in this sense is to compare the norm of the residual with the biggest between external loads $\boldsymbol{P}_{\mathrm{ext}}$, internal forces $\boldsymbol{F}_{\mathrm{int}}$, inertial loads $\boldsymbol{M}\ddot{\boldsymbol{s}}$ and the damping loads $\boldsymbol{C}_d\,\dot{\boldsymbol{s}}$ [11]; a drawback of this method is that convergence is numerically difficult to be reached in those cases when very small external loads are acting, since each term of the residual is approaching to zero with the same order of magnitude of the comparison term (the residual itself); an option in this sense could be to select an absolute value of the residual (depending of the user experience on the problem) under which the solution is considered converged. Together with the residual, a check on the ratio of the norm of the iterative displacement $\boldsymbol{u}$ to the norm of the predictor's displacement can be performed.

In eq.(2.21) the term ${}^{t+\Delta t}\frac{\partial \boldsymbol{F}_{\mathrm{int}}}{\partial \boldsymbol{s}}$ is called *structural* tangent matrix, while ${}^{t+\Delta t}\frac{\partial \boldsymbol{P}_{\mathrm{ext}}}{\partial \boldsymbol{s}}$ is the *load* tangent matrix, that in the present study is related to the aerodynamic forces acting on the body. As stated in eq.(2.3), the external loads results as a function of not just displacement, but both of velocity and acceleration, indeed to perform the evaluation of the related *aerodynamic* tangent matrix this dependence has to be carried out. Before showing the models adopted to solve the coupling between aerodynamic and structural framework which enables to evaluate this matrix, a further refinement of the time-integration scheme is presented because this influences eq.(2.17) and so the evaluation of both the residual and the tangent matrices.

2.2.4 The generalized α-method

It is desirable in structural dynamics problems solved through step-by-step time integration algorithms to possess algorithmic damping. Particularly, it is necessary to control the dissipation on the high frequency modes since using standard FEM to discretize the spatial domain, the spatial resolution of these modes is poor. Thus, spurious high frequency modes should be damped out without affecting the low frequency modes, otherwise the accuracy of the results may be compromised. For example the Newmark β-method family algorithms provides high-frequency dissipation if a different choice of the parameters in eq.(2.11) is made, with the drawbacks of only a first-order accuracy in time and too much dissipation on the low frequency modes [25]. This has driven the formulation of improved methods which enable to overcome these limitations, mantaining second-order accuracy: the HHT-α method [55] and the WBZ-α method [115] are just some examples. All these schemes are particular cases of the more general *Generalized α-method* (GAM), which represents a family of implicit time-integration schemes, introduced in reference [25].

The scheme giving the relationships between the values of $\boldsymbol{s}$, $\dot{\boldsymbol{s}}$ and $\ddot{\boldsymbol{s}}$ is the same carried out for eqs.(2.9) and (2.10), but now the additional equation needed to close the problem is a modified version of the standard choice of eq.(2.13): the idea is to force the dynamic equilibrium using convex combinations of these variables, defining the following quantities

$$\begin{cases} {}^{t+\alpha_f\Delta t}\boldsymbol{s} = (1-\alpha_f)\ {}^{t}\boldsymbol{s} + \alpha_f\ {}^{t+\Delta t}\boldsymbol{s} \\ {}^{t+\alpha_f\Delta t}\dot{\boldsymbol{s}} = (1-\alpha_f)\ {}^{t}\dot{\boldsymbol{s}} + \alpha_f\ {}^{t+\Delta t}\dot{\boldsymbol{s}} \\ {}^{t+\alpha_m\Delta t}\ddot{\boldsymbol{s}} = (1-\alpha_m)\ {}^{t}\ddot{\boldsymbol{s}} + \alpha_m\ {}^{t+\Delta t}\ddot{\boldsymbol{s}} \end{cases} \tag{2.23}$$

where, differently from the previous section, the superscripts of the variables on the l.h.s. are here used to indicate a convex combination of the values at the beginning (t) and at the end ($t+\Delta t$) of the timestep, and not values evaluated at time $t+\alpha\Delta t$. Clearly, α_m=α_f=1 takes back to the Newmark β-method. The task is now to determine the relations between the algorithmic parameters α_m, α_f, γ and β to gain the desired numerical features.

It can be demonstrated [25], that the generalized α-method is second-order accurate, provided that

$$\gamma = \frac{1}{2} + \alpha_m - \alpha_f \tag{2.24}$$

The stability property of an algorithm applied to linear problems depends upon the eigenvalues of its amplification matrix, say λ_1, λ_2 and λ_3 where the spectral radius ϱ is defined as the maximum of those; as this is a function of the parameter $\Omega = \omega\Delta t$ where ω is the

generical natural frequency of the system and Δt is the timestep adopted, unconditionally stability is reached if $\varrho \leq 1$ for all $\Omega \in [0,\infty[$, which provides these relations

$$\begin{aligned} \alpha_m &\geq \alpha_m \geq \frac{1}{2} \\ \beta &\geq \frac{1}{4} + \frac{1}{2}(\alpha_m - \alpha_f) \end{aligned} \tag{2.25}$$

The spectral radius is also important because it is a measure of the numerical dissipation, i.e. a smaller spectral radius value corresponds to greater numerical dissipation; to obtain a numerical algorithm which gives the desired numerical damping at the high frequencies without an excessive dissipation in the low frequency region its spectral radius should be close to unity in this latter domain and smoothly decreasing as Ω increases. This property imposes restrictions on the values of the eigenvalues of the amplification matrix, requiring these smoothness design conditions

$$\begin{aligned} \beta &= \frac{1}{4}(1 + \alpha_m - \alpha_f)^2 \\ \varrho_\infty &= \frac{\alpha_m - \alpha_f - 1}{\alpha_m - \alpha_f + 1} \end{aligned} \tag{2.26}$$

where ϱ_∞ denotes the value of the spectral radius in the high-frequency limit ($\Omega \to \infty$) and as will be shortly shown, is the user-specified value to control high-frequency dissipation. The last relation is provided by the result that for a given level of high-frequency dissipation, i.e., for fixed ϱ_∞, low-frequency dissipation is minimized when

$$\alpha_m = 3\alpha_f - 1 \tag{2.27}$$

Combining eqs.(2.26) and (2.27), the values of α_m and α_f as a function of ϱ_∞ are obtained

$$\begin{aligned} \alpha_f &= \frac{1}{1 + \varrho_\infty} \\ \alpha_m &= \frac{2 - \varrho_\infty}{1 + \varrho_\infty} \end{aligned} \tag{2.28}$$

Eqs. (2.24), (2.26) and (2.28) completely define this algorithm unconditionally stable (for linear problems), second-order accurate and with optimal numerical damping combination. Defining the parameter ϱ_∞, that as stated before is related with the amount of numerical damping applied to the high frequencies of the system, the parameters of the scheme can be evaluated and the quantities in eq.(2.23) are thus known.

Application of this method to eq.(2.4) nevertheless is not straightforward. In fact in literature [25,28] this method has been developed mainly for linear cases in which the forces were

depending on time or linearly on displacements only. Thus, using the convex combination of the generalized coordinates as shown in eq.(2.23) would be completely identical to the case in which the convex combination is used for the different terms of the residual (that is, acting on the forces instead on the coordinates and their derivatives). However, in the present case, there is the internal force term depending nonlinearly from the displacement ($\boldsymbol{F}_{\text{int}}$) and the aerodynamic force term depending on t, $\boldsymbol{s}$, $\dot{\boldsymbol{s}}$ and $\ddot{\boldsymbol{s}}$ ($\boldsymbol{P}_{\text{ext}}$).
Focusing at first on the external forces, one option is to remain consistent with the evaluation in time dictated by eq.(2.23) (and with the original algorithm presented in reference [25]), i.e., to apply the convex combinations at the displacements and their derivatives and consequently take the forces

$$\boldsymbol{P}_{\text{ext}}\big|_{\left({}^{t+\alpha_f\Delta t}\boldsymbol{s},\, {}^{t+\alpha_f\Delta t}\dot{\boldsymbol{s}},\, {}^{t+\alpha_m\Delta t}\ddot{\boldsymbol{s}},\, t+\alpha_f\Delta t\right)} \tag{2.29}$$

If this approach is followed, in cases for which an explicit linear dependence of the external forces on the displacements, velocities, accelerations, and a dependence (not necessarily linear) on time, is found, the residual in eq.(2.4) can be written as

$$\boldsymbol{\mathcal{R}}(\boldsymbol{s},\dot{\boldsymbol{s}},\ddot{\boldsymbol{s}},t) = \left(\boldsymbol{M}-\boldsymbol{M}^A\right)\,\ddot{\boldsymbol{s}} + \left(\boldsymbol{C}_d-\boldsymbol{C}_d^A\right)\,\dot{\boldsymbol{s}} - \boldsymbol{K}^A\,\boldsymbol{s} - \left(\boldsymbol{P}_{\text{ext}}^A(t)-\boldsymbol{F}_{\text{int}}(\boldsymbol{s})\right) = \boldsymbol{0} \tag{2.30}$$

where $\boldsymbol{M}^A$, $\boldsymbol{C}_d^A$ and $\boldsymbol{K}^A$ express the linear dependence of the aerodynamic forces, and $\boldsymbol{P}_{\text{ext}}^A(t)$ represents the time dependence.

Applying this first approach also to the internal forces, the discrete equation for the residual can be written as:

$${}^{t+\Delta t}\boldsymbol{\mathcal{R}} = \boldsymbol{M}\,{}^{t+\alpha_m\Delta t}\ddot{\boldsymbol{s}} + \boldsymbol{C}_d\,{}^{t+\alpha_f\Delta t}\dot{\boldsymbol{s}} - \boldsymbol{P}_{\text{ext}}\big|_{\left({}^{t+\alpha_f\Delta t}\boldsymbol{s},\, {}^{t+\alpha_f\Delta t}\dot{\boldsymbol{s}},\, {}^{t+\alpha_m\Delta t}\ddot{\boldsymbol{s}},\, t+\alpha_f\Delta t\right)} + \boldsymbol{F}_{\text{int}}\big|_{\left({}^{t+\alpha_f\Delta t}\boldsymbol{s}\right)} \tag{2.31}$$

If the structural model is linear, then

$$\boldsymbol{F}_{\text{int}}\big|_{\left({}^{t+\alpha_f\Delta t}\boldsymbol{s}\right)} = {}^{t+\alpha_f\Delta t}\boldsymbol{F}_{\text{int}} \tag{2.32}$$

or rather is equivalent to consider a convex combination of the terms of the residual equation or the displacements. This no longer holds if the forces are nonlinear, arising the question of which form should be considered.

Generalized Energy-Momentum Method

The second possible approach, consisting to apply the convex combination directly to the edge values of the internal and external loads and not to the displacements, proves to be very important for the properties of the numerical scheme, in particular the stability one. In

fact, algorithms which are unconditionally stable for linear dynamics often lose this stability in the non-linear case [28,58,59,66,67,89,116], also when algorithmic damping is employed. A further criterion for the stability of time-integration algorithms (other than the eigenvalue analysis shown earlier for the Generalized α-method) is the conservation of energy, motivated by the theorem presented in reference [12] which states that, when applied to Hamiltonian systems, a numerical algorithm is stable in energy if the sum of kinetic and internal energies are bounded within each timestep relative to the external work, kinetic and internal energies in the previous timestep. The first algorithm which guaranteed unconditional stability in nonlinear dynamics of three-dimensional elastic bodies was the Energy-Momentum Method [105]. Its appeal has been redimensioned by some numerical experiments [35,66,67] which showed convergence problems and the necessity of considering small timesteps to obtain a stable and converged solution. These difficulties have been put in relation to high modes which are responsible of numerical collapse driven by an unphysical highly oscillatory response. It seems then advisable to introduce some form of damping in order to keep under control difficult cases [67].

A strategy to introduce controllable numerical dissipation to the Energy-Momentum Method, denoted as Generalized Energy-Momentum Method was presented in [66,68], applied to three-dimensional truss element and nonlinear dynamics of shells respectively. It includes numerical dissipation adopting the Generalized α-method to advance the solution within time and guarantees the energy conservation or decay using the convex combination of the internal forces at the beginning and at the end of the time interval, ${}^{t+\alpha_f \Delta t}\boldsymbol{F}_{\text{int}}$.

Unfortunately, is it not possible to automatically extend this approach to the aerodynamic forces, since the simultaneous dependence on acceleration, velocity and displacement does not make straightforward the use of a unique convex combination. In this effort, both the option ${}^{t+\alpha_f \Delta t}\boldsymbol{P}_{\text{ext}}$, namely:

$$ {}^{t+\alpha_f \Delta t}\boldsymbol{P}_{\text{ext}} = (1-\alpha_f)\, {}^{t}\boldsymbol{P}_{\text{ext}} + \alpha_f\, {}^{t+\Delta t}\boldsymbol{P}_{\text{ext}} \tag{2.33} $$

and the one previously introduced in eq.(2.29), have been used.
Summarizing, the algorithm adopted to discretize in time the equations of motion is the GEMM, whereas the aerodynamic term is evaluated both with a GAM and a GEMM-like approach. For the particular considered cases, no appreciable differences were noticed between the two approaches.

In the following, the derivation of the Newton process for convergence is shown for the

GEMM-like approach. The residual equation becomes:

$$
{}^{t+\Delta t}\boldsymbol{\mathcal{R}} = \boldsymbol{M}\ \left((1-\alpha_m)\ {}^{t}\ddot{\boldsymbol{s}} + \alpha_m\ {}^{t+\Delta t}\ddot{\boldsymbol{s}}\right) + \boldsymbol{C}_d\ \left((1-\alpha_f)\ {}^{t}\dot{\boldsymbol{s}} + \alpha_f\ {}^{t+\Delta t}\dot{\boldsymbol{s}}\right) - \\
(1-\alpha_f)\ {}^{t}\boldsymbol{P}_{\text{ext}} - \alpha_f\ {}^{t+\Delta t}\boldsymbol{P}_{\text{ext}} + (1-\alpha_f)\ {}^{t}\boldsymbol{F}_{\text{int}} + \alpha_f\ {}^{t+\Delta t}\boldsymbol{F}_{\text{int}} \quad (2.34)
$$

and the tangent matrix for the system is now

$$
{}^{t+\Delta t}\left[\frac{\mathrm{d}\boldsymbol{\mathcal{R}}}{\mathrm{d}\,\boldsymbol{s}}\right] = \frac{\alpha_m}{\beta\,\Delta t^2}\boldsymbol{M} + \frac{\alpha_f\,\gamma}{\beta\Delta t}\boldsymbol{C}_d - \alpha_f\left(\frac{\mathrm{d}\ {}^{t+\Delta t}\boldsymbol{P}_{\text{ext}}}{\mathrm{d}\ {}^{t+\Delta t}\boldsymbol{s}} - \frac{\mathrm{d}\ {}^{t+\Delta t}\boldsymbol{F}_{\text{int}}}{\mathrm{d}\ {}^{t+\Delta t}\boldsymbol{s}}\right) \quad (2.35)
$$

where the iteration superscript has been dropped for clarity. As already made for the β-Newmark case, for an iterative oriented implementation it is convenient to express the residual combining eq.(2.34) with the Bathe predictor in eq.(2.14), leading to

$$
{}^{t+\Delta t}\boldsymbol{\mathcal{R}} = \frac{1}{\beta\Delta t}\left(\frac{\alpha_m}{\Delta t}\boldsymbol{M} + \alpha_f\gamma\boldsymbol{C}_d\right)\left({}^{t+\Delta t}\boldsymbol{p} - {}^{t+\Delta t}\boldsymbol{p}_{\text{pred}}\right) + \\
\alpha_m\boldsymbol{M}\,{}^{t+\Delta t}\ddot{\boldsymbol{p}}_{\text{pred}} + \alpha_f\boldsymbol{C}_d\,{}^{t+\Delta t}\dot{\boldsymbol{p}}_{\text{pred}} + (1-\alpha_m)\boldsymbol{M}\ {}^{t}\ddot{\boldsymbol{p}} + (1-\alpha_f)\boldsymbol{C}_d\ {}^{t}\dot{\boldsymbol{p}} - \\
(1-\alpha_f)\left({}^{t}\boldsymbol{P}_{\text{ext}} - {}^{t}\boldsymbol{F}_{\text{int}}\right) - \alpha_f\left({}^{t+\Delta t}\boldsymbol{P}_{\text{ext}} - {}^{t+\Delta t}\boldsymbol{F}_{\text{int}}\right) \quad (2.36)
$$

As it can be seen, the residual expression can be divided in a term that doesn't vary during the iterative process to convergence, containing all the terms referring to the predictors and the initial time-point ${}^{t}\boldsymbol{p}$, and in another one with terms directly related to the end-time point ${}^{t+\Delta t}\boldsymbol{p}$ that gives a direct contribution to the tangent matrix; it is useful to give an expression of eq.(2.36) in this sense, ascertaining the nature of the term (inertial, damping and loads) as it follows

$$
{}^{t+\Delta t}\boldsymbol{R} = (\boldsymbol{MTX}_1 + \boldsymbol{MTX}_2)\,{}^{t+\Delta t}\boldsymbol{p} + \boldsymbol{VCT}_{\text{inert}} + \boldsymbol{VCT}_{\text{damp}} - \\
\boldsymbol{VCT}_6 - \alpha_f\left({}^{t+\Delta t}\boldsymbol{P}_{\text{ext}} - {}^{t+\Delta t}\boldsymbol{F}_{\text{int}}\right) \quad (2.37)
$$

where

$$\begin{cases} \boldsymbol{MTX}_1 = \dfrac{1}{\beta\Delta t}\dfrac{\alpha_m}{\Delta t}\boldsymbol{M} \\ \boldsymbol{MTX}_2 = \dfrac{1}{\beta\Delta t}\alpha_f\,\gamma\boldsymbol{C_d} \\ \boldsymbol{VCT}_{1a} = \boldsymbol{MTX}_1\,{}^{t+\Delta t}\boldsymbol{p}_{\text{pred}} \\ \boldsymbol{VCT}_{1b} = \boldsymbol{MTX}_2\,{}^{t+\Delta t}\boldsymbol{p}_{\text{pred}} \\ \boldsymbol{VCT}_2 = \alpha_m\boldsymbol{M}\,{}^{t+\Delta t}\ddot{\boldsymbol{p}}_{\text{pred}} \\ \boldsymbol{VCT}_3 = \alpha_f\boldsymbol{C_d}\,{}^{t+\Delta t}\dot{\boldsymbol{p}}_{\text{pred}} \\ \boldsymbol{VCT}_4 = (1-\alpha_m)\,\boldsymbol{M}\,{}^{t}\ddot{\boldsymbol{p}} \\ \boldsymbol{VCT}_5 = (1-\alpha_f)\,\boldsymbol{C_d}\,{}^{t}\dot{\boldsymbol{p}} \\ \boldsymbol{VCT}_6 = (1-\alpha_f)\left({}^{t}\boldsymbol{P}_{\text{ext}} - {}^{t}\boldsymbol{F}_{\text{int}}\right) \\ \boldsymbol{VCT}_{\text{inert}} = -\boldsymbol{VCT}_{1a} + \boldsymbol{VCT}_2 + \boldsymbol{VCT}_4 \\ \boldsymbol{VCT}_{\text{damp}} = -\boldsymbol{VCT}_{1b} + \boldsymbol{VCT}_3 + \boldsymbol{VCT}_5 \end{cases} \tag{2.38}$$

2.2.5 Structural Damping

The structural model provides the possibility to reproduce more consistently the dynamic behaviour taking into account the presence of structural damping, represented by the damping matrix $\boldsymbol{C}_{\text{d}}$; the approach consists in the extrapolation of structural modal damping from the system. Considering a problem with one degree of freedom, the unforced spring-damping-mass system is described by equation

$$m\,\ddot{s} + 2c\,\dot{s} + k\,s = 0 \tag{2.39}$$

being s the generic coordinate describing the motion, m the mass, c the damping coefficient and k the spring constant. Rearranging the equation, the canonical form is easily obtained

$$\ddot{s} + 2\zeta\omega_n\dot{s} + \omega_n^2 s = 0 \tag{2.40}$$

where ω_n represents the natural frequency of the system and ζ the damping factor. Once eq.(2.39) is stated in canonical form, is easy to choose the c damping coefficient since common values for the damping factor are in the range of $0.05 - 0.01$.

If the system has more than one degree of freedom, and the differential equations of motion are linear, it is possible, by means of the so called light damping approximation [45], to describe the evolution of the system decoupling the evolution of each natural mode. Thus,

for the generic i-th mode the following relation holds:

$$\ddot{q}_i + 2\zeta_i \omega_{n_i} \dot{q}_i + \omega_{n_i}^2 q_i = 0 \tag{2.41}$$

which in matrix form is written as

$$\ddot{\boldsymbol{q}} + \boldsymbol{C}_\Delta \, \dot{\boldsymbol{q}} + \boldsymbol{\Omega} \, \boldsymbol{q} = \boldsymbol{0} \tag{2.42}$$

The addition of damping to the lower frequencies influences the solution so it is introduced only if it is desired to model a physical phenomenon and in this sense eq.(2.41) represents a convenient strategy since it shows that is possible to set this damping factor for each mode independently.

The starting point is the generic n dimensional system which describe the dynamic behaviour of the degrees of freedom $\boldsymbol{s}$ of the structure

$$\boldsymbol{M} \, \ddot{\boldsymbol{s}} + \boldsymbol{C}_\mathrm{d} \, \dot{\boldsymbol{s}} + \boldsymbol{K} \, \boldsymbol{s} = \boldsymbol{0} \tag{2.43}$$

For linear systems, the matrices are constant, and it is possible to write the response as a superposition of elementary solutions through the modal coordinates $\boldsymbol{q}$:

$$\boldsymbol{s} = \boldsymbol{\Phi} \, \boldsymbol{q} \tag{2.44}$$

where $\boldsymbol{\Phi}$ is the modal matrix. Substituing eq.(2.44) in eq.(2.43) and pre-multiplying by $\boldsymbol{\Phi}^T$, it holds

$$\hat{\boldsymbol{M}} \, \ddot{\boldsymbol{q}} + \hat{\boldsymbol{C}} \, \dot{\boldsymbol{q}} + \hat{\boldsymbol{K}} \, \boldsymbol{q} = \boldsymbol{0} \tag{2.45}$$

where $\hat{\boldsymbol{M}}$ and $\hat{\boldsymbol{K}}$ are respectively the mass and stiffness modal matrices, both diagonal for the properties of the modal coordinates; the aims is thus to define $\boldsymbol{C}_d$ through $\hat{\boldsymbol{C}}$. Assuming that $\hat{\boldsymbol{C}}$ is diagonal, the equation for the generic i-th mode reads

$$\mu_i \ddot{q}_i + 2\zeta_i \mu_i \omega_{n_i} \dot{q}_i + \mu_i \omega_{n_i}^2 q_i = 0 \tag{2.46}$$

that differs from eq.(2.41) because generally the modal mass $\mu_i \neq 1$; anyway, for a known property, it holds

$$[\boldsymbol{\Phi}^T \hat{\boldsymbol{M}} \boldsymbol{\Phi}]_{\mathrm{ij}} = \delta_{\mathrm{ij}} \mu_i \tag{2.47}$$

where δ_{ij} is the Kronecker's delta. It is then possible to define the damping ratios ζ_i for each mode in this form and reconstruct the matrix $\boldsymbol{C}_d$ using the inverse of the relation in eq.(2.44) and left-multiplying by $\boldsymbol{\Phi}^{-T}$, namely:

$$\boldsymbol{C}_d = \boldsymbol{\Phi}^{-T} \, \hat{\boldsymbol{C}} \, \boldsymbol{\Phi}^{-1} \tag{2.48}$$

Actually the dynamic behaviour of a system is ruled by the most meaningful modes that are associated with the lower natural frequencies, so it can be preferable both from a computational and accuracy point of view to consider the previous process just for the n modes on which is significant to apply the damping. If N is the total number of degrees of freedom of the structure, $\boldsymbol{\Phi}$ is now an N×n matrix; eqs.(2.45) and (2.47) are thus still valid, but hold just for the first n modes, whereas eq.(2.48) it has no more sense since $\boldsymbol{\Phi}$ is not a square matrix. To perform a similar equivalence, but in a least square sense [32], the following operations are performed starting from eq.(2.44)

$$\begin{aligned} &\boldsymbol{\Phi}^T \boldsymbol{s} = \boldsymbol{\Phi}^T \boldsymbol{\Phi}\, \boldsymbol{q} \\ &\boldsymbol{T} = [\boldsymbol{\Phi}^T \boldsymbol{\Phi}]^{-1} \boldsymbol{\Phi}^T \\ &\boldsymbol{T}\boldsymbol{s} = \boldsymbol{q} \\ &\boldsymbol{C}_d = \boldsymbol{T}^T \hat{\boldsymbol{C}} \boldsymbol{T} \end{aligned} \tag{2.49}$$

2.3 Aerodynamic model

2.3.1 Introduction

In the present section will be presented the aerodynamic model adopted. The hypothesis of irrotational, non viscous and incompressible flow are assumed to be valid; in addition, non-linearities in the flow field like stall and dynamic stall are neglected. This flow model allow the existence of a potential function, the *velocity potential* Φ, such that its gradient is the flow velocity. The continuity equation in this circumstances reduces to the Laplace equation

$$\nabla^2 \Phi = 0$$

which is a linear, second order partial differential equation requiring the boundary condition of zero normal velocity on the body surface. This equation can be solved by means of different numerical methods. Since the Laplace equation is linear, particular solutions of this equation can be combined. A potential flow numerical code assumes certain types of singularities to describe the flow field; by their definition, these singularities satisfy the Laplace equation and have a strength which is found imposing the no-penetration boundary condition in a finite number of points over the aerodynamic body. The speed induced by the singularities produce a resultant flow at the control points whose normal component to the wing balances the normal component of the free stream velocity.

In order to establish a numerical solution to solve this aerodynamic problem, some steps have to be covered:

- selection of type (source, doublet or vortex) and number of singularity elements
- discretization of geometry (grid generation): once the basic solution elements are selected, the geometry of the problem has to be subdivided in such a way that it consists of these elements and that notable points useful for the prosecution are defined (for example control points, load points)
- calculation of influence coefficients used to impose the boundary conditions in the prescribed points (collocation points)
- statement of the Right Hand Side (RHS) of the matrix equation, that is the known portion of the flow (free-stream and wake contribution usually) in terms of velocity or potential depending on the type of boundary condition adopted (Dirichlet or Neumann)

- solve linear set of equations to find the strength of the unknown singularities
- evalutation of pressures and loads through Bernoulli theorem

In the following, the application of this strategy at the present problem is presented.

2.3.2 Geometry definition and evaluation of induced velocity

The decision is to choose as singularity the vortex ring element, adopting the Unsteady Vortex Lattice Method (UVLM) as aerodynamic model; its main advantage is the simple programming effort that it requires, which makes it preferable when operating with thin wings. This method treats the airfoil as a series of flat plates and neglects both thickness and viscous effects: however for most cases these effects offset each other producing good agreement between predictions and experimental data [14].

Each vortex ring is composed by four constant-strength vortex line segments with the same value of circulation Γ. The wing is discretized in an arbitrary number of quadrilateral aerodynamic panels subdividing it spanwise and chordwise; after that the ring elements are located over the wing in the way showed in Fig. 2.1: the leading segment of the vortex ring is placed on the panel's quarter chord line and the collocation point P (the point where the boundary condition is applied) is at the center of the three-quarter chord line (the normal vector $\mathbf{n}$ is also specified at this point). By placing the leading segment of the vortex ring at the quarter chord line of the panel the two-dimensional Kutta condition is satisfied along the chord (this result is demonstrated for the lumped-vortex element). In the same figure is shown how from the numerical point of view it would be useful to store these ring elements in rectangular patches with i,j indexing, from which is automatically possible to obtain, defining an arbitrary way to numerate the rings, a unique sequential counter K that scan all the vortex rings on the wing surface. The velocity induced at an arbitrary point P, obtainable from the Biot-Savart law, by the generical vortex segment of circulation Γ that points from vertex A to vertex B, is given by:

$$\boldsymbol{q}_{\mathrm{A,B}} = \frac{\Gamma}{4\pi h}(\cos\theta_1 - \cos\theta_2)\boldsymbol{e} \tag{2.50}$$

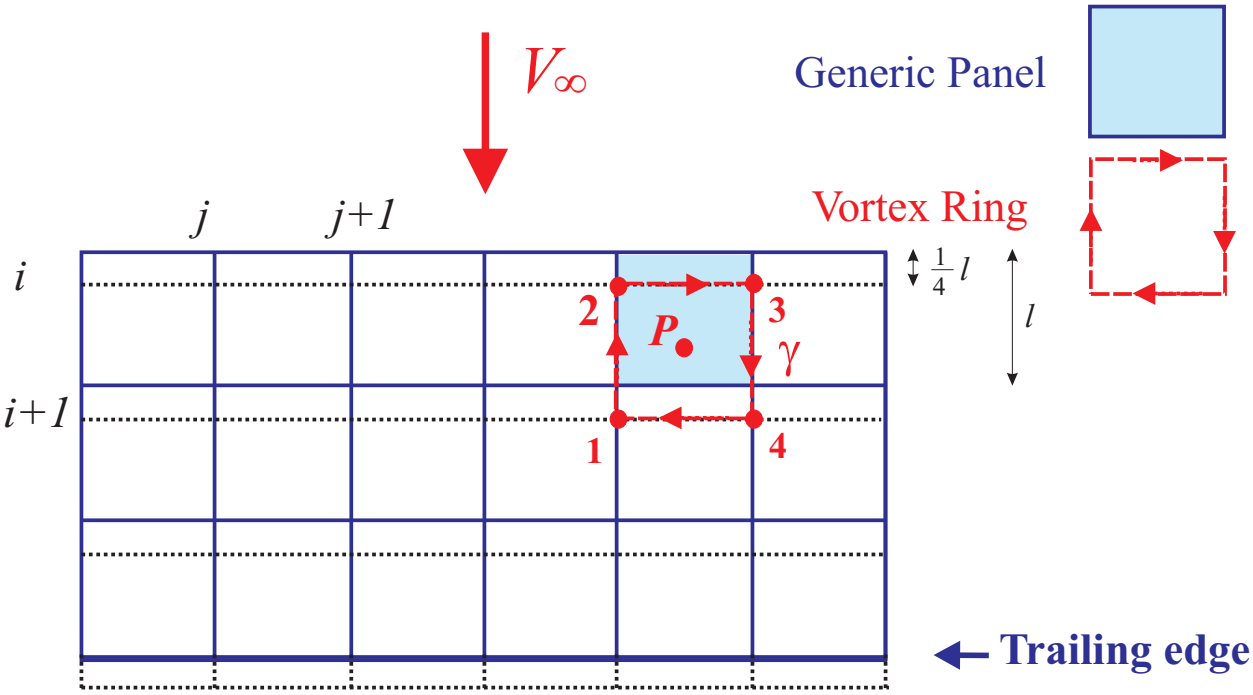

Fig. 2.1: Location of the vortex rings in the aerodynamic grid

with

$$
\begin{aligned}
\boldsymbol{e} = (e_\mathrm{x}, e_\mathrm{y}, e_\mathrm{z}) &= \frac{\boldsymbol{l}_{12} \times \boldsymbol{r}_1}{|\boldsymbol{l}_{12} \times \boldsymbol{r}_1|} \\
\boldsymbol{r}_1 &= \boldsymbol{r}_\mathrm{P} - \boldsymbol{r}_\mathrm{A} \\
\boldsymbol{r}_2 &= \boldsymbol{r}_\mathrm{P} - \boldsymbol{r}_\mathrm{B} \\
\boldsymbol{l}_{12} &= \boldsymbol{r}_\mathrm{B} - \boldsymbol{r}_\mathrm{A} \\
h &= r_1 \sin\theta_1 \\
\cos\theta_1 &= \frac{\boldsymbol{l}_{12} \cdot \boldsymbol{r}_1}{|\boldsymbol{l}_{12}||\boldsymbol{r}_1|} \\
\cos\theta_2 &= \frac{\boldsymbol{l}_{12} \cdot \boldsymbol{r}_2}{|\boldsymbol{l}_{12}||\boldsymbol{r}_2|}
\end{aligned}
\tag{2.51}
$$

Symbols are schematically shown in Fig. 2.2: $\boldsymbol{r}_\mathrm{A}$, $\boldsymbol{r}_\mathrm{A}$ and $\boldsymbol{r}_\mathrm{A}$ are the position vectors of points A,B and P, respectively; h is the perpendicular distance between P and the line AB and θ_1 and θ_2 are the included angles. The positive sign of Γ is defined accordingly to the right-hand rotation rule, as pointed out in Fig. 2.1. Calling $\boldsymbol{V}_{\mathrm{SI}_{\mathrm{km}}}$ the velocity induced by m-th body ring of unitary circulation in the k-th collocation (or control) point whose local normal direction is $\boldsymbol{n}_k$, it is possible to define the generic term of matrix of body influence

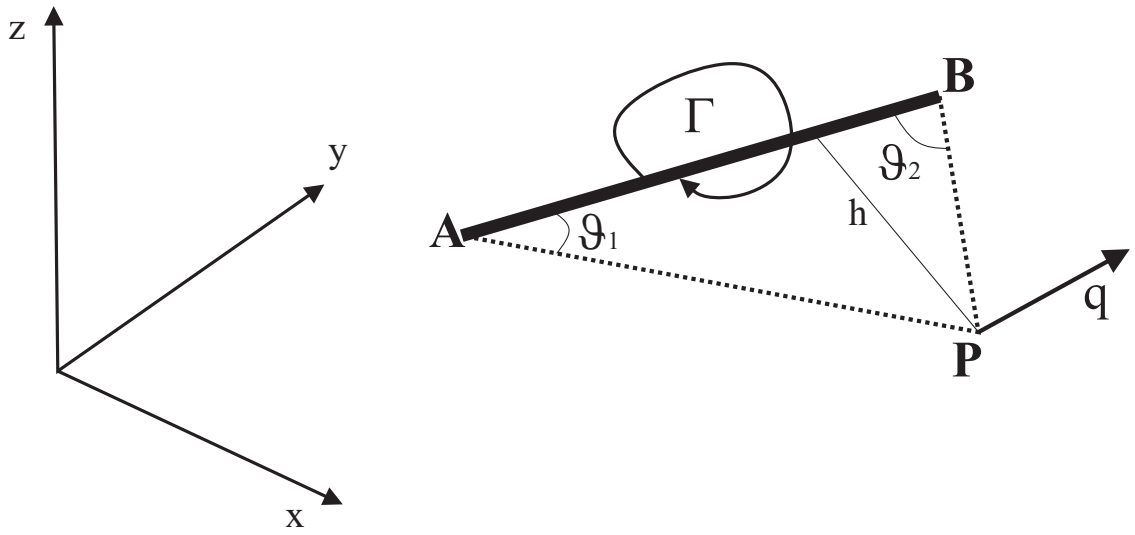

Fig. 2.2: Nomenclature adopted for the calculation of the induced velocity of a single vortex line

coefficients $\boldsymbol{A}$

$$a_{\mathrm{km}} = \boldsymbol{V}_{\mathrm{SI_{km}}} \cdot \boldsymbol{n}_k \tag{2.52}$$

If N is the total number of rings of the wing, this matrix has dimension N×N

$$\boldsymbol{A} = \begin{bmatrix} a_{11} & a_{12} & \dots & a_{1\mathrm{m}} & \dots & a_{1\mathrm{N}} \\ \dots & \dots & \dots & \dots & \dots & \dots \\ a_{\mathrm{k1}} & a_{\mathrm{k2}} & \dots & a_{\mathrm{km}} & \dots & a_{\mathrm{kN}} \\ \dots & \dots & \dots & \dots & \dots & \dots \\ a_{\mathrm{N1}} & a_{\mathrm{N2}} & \dots & a_{\mathrm{Nm}} & \dots & a_{\mathrm{NN}} \end{bmatrix}$$

2.3.3 Wake model

Now the wake has to be considered; assuming for a moment a stationary flow, it is prescribed that the trailing vortex of the last panels row is cancelled to satisfy the three-dimensional Kutta condition, that is $\gamma_{\mathrm{T.E.}} = 0$. This is done attempting to align the wake vortex panels (modelled as horseshoe elements) parallel to the local streamlines and imposing their strength equal to the strength of the corresponding shedding panel at the trailing edge ($\Gamma_{\mathrm{T.E.}} = \Gamma_{\mathrm{W}}$ for each wake panel) as showed in Fig. 2.3. The matrix which contains all the influence coefficients, the $\boldsymbol{A}$ matrix previously presented, can be completely evaluated.

For an unsteady flow a key role is played by the modelling of the wake. The most accurate model prescribes that each vortex moves with the local stream velocity since the

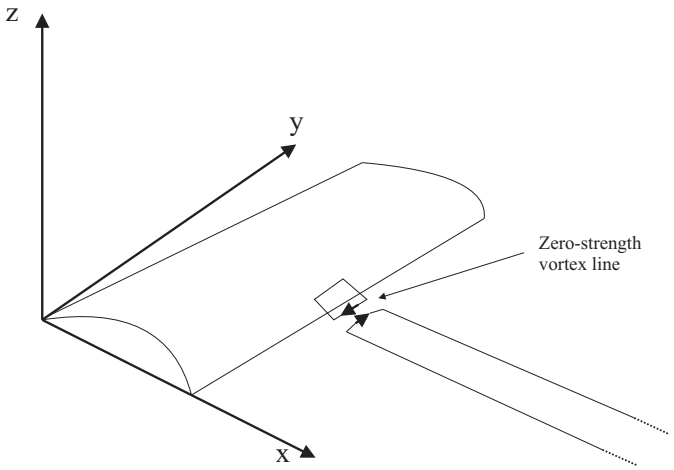

Fig. 2.3: Method of attaching an horseshoe vortex wake element to fulfill the Kutta condition (steady case)

vortex wake is force free, obtaining the so called "wake rollup"; however this approach is quite time consuming and so often a simplifying one, consisting on assuming a prescribed shape for the wake, is adopted.

In both cases, the wake is modelled with several rows of vortex ring elements of different strength (and not more with horseshoe elements like for the steady problem) and the wake shedding procedure is thought in a time-stepping tecnhique perspective: during the first timestep only the wing bound vortex rings exist (as pointed out in Fig. 2.1); consequently, there are no wake panels and the solution is easily found by specifying the zero normal flow boundary condition on the K collocation points. During the second timestep, the wing moves along its flight path and each trailing edge vortex panel sheds a wake ring with a vortex strength equal to its circulation in the previous timestep, automatically satisfying the Kelvin condition which prescribes no time variation of the circulation Γ around a fluid curve enclosing the wing and its wake. For the case of prescribed wake, it's enough to impose that each wake's point is convected by the free stream velocity and so the procedure can be continued at each successive timestep determining in such a way a wake of known geometry and known strength (assuming no decay in vortex, as Helmotz's theorems state, once the wake ring is shed it maintains its known intensity in the other timesteps).

On the other hand, if the free wake is modelled, at the end of each timestep, once the problem is solved and the unknown intensity of the circulation Γ of every ring of the body is known, the evaluation of the induced velocity (u,v,w) at each vortex ring corner point l is requested; after this calculation, the vortex elements are moved, other than for the contribution of the

free stream, by

$$(\Delta x, \Delta y, \Delta z)_l = (u, v, w)_l \cdot \Delta t \tag{2.53}$$

This is the only difference between the two methods, because once the wake geometry is defined, the calculation of influence matrices and so the solution of the problem at the following timestep are established in an identical manner.
For the numerical implementation of the wake shedding procedure, both prescribed and free, a subtle aspect is the specification of the position of the leading segment of the rings belonging to the first row of the wake (the closest to the body); the wake is presumably shed along the wing trailing edge so at a first estimate it can be placed on a generic point of the path where it has moved during the latest timestep; for the choice of the distance where it's located, the reference [62] suggests to place the leading corners of the rings shed in the considered timestep at a distance of 0.2-0.3 UΔt from the wing trailing edge (where U is the speed with which the wing moves and Δt is the timestep) to take in account in such a way the effective continuous wake vortex sheet geometry and so the correct induction, because it would produce an understimation the choice to put this points at the middle of the interval covered by the trailing edge in a timestep (as an average approach at the problem could suggest).

This strategy (in good agreement with experimental results for 2D case when a lumped vortex wake is adopted) however proved to result, after testing the model through simulations, in an unacceptable dipendance of the steady-state solution (in terms, for example, of the C_L value of the configuration), from the Δt chosen, being dependent from that the position where the leading segments of the shed wake rings are placed (with a strong consequence on the influence over the body). This drawback, encountered also in Ref.[29] is resolved considering that in the steady-state flow conditions all wake panels shed from a particular trailing-edge panel should have the same vortex strength, which equal to the strength of the shedding panel. The trailing and leading segments of the adjacent vortex rings of the wake should indeed cancel each other and only a horseshoe-like vortex has to remain, such that the situation returns the one pointed out in Fig. 2.3. The only way that this can happen is to place the two leading corners of the wake rings shed in the actual timestep at a quarter chord (of the corresponding shedding wing panel) distance from the trailing edge of the wing, so to make these corners coincide with the ones of the trailing segment of the trailing edge wing rings (as indeed happens in the steady model between the trailing-edge panel and its corresponding horseshoe vortex). In this way the position of the leading segment of the ring is univocally defined.

This strategy is shown in Fig. 2.4 where the blank spaces between rings are just used for clarity. The modelling of the wake is completed and so it is possible to evaluate the

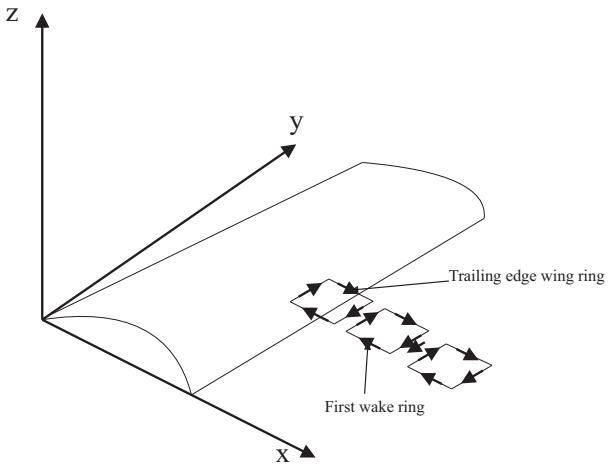

Fig. 2.4: Method of placing the wake rings at a typical trailing edge panel

contribution of each wake ring r-th to the local velocity in the k-th control point. It's interesting to notice that, on the contrary of the steady case, in the unsteady case only the body rings give a contribution to the $\boldsymbol{A}$ matrix of influence coefficients that multiplies the vector of unknown strengths $\boldsymbol{\Gamma}$. Each ring r of the wake contributes in fact just to the RHS of the boundary condition equation with the component of the wake-induced velocity $\boldsymbol{V}_{\mathrm{WI}}$ along the direction $\boldsymbol{n}_{\mathrm{k}}$ that can be easily evaluated with eq.(2.50) and is stored in the $\boldsymbol{A}_{\mathrm{w}}$ matrix of wake influence coefficients

$$\boldsymbol{A}_{\mathrm{w}} = \begin{bmatrix} a_{\mathrm{w,11}} & a_{\mathrm{w,12}} & \dots & a_{\mathrm{w,1r}} & \dots & a_{\mathrm{w,1R}} \\ \dots & \dots & \dots & \dots & \dots & \dots \\ a_{\mathrm{w,k1}} & a_{\mathrm{w,k2}} & \dots & a_{\mathrm{w,kr}} & \dots & a_{\mathrm{w,kR}} \\ \dots & \dots & \dots & \dots & \dots & \dots \\ a_{\mathrm{w,N1}} & a_{\mathrm{w,N2}} & \dots & a_{\mathrm{w,Nr}} & \dots & a_{\mathrm{w,NR}} \end{bmatrix}$$

with

$$a_{\mathrm{w,kr}} = \boldsymbol{V}_{\mathrm{WI}_{kr}} \cdot \boldsymbol{n}_{\mathrm{k}} \tag{2.54}$$

where N is always the number of body rings while R is the total number of wake rings at the considered timestep. Before going on in the description of the model, it's worth to highlight a few important aspects concerning the roll up modelling.

The use of discrete vortex segments to account for the vorticity in the shed wake originates accuracy issues due to the singularity that arises from eq.(2.50) when the induced point

is located very close to the vortex line, leading to unphysically values of the local induced velocity assigned to it. This usually occurs when a wake encounters another body or when the wake has an intense roll-up causing intersections in the wake itself. Aeroelastic response of a highly deformable wing seems to emphasize this aspect, since the trailing edge of the body changes significantly position with time thus causing a variation in the position where the wake is shed.

In order to prevent this kind of numerical problems and lack of accuracy, many techniques have been introduced, as for example the vortex-core model. This model comes from the rotary wing field, where the blade tip vortex interaction with the oncoming rotating blades has a significant impact on loads; the basic idea is that [74] the formation of the wake behind any lifting surface must be considered as a viscous phenomenon, with the vorticity contained in the vortex core diffused radially outward with time. This observation is corroborated, for example, by experimental measurements of the distribution of tangential velocity surrounding a tip vortex shed from a blade at various wake ages [73], which show how the distance between two velocity peaks, a measure of the size of the region where vorticity is concentrated, increases with time. According to a potential theory, this region is infinitesimal because all the vorticity is concentrated along the axis of the vortex filament and this leads to singularity in the evaluation of the Biot-Savart law near the vortex; in a more realistic model, this segment should have an inner part, that is a finite core, where the flow rotates almost as a solid body whereas in the outer part behaves almost as a potential flow, as depicted in Fig. 2.5. With this line of reasoning, it's possible to define the core radius r_c both

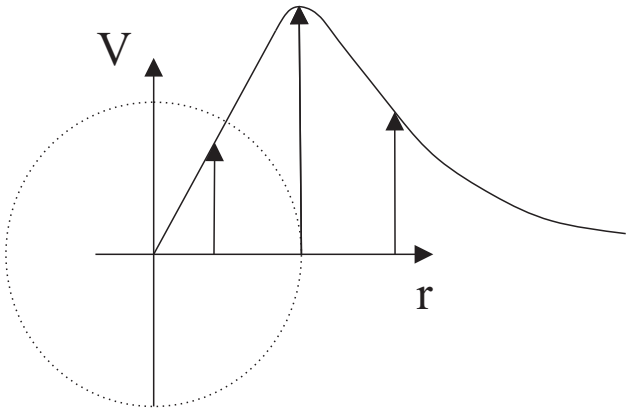

Fig. 2.5: 2-D tangential velocity profile inside a tip vortex

as the radial location where the tangential speed induced by the vortex has a maximum and as the boundary from the inner rotational flow field and the outer potential flow. Now that

the physical meaning of the sought de-singularization of the induction expression is pointed out, a revisited version of the Biot-Savart law [73] is presented in eq.(2.55)

$$\boldsymbol{V} = \frac{\Gamma}{4\pi} \frac{h}{(r_c^{2n} + h^{2n})^{\frac{1}{n}}} (\cos\theta_1 - \cos\theta_2) \cdot \boldsymbol{e} \tag{2.55}$$

where the notation is the same of eq.(2.50) and it can easily be seen that the singularity presented in the original law is removed by the introduction of the core radius, which enables to model a profile velocity similar to that on of Fig. 2.5; n defines the particular velocity profile among the family of algebraic models proposed by Vatistas [111], which show a good comparison with the measured swirl velocities [72].

The size of core radius is still an open problem, since the literature for the rotary wing shows a big variety of experimental results for different particular cases (mainly referred to the tip vortex structure, which has presumably a different evolution than the vortices shed from the inner part of the aerodynamic body) and doesn't give general instructions for a proper estimate, suggesting semi-empirical models to be validated through experimental measurements. Moreover, this dimension is not constant because of a diffusive growth with time: considering a vortex tube, it is known that its strength (given by the circulation around it) has to be constant (second Helmholtz theorem), which implies that as the vorticity diffuses because of the viscosity its cross-section has to increase. Another source of change in the core dimension is the strain of the vortex filaments with a consequent stretching or contraction process that determines a change in the vorticity of the flow field (according to the vorticity equation) and indeed a new radius; the significance of this phenomenon is mainly related to conditions typical of rotary wings, such roll up of tip vortices shed from lateral edges of a rotor disk in forward flight or descending flight with wake distortions caused by blade/vortex interaction [5], so in the present analysis is taken into account only the diffusive contribution to the vortex core dimension. An estimate of the growth rate can be made using the Lamb-Oseen model [69] , that is a solution of the one-dimensional (axial and radial velocity are assumed to be zero), laminar, Navier-Stokes equations, with the hypothesis of absence of an external velocity gradient which can cause stretching and so affect the core development; once the velocity profile is analitically obtained, the core radius is by definition the radial location where the swirl velocity has a maximum and so can be obtained by differentiating the speed with respect to r and setting the derivative to zero. The expression of the core radius so found is

$$r_c = \sqrt{4\alpha\nu t} \tag{2.56}$$

where ν is the kinematic viscosity and α is the Oseen parameter and has a value of 1,25643

[73]. This equation predicts the way the core radius varies taking in account just molecular diffusion; actually after an initial laminar behavior, the vortex progressively becomes turbolent and the diffusion of vorticity contained in it is much quicker than using eq.(2.56). It is possible to give a measure of the tendency toward turbulance generation with the vortex Reynolds number, a parameter defined as $Re_\nu = \frac{\Gamma_\nu}{\nu}$ where Γ_ν is the circulation of the considered vortex. The vortex Reynolds number allows to introduce the average turbulent viscosity coefficient [107] which is given by $\delta = 1 + a_1\left(\frac{Re_\nu}{\nu}\right)$, where a_1 is obtained through experimental observations and correlation studied proving to have an average value of 2×10^{-4} for rotating wings and 5×10^{-5} for fixed wings [5]. With this relations δ is known (and constant as the vortex ages in the flow since its circulation is conserved) and eq.(2.56), considering also the turbulent diffusion, becomes

$$r_c = \sqrt{4\delta\alpha\nu(t - t_0)} \tag{2.57}$$

where with the introduction of t_0 it has been hypothesized that the vortex has a starting radius immediately after its formation. Considering the typical values of the physical quantities involved, it can be observed that in a real flow the viscous diffusion process occurs 100 times faster than what would be expected on the basis of only molecular diffusion. A final comment involves the rate of growth of the vortex core that as is pointed out in eq.(2.57) is proportional to the square root of time, revealing how for older wake ages the core grows less: this is consistent with experimental observations which show especially for rotor vortices how they can exist persistently as coherent structures.

The other important aspect is related to the issue of reducing as much as possible the time needed to update at each timestep the new geometry of the wake; as said before, vortex filaments are choosen as singularity to simulate the vorticity field, but it has been demonostrated [54] that an equivalence subsists between a general surface doublet distribution and a surface vortex distribution whose order is one less than the order of the doublet one plus a vortex ring whose strength is equal to the edge value of the doublet distribution; so in this particular case one can arbitrarily substitutes a vortex ring of intensity Γ with a doublet panel with constant strength μ=Γ. This is made to take advantage of the diminishing influence of the inducing singularity as its distance from the point of evaluation increases, which in turn allows to approximate the quadrilateral panel (in this case, thanks to the equivalence, the ring) with an area A by a point doublet when the point of interest P is far from the center of the element. Usually the approximation can be assumed valid when the distance is more than 3-5 average panels diameters [62]. In order to formulate the induction

of a point source, its position and orientation (given by the direction $\boldsymbol{n}$) are requested to be known: the first is assumed as the center of the element and the second is given by its normal following the convention depicted in Fig. 2.6. In these calculations, as the geometry of the free wake consists no more of planar rings, a medium plane is assumed.

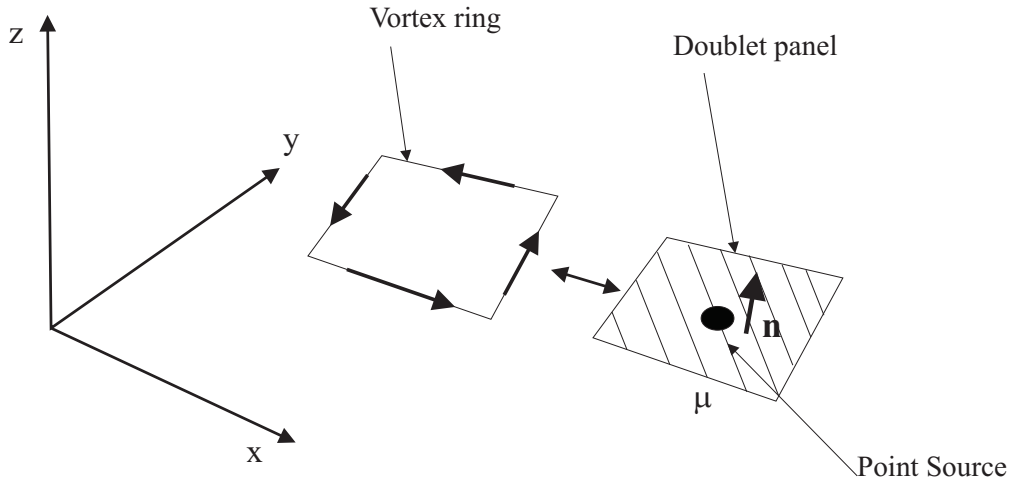

Fig. 2.6: Equivalence and conventions for the far field approximation

The speed induced by a generical doublet distribution depends explicitly from the direction of the normal to its plane; to give a general expression of the induced velocity in the generical point P by a point doublet of arbitrary orientation $\boldsymbol{n}$=(n_{x},n_{y},n_{z}), three generic doublet elements aligned with the absolute coordinate directions and with strength μ_{x}, μ_{y} and μ_{z} respectively are considered, where

$$\begin{aligned} \mu_{\mathrm{x}} &= \Gamma A n_{\mathrm{x}} \\ \mu_{\mathrm{y}} &= \Gamma A n_{\mathrm{y}} \\ \mu_{\mathrm{z}} &= \Gamma A n_{\mathrm{z}} \end{aligned} \tag{2.58}$$

In eqs.(2.59),(2.60) and (2.61) are given the expressions of the scalar components of the velocity $\boldsymbol{V}_{\mathrm{x}}$, $\boldsymbol{V}_{\mathrm{y}}$ and $\boldsymbol{V}_{\mathrm{z}}$ induced by the generic unit doublet point which orientation is

respectively along x, y and z direction

$$\begin{aligned} u_{\mathrm{x}} &= -\frac{1}{4\pi}\frac{(y-y_0)^2+(z-z_0)^2-2(x-x_0)^2}{[(x-x_0)^2+(y-y_0)^2+(z-z_0)^2]^{\frac{5}{2}}} \\ v_{\mathrm{x}} &= \frac{3}{4\pi}\frac{(y-y_0)(x-x_0)}{[(x-x_0)^2+(y-y_0)^2+(z-z_0)^2]^{\frac{5}{2}}} \\ w_{\mathrm{x}} &= \frac{3}{4\pi}\frac{((z-z_0)(x-x_0)}{[(x-x_0)^2+(y-y_0)^2+(z-z_0)^2]^{\frac{5}{2}}} \end{aligned} \tag{2.59}$$

$$\begin{aligned} u_{\mathrm{y}} &= \frac{3}{4\pi}\frac{(y-y_0)(x-x_0)}{[(x-x_0)^2+(y-y_0)^2+(z-z_0)^2]^{\frac{5}{2}}} \\ v_{\mathrm{y}} &= -\frac{1}{4\pi}\frac{(x-x_0)^2+(z-z_0)^2-2(y-y_0)^2}{[(x-x_0)^2+(y-y_0)^2+(z-z_0)^2]^{\frac{5}{2}}} \\ w_{\mathrm{y}} &= \frac{3}{4\pi}\frac{(z-z_0)(y-y_0)}{[(x-x_0)^2+(y-y_0)^2+(z-z_0)^2]^{\frac{5}{2}}} \end{aligned} \tag{2.60}$$

$$\begin{aligned} u_{\mathrm{z}} &= \frac{3}{4\pi}\frac{(z-z_0)(x-x_0)}{[(x-x_0)^2+(y-y_0)^2+(z-z_0)^2]^{\frac{5}{2}}} \\ v_{\mathrm{z}} &= \frac{3}{4\pi}\frac{(y-y_0)(x-x_0)}{[(x-x_0)^2+(y-y_0)^2+(z-z_0)^2]^{\frac{5}{2}}} \\ w_{\mathrm{z}} &= -\frac{1}{4\pi}\frac{(x-x_0)^2+(y-y_0)^2-2(z-z_0)^2}{[(x-x_0)^2+(y-y_0)^2+(z-z_0)^2]^{\frac{5}{2}}} \end{aligned} \tag{2.61}$$

Finally the velocity $\boldsymbol{V}$ induced in the point P by the point doublet is given by

$$\boldsymbol{V} = \mu_{\mathrm{x}}\boldsymbol{V}_{\mathrm{x}} + \mu_{\mathrm{y}}\boldsymbol{V}_{\mathrm{y}} + \mu_{\mathrm{z}}\boldsymbol{V}_{\mathrm{z}} \tag{2.62}$$

Another option to reduce the computational cost is the truncation of the wake domain: a threshold is defined so that beyond that distance the contribution of the wake on the local velocity of the control points over the body is assumed negligible and so there's no need to update the *far wake* geometry; this wake truncation is thought to be sufficiently reliable because here there's only interest in the wake influence over the body, and this considerably diminishes with the distance as stated before.

2.3.4 Boundary Condition

In order to be able to write the wall tangency condition, which states the *no normal velocity* condition on the control points over the body, all the contribution have to be taken into account: the self-induced velocity $\boldsymbol{V}_{\mathrm{SI}}$, the wake-induced velocity $\boldsymbol{V}_{\mathrm{WI}}$ and the kinematic velocity $\boldsymbol{V}_{\mathrm{KIN}}$. The last one is the velocity due to the motion of the wing, as viewed in the body frame of reference, and can be expressed as

$$\boldsymbol{V}_{\mathrm{KIN}} = \boldsymbol{V}_0 + \boldsymbol{\Omega} \wedge \boldsymbol{r} + \boldsymbol{V}_{\mathrm{rel}} \tag{2.63}$$

where $\boldsymbol{V}_0$ is the velocity of the (x,y,z) system's origin, $\boldsymbol{r}$ is the position vector, $\boldsymbol{\Omega}$ is the rate of rotation of the body's frame of reference and $\mathbf{V}_{\mathrm{rel}}$ is an additional contribution that is present when the points of the wing don't experience just a rigid motion, that is the wing is elastically deformed

In the present treatise the motion considered is a pure translation, i.e. $\boldsymbol{\Omega}$=0, but an important contribution to the loads and so to the dynamic behaviour of the structure is given by the term $\boldsymbol{V}_{\mathrm{rel}}$.

At the present stage is possible to write in a matrix form the equation that gives the unknown strengths for each k-th vortex ring

$$\boldsymbol{A\Gamma} = \boldsymbol{RHS} \tag{2.64}$$

where $\boldsymbol{A}$ is the matrix of body influence previously defined, $\boldsymbol{\Gamma}$ is the array containing the unknowns

$$\boldsymbol{\Gamma} = \begin{bmatrix} \Gamma_1 \\ \Gamma_2 \\ \dots \\ \Gamma_{\mathrm{k}} \\ \dots \\ \Gamma_{\mathrm{N}} \end{bmatrix}$$

and $\boldsymbol{RHS}$ is the vector containing the known part of the normal velocity components

$$\boldsymbol{RHS} = \begin{bmatrix} RHS_1 \\ RHS_2 \\ \dots \\ RHS_{\mathrm{k}} \\ \dots \\ RHS_{\mathrm{N}} \end{bmatrix}$$

with $RHS_{\mathrm{k}} = -(\boldsymbol{V}_{\mathrm{WI}} + \boldsymbol{V}_{\mathrm{KIN}})_{\mathrm{k}} \cdot \boldsymbol{n}_{\mathrm{k}}$.

2.3.5 Evaluation of Loads

Once solved the linear set of equations, next step is the evaluation of pressure p_k over each panel and subsequently the lift force applied in the load points. The Bernoulli equation for incompressible and irrotational flow with the hypothesis of negligible body force states that the sum of the left-hand side terms of eq.(2.65) are a function of time only

$$\frac{p}{\rho} + \frac{q^2}{2} + \frac{\partial \Phi}{\partial t} = C(t) \tag{2.65}$$

where p is the pressure, ρ is the density, q is the local fluid velocity and Φ its potential. Evaluating the left-hand side of eq.(2.65) in two points of the fluid, an arbitrary point and a reference point at infinity (where $\phi = 0$), eq.(2.66) is obtained

$$\frac{p_\infty - p}{\rho} = \frac{q^2}{2} + \frac{\partial \Phi}{\partial t} \tag{2.66}$$

The pressure difference between the upper and lower surfaces is then

$$\Delta p = p_{\mathrm{l}} - p_{\mathrm{u}} = \rho \left(\left(\frac{Q_{\mathrm{t}}^2}{2} \right)_{\mathrm{l}} - \left(\frac{Q_{\mathrm{t}}^2}{2} \right)_{\mathrm{u}} + \left(\frac{\partial \Phi}{\partial t} \right)_{\mathrm{l}} - \left(\frac{\partial \Phi}{\partial t} \right)_{\mathrm{u}} \right) \tag{2.67}$$

The tangential velocity component Q_t can be developed in two arbitrary directions r and m (chordwise and spanwise for example) such that

$$\begin{aligned} Q_{\mathrm{t_r}} &= (\boldsymbol{V}_{\mathrm{WI}} + \boldsymbol{V}_{\mathrm{KIN}}) \cdot \boldsymbol{\tau}_{\mathrm{r}} \pm \frac{\partial \Phi}{\partial \tau_{\mathrm{r}}} \\ Q_{\mathrm{t_m}} &= (\boldsymbol{V}_{\mathrm{WI}} + \boldsymbol{V}_{\mathrm{KIN}}) \cdot \boldsymbol{\tau}_{\mathrm{m}} \pm \frac{\partial \Phi}{\partial \tau_{\mathrm{m}}} \end{aligned} \tag{2.68}$$

where the $\pm$ stands for under and above the surface, respectively. The last contribute, that is the tangential velocity due to the wing vortices, can be approximated considering that a relation exists between the potential and the circulation Γ of the ring. Recalling the i,j indexing shown in Fig.2.1, the following holds for the leading-edge panels

$$\begin{aligned} \pm \frac{\partial \Phi}{\partial \tau_{\mathrm{r}}} &\approx \pm \frac{\Gamma_{\mathrm{i,j}}}{2\Delta c_{\mathrm{i,j}}} \\ \pm \frac{\partial \Phi}{\partial \tau_{\mathrm{m}}} &\approx \pm \frac{\Gamma_{\mathrm{i,j}}}{2\Delta b_{\mathrm{i,j}}} \end{aligned} \tag{2.69}$$

while for all the panels behind them (making use of a first order finite difference scheme for the differentiation)

$$\begin{aligned} \pm \frac{\partial \Phi}{\partial \tau_{\mathrm{r}}} &\approx \pm \frac{\Gamma_{\mathrm{i,j}} - \Gamma_{\mathrm{i\text{-}1,j}}}{2\Delta c_{\mathrm{i,j}}} \\ \pm \frac{\partial \Phi}{\partial \tau_{\mathrm{m}}} &\approx \pm \frac{\Gamma_{\mathrm{i,j}} - \Gamma_{\mathrm{i,j\text{-}1}}}{2\Delta b_{\mathrm{i,j}}} \end{aligned} \tag{2.70}$$

where $\Delta c_{\mathrm{i,j}}$ and $\Delta b_{\mathrm{i,j}}$ are the panel lengths in the r and m directions and $\boldsymbol{\tau}_r$ and $\boldsymbol{\tau}_m$ are the panel tangential vectors in the r and m directions (of course they are different for each panel and the i, j subscript is dropped for the sake of simplicity). The time derivative of potential in eq.(2.67) can then be obtained, leading to

$$\pm\frac{\partial\Phi}{\partial t} = \pm\frac{\partial}{\partial t}\frac{\Gamma_{\mathrm{i,j}}}{2} \tag{2.71}$$

Substituting these terms into the eq.(2.67) the pressure difference over the generical panel is evaluated

$$\begin{aligned}\Delta p_{\mathrm{k}} = \Delta p_{\mathrm{i,j}} = \rho[\boldsymbol{V}_{\mathrm{WI}} + \boldsymbol{V}_{\mathrm{KIN}}] \cdot \boldsymbol{\tau}_{\mathrm{r}} \frac{\Gamma_{\mathrm{i,j}} - \Gamma_{\mathrm{i\text{-}1,j}}}{\Delta c_{\mathrm{i,j}}} \\ + \rho[\boldsymbol{V}_{\mathrm{WI}} + \boldsymbol{V}_{\mathrm{KIN}}] \cdot \boldsymbol{\tau}_{\mathrm{m}} \frac{\Gamma_{\mathrm{i,j}} - \Gamma_{\mathrm{i,j\text{-}1}}}{\Delta b_{\mathrm{i,j}}} + \rho\frac{\partial\Gamma_{\mathrm{i,j}}}{\partial t}\end{aligned} \tag{2.72}$$

for the panels behind the leading edge, while for the leading edge panels it is

$$\Delta p_{\mathrm{k}} = \rho\left\{[\boldsymbol{V}_{\mathrm{WI}} + \boldsymbol{V}_{\mathrm{KIN}}] \cdot \boldsymbol{\tau}_{\mathrm{r}} \frac{\Gamma_{\mathrm{i,j}}}{\Delta c_{\mathrm{i,j}}} + [\boldsymbol{V}_{\mathrm{WI}} + \boldsymbol{V}_{\mathrm{KIN}}] \cdot \boldsymbol{\tau}_{\mathrm{m}} \frac{\Gamma_{\mathrm{i,j}}}{\Delta b_{\mathrm{i,j}}} + \frac{\partial\Gamma_{\mathrm{i,j}}}{\partial t}\right\} \tag{2.73}$$

Then its contribution to the loads in terms of the force vector is

$$\Delta\boldsymbol{F}_k = (\Delta p \Delta S)_k \boldsymbol{n}_k \tag{2.74}$$

which directly takes to the expression of the lift produced by each panel $\Delta\mathbf{L}$ projecting eq.(2.74) along the lift direction $\boldsymbol{n}_{\mathrm{L}}$.

2.4 Aero-Structural Coupling

In Sec. 2.3 it was discussed the aerodynamic model considered for this study and how the evaluation of loads could be carried out. In this section the goal is to express the aerodynamic loads so that they can be combined with the dynamic model presented in Sec. 2.2 in order to formulate the aeroelastic problem, that is the dependence of the aerodynamic loads from displacements of the structural nodes and their derivatives is stressed out.

2.4.1 New expression of the boundary condition

The starting point to obtain the sought expression is the boundary condition, enforced in the control points; recalling its matrix formulation from eq.(2.64), with the same notation it is

$$\boldsymbol{A\Gamma} = \boldsymbol{RHS} \tag{2.75}$$

where $\boldsymbol{A}$ is body influence coefficients matrix and $\boldsymbol{\Gamma}$ is the array with the unknown circulation on the rings of the body. It is worth to highlight the various contributions to the $\boldsymbol{RHS}$ vector. The first contribution can be written as

$$\boldsymbol{RHS}_1 = -\boldsymbol{A}_w\boldsymbol{\Gamma}_w \tag{2.76}$$

where $\boldsymbol{A}_w$ is the wake influence coefficients matrix and $\boldsymbol{\Gamma}_w$ is the vector with the strength of the wake singularities, both completely defined from the previous time steps calculations. The second term is the free stream contribution

$$\boldsymbol{RHS}_2 = -\boldsymbol{V}_\infty^n \tag{2.77}$$

where $\boldsymbol{V}_\infty^{\mathrm{n}}$ is the component of the free stream velocity along the normal to the ring. In order to evaluate this term, it's useful to consider Fig.2.7, where is depicted the k-th body ring with the position of the control point and a sketch of both the deformed and undeformed configurations. Unit vector $\boldsymbol{i}$ is parallel to the free stream, while $\boldsymbol{i}^{\mathrm{S}}$ is the direction of the free stream projected to the undeformed ring plane. By definition, the k-th element of $\boldsymbol{V}_\infty^{\mathrm{n}}$ is given by $V_\infty \boldsymbol{i}\cdot\boldsymbol{n}_k$, where $\boldsymbol{n}_k$ is the normal to the ring in its *actual* configuration, and the following holds

$$\boldsymbol{i}\cdot\boldsymbol{n}_{\mathrm{k}} = \cos\left(\frac{\pi}{2} - \alpha^{\mathrm{k}}\right) = \sin\alpha^{\mathrm{k}} = \sin\left(\overline{\alpha}^{\mathrm{k}} + \beta^{\mathrm{k}}\right) = \sin\overline{\alpha}^{\mathrm{k}}\cos\beta^{\mathrm{k}} + \cos\overline{\alpha}^{\mathrm{k}}\sin\beta^{\mathrm{k}} \tag{2.78}$$

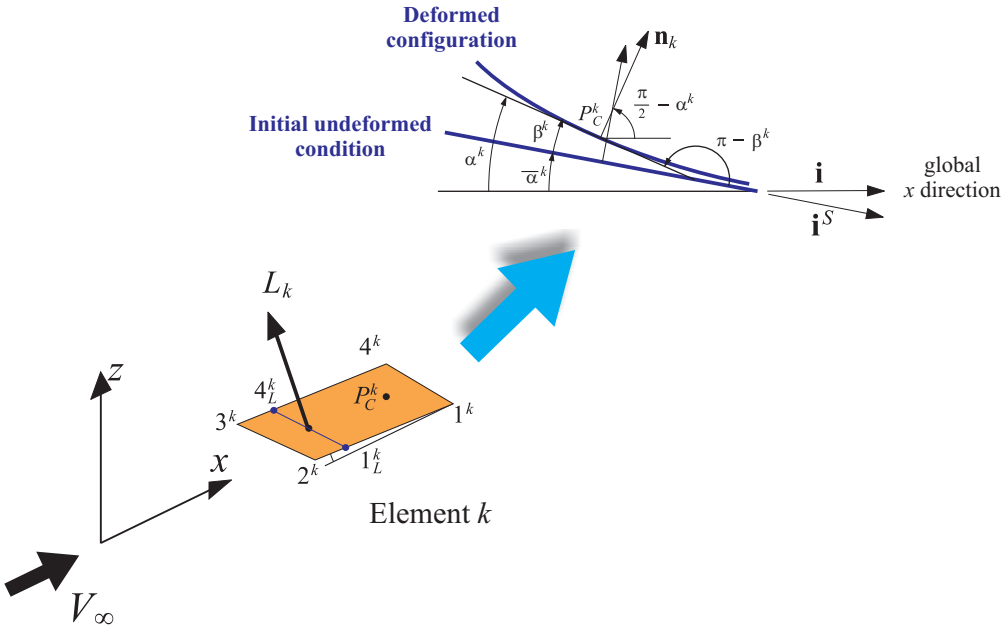

Fig. 2.7: Geometry and local normal of the body ring

being $\overline{\alpha^{\mathrm{k}}}$ the angle of attack of ring k in the undeformed configuration and the angles α^{k} and β^{k} are explained in Fig.2.7. Under the assumption of small angles, it's easy to see that

$$\begin{aligned} &\cos\overline{\alpha}^{\mathrm{k}} \approx 1 \\ &\cos\beta^{\mathrm{k}} \approx 1 \\ &\sin\beta^{\mathrm{k}} \approx \tan\beta^{\mathrm{k}} = -\tan\left(\pi - \beta^{\mathrm{k}}\right) \end{aligned} \tag{2.79}$$

A synthetic expression of eq.(2.77) can be given, discerning the different meanings of the terms involved

$$V_\infty \boldsymbol{i} \cdot \boldsymbol{n}_k = V_{\infty,0}^{n_k} + V_{\infty,d}^{n_k} \tag{2.80}$$

where $V_{\infty,0}^{n_k} = V_\infty \sin\overline{\alpha}^k$ is the k-th element of $\boldsymbol{V}_{\infty,0}^{n}$, and is related to just the change in the rigid angle of attack (*rigid aoa*). The other term $V_{\infty,d}^{n_k}$ is the contribution of the free stream due to the deformation of the wing (*elastic aoa*) and is a function of the deformed shape. Observing that $\tan\beta^k$ is equal to the opposite of the derivative of the displacement of the control point in the direction of the *undeformed* normal in respect to the direction $\boldsymbol{i}^S$ (*undeformed* x direction), it can be written:

$$V_{\infty,d}^{n_k} = -V_\infty \frac{\mathrm{d}\hat{Z}_k}{\mathrm{d}x_k^S} \tag{2.81}$$

where the vector $\hat{\boldsymbol{Z}}$ collects the displacements of the control points along the undeformed aerodynamic rings' normals. This contribution can thus be directly related to the slope of the normal component of displacement of the control point k.

The third term depends on the strain rate of the structure: it originates from the relative body-flow velocity that is established as the body changes its shape, giving a contribution to the effective flow speed that has to be taken into account for a correct evaluation of eq.(2.64). This proved to be an important source of aerodynamic damping, in that as the body increase its rate of strain, the consequent induction on it in order to have satisfied the boundary condition is such that the external load is decreased, and viceversa. It holds:

$$\boldsymbol{RHS}_3 = \dot{\boldsymbol{Z}} \tag{2.82}$$

where the sign in eq.(2.82) is attributed according to the fact that the *relative* velocity of the fluid respect to the body is sought. The generical term of $\dot{\boldsymbol{Z}}$ can be obtained multiplying the array $\dot{\boldsymbol{U}}$ which contains the translational velocity of the structural nodes by an interpolation matrix that gives this information on the control points and multiplying it by the normal to the k-th ring $\boldsymbol{n}_k$, in its *actual* configuration.

Now that all the RHS terms have been conveniently treated, eq.(2.64) can be re-written as

$$\begin{aligned} \boldsymbol{A} \cdot \boldsymbol{\Gamma} &= \boldsymbol{RHS}_1 + \boldsymbol{RHS}_2 + \boldsymbol{RHS}_3 \\ &= -\boldsymbol{A}_w \cdot \boldsymbol{\Gamma}_w - \boldsymbol{V}_\infty^n + \dot{\boldsymbol{Z}} \end{aligned} \tag{2.83}$$

and inverting $\boldsymbol{A}$, this final form is obtained

$$\boldsymbol{\Gamma} = \boldsymbol{\Gamma}_1 + \boldsymbol{\Gamma}_2 \cdot \boldsymbol{U} + \boldsymbol{\Gamma}_3 \cdot \dot{\boldsymbol{U}} \tag{2.84}$$

$\boldsymbol{\Gamma}_1$ is the known contribution due to the wake and to the *rigid aoa*, i.e., the first term in eq.(2.80)

$$\boldsymbol{\Gamma}_1 = -\boldsymbol{A}^{-1}\boldsymbol{A}_w \cdot \boldsymbol{\Gamma}_w - \boldsymbol{A}^{-1}\boldsymbol{V}_{\infty 0}^n \tag{2.85}$$

$\boldsymbol{\Gamma}_2$ is the matrix that multiplies the displacement field $\boldsymbol{U}$; it features a matrix performing the interpolation between the aerodynamic and structural meshes in order to get the derivative in respect to x^S of the displacement ($\boldsymbol{H}_{\mathrm{dx}}$). This matrix is multiplied by $\boldsymbol{N}_0$ in order to sample correctly just the component parallel to the *undeformed* normal of the ring

$$\boldsymbol{\Gamma}_2 = -V_\infty \boldsymbol{A}^{-1}\boldsymbol{N}_0\boldsymbol{H}_{\mathrm{dx}} \tag{2.86}$$

$\boldsymbol{\Gamma}_3$ multiplies the given velocity field $\dot{\boldsymbol{U}}$. Matrix $\boldsymbol{H}_{\mathrm{disp}}$ performs the interpolation between the two meshes, and is multiplied by $\boldsymbol{N}_{\mathrm{d}}$ in order to sample correctly just the component

parallel to the *actual* normal of the ring.

$$\boldsymbol{\Gamma}_3 = \boldsymbol{A}^{-1}\boldsymbol{N}_{\mathrm{d}}\boldsymbol{H}_{\mathrm{disp}} \tag{2.87}$$

2.4.2 Aeroelastic expression of Loads

In Sec. 2.3.5 it has been demonstrated as starting from the Bernoulli equation for an incompressible, irrotational and unsteady flow, the pressure difference acting on the k-th panel is the one predicted by the Kutta-Joukowsky theorem for the unsteady case, as expressed in eqs.(2.72) and (2.73) respectively for rings behind the leading-edge and for leading edge panels. These relations can be advantageously expressed in matrix form as

$$\boldsymbol{p} = \rho\boldsymbol{\Delta\Gamma} + \rho\frac{\partial\boldsymbol{\Gamma}}{\partial t} \tag{2.88}$$

where $\boldsymbol{p}$ is the array containing the difference between upper and lower pressure for each panel, $\boldsymbol{\Delta}$ is the matrix that, for each ring of the body, applies the finite difference derivative scheme to $\boldsymbol{\Gamma}$ and multiplies it with the suitable dimensional coefficients. To finally obtain the expression of the lift acting on the load points of the aerodynamic mesh, the direction $\boldsymbol{r}_{\mathrm{L}}^{\mathrm{k}}$ of the lift over the k-th panel is chosen accordingly to the Kutta-Joukowsky theorem as

$$\boldsymbol{r}_{\mathrm{L}}^{\mathrm{k}} = \boldsymbol{i} \times \boldsymbol{r}_{4_L^k - 1_L^k} \tag{2.89}$$

where $\boldsymbol{r}_{4_L^k - 1_L^k}$ connects the projections of the load point $P_{\mathrm{L}}^{\mathrm{k}}$ along the segments $3^{\mathrm{k}} - 4^{\mathrm{k}}$ and $2^{\mathrm{k}} - 1^{\mathrm{k}}$ as depicted in Fig.2.8 and has a modulus equal to the width of the ring panel. Calling

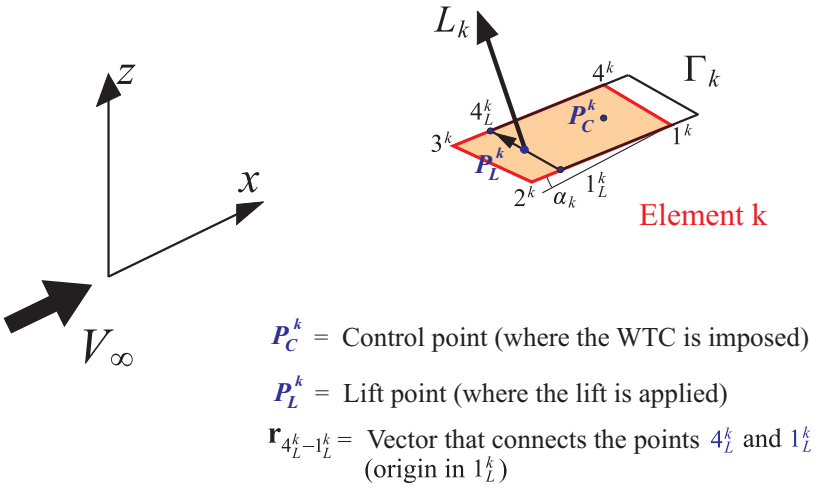

Fig. 2.8: Direction of the lift over the ring k

c_k the chord of the ring and $\boldsymbol{i}$, $\boldsymbol{j}$, $\boldsymbol{k}$ the unit vectors of the global coordinate system, it is possible to give a general expression of the three components of the lift force acting on the k-th panel

$$\begin{aligned} L_\mathrm{x}^\mathrm{k} &= c_\mathrm{k}\boldsymbol{i}\cdot\boldsymbol{r}_{4_L^k-1_L^k}p_\mathrm{k} \\ L_\mathrm{y}^\mathrm{k} &= c_\mathrm{k}\boldsymbol{j}\cdot\boldsymbol{r}_{4_L^k-1_L^k}p_\mathrm{k} \\ L_\mathrm{z}^\mathrm{k} &= c_\mathrm{k}\boldsymbol{k}\cdot\boldsymbol{r}_{4_L^k-1_L^k}p_\mathrm{k} \end{aligned} \tag{2.90}$$

which in matrix form becomes

$$\boldsymbol{L} = \boldsymbol{S}\cdot\boldsymbol{p} \tag{2.91}$$

If N is the number of body rings, $\boldsymbol{S}$ is a $3N \times N$ matrix such that when multiplied by $\boldsymbol{p}$ gives rise to the array $\boldsymbol{L}$ with $3N$ elements.

As it can be seen from eq.(2.88), the unsteady part of the pressure depends on the derivative of $\boldsymbol{\Gamma}$ with respect to time. The derivation can be carried out from eq.(2.84), leading to

$$\frac{\partial\boldsymbol{\Gamma}}{\partial t} = \frac{\partial\boldsymbol{\Gamma}_1}{\partial t} + \boldsymbol{\Gamma}_2\cdot\dot{\boldsymbol{U}} + \boldsymbol{\Gamma}_3\cdot\ddot{\boldsymbol{U}} \tag{2.92}$$

where the derivatives of $\boldsymbol{\Gamma}_2$ and $\boldsymbol{\Gamma}_3$ are considered negligible. Now eq.(2.88) combined with eqs.(2.84) and (2.92) leads to the sought expression of the aerodynamic loads

$$\boldsymbol{L}^\mathrm{LP} = \boldsymbol{L}_1^\mathrm{LP} + \boldsymbol{L}_2^\mathrm{LP}\cdot\boldsymbol{U} + \boldsymbol{L}_3^\mathrm{LP}\cdot\dot{\boldsymbol{U}} + \boldsymbol{L}_4^\mathrm{LP}\cdot\ddot{\boldsymbol{U}} \tag{2.93}$$

with

$$\begin{aligned} \boldsymbol{L}_1^\mathrm{LP} &= \rho\boldsymbol{S}\cdot\boldsymbol{\Delta}\cdot\boldsymbol{\Gamma}_1 + \rho\boldsymbol{S}\cdot\frac{\partial\boldsymbol{\Gamma}_1}{\partial t} \\ \boldsymbol{L}_2^\mathrm{LP} &= \rho\boldsymbol{S}\cdot\boldsymbol{\Delta}\cdot\boldsymbol{\Gamma}_2 \\ \boldsymbol{L}_3^\mathrm{LP} &= \rho\boldsymbol{S}\cdot\boldsymbol{\Delta}\cdot\boldsymbol{\Gamma}_3 + \rho\boldsymbol{S}\cdot\boldsymbol{\Gamma}_2 \\ \boldsymbol{L}_4^\mathrm{LP} &= \rho\boldsymbol{S}\cdot\boldsymbol{\Gamma}_3 \end{aligned} \tag{2.94}$$

The superscript LP is used here to outline how these are the forces applied on the load points of the ring. The interface algorithm will provide the way to transfer these quantities on the structural nodes, together with the definition of the matrices $\boldsymbol{H}_\mathrm{dx}$ and $\boldsymbol{H}_\mathrm{disp}$.

2.4.3 Residual and tangent matrix expression with aerodynamic loads

As pointed out in Sec. 2.2.3, to start the iterative process for the resolution of the dynamic equation it is necessary to give an operative expression of the residual term in eq.(2.34) and

of the tangent matrix in eq.(2.35) that both request the formal expression of the external loads as a function of the unknowns of the equation, i.e. $\boldsymbol{s}$, $\dot{\boldsymbol{s}}$ and $\ddot{\boldsymbol{s}}$. This task has been accomplished in Sec. 2.4.2, with the final relation presented in eq.(2.93).

First is observed that since $\boldsymbol{s}$ was expressing the generalized structural coordinates whereas $\boldsymbol{U}$ represents the displacement from an initial reference configuration, it holds

$$\frac{\mathrm{d}}{\mathrm{d}\boldsymbol{s}} = \frac{\mathrm{d}}{\mathrm{d}\boldsymbol{U}} \tag{2.95}$$

It is the possible to give a new expression of the residual and of the tangent matrix (always in the generalized α-method framework)

$$^{t+\Delta t}\boldsymbol{\mathcal{R}} = (\boldsymbol{MTX}_1 + \boldsymbol{MTX}_2 - \boldsymbol{AERO})\,{}^{t+\Delta t}\boldsymbol{s} + \boldsymbol{VCT}_{\text{inert}} + \boldsymbol{VCT}_{\text{damp}} - \boldsymbol{VCAE} - \boldsymbol{VCT}_6 + \alpha_f\,{}^{t+\Delta t}\boldsymbol{F}_{\text{int}} \tag{2.96}$$

$$^{t+\Delta t}\left[\frac{\mathrm{d}\boldsymbol{\mathcal{R}}}{\mathrm{d}\,\boldsymbol{s}}\right] = \boldsymbol{MTX}_1 + \boldsymbol{MTX}_2 - \boldsymbol{AERO} + \alpha_f \frac{\partial\,{}^{t+\Delta t}\boldsymbol{F}_{\text{int}}}{\partial\,{}^{t+\Delta t}\boldsymbol{s}} \tag{2.97}$$

where have been defined $\boldsymbol{AERO}$ and $\boldsymbol{VCAE}$, while the other quantities have just been previously introduced in Sec. 2.2.4 . The generalized α-method in the form adopted in the present study (Generalized Energy Momentum Method) prescribes the convex combination of the forces and not of the variables (for reasons earlier investigated) when dealing with the internal forces; now as showed in eq.(2.93), the external loads prove to depend from the acceleration $\ddot{\boldsymbol{U}}$ too, so again as for the non linear internal forces case, but for different reasons, it's not coincident the expression obtained making the combination of the variables and the one obtained with the combinations of the forces.
The difference between the two expressions is hidden in the definitions of $\boldsymbol{AERO}$ and

$\boldsymbol{VCAE}$, which for the first case (convex combination of variables) is

$$\begin{cases} \boldsymbol{AERO} = \boldsymbol{AERO}_1 + \boldsymbol{AERO}_2 + \boldsymbol{AERO}_3 \\ \boldsymbol{AERO}_1 = \boldsymbol{L}_2^{\mathrm{S}} \\ \boldsymbol{AERO}_2 = \dfrac{1}{\beta \Delta t} \alpha_f \, \gamma \boldsymbol{L}_3^{\mathrm{S}} \\ \boldsymbol{AERO}_3 = \dfrac{1}{\beta \Delta t} \dfrac{\alpha_m}{\Delta t} \boldsymbol{L}_4^{\mathrm{S}} \\ \boldsymbol{VCAE} = \boldsymbol{VCAE}_1 + \boldsymbol{VCAE}_2 + \boldsymbol{VCAE}_3 + \boldsymbol{VCAE}_4 + \boldsymbol{VCAE}_5 \\ \boldsymbol{VCAE}_1 = \alpha_f \boldsymbol{L}_1^{\mathrm{S}} \\ \boldsymbol{VCAE}_2 = \alpha_f \boldsymbol{L}_3^{\mathrm{S}} \, {}^{t+\Delta t}\dot{\boldsymbol{s}}_{\mathrm{pred}} \\ \boldsymbol{VCAE}_3 = -\boldsymbol{AERO}_2 \, {}^{t+\Delta t}\boldsymbol{s}_{\mathrm{pred}} \\ \boldsymbol{VCAE}_4 = -\boldsymbol{AERO}_3 \, {}^{t+\Delta t}\boldsymbol{s}_{\mathrm{pred}} \\ \boldsymbol{VCAE}_5 = \alpha_m \boldsymbol{L}_4^{\mathrm{S}} \, {}^{t+\Delta t}\ddot{\boldsymbol{s}}_{\mathrm{pred}} \end{cases} \tag{2.98}$$

instead for the second case (convex combination of forces) is

$$\begin{cases} \boldsymbol{AERO} = \boldsymbol{AERO}_1 + \boldsymbol{AERO}_2 + \boldsymbol{AERO}_3 \\ \boldsymbol{AERO}_1 = \boldsymbol{L}_2^{\mathrm{S}} \\ \boldsymbol{AERO}_2 = \dfrac{1}{\beta \Delta t} \alpha_f \, \gamma \boldsymbol{L}_3^{\mathrm{S}} \\ \boldsymbol{AERO}_3 = \dfrac{1}{\beta \Delta t} \dfrac{\alpha_f}{\Delta t} \boldsymbol{L}_4^{\mathrm{S}} \\ \boldsymbol{VCAE} = \boldsymbol{VCAE}_1 + \boldsymbol{VCAE}_2 + \boldsymbol{VCAE}_3 + \boldsymbol{VCAE}_4 + \boldsymbol{VCAE}_5 \\ \boldsymbol{VCAE}_1 = \alpha_f \boldsymbol{L}_1^{\mathrm{S}} \\ \boldsymbol{VCAE}_2 = \alpha_f \boldsymbol{L}_3^{\mathrm{S}} \, {}^{t+\Delta t}\dot{\boldsymbol{s}}_{\mathrm{pred}} \\ \boldsymbol{VCAE}_3 = -\boldsymbol{AERO}_2 \, {}^{t+\Delta t}\boldsymbol{s}_{\mathrm{pred}} \\ \boldsymbol{VCAE}_4 = -\boldsymbol{AERO}_3 \, {}^{t+\Delta t}\boldsymbol{s}_{\mathrm{pred}} \\ \boldsymbol{VCAE}_5 = \alpha_f \boldsymbol{L}_4^{\mathrm{S}} \, {}^{t+\Delta t}\ddot{\boldsymbol{s}}_{\mathrm{pred}} \end{cases} \tag{2.99}$$

where, as it can be seen, α_m is not more present in the expressions of $\boldsymbol{AERO}_3$ and $\boldsymbol{VCAE}_5$. The previously defined $\boldsymbol{L}_1^{\mathrm{LP}}$, $\boldsymbol{L}_2^{\mathrm{LP}}$, $\boldsymbol{L}_3^{\mathrm{LP}}$ and $\boldsymbol{L}_4^{\mathrm{LP}}$ are now named as $\boldsymbol{L}_1^{\mathrm{S}}$, $\boldsymbol{L}_2^{\mathrm{S}}$, $\boldsymbol{L}_3^{\mathrm{S}}$ and $\boldsymbol{L}_4^{\mathrm{S}}$ assuming that the aerodynamic forces have been projected to the nodes of the structural solver trough one of the load transferring techniques.

Chapter 3

Interface Algorithms

In Sec. 2.4 the steps which finally leads to the aero-structural coupling have been shown. It raised the need to provide an interface algorithm which enables to transfer geometry and loads between the aerodynamic and the structural fields. In this chapter two possible ways to perform this task are presented, namely the *Infinite Plate Spline* and the *Moving Least Square* methods. Differences, advantages and drawbacks are shown, since both of them will be used in the aeroelastic analysis of the Joined-Wing configurations.

3.1 Infinite Plate Splines

3.1.1 Theory

The Infinite Plate Spline concept was introduced in [52] and is employed in several of the interpolation schemes used in today's aeroelastic solvers (MSC/NASTRAN and ASTROS for example). This method is based on a superposition of the solutions of the equilibrium equation describing an infinite plate subjected to bending actions in the hypothesis of small deflections. The key idea is to consider a set of discrete points (x_i,y_i) lying within a two-dimensional domain, each of them has associated a known deflection w_i that defines the *vertical* position of the surface on which both structural and aerodynamic points are presumed to be. Using a superposition of solutions, it is possible to calculate the values of a set of *fictitious* concentrated loads acting at the known set of points that give rise to the required deflection w. In this way given the deflections of the structural grid points, the concentrated forces are obtained and it is possible to interpolate the position in a set of aerodynamic grid points considering them on the same smooth surface. The interpolated

function is differentiable everywhere and points far away from known points are extrapolated linearly. The main drawback of the method is that it is inherently 2-D and so it is limited to interpolate out-of-plane displacement; moreover, a piecewise flat planform for the wing has to be assumed, also when the wing is deformed. The mathematical procedure to establish the interface algorithm [106] is reported in Appendix A, while in the following just the major features are outlined.

The governing equation for a plate extending to infinity in both directions and subjected to bending only is

$$D_{11}\frac{\partial^4 w}{\partial x^4} + 2\left(D_{12} + 2D_{66}\right)\frac{\partial^4 w}{\partial x^2 \partial y^2} + D_{22}\frac{\partial^4 w}{\partial y^4} = p \tag{3.1}$$

where p is the applied pressure. The material is considered to be isotropic, giving this a specific value for the D_{11}, D_{12}, D_{22}, D_{66} terms. Radial symmetry is imposed to the problem and a concentrated load is considered applied at the origin of the reference system. After that, with the argument that no singular displacement is acceptable at the origin and that at infinity oscillations must be avoided, some terms in the closed form of the solution of eq.(3.1) are set to zero.

If $\tilde{N}$ concentrated loads are applied, each of them thought to act in the point i where the deflection (w_i) is known, by superimposition of elementary solutions of eq.(3.1) it is possible to obtain the vertical displacement w in a generical point of the two-dimensional domain as

$$w\left(x,y\right) = a_0 + a_1 x + a_2 y + \sum_{i=1}^{\tilde{N}} \tilde{F}_i r_i^2 \ln r_i^2 \tag{3.2}$$

with:

$$\begin{aligned} a_0 &= \sum_{i=1}^{\tilde{N}} \left[A_i + B_i\left(x_i^2 + y_i^2\right)\right] \\ a_1 &= -2\sum_{i=1}^{\tilde{N}} B_i x_i \\ a_2 &= -2\sum_{i=1}^{\tilde{N}} B_i y_i \end{aligned} \tag{3.3}$$

A_i, B_i and r_i are known quantities and $\tilde{F}_i$ are the fictitious concentrated loads used to reconstruct the shape of the plate, given the actual position of the set of the $\tilde{N}$ known points.

3.1.2 Application to the aero-structural coupling

The goal of this interface algorithm is to provide a relation between the vectors representing the unknowns (i.e. the degrees of freedom and their derivatives) associated with the structural nodes and the corresponding aerodynamic quantities in order to get an expression of the external loads that allows the resolution of the dynamic equation. Then these forces have to be transferred from the aerodynamic load points to the structural nodes, where the equilibrium is enforced.

The reference planes where the splines are specified are planar, and have the local x-axis (x^S) along the free stream direction. The local vertical displacement (which is perpendicular to the spline plane but of course not necessarily coincident with the vertical displacement in the global coordinates z) are denoted with Z^S and $\mathcal{Z}^S$ for the generic structural node and aerodynamic control point respectively, where S specifies that these are quantities evaluated in the spline's plane. Eq.(3.2) shows how IPS is employed to evaluate the z coordinate of a generic point of the system once both its position through the local coordinates x and y and the required coefficients are given; this can be applied, for example, to the i-th structural node, allowing to write

$$Z_i^S\left(x_i, y_i\right) = a_0 + a_1 x_i + a_2 y_i + \sum_{j=1}^{\tilde{N}} \tilde{F}_j K_{ij} \tag{3.4}$$

Writing this relation for the $\tilde{N}$ structural nodes of the system, eq.(3.4) can be rearranged in matrix form leading to

$$\boldsymbol{Z}^S = \boldsymbol{G}\,\tilde{\boldsymbol{F}} \tag{3.5}$$

where $\tilde{\boldsymbol{F}}$ is the array of *fictitious* concentrated loads acting at the known set of points which enable to rebuild the deflection associated with the local vertical displacements stored in $\boldsymbol{Z}^S$. Since $\boldsymbol{G}$ is a known matrix once the set of points and the geometry has been fixed, eq.(3.5) can be advantageously used to get an expression of the unknown array

$$\tilde{\boldsymbol{F}} = \boldsymbol{G}^{-1}\boldsymbol{Z}^S \tag{3.6}$$

In order to avoid the time consuming task of updating the vector $\tilde{\boldsymbol{F}}$ at each timestep, the assumption that during the deformation process the original local coordinates x_i and y_i of the generical point i do not change is made, i.e. the vertical projection is always corresponding (or at least in good approximation) to the initial position of the structural point considered. If this hypothesis is not satisfied, $\boldsymbol{G}$ changes during the simulation and has to be continuously evaluated.

The expression of the aerodynamic loads is calculated starting from the boundary condition applied on the *control points* and the involved quantities are thus related to the derivative of the vertical displacement with respect to the x^S direction $\frac{\mathrm{d}\mathcal{Z}^S}{\mathrm{d}x^S}$ (which has been shown to be related to the changing of relative angle of attack), the speed $\dot{\mathcal{Z}}^S$ and the acceleration $\ddot{\mathcal{Z}}^S$ of these set of points. Considering that eq.(3.2) holds for whatever set of points lying in the plane of the splines, a relation similar to eq.(3.5) holds

$$\boldsymbol{\mathcal{Z}}^S = \boldsymbol{C}\,\tilde{\boldsymbol{F}} \tag{3.7}$$

where $\boldsymbol{\mathcal{Z}}^S$ is the array containing the local vertical displacements of control points, $\boldsymbol{C}$ has a similar expression of $\boldsymbol{G}$ but with different terms because now eq.(3.4) is written referring to another set of points. Using the result in eq.(3.6) and defining $\boldsymbol{H} = \boldsymbol{C}\boldsymbol{G}^{-1}$ as the interface matrix for the displacement field, the following holds

$$\boldsymbol{\mathcal{Z}}^S = \boldsymbol{H}\boldsymbol{Z}^S \tag{3.8}$$

which can advantageously used to establish the sought relations

$$\begin{aligned} \dot{\boldsymbol{\mathcal{Z}}}^S &= \boldsymbol{H}\dot{\boldsymbol{Z}}^S \\ \ddot{\boldsymbol{\mathcal{Z}}}^S &= \boldsymbol{H}\ddot{\boldsymbol{Z}}^S \end{aligned} \tag{3.9}$$

since for the fixed expression (earlier motivated) of the spline's matrices $\boldsymbol{G}$ and $\boldsymbol{C}$, the time derivatives have the same interface matrix of the displacements.

In order to calculate the spatial derivative of the vertical displacement is necessary to differentiate the spline equation (eq.(3.4)) specialized for the control points which, leaving the details in appendix A, leads to

$$\frac{\mathrm{d}\boldsymbol{\mathcal{Z}}^S}{\mathrm{d}x^S} = \boldsymbol{H}^D\boldsymbol{Z}^S \tag{3.10}$$

with $\boldsymbol{H}^D$ the interface matrix for the spatial derivative of the displacement.
Once the rotation matrices are built to shift from the local reference system of the spline to the global coordinate system (this choice can be performed considering the wing as piecewise-planar and assuming a local reference for every section that has a different normal), eqs.(3.9) and (3.10) allow to completely define the aerodynamic loads providing the sought interface matrices.

3.1.3 Load transfer

The last task to be performed to completely stress out the present interface algorithm for the aerodynamic-structural coupling originates from the following issue. For a correct application of the Kutta-Joukowsky theorem, the aerodynamic loads have to be applied in the load points of the vortex ring. In order to use a FEM structural solver, the loads are thought to act on the structural nodes (where the equilibrium is enforced) and so this transfer has to be achieved; in the present structural model, triangular shell elements are adopted, thus first is needed an algorithm that can determine whether a point (the load point in this case) is inside a triangle or not. After each load point has been associated with a structural element, the goal is to find the nodal forces equivalent to the given concentrated load applied in an internal point P. The problem, depicted in Fig. 3.1 can be tackled with an energy conserving

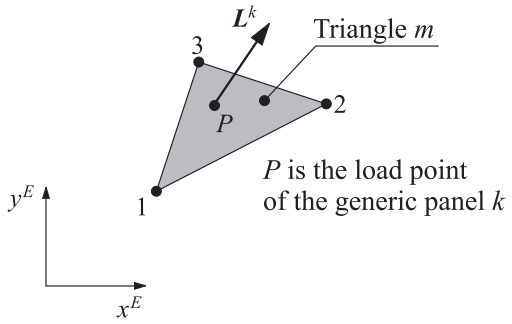

Fig. 3.1: Applied load in a triangular element

approach imposing that the virtual work done by the external force is equal to the virtual work done by the nodal forces of the element. The expression of the forces acting on the three vertices of the triangle m equivalent to the aerodynamical load applied in the point P with coordinates (x_P,y_P) is given by

$$\begin{aligned} \boldsymbol{L}_1^m &= h_1^m\left(x_P, y_P\right)\boldsymbol{L}^k \\ \boldsymbol{L}_2^m &= h_2^m\left(x_P, y_P\right)\boldsymbol{L}^k \\ \boldsymbol{L}_3^m &= h_3^m\left(x_P, y_P\right)\boldsymbol{L}^k \end{aligned} \tag{3.11}$$

The shape functions corresponding to the nodes 1, 2 and 3 of the triangle m, here indicated respectively as h_1^m, h_2^m and h_3^m, depend on the generic point of the triangle where they are evaluated (with generic local coordinates $\left(x^E, y^E\right)$) and can be evaluated making use of the area coordinates [9].

3.2 Moving Least Square derivated algorithm

The present interface algorithm has the purpose to satisfy the coupling of the aerodynamic and structural fields granting important features [95]: possibility to interface both non-matching surfaces or non-matching topologies; capability to deal with situations when a control point fall outside the range of the source mesh; computational efficiency in the evaluation of interface operators; capability to deal with a wide variation of the node density in the source mesh; indipendence from the numerical formulation of the solvers of the two fields (if differents). A very important feature is the conservation of exchanged quantities, in particular momentum and energy: this is a keypoint since in literature [22] it has been shown how nonconservartive interfaces may lead to wrong results.

3.2.1 Meshless Problem Statement

To reach the goals previously listed, a *meshless* approach is considered. Traditionally, the complex partial differential equations that govern physical phenomena in engineering systems are solved using numerical method such as finite element method (FEM), finite difference method (FDM) and finite volume method (FVM) where the spatial domain is often discretized into meshes. A mesh is any of the open spaces formed by the strands of the net obtained connecting nodes in a certain manner and is specified by the definition of a property which provides a certain relationship between the nodes. The strategy is then to approximate the differential equations by a set of algebraic equations for each mesh and then get the system of algebraic equations for the whole problem by assembling in the proper way the contribution of all of them.

In a mesh free method [78], this system of algebraic equations for the whole problem is obtained using a set of nodes scattered in the domain which not form a mesh because no informations on the relationship between the node are required. These methods seem to solve some issues of the classical approaches. First, the creation of an adequately discretized mesh is notoriously a bottleneck in the process since it is both manpower and computer time consuming. Second, the classical approaches have a limited regularity of the solution, especially in derivatives evaluation at the elements boundaries (although approaches using higher order continuous basis function like *NURBS* were already proposed in [23]). Moreover, with lagrangian grids/meshes there is a lost of accuracy when large deformations are investigated because of the element's distortion. Adaptive techniques to upload the mesh in successive stages of the problem solution, which usually presents lack of accuracy and sig-

nificant computational cost, are no longer needed. A close examination of these difficulties shows as the root of the problem is the necessity to use elements (mesh); on the contrary a meshless method does not have these limitations, and could add or delete nodes when they are needed, providing a great flexibility to the analysis.

In the present work is not actually adopted a meshless method, but one of its central and most important feature: the shape functions. A number of ways to construct shape functions have been proposed and the choice is to rely on Moving Least Square approximation (MLS), which belongs to the family of finite series representation methods. This shape functions were originally introduced for data fitting and surface reconstruction [70], while in [87] they were used for the first time to build shape functions for the Diffuse Element Method (DEM), which was among the firsts properly called mesh free method and had a strong impact on the field. The two main features of MLS are that the appoximated field function obtained is continuous and smooth in the entire problem domain and it is capable of produce the desired order of consistency, where a method is said to have k-th order consistency if can reproduce polynomials up to the k-th order. The procedure of constructing shape functions using MLS approximation is fully presented in Appendix B, while in this section just the main features are outlined.

3.2.2 Main features of the algorithm

The basic idea is to compute the value of a function $u(\boldsymbol{x})$ on a set of nodes $\{\boldsymbol{\eta}_1, \boldsymbol{\eta}_2, ..., \boldsymbol{\eta}_{\hat{N}}\}$ from its values $\hat{u}(\boldsymbol{\xi}_1)$, $\hat{u}(\boldsymbol{\xi}_2)$, ..., $\hat{u}(\boldsymbol{\xi}_{\hat{n}})$ on scattered centers (or sources) $\{\boldsymbol{\xi}_1, \boldsymbol{\xi}_2, ..., \boldsymbol{\xi}_{\hat{n}}\}$ without deriving an analytical expression. The result of this extrapolation is denoted $\hat{u}^h$ and is built as a sum of $\hat{m}$ basis functions $\hat{p}_i$

$$\hat{u}^h(\boldsymbol{\eta}) = \sum_{i=1}^{\hat{m}} \hat{p}_i(\boldsymbol{\eta})\, a_i^{\boldsymbol{\xi}}(\boldsymbol{\eta}) = \hat{\boldsymbol{p}}(\boldsymbol{\eta})\boldsymbol{a}^{\boldsymbol{\xi}}(\boldsymbol{\eta}) \tag{3.12}$$

where $a_i^{\boldsymbol{\xi}}$ are the unknown coefficients of the basis functions which depend on the point $\boldsymbol{\eta}$ where the value is sought and on the set of scattered centers $\boldsymbol{\xi}$ where the function is known (this latter dependence, denoted by the superscript in eq.(3.12), will be omitted in the following for clearness). The array $\hat{\boldsymbol{p}}$ of basis functions consists often of monomials of the lowest order such to form polynomial basis with minimum completeness but particular functions can be added to reproduce a particular behaviour of the investigated variables. In the present study linear and quadratic polynomials are adopted leading to the following

expressions for $\boldsymbol{p}$

$$\begin{aligned}\hat{\boldsymbol{p}}^T &= (1, x, y, z)^T \\ \hat{\boldsymbol{p}}^T &= (1, x, y, z, x^2, xy, y^2, yz, z^2, zx)^T\end{aligned} \tag{3.13}$$

Eq.(3.12) is similar to that one used in the Finite Element Method, but the interpolation valid only element by element is replaced here by a local weighted least square fitting in a neighbourhood of point $\boldsymbol{\eta}$. The neighbourhood of point $\boldsymbol{\eta}$, called its *support domain*, is given by a subset of $\boldsymbol{\xi}$, namely $\boldsymbol{\xi}^s$, made of $\hat{n}_s$ nodes which are the only ones used locally to approximate the field function. Each node $\boldsymbol{\eta}$ has a different set $\boldsymbol{\xi}_s$ with in general a different number of nodes $\hat{n}_s$, that is $\hat{n}_s$=$\hat{n}_s(\boldsymbol{\eta})$. The $\hat{m}$ coefficients a_i describing (as shown in eq.(3.12)) the function in the point $\boldsymbol{\eta}$ are obtained minimizing the functional weighted residual (a weighted discrete L_2 norm) $J(\boldsymbol{\eta})$

$$J(\boldsymbol{\eta}) = \sum_{i=1}^{\hat{n}} W(\boldsymbol{\eta} - \boldsymbol{\xi}_i) \left[\tilde{u}(\boldsymbol{\xi}_i, \boldsymbol{\eta}) - \hat{u}(\boldsymbol{\xi}_i)\right]^2 \tag{3.14}$$

where

$$\tilde{u}(\boldsymbol{\xi}_i, \boldsymbol{\eta}) = \hat{\boldsymbol{p}}(\boldsymbol{\xi_i})\boldsymbol{a}(\boldsymbol{\eta}) \tag{3.15}$$

is the approximated value of the the field function in the generical center of the set $\boldsymbol{\xi}$ obtained by means of the same extrapolation process pointed out in eq.(3.12).

The weight function W used in eq.(3.14) is positive for all the $\boldsymbol{\xi}_i$ centers in the support of node $\boldsymbol{\eta}$ and zero outside, and fulfills two important roles in constructing the MLS shape functions: it provides weighting for the residual at different nodes in the support domain (small weights are wanted for centers far from $\boldsymbol{\eta}$); it ensures a smooth manner for centers to leave and enter the support domain of the considered node. Here comes out the important difference with the FEM shape functions, which are obtained minimizing the residual J in eq.(3.14) assuming a unitary constant weight function and repeating this operation element by element (which coincides in that case with the support domain of the nodes). By replacing the discontinuous weights of FEM approach with continuous weighting functions evaluated in the centers of the nodes the smoothness of the approximate function is granted. Solving the minimization problem

$$\frac{\partial J(\boldsymbol{\eta})}{\partial \boldsymbol{a}} = 0 \tag{3.16}$$

an expression for the coefficient vector $\boldsymbol{a}(\boldsymbol{\eta})$ is obtained, allowing to rewrite eq.(3.12) as

$$\hat{u}^h(\boldsymbol{\eta}) = \boldsymbol{\Phi}(\boldsymbol{\eta})\hat{\boldsymbol{u}} \tag{3.17}$$

where $\boldsymbol{\Phi}(\boldsymbol{\eta})$ is the array containing the coefficients of the MLS shape function corresponding to the node $\boldsymbol{\eta}$, while $\hat{\boldsymbol{u}}$ holds the values of the field function on the centers. For more details on the derivation refer to Appendix B.
It should be observed that the shape functions in eq.(3.17) do not satisfy the Kronecker delta criterion $\Phi_i(\boldsymbol{\xi}_j) = \delta_{ij}$ resulting in $\hat{u}^h(\boldsymbol{\xi}_i) \neq \hat{u}(\boldsymbol{\xi}_i)$, that is, the nodal parameters $\hat{u}(\boldsymbol{\xi}_i)$ are not coincident with the nodal values $\hat{u}^h(\boldsymbol{\xi}_i)$; this means that they are not interpolants, but rather approximates of a function; this property can represents a drawback when the imposition of essential boundary conditions is requested, but it is possible to overcome it as shown in Appendix B.

As stated, the MLS approximation is able to reproduce the desired order of consistency, depending on the complete order of the monomial basis $\hat{\boldsymbol{p}}$: if the complete order of the base is k, it can be demonstrated that the shape function will possess k consistency.

The calculation of spatial derivatives of the function $\hat{u}$, requires to derive eq.(3.12), that is:

$$\frac{\partial u}{\partial x} \simeq \frac{\partial u^h}{\partial x} = \frac{\partial \hat{\boldsymbol{p}}}{\partial x} \cdot \boldsymbol{a} + \hat{\boldsymbol{p}} \cdot \frac{\partial \boldsymbol{a}}{\partial x} \tag{3.18}$$

The second term of eq.(3.18) is not trivial to evaluate and a straight procedure is showed in [78]; it is not an expensive task itself, however it requires the knowledge of the cloud of particles surrounding each point $\boldsymbol{\eta}$ and, thus, it depends on the point where the information is evaluated; on the contrary, the first term can be evaluated *a priori*. Work [87] proposed the concept of diffusive derivative, which consists in approximating the derivative only with the first term on the right hand side of eq.(3.18), and it proved convergence at optimal rate.

3.2.3 Issues connected to the minimization problem

The minimization problem in eq.(3.16) involves the inversion of the symmetric matrix $\hat{\boldsymbol{A}}$, called *moment matrix*, and proves to have a unique solution if $\hat{\boldsymbol{A}}$ is positive definite; as can be seen by its expression presented in Appendix B, this matrix may become singular when the interface is not a well-posed problem, as for example when the number of terms of polynomial basis $\hat{m}$ is bigger than the number $\hat{n}$ of nodes used in the support domain or when nodes and relative centers are such that the basis functions vanish in the local support. Especially the latter case can often represent an issue; in fact it can happen to study configurations lying, at least partly, in one of the three main planes of the global system (xy,xz,yz). It is useful in these situations to resort to the concept of Moore-Penrose pseudoinverse. The so-called Moore-Penrose pseudoinverse of a matrix [83] is a concept that

generalizes the usual notion of inverse of a square matrix, but that is also applicable to singular square matrices or even to non-square matrices. For this reason it proves to be particularly useful in dealing with certain least squares problems, when an approximation for solutions of linear equations like $\hat{\boldsymbol{A}}\boldsymbol{z} = \boldsymbol{c}$ is sought, where $\hat{\boldsymbol{A}}$ is a given $\hat{m} \times \hat{n}$ matrix and $\boldsymbol{c}$ is a column vector with $\hat{m}$ components; the solution is expressed as the set of all vectors $\boldsymbol{z}^\star$ such that the Euclidean norm $||\hat{\boldsymbol{A}}\boldsymbol{z}^\star - \boldsymbol{c}||$ has the least possible value, called the minimizing set of the linear problem; it can be demonstrated that this set is obtained through a matrix $\hat{\boldsymbol{A}}^+$, named the Moore-Penrose pseudoinverse of $\hat{\boldsymbol{A}}$ and satisfying the following properties:

$$\begin{aligned} &\hat{\boldsymbol{A}}\hat{\boldsymbol{A}}^+\hat{\boldsymbol{A}} = \hat{\boldsymbol{A}} \\ &\hat{\boldsymbol{A}}^+\hat{\boldsymbol{A}}\hat{\boldsymbol{A}}^+ = \hat{\boldsymbol{A}}^+ \\ &\hat{\boldsymbol{A}}\hat{\boldsymbol{A}}^+ \text{ and } \hat{\boldsymbol{A}}^+\hat{\boldsymbol{A}} \text{ are self-adjoint} \end{aligned} \tag{3.19}$$

For the Singular Value Decomposition Theorem [8] a matrix $\hat{\boldsymbol{A}}$ can always be written as

$$\hat{\boldsymbol{A}} = \boldsymbol{V}\boldsymbol{S}\boldsymbol{W}^\star \tag{3.20}$$

where $\boldsymbol{V}$ and $\boldsymbol{W}$ are unitary matrices given by the *Polar Decomposition Theorem* and $\boldsymbol{S}$ is a diagonal matrix whose diagonal elements are the N *singular values* of $\hat{\boldsymbol{A}}$, by definition the square root of the eigenvalues of $\hat{\boldsymbol{A}}^T\hat{\boldsymbol{A}}$

$$\boldsymbol{S} = \begin{bmatrix} s_1 & 0 & 0 & 0 & 0 \\ 0 & \ddots & 0 & 0 & 0 \\ 0 & 0 & s_r & 0 & 0 \\ 0 & 0 & 0 & \ddots & 0 \\ 0 & 0 & 0 & 0 & s_N \end{bmatrix} \tag{3.21}$$

Eq.(3.20) shows the so-called singular value decomposition of the matrix $\hat{\boldsymbol{A}}$. It can be demonstrated that the Moore-Penrose pseudoinverse is given by

$$\hat{\boldsymbol{A}}^+ = \boldsymbol{W}\boldsymbol{S}^+\boldsymbol{V}^\star \tag{3.22}$$

where $\boldsymbol{S}^+$ is a diagonal matrix whose diagonal elements are the reciprocal of the singular values of $\hat{\boldsymbol{A}}$. The crucial point is thus the choice of which diagonal elements have to be retained in $\boldsymbol{S}^+$: the way an inverse matrix of a singular one is given adopting the Moore-Penrose pseudoinverse consists indeed in replacing the diagonal terms of $\boldsymbol{S}^+$ corresponding

to a zero singular value of $\hat{\boldsymbol{A}}$ with 0, i.e., just the *invertible* part is inverted, as shown in eq.(3.23) where s_n is the first non zero eigenvalue

$$\boldsymbol{S}^{+} = \left[\begin{array}{ccc|ccc} \frac{1}{s_1} & 0 & 0 & 0 & 0 & 0 \\ 0 & \ddots & 0 & 0 & 0 & 0 \\ 0 & 0 & \frac{1}{s_n} & 0 & 0 & 0 \\ \hline 0 & 0 & 0 & 0 & 0 & 0 \\ 0 & 0 & 0 & 0 & \ddots & 0 \\ 0 & 0 & 0 & 0 & 0 & 0 \end{array}\right] \tag{3.23}$$

It should be observed that when the matrix $\hat{\boldsymbol{A}}$ is singular (ill-conditioned), it has at least one of its singular values equal to zero and so this procedure enables to find an inverse of the matrix: this happens for example when the support domain of $\boldsymbol{\eta}$ is contained in one of the three main planes of the global system such that at least one of the basis function vanishes. More insidiously it can happen that the support domain lies in a plane which is slightly different from the main ones (for example it can be caused by the dihedral angle of the wing): although $\hat{\boldsymbol{A}}$ is non singular from a mathematical point of view (no zero eigenvalues) it has a high condition number and eq.(3.22) without further modifications would lead to inaccurate results. The procedure which generalized the process shown in eq.(3.23) consists in the esteem of a cut-off value s_c (to make this threshold independent of the particular case, a good way could be to normalize the singular values of $\hat{\boldsymbol{A}}$ dividing them by the maximum one) such that just the greater are retained

$$\boldsymbol{S}^{+} = \left[\begin{array}{ccc|ccc} \frac{1}{s_1} & 0 & 0 & 0 & 0 & 0 \\ 0 & \ddots & 0 & 0 & 0 & 0 \\ 0 & 0 & \frac{1}{s_{c-1}} & 0 & 0 & 0 \\ \hline 0 & 0 & 0 & 0 & 0 & 0 \\ 0 & 0 & 0 & 0 & \ddots & 0 \\ 0 & 0 & 0 & 0 & 0 & 0 \end{array}\right] \tag{3.24}$$

This procedure is equal to fix a cut-off value for the singular values of $\hat{\boldsymbol{A}}$ as obtained from its *Polar Decomposition Theorem* in eq.(3.20).

3.2.4 Locality of the algorithm

The great advantage of the problem expressed in this form is the possibility to preserve the locality of the MLS approximation choosing a compact support weight function W, which is

supposed to satisfy the following requirements:

- W is a monotonically decreasing function that depends only on a scalar parameter r that represents the Euclidean distance from the two considered points
- W has a compact support, so

$$\begin{cases} W(r) > 0 \text{ if } r < \overline{r} \\ W(r) = 0 \text{ if } r > \overline{r} \end{cases} \tag{3.25}$$

- W enjoys normal property such that

$$\int_{\Omega} W(\boldsymbol{\eta} - \boldsymbol{x})\, d\Omega = 1 \tag{3.26}$$

  where $\overline{r}$ is the radius delimiting Ω, the local support of node $\boldsymbol{\eta}$

Examples of functions that satisfy these requirements are the Radial Basis Function (RBF) family, which can be found in different forms as Multiquadratics, Gaussian, Thin Plate Spline and Logarithmic. In this study are adopted functions which possess the lowest possible degree among all piecewise polynomial compactly supported radial functions of a given order of smoothness [112]: this is an important property since the approximate functions are as smooth as the involved weight function.

After the dimension of the local support is chosen, the last operation to completely define the local domain is the determination of the centers which belong to each node $\boldsymbol{\eta}$; several strategies exist to solve this task and a suitable choice from the computational point of view is to rely on *nearest neighbor searching algorithms* [6]: given a set S of n data points in a metric space X in real d-dimensional space, the idea is to preprocess these points so that, given any query point $q \in X$, the k nearest points to q can be efficently reported. These algorithms perform the geometric preprocessing of building the structure at $O(d)$ cost and the subsequent operation to get the nearest neighbor from the data set with $\mathrm{O}(k \log d)$ cost.

3.2.5 Conservation of energy

As previously stated, an important property sought in the present interface algorithm is the conservation of momentum and energy; using eq.(3.17) to exchange the information of displacement and velocity from the structure to the aerodynamic field, conservation (although not in a strictly mathematical sense) is achieved because a minimization process is

performed and so a limited amount of information can be transmitted [95]. While indeed the conservation of momentum transmitted is taken in account with the definition of the $\boldsymbol{\Phi}$ interface matrix, other considerations lead to conservation of energy. As demonstrated in Appendix B, to ensure the balance of the energy exchanged bewteen fluid and structure, the loads on the structural nodes $\boldsymbol{f}_i$ have to be evaluated by multiplying the loads $\boldsymbol{F}_i$ on the aerodynamic grid by the transpose of the interpolation matrix $\boldsymbol{H}$ (same as $\boldsymbol{\Phi}$ of eq.(3.17)) that matches the two displacement fields.

Chapter 4

Stability and Bifurcations of Nonlinear Dynamical Systems

4.1 Introduction

Dynamics is the subject that deals with systems that evolve in time, whether the system in question settles down to equilibrium, keeps repeating in cycles or does something more complicated. There are two main ways to study dynamical systems: *differential equations* and *iterated maps* (or *difference equations*), the former describing the evolution of systems in continuous time (widely used in science and engineering), whereas the latter involves problems where time is discrete. One of the main goal is to control the system, finding out how one or more parameters affect its state bringing it close to a critical threshold where the response may change abruptly resulting in a transition, i.e. a *bifurcation* is encountered.

4.2 Fixed points and their stability

Ordinary Differential Equations (ODEs), written in terms of the states variables of the system (for example position and velocity of a particle), represent a valid way to study qualitative changes in the behaviour system under investigation; in vectorial notation, this can be written as

$$\dot{\boldsymbol{y}} = \boldsymbol{f}(\boldsymbol{y}) \tag{4.1}$$

This system is called autonomous since the functions in $\boldsymbol{f}$ (namely the *vector field*) do not depend explicitly on the independent variable t, which is often time. For non-autonomous

systems instead it holds

$$\dot{\boldsymbol{y}} = \boldsymbol{f}(\boldsymbol{y}, t) \tag{4.2}$$

If $\boldsymbol{y}$ has m components, the trajectories sorting out from the solution of eq.(4.1) can be represented in the *state space* $\in \mathbb{R}^{\mathrm{m}}$; this solution are selected by requesting that it passes through a prescribed state $\boldsymbol{z}$ of initial values, as depicted in Fig.4.1. Of great interest are

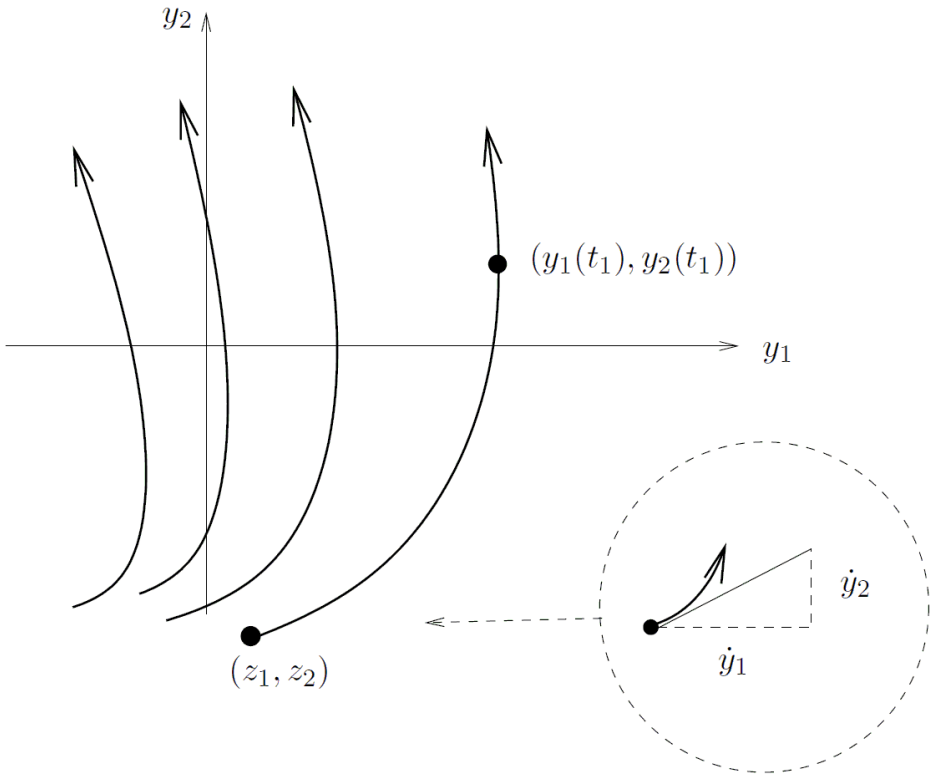

Fig. 4.1: Example of Phase Diagram for a two dimensional system varying the initial values, taken from [104]

the equilibrium points $\boldsymbol{y}^{\mathrm{s}}$ (also called *stationary solutions* or *fixed points*), so called because the system is at rest as they are defined by

$$\boldsymbol{f}(\boldsymbol{y}^{\mathrm{s}}) = 0 \tag{4.3}$$

The resolution of the system in eq.(4.3) is not a trivial task, so when two dimensional problems are handled it's helpful to plot the *nullclines*, defined as the curves where either $\dot{y}_1 = 0$ and $\dot{y}_2 = 0$; hence, stationary solutions in the plane are given by the intersections of these lines.

Stability of stationary point is a wide subject [86], here are just reported the basic definitions and a possible classification. A stationary solution $\boldsymbol{y}^{\mathrm{s}}$ is *asymptotically stable*, also called sink, if the response to a small perturbation approaches zero (i.e. the system comes back to its starting state) as the time approaches infinity; these kind of stables equilibria are examples of *attractors* and the set of initial values $\boldsymbol{z}$ from which trajectories converge to the attractor is called *domain of attraction*. A different notion of stability exists, related to the behaviour of the solution for all time, not just when infinity is approached: $\boldsymbol{y}^{\mathrm{s}}$ is referred as *Liapunov stable* (or *neutrally stable*) if all trajectories that start sufficiently close to it remain close for all time. Otherwise $\boldsymbol{y}^{\mathrm{s}}$ is *unstable* or a source.

To handle the stability issue from a quantitative point of view, first a system of two ODEs is considered

$$\begin{aligned} \dot{y_1} &= f_1(y_1, y_2) \\ \dot{y_2} &= f_2(y_1, y_2) \end{aligned} \tag{4.4}$$

A Taylor series expansion of f_1 about the investigated fixed point $(y_1^{\mathrm{s}}, y_2^{\mathrm{s}})$ gives

$$\begin{aligned} \dot{y_1} = f_1(y_1, y_2) = f_1(y_1^{\mathrm{s}}, y_2^{\mathrm{s}}) &+ \frac{\partial f_1}{\partial y_1}(y_1^{\mathrm{s}}, y_2^{\mathrm{s}})(y_1 - y_1^{\mathrm{s}}) \\ &+ \frac{\partial f_1}{\partial y_2}(y_1^{\mathrm{s}}, y_2^{\mathrm{s}})(y_2 - y_2^{\mathrm{s}}) + \text{ terms of higher order} \end{aligned} \tag{4.5}$$

Expanding also f_2, observing that $f_1(y_1^{\mathrm{s}}, y_2^{\mathrm{s}}) = f_2(y_1^{\mathrm{s}}, y_2^{\mathrm{s}}) = 0$ and dropping the higher-order terms (that are at least of order 2) leads to a system of two differential equations where the *Jacobian matrix* $\boldsymbol{f}_{\boldsymbol{y}}^{\mathrm{s}}$ is introduced, containing the first-order partial derivatives evaluated at the equilibrium

$$\boldsymbol{f}_{\boldsymbol{y}}^{\mathrm{s}} = \frac{\partial \boldsymbol{f}}{\partial \boldsymbol{y}}(\boldsymbol{y}^{\mathrm{s}}) = \begin{bmatrix} \frac{\partial f_1}{\partial y_1}(y_1^{\mathrm{s}}, y_2^{\mathrm{s}}) & \frac{\partial f_1}{\partial y_2}(y_1^{\mathrm{s}}, y_2^{\mathrm{s}}) \\ \frac{\partial f_2}{\partial y_1}(y_1^{\mathrm{s}}, y_2^{\mathrm{s}}) & \frac{\partial f_2}{\partial y_2}(y_1^{\mathrm{s}}, y_2^{\mathrm{s}}) \end{bmatrix} \tag{4.6}$$

Introducing $\boldsymbol{h}$ as the array representing the first order approximations of distances (considered small accordingly with the previous linearization) between the actual state and the stationary points

$$\begin{aligned} h_1(t) &\simeq y_1(t) - y_1^{\mathrm{s}} \\ h_2(t) &\simeq y_2(t) - y_2^{\mathrm{s}} \end{aligned} \tag{4.7}$$

the linearized system in vectorial notation is

$$\dot{\boldsymbol{h}} = \boldsymbol{f}_{\boldsymbol{y}}^{\mathrm{s}} \boldsymbol{h} \tag{4.8}$$

Eq.(4.8) describes the evolution of a deviation from the fixed point, that can be of various kind, as a numerical disturbance when these equations are integrated numerically, fluctuations of the model due to the the formulation of the problem adopted or an impulse from

the external force not included in the law $\boldsymbol{f}$; mathematically speaking, these perturbations can be described as a jump in the trajectory at some instant t_1

$$(y_1(t_1), y_2(t_1)) \to (z_1, z_2) \tag{4.9}$$

The way the perturbation influences the state of the system is so described by eq.(4.8), that is $\boldsymbol{h}(t)$ describes the *local* (due to the assumptions to neglect higher order terms) behaviour of the solution. The question of local stability is reduced to the eigenvalue problem

$$(\boldsymbol{f}^{\mathrm{s}}_{\boldsymbol{y}} - \mu \boldsymbol{I})\boldsymbol{w} = 0 \tag{4.10}$$

which underlines the hypothesis that

$$\boldsymbol{h}(t) = e^{\mu t}\boldsymbol{w} \tag{4.11}$$

The two eigenvalues describe qualitative behavior of trajectories close to the equilibrium and give rise to three definitions for the fixed point $\boldsymbol{y}^{\mathrm{s}}$ about which the linearization is performed

$$\begin{cases} \textbf{Node } \mu_1, \mu_2 \text{ real, } \mu_1 \cdot \mu_2 \geq 0, \mu_1 \neq \mu_1 \\ \textbf{Saddle } \mu_1, \mu_2 \text{ real, } \mu_1 \cdot \mu_2 \leq 0 \\ \textbf{Focus } \mu_1, \mu_2 \text{ complex coniugate with nonzero real part} \end{cases}$$

In the **Node** case, if $\mu < 0$ $\boldsymbol{h}(t)$ tends to zero, thus small perturbations die out and this type of node is called *stable node*, whereas $\mu > 0$ means that locally the trajectories $\boldsymbol{y}(t)$ leave the neighborhood of the stationary solution and so this type of node is called *unstable node*. The two real eigenvectors $\boldsymbol{w}_1$ and $\boldsymbol{w}_2$ have a geometrical meaning: they define two straight lines passing through the stationary point (*eigenspace*) such that the local trajectories directed toward (or outward) it are tangent to them; an example is shown in Fig.4.2, where the *eigenspace* is depicted with dashed lines for the case of stable node. A **Saddle** point is always unstable as two of the four trajectories associated with the eigenspace leave the equilibrium. In the **Focus** case, going back to eq.(4.11), it's clear that, assuming $\mu_1 = \alpha + \mathrm{i}\beta$ and $\mu_2 = \alpha - \mathrm{i}\beta$, the time-dependent part of $\boldsymbol{h}(t)$ is made of a factor $e^{\mathrm{i}\beta t}$ representing a rotation in the phase plane and the factor $e^{\alpha t}$ which is a radius (i.e. the distance of the actual state from the origin of the plane), increasing if $\alpha > 0$ (*unstable focus*) and decreasing if $\alpha < 0$ (*stable focus*), such that any trajectories close to the equilibrium resembles a spiral.

The introduced *eigenspace* is useful to handle the concept of *manifold* (see [113] for a complete definition); simplifying, an n-dimensional manifold $\mathrm{M} \subset \mathbb{R}^{\mathrm{N}}$ can be seen as a set

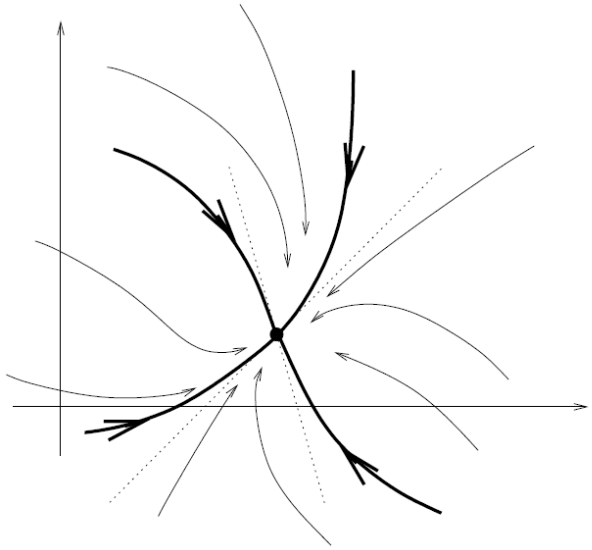

Fig. 4.2: Eigenspace of a stable node (dashed lines),taken from [104]

which *locally* has the structure of an Euclidean space and in applications in often used to indicate n-dimensional surfaces embedded in $\mathbb{R}^N$. Referring to the bifurcation case, if the set of initial conditions in the phase plane is such that as $t \to +\infty$ the solution enter (leave) the fixed point, this set is called a *stable manifold* (*unstable manifold*). Thus for example the stable node of Fig.4.2 is surrounded by a two-dimensional stable manifold; a saddle node instead has both.

As seen above, the eigenvalues of the Jacobian matrix determine the dynamic behaviour in the neighborhood of the equilibrium point; when $\boldsymbol{f}_{\boldsymbol{y}}^{\mathrm{s}}$ has no eigenvalue with zero real part (as the cases previously presented) the corresponding fixed point is called *hyperbolic*, while if $\mu_{1,2} = \pm \mathrm{i}\beta$ it is called *nonhyperbolic*; one of the main meaning of this classification lies in its impact on the reliability of the linearized stability analysis presented, where the set of trajectories of the nonlinear ODE in eq.(4.1) in a neighborhood of a stationary solution is compared with the behaviour of its linearization (Eq.4.8). This results passes through the importance of the small nonlinear terms neglected in eq.(4.5): for hyperbolic fixed points, stability is not affected by them as assured by the Hartman-Grobman theorem [53] which states that the local phase diagram near a hyperbolic fixed point is topologically equivalent to the one of the linearization (for which it can be defined the manifolds and so on) and as a consequence the stability type of the fixed point is faithfully captured by the linearization; stable and unstable manifolds at equilibria are tangent to the corresponding eigenspaces of

the linearization, formed by linear combinations of the eigenvectors of the stable eigenvalues and of the unstable eigenvalues, respectively. Conversely for the nonhyperbolic case, the condition $\mathrm{Re}(\mu) = 0$ makes this result fall and also the higher order nonlinear terms should be considered in the analysis .

Most of the above results generalize to systems of n ODEs: the Jacobian matrix consists now of n^2 first-order partial derivatives $\frac{\partial f_k}{\partial y_j}$ where $k, j = 1, ..., n$ and the stability of the equilibria is characterized by its eigenvalues $\mu_1, ..., \mu_n$. A general stability result [80] states that if $\boldsymbol{f_y}$ is two times continuously differentiable and $\boldsymbol{f}(\boldsymbol{y}^s) = 0$, the real parts of the eigenvalues μ_j of the Jacobian evaluated at the stationary solution $\boldsymbol{y_S}$ determine stability: $\mathrm{Re}(\mu_j) < 0$ for all j implies asymptotic stability; $\mathrm{Re}(\mu_j) > 0$ for at least one eigenvalue implies instability. Since the number of cases generated by the various combinations of the signs of the eigenvalues enormously increases with n, a classification is not simple as in the planar situation. The Hartman-Grobman theorem is still valid and here the dimension of the stable manifold equals the number of eigenvalues with negative real part as well as the dimension of the unstable manifold is equal to the number of the eigenvalues with positive real part.

4.3 Periodic Orbits

As earlier emphasized, these concepts of stability and instability have a local meaning and so even defining all kind of equilibria of a particular system, there are possibly other attractors, for example the *limit cycle*. A limit cycle is an isolated closed trajectory [108], where isolated means that neighboring trajectories are not closed and spiral either toward or away from the limit cycle; if all neighboring trajectories approach the limit cycle, it's said to be *stable*, otherwise it's *unstable*, as depicted in Fig.4.3. Limit Cycle Oscillations (LCOs) model systems that exhibit self-sustained oscillations (even in the absence of external periodic forcing). Limit cycles are inherently nonlinear phenomena: a linear system can have closed orbits but they won't be isolated, since if $\boldsymbol{f}$ gives rise to a periodic orbit $\boldsymbol{y}$, the same will be for $c \cdot \boldsymbol{f}$ for any constant c$\neq$0, thus $\boldsymbol{y}$ it's surrounded by a family of closed orbits. Consequently, while the amplitude of a linear oscillation is set by the initial conditions and any slight disturbance to the amplitude will persist forever, the limit cycle oscillations are determined by the structure of the system itself, $\boldsymbol{f}(\boldsymbol{y})$. Normally it's difficult to tell whether a given system has a limit cycle from the governing equation alone. One of the most common

Fig. 4.3: Stable and unstable limit cycle,taken from [108]

way is to follow the definition of limit cycle

$$\boldsymbol{y}(t+T) = \boldsymbol{y}(t) \tag{4.12}$$

where the minimum T satisfying this equation is called period, performing numerical simulations of eq.(4.1) given an initial condition $\boldsymbol{y}(0) = \boldsymbol{z}$ and a final time t=t_{f} to cover.

4.4 Center Manifold Theory and Normal Forms

It is desirable to reduce the complexity of the analysis of real dynamical systems allowing the use of simplified geometrical and algebraic schemes.
Two possible approaches are to reduce the dimensionality of the system and to eliminate some nonlinearities; these tasks can be accomplished through two rigorous mathematical techniques: *center manifold theory* and *method of normal forms*.

The basis of the first theory [49] is the *Center Manifold Theorem* which provides a means for systematically reducing the dimension of the state spaces being considered; in Sec. 4.2 the concepts of eigenspace and manifold have been introduced, which together with the Hartman-Grobman theorem enable to describe quite simply the *flow* near a fixed point from its linearized vector field. In general once the eigenvalue problem of Eq.4.10 is solved, the subspace spanned by the n eigenvectors $\boldsymbol{w}_i$ can be divided in three classes

$$\begin{cases} \text{the } \textit{stable subspace, } E^s = \text{span}\left\{a^1, ..., a^{n_s}\right\} \\ \text{the } \textit{unstable subspace, } E^u = \text{span}\left\{b^1, ..., b^{n_u}\right\} \\ \text{the } \textit{center subspace, } E^c = \text{span}\left\{c^1, ..., c^{n_c}\right\} \end{cases}$$

such that n_s+n_u+n_c=n; $a^1, ..., a^{n_s}$ are the n_s generalized eigenvectors whose eigenvalues have negative real parts, $b^1, ..., b^{n_u}$ are the n_u generalized eigenvectors whose eigenvalues

have positive real parts and $c^1, ..., c^{n_c}$ are those whose eigenvalues have zero real parts. The name reflects the facts that solutions lying on E^s (E^u) are characterized by exponential decay (growth), either monotonic or oscillatory, leading to the concept of stable (unstable) manifold that eases the description of the local dynamical behavior since it is controlled just by exponential contraction (expansion). The goal is to gain a similar type of 'reduction principle' applied to the study of nonhyperbolic fixed points, that is a *center manifold* passing through the fixed point to which the system could be restricted in order to study its behaviour in its neighborhood. The Center Manifold Theorem states the existence of such a manifold (together with the other two), defining it as an invariant manifold *tangent* to the center subspace; the term invariant is used to enlighten the property that each x ∈ M, where M is a n-dimensional manifold embedded in $\mathbb{R}^{\mathrm{N}}$, has a neighborhood U for which there is a smooth invertible mapping $\phi : \mathbb{R}^{\mathrm{n}} \to U$ (n ≤ N).
The idea underlying the center manifold method is to isolate the asymptotic behaviour associated to the center eigenspace E^c by locating an *invariant* manifold tangent to it, where the invariant property assures that a trajectory that starts on it stays there. The resulting stable, unstable and center manifolds are denoted as W^s, W^u and W^c.

The sought consequence of this theorem [49] is that a bifurcating system is topologically equivalent to

$$\begin{aligned} \dot{\hat{x}} &= \hat{f}(x) \\ \dot{\hat{y}} &= -\hat{y} \\ \dot{\hat{z}} &= \hat{z} \end{aligned} \tag{4.13}$$

where $(\hat{x} , \hat{y} , \hat{z}) \in W^c \times W^s \times W^u$; eq.(4.13) represents a partition of the entire vector field $\boldsymbol{f}$ in its three parts each of them referring to a different dynamical behaviour.

In order to compute the vector fields involved in eq.(4.13) (especially $\hat{f}(x)$ which describe what locally happens in its center manifold), the system early introduced in eq.(4.1) is expressed in a block diagonal form after a Taylor expansion and a linear transformation

$$\begin{aligned} \dot{\boldsymbol{y}}^- &= \boldsymbol{A}^- \boldsymbol{y}^- + \boldsymbol{f}^-(\boldsymbol{y}^-, \boldsymbol{y}^+, \boldsymbol{y}^0) \\ \dot{\boldsymbol{y}}^+ &= \boldsymbol{A}^+ \boldsymbol{y}^+ + \boldsymbol{f}^+(\boldsymbol{y}^-, \boldsymbol{y}^+, \boldsymbol{y}^0) \\ \dot{\boldsymbol{y}}^0 &= \boldsymbol{A}^0 \boldsymbol{y}^0 + \boldsymbol{f}^0(\boldsymbol{y}^-, \boldsymbol{y}^+, \boldsymbol{y}^0) \end{aligned} \tag{4.14}$$

where the square matrices $\boldsymbol{A}^-$, $\boldsymbol{A}^+$ and $\boldsymbol{A}^0$ of sizes n_s, n_u and n_c have eigenvalues with negative, positive and zero real part respectively and the vector $\boldsymbol{y}$ is partitioned into three subvectors of lengths n_s, n_u and n_c. If, without loss of generality, a stationary solution is assumed in the coordinate origin $\boldsymbol{f}(\boldsymbol{0})=\boldsymbol{0}$ and for simplicity (it's the most interesting case

physically) it's assumed n_u=0 (i.e. the unstable manifold is empty), it holds

$$\begin{aligned} \dot{\boldsymbol{y}}^- &= \boldsymbol{A}^- \boldsymbol{y}^- + \boldsymbol{f}^-(\boldsymbol{y}^-, \boldsymbol{y}^0) \\ \dot{\boldsymbol{y}}^0 &= \boldsymbol{A}^0 \boldsymbol{y}^0 + \boldsymbol{f}^0(\boldsymbol{y}^-, \boldsymbol{y}^0) \end{aligned} \tag{4.15}$$

As by definition the center manifold is tangent to the eigenspace E^c (here the $\boldsymbol{y}^-$=$\mathbf{0}$ space), it can be represented as a (*local*) graph

$$W^c = \left\{ (\boldsymbol{y}^0, \boldsymbol{y}^-) \mid \boldsymbol{y}^- = \boldsymbol{C}(\boldsymbol{y}^0) \right\} \; ; \boldsymbol{C}(\mathbf{0}) = \mathbf{0} \; , \boldsymbol{C}'(\mathbf{0}) = \mathbf{0} \tag{4.16}$$

where the existence of the function $\boldsymbol{C}(\boldsymbol{y}^0)$ is assured by the invariant manifold theorem. In Fig.4.4 the representation of the central manifold and its local graph is shown for the case of one-dimensional manifolds; it's worth to note that it's not possible to assign *apriori* directions to the flow without specific information on the higher-order terms of $\boldsymbol{f}^0$ near $\mathbf{0}$. Eq.(4.13) is finally obtained, considering the projection of the vector field $\boldsymbol{f}^0$ on the center

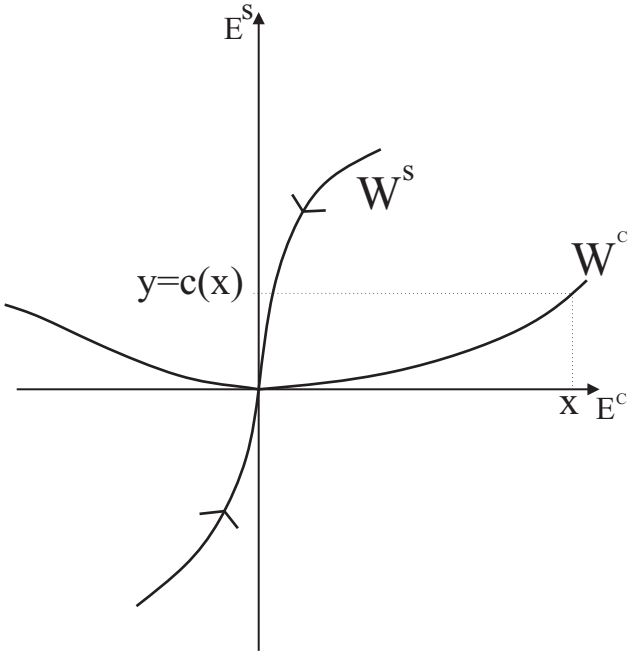

Fig. 4.4: Stable and unstable manifold with the respective subspaces

manifold

$$\dot{\boldsymbol{y}}^0 = \boldsymbol{A}^0 \boldsymbol{y}^0 + \boldsymbol{f}^0(\boldsymbol{C}(\boldsymbol{y}^0), \boldsymbol{y}^0) \tag{4.17}$$

One of the main conclusions of the Center Manifold theory states that the stability of the equilibrium $\boldsymbol{y}$=$\mathbf{0}$ of eq.(4.15) is reflected by the reduced (n_c-dimensional system) in eq.(4.17).

An approximate procedure to find the function $\boldsymbol{C}$ describing the center manifold can be found in [18].

Assuming that the center manifold theorem has been applied to the system (eq.(4.17) is considered), the goal of the *Method of Normal Forms* is to provide an additional coordinate transformation which simplify the analytic expression of the vector field on the center manifold $\boldsymbol{f}^0(\boldsymbol{C}(\boldsymbol{y}^0), \boldsymbol{y}^0)$; this procedure can be applied of course to the other two manifolds too. The resulting 'simplified' vector field is called normal form.
Given a system of differential equations

$$\dot{\boldsymbol{x}} = \boldsymbol{f}(\boldsymbol{x}) \tag{4.18}$$

which has an equilibrium at $\boldsymbol{x} = \boldsymbol{0}$, a coordinate change $\boldsymbol{x} = \boldsymbol{H}(\boldsymbol{z})$ brings to

$$\begin{aligned} D\boldsymbol{H}(\boldsymbol{z})\dot{\boldsymbol{z}} &= \boldsymbol{f}(\boldsymbol{H}(\boldsymbol{z})) \\ \dot{\boldsymbol{z}} &= (D\boldsymbol{H}(\boldsymbol{z}))^{-1}\boldsymbol{f}(\boldsymbol{H}(\boldsymbol{z})) \end{aligned} \tag{4.19}$$

where D is the derivative operator in respect to $\boldsymbol{z}$. Depending on the maximum grade of nonlinear terms sorting out from eq.(4.19) one can try to iteratively find a sequence of coordinate transformations $\boldsymbol{H}_1$, $\boldsymbol{H}_2$, ... which remove terms of increasing degree from the Taylor series of eq.(4.19), neglecting all the inessential terms. Recalling eq.(4.17), a coordinate change $\boldsymbol{H}$ of the form identity plus higher order terms is sought which has the property that, assuming $\boldsymbol{x} = \boldsymbol{y}^0$ in eq.(4.18), eq.(4.19) has non-linear terms that vanish to higher order than those of $\boldsymbol{f}^0$ in eq.(4.17).
If k is the smallest degree of nonvanishing term of $\boldsymbol{f}_i^0$, this transformation could be chosen as

$$\boldsymbol{x} = \boldsymbol{z} + \boldsymbol{P}(\boldsymbol{z}) \tag{4.20}$$

with $\boldsymbol{P}_i$ a polynomial of degree k so that the lowest degree of the nonlinear terms in eq.(4.17) is now k+1. Without probing the mathematical aspects of this method [113], it's worth to stress out some important characteristics: the method is local in the sense that the coordinate transformations are generated in a neighborhood of a known solution (usually a fixed point), reflecting thus only the local dynamic behaviour; the coordinate transformations are nonlinear functions of the dependent variables and are found solving a sequence of linear problems.

4.5 Dependence on parameters

Usually the ODEs giving rise to eq.(4.1) involve one or more parameters; denoting one real parameter by λ, the systems of ODES governing the problem can be written as

$$\dot{\boldsymbol{y}} = \boldsymbol{f}(\boldsymbol{y}, \lambda) \tag{4.21}$$

where the dipendence from λ gives reason of the common expression *family* of differential equations; solutions (as well as stationary points, Jacobian matrix and its eigenvalues) depend now on both the independent variable t and the parameter λ. Varying the parameter λ, the position and the qualitative features of a fixed point can vary. In order to show graphically the dependence of $\boldsymbol{y}$ on λ in a two-dimensional diagram, a scalar measure of the n-vector $\boldsymbol{y}$ has to be chosen: options are any norm of this vector or a particular component, i.e. $[\boldsymbol{y}]$=y_{k}(t). A diagram depicting $[\boldsymbol{y}]$ versus λ with ($[\boldsymbol{y}]$,λ) solving eq.(4.21), is called *bifurcation diagram*; the continuous curves in these diagrams are called *branches* and enables to observe many aspects of the dynamic behaviour of the system, like for example the change in the number of the solutions as the parameter is changed, as shown in Fig.4.5. The solu-

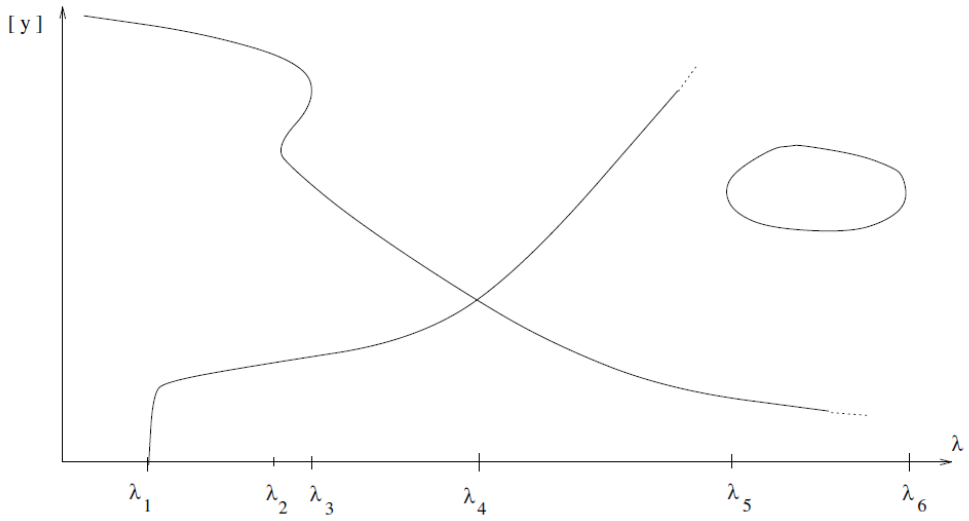

Fig. 4.5: Example of bifurcation diagram: varying the parameter the number of fixed points varies

tion ($\boldsymbol{y}_0$,λ_0) of eq.(4.21) where the number of possible equilibrium points changes is called *bifurcation*; bifurcations are important from a practical point of view since they provide models of transition and instabilities as some control parameters are varied. As λ increases

(or decreases) the eigenvalues move in the complex plane and the original equilibrium point describes an equilibrium path in the n-dimensional phase space of the variables $\boldsymbol{y}$ that has interesting geometrical properties at the bifurcation points. However they are difficult to visualize in such a complicated space; the two mathematical theory previously introduced are valid instruments to legitimate the adoption of simple reduced systems, in one or two dimensions, that preserve all the qualitative properties of the general n-dimensional system.

4.5.1 Stationary Bifurcations

The first bifurcation among stationary solutions to be examined is the **Saddle-Node** bifurcation, which is the basic mechanism by which fixed points are created and destroyed: as a parameter is varied, two fixed points move toward each other, collide and mutually annihilate (or reversely they both can originate). The normal form for this bifurcation is given by eq.(4.22)

$$\dot{y} = y^2 \pm \lambda \tag{4.22}$$

The solutions y(λ) form a parabola defined only for $\lambda \geq 0$; anyway in general (when a normal form slightly different than the basic on in eq.(4.22) is considered) it will exist a point where the solutions begin to exist, resulting in no solutions on one side of a turning point and two solutions on the other side: two solutions are born or two solutions annihilate each other. The name given to this phenomenon derives from the stability behaviour of the solutions when the earlier presented stability criteria are employed (if the normal form is considered, the Jacobian is a scalar): referring to eq.(4.22), it's clear than one branch of the parabola is stable and the other is unstable.

In the **Transcritical** bifurcation a fixed point that exists for all values of the parameter changes its stability as this is varied. The normal form for this bifurcation is given by eq.(4.22)

$$\dot{y} = -y^2 + \lambda y \tag{4.23}$$

The equilibria are y=λ and y=0, with the latter that loses its stability at the bifurcation point (y,λ)=(0,0) and the former that gains (considering increasing values for λ) it, showing a sort of exchange of stability between the branches. The important difference between this bifurcation and the previous one is that the two fixed points don't disappear after the bifurcation and just switch their stability, as depicted in Fig.4.6.

The **Pitchfork Bifurcation** is common in physical problems that have a symmetry and so fixed points tend to appear and disappear in symmetrical pairs; this property reflects on

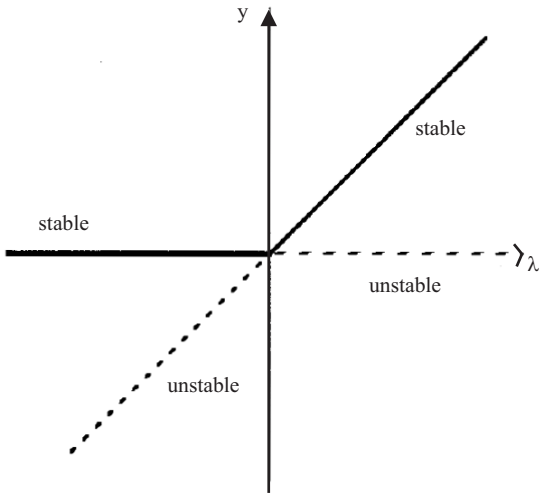

Fig. 4.6: Transcritical bifurcation, taken from [108]

the normal forms that as will be clear are invariants under the change of variables y → -y. There are two very different types of pitchfork bifurcation: *supercritical* and *subcritical*. The normal form for the **Supercritical Pitchfork Bifurcation** is given by eq.(4.24)

$$\dot{y} = -y^3 + \lambda y \tag{4.24}$$

For $\lambda \geq 0$ there are two stable equilibria $\pm\lambda$ while the fixed point y=0, stable for $\lambda \leq 0$, loses its stability in the bifurcation point (y,λ)=(0,0), exactly where the other two branches are emanated; an example of this loss of stability is given by the buckling of a beam: the beam is stable in the vertical position if the load (the role played by λ here) is small and the stable stationary point corresponds to zero deflection. If the compression load exceeds the buckling threshold the vertical position becomes unstable and the new two symmetrical equilibria, corresponding to left and right buckled configurations, have been born. The reason why there are stable solutions on both sides of the bifurcation has to be sought in the stabilizing cubic term, which acts like a restoring force pulling the solution toward the two stable fixed points. If in eq.(4.24) the minus of the cubic term is substituted with a plus, the normal form of the **Subcritical Pitchfork Bifurcation** is gained. The behaviour of the fixed point y=0 doesn't change, while the non-zero fixed points, existing now for $\lambda \leq 0$ are unstable, that is a loss of stability occurs at the bifurcation point, as depicted in Fig.4.7. In a system like that, a *blow up* takes place, as starting from any initial condition z≠0, the solution $y \to \infty$ in finite time; in real physical systems, such an explosive instability is usually opposed by the stabilizing influence of higher-order terms. If symmetry holds, the first stabilizing term

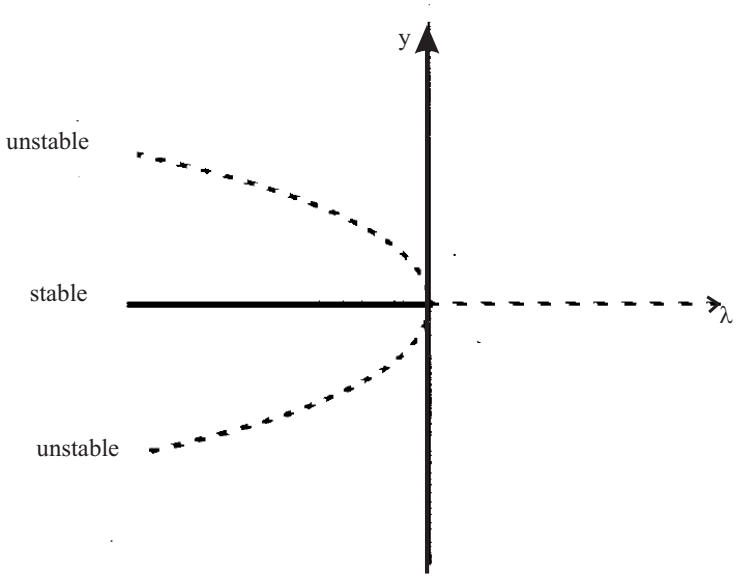

Fig. 4.7: Subcritical pitchfork bifurcation

is y^5 and the new normal form is of this kind

$$\dot{y} = -y^5 + +y^3 + \lambda y \tag{4.25}$$

The bifurcation diagram for eq.(4.25) is shown in Fig.4.8. For small y the behaviour is

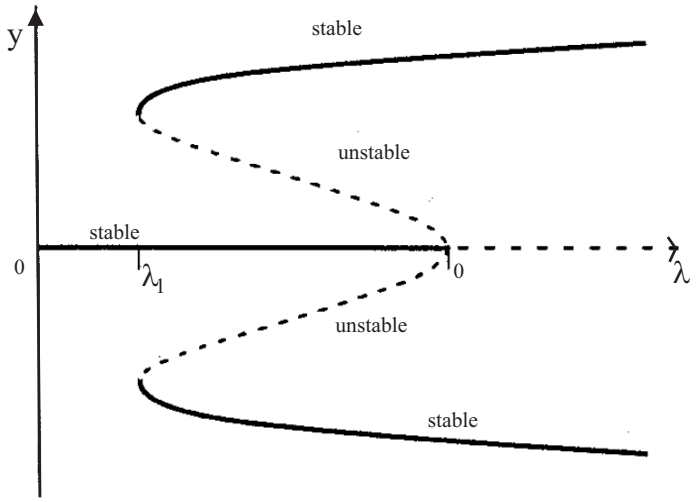

Fig. 4.8: Subcritical pitchfork bifurcation with the higher order stabilizing term

analogous to the one shown in Fig.4.7: the origin is locally stable and two backward branches of unstable fixed points bifurcate; as y increases, the new feature due to the term y^5 becomes

evident as the two branches turn around and become stables; the bifurcation at λ_1 is clearly a saddle-node bifurcation and for $\lambda \geq \lambda_1$ these large amplitude branches exist. In the range $\lambda_1 \leq \lambda \leq 0$ three stationary points exist, as shown by the continuous lines, with the initial condition determining which fixed point is approached; it can be stated that the origin is stable to small perturbations, but not to large ones (local stability). Moreover the existence of different stable states allows for the possibility of *jumps* and *hysteresis* as the parameter is varied.

The bifurcations presented so far have a common feature: all the branches intersecting in the bifurcation point consists of stationary solutions (eq.(4.3) holds), that is the bifurcation, called *stationary bifurcations* involve the collision of two or more fixed points. When the request that $\dot{\boldsymbol{y}}=\mathbf{0}$ is removed, equilibrium can be superseded by motion and new kind of bifurcations can be detected.

4.5.2 Hopf Bifurcations

The **Hopf Bifurcation** is a bifurcation from a branch of fixed points to a branch of periodic oscillations; from a linearized stability analysis point of view, when the Jacobian is evaluated at the Hopf point, it has a pair of purely imaginary eigenvalues: in the previous cases, when a bifurcation occurred there was a real eigenvalue $\mu_1(\lambda_0)=0$ (*zero-eigenvalue bifurcations*), whereas now two complex conjugate eigenvalues simultaneously cross the imaginary axis into the right half of the Gauss plane. A formal definition of Hopf bifurcation can be found in the following theorem by Hopf: assuming $\boldsymbol{f} \in C^2$, if $\boldsymbol{f}(\boldsymbol{y}_0,\lambda_0)=\mathbf{0}$, $\boldsymbol{f}_{\boldsymbol{y}}(\boldsymbol{y}_0,\lambda_0)$ has only a simple pair of purely imaginary eigenvalues $\mu_{1,2}(\lambda_0)=\pm \mathrm{i}\beta$ and $\frac{d\,\mathrm{Re}\,\mu(\lambda_0)}{d\lambda_0} \neq 0$ then at $(\boldsymbol{y}_0,\lambda_0)$ there is a birth of limit cycles with initial period $T_0=\frac{2\pi}{\beta}$. In Fig.4.9 is summarized the difference between these two families of bifurcations showing what happens in the complex plane to the eigenvalues $\mu(\lambda)$.

Like pitchfork bifurcations, Hopf bifurcations can be supercritical and subcritical. In Fig.4.9 it can be seen that before the eigenvalues cross the imaginary axis the physical system settles down to equilibrium through exponentially damped oscillations (stable focus); assuming that the decay rate depends on the control parameter λ, if it becomes slower and finally changes to growth at a critical value λ_s the stationary solution loses its stability: the system has undergone a **supercritical Hopf bifurcation**. In polar coordinates, a simple

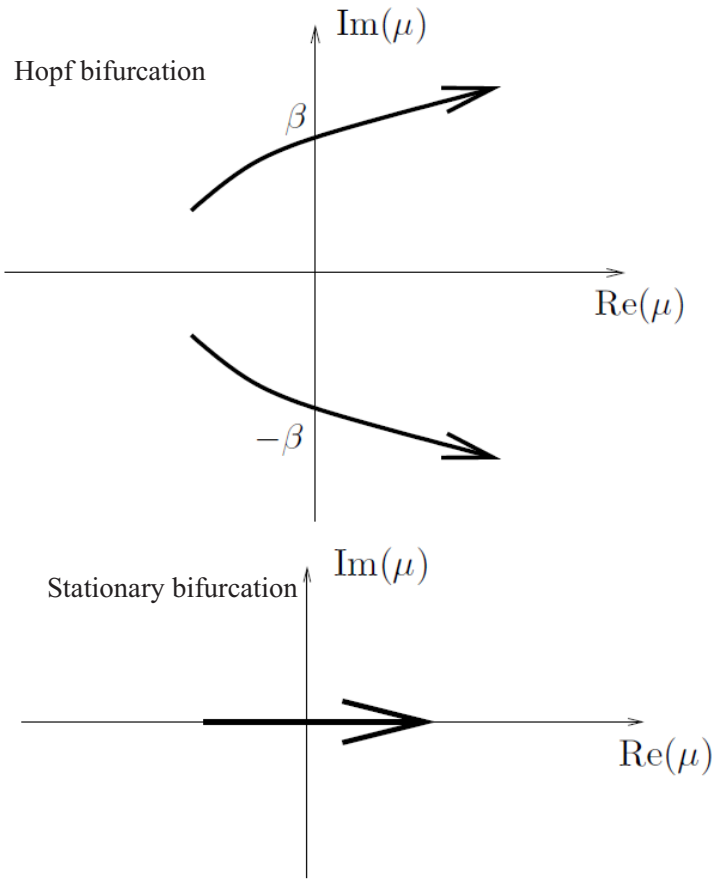

Fig. 4.9: Behaviour of the critical eigenvalue in the complex plane

example of supercritical Hopf bifurcation is given by the following system:

$$\begin{cases} \dot{r} = \lambda r - r^3 \\ \dot{\theta} = \beta + b\theta^3 \end{cases} \tag{4.26}$$

where λ controls the stability of the fixed point (coincident in this example with the origin), β determines the frequency of the infinitesimal oscillation and b gives the dependence of frequency on amplitude for larger amplitude oscillations; the behaviour of this system is the same of the general case previously pointed out: when $\lambda \leq 0$ the origin is a stable spiral while for $\lambda \geq 0$ the origin becomes an unstable spiral and it starts a limit cycle at r$\simeq \sqrt{\lambda}$. In general the size of the limit cycle grows continuously from zero and increases like $\sqrt{\lambda - \lambda_s}$ if the parameter is kept close to its critical value λ_s.

In the **subcritical Hopf bifurcation** the cubic term is destabilizing, thus driving trajectories away from the origin. The same argument introduced for subcritical pitchfork

bifurcation concerning the stabilizing effect of high-order terms can be adopted. The normal form becomes

$$\begin{cases} \dot{r} = \lambda r + r^3 - r^5 \\ \dot{\theta} = \beta + b\theta^3 \end{cases} \tag{4.27}$$

The situation here is more complex and Fig.4.10 can be considered. Making use of the

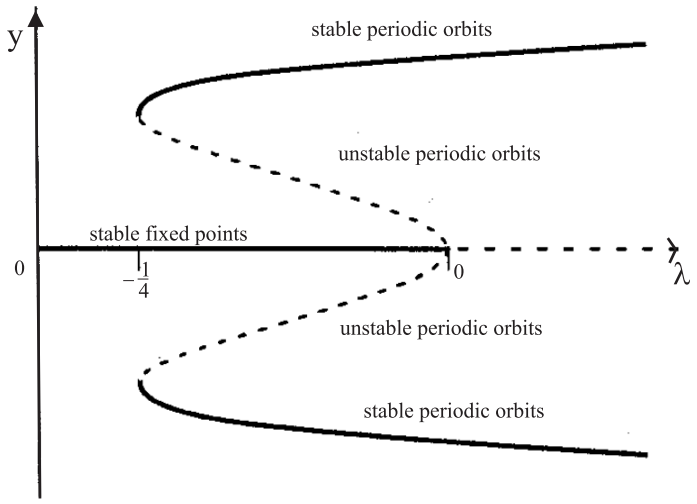

Fig. 4.10: Subcritical Hopf bifurcation with the higher order stabilizing term

eigenvalues analysis, it's clear that for $\lambda \leq -\frac{1}{4}$ there is only the stationary point in the origin, while in the range $-\frac{1}{4} \leq \lambda \leq 0$ there are also a stable and an unstable limit cycle; when $\lambda \geq 0$ the latter one engulfs the origin making it unstable and *suddenly* the limit cycle becomes the only attractor remained: solutions that used to remain near the origin are now forced to grow into large-amplitude oscillations (similar behaviour to the one depicted in Fig.4.8). As it can be argued, subcritical case is always more dramatic and potentially dangerous in engineering applications (these kind of bifurcations often exhibits in aeroelastic flutter and other vibrations of airplane wings). Given a Hopf bifurcation, it's a difficult task to tell on which of the two families it belongs: the linearized analysis doesn't help since in both cases a pair of eigenvalues moves from the left to the right half-plane and an analytical criterion exists but it can be difficult to use; a quick approach can be performed using numerical simulations: if a small, attracting limit cycle appears immediately after the fixed point loses its stability and no hysteresis phenomena arise when the parameter is reversed, the bifurcation is supercritical, otherwise it's probably subcritical.

4.5.3 Stability of Periodic Solutions

In Sec. 4.3 it has been discussed the existence of attractors such that for the solution of eq.(4.1) there is a minimum time interval $T \geq 0$ after which the system returns to its original state:

$$\boldsymbol{y}(t+T) = \boldsymbol{y}(t) \tag{4.28}$$

The goal is here to provide a qualitative description of these possible behaviours of particular dynamical systems under certain conditions (for the formal mathematical treatise good references are [104],[86]). When tracing a branch of periodic solutions and the question arises whether the periodic solutions are stable and in which way the stability is eventually lost. The basic tools to answer this question are the *monodromy matrix* and the *Poincaré map*. In what follows, it is first investigated the stability of one particular periodic solution $\boldsymbol{y}^*$ and later the dependence on λ.

The stability of a periodic solution (in particular a limit cycle) rely on the way neighboring trajectories behave; defining $\varphi(t;\boldsymbol{z})$ the periodic trajectory of eq.(4.1) with the initial condition $\boldsymbol{y}(0)=\boldsymbol{z}^*$, a trajectory that starts from the perturbed initial vector $\boldsymbol{z}^* + \boldsymbol{d}_0$ progresses with the distance

$$\boldsymbol{d}(t) = \varphi(t;\boldsymbol{z}^* + \boldsymbol{d}_0) - \varphi(t;\boldsymbol{z}^*) \tag{4.29}$$

from the periodic orbit. The distance $\boldsymbol{d}(T)$ after one period T is given by $\varphi(T;\boldsymbol{z}^* + \boldsymbol{d}_0) - \varphi(T;\boldsymbol{z}^*)$ and its Taylor expansion yields:

$$\boldsymbol{d}(T) = \frac{\partial\varphi(T;\boldsymbol{z}^*)}{\partial\boldsymbol{z}}\boldsymbol{d}_0 + \text{ terms of higher order} \tag{4.30}$$

The matrix $\frac{\partial\varphi(T;\boldsymbol{z}^*)}{\partial\boldsymbol{z}}$, called monodromy matrix, plays an important role in deciding whether the initial perturbation decays or grows. The definition of φ implies that $\varphi(0;\boldsymbol{z})=\boldsymbol{z}$ and so $\frac{\partial\varphi(0;\boldsymbol{z})}{\partial\boldsymbol{z}}=\boldsymbol{I}$. Thus, since the trajectory has to obey the differential equation

$$\frac{d\varphi(t,\boldsymbol{z})}{dt} = \boldsymbol{f}(\varphi(t;\boldsymbol{z})) \tag{4.31}$$

differentiating this identity with respect to $\boldsymbol{z}$, it's easy to see that the monodromy matrix solves the matrix initial-value problem

$$\dot{\Phi} = \boldsymbol{f}_{\boldsymbol{y}}(\boldsymbol{y}^*)\Phi \ , \ \Phi(0) = \boldsymbol{I} \tag{4.32}$$

The monodromy matrix $\boldsymbol{M} := \Phi(T)$ of the periodic solution $\boldsymbol{y}^*(t)$ with period T and initial vector $\boldsymbol{z}^*$ given from eq.(4.32) has the two important properties :

- $\Phi(pT)=\boldsymbol{M}^p$
- $\boldsymbol{M}$ has +1 as eigenvalue with eigenvector $\boldsymbol{f}(\boldsymbol{y}(0))$.

The class of dynamical systems in which the state $\boldsymbol{y}$ is determined just for discrete time instances t_1,t_2,...,t_m is governed by a law $\boldsymbol{f}_M$ called *map* such that

$$\boldsymbol{y}^{N+1} = \boldsymbol{f}_M(\boldsymbol{y}^N) \tag{4.33}$$

The *Poincaré map* is extremely useful for describing oscillating systems; calling n the dimension of the state of the system, an (n-1)-dimensional hypersurface Ω can be chosen such that all trajectories that cross Ω in a neighborhood of a point $\boldsymbol{q}^* \in \Omega$ intersect it transversally and all in the same direction: these requirements allow to define Ω, also called the *Poincaré section*, as a local set, which generally changes if another $\boldsymbol{q}^*$ is considered. Let $T_\Omega(\boldsymbol{q})$ be the time taken for a trajectory $\varphi(t;\boldsymbol{q})$ to first return to Ω

$$\varphi(T_\Omega(\boldsymbol{q});\boldsymbol{q}) \in \Omega \ , \ \varphi(t;\boldsymbol{q}) \notin \Omega \quad \text{for} \quad 0 < t < T_\Omega(\boldsymbol{q}) \tag{4.34}$$

the Poincaré map $\boldsymbol{P}(\boldsymbol{q})$ is defined by

$$\boldsymbol{P}(\boldsymbol{q}) := \boldsymbol{P}_\Omega(\boldsymbol{q}) = \varphi(T_\Omega(\boldsymbol{q});\boldsymbol{q}) \quad \text{for} \quad \boldsymbol{q} \in \Omega \tag{4.35}$$

The geometrical meaning of this map and the relative section Ω previously defined is shown in Fig.4.11. Calling back the periodic solution $\boldsymbol{y}^*$ with period T, it intersects Ω in $\boldsymbol{z}^* \in \mathbb{R}^n$,

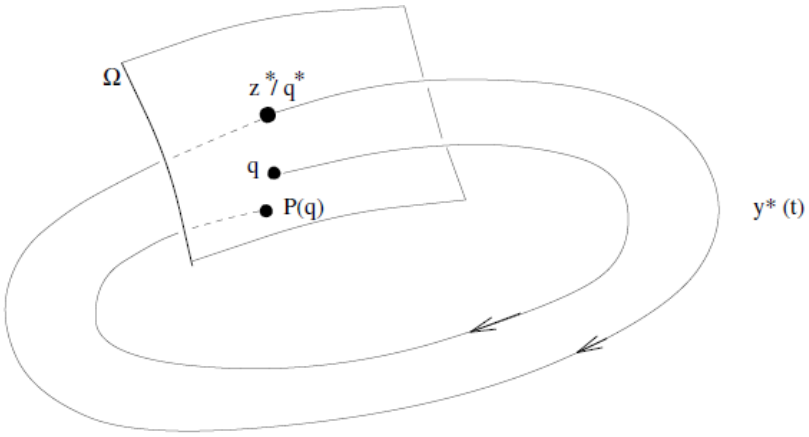

Fig. 4.11: Poincaré map and section

which can be represented in a coordinate system on Ω and indicated as $\boldsymbol{q}^*$; this is a fixed point of $\boldsymbol{P}$, that is

$$\boldsymbol{P}(\boldsymbol{q}^*) = \boldsymbol{q}^* \tag{4.36}$$

The idea underlying this line of reasoning is that the stability of the periodic orbit $\boldsymbol{y}^*$ is reduced to the behavior of the Poincaré map near its fixed point $\boldsymbol{q}^*$, checking whether this is repelling or attracting. As for the analysis of stability of fixed point, the linearization of $\boldsymbol{P}$ around the fixed point $\boldsymbol{q}^*$ is considered: this matrix is given by the monodromy matrix restricted to the (n-1)-dimensional set Ω.

As stated before, this matrix has +1 as an eigenvalue with eigenvectors $\dot{\boldsymbol{y}}(0)$ tangent to the intersecting curve $\boldsymbol{y}(t)$; since Ω is a local set, the intersection is transversal to this set and so this eigenvector doesn't belong to Ω: it can be concluded that the remaining n-1 eigenvalues of $\boldsymbol{M}$ are those of $\frac{\partial \boldsymbol{P}(\boldsymbol{q}^*)}{\partial \boldsymbol{q}}$. Consequently, the periodic orbit is stable if all the remaining n-1 eigenvalues of the monodromy matrix are smaller than unity in modulus, since they describe what happens to small perturbations within Ω; the eigenvalues of $\boldsymbol{M}$ are known as *Floquet multipliers* and are a milestone for the investigation of local stability of periodic solution by the Floquet theory [97]. Summarizing, to each periodic orbit corresponds one set of eigenvalues μ_1,...,μ_{n-1}: if the modulus of all n-1 eigenvalues are smaller than 1, then $\boldsymbol{q}^*$ is a stable fixed point (attracting) in the Poincaré map and so $\boldsymbol{y}^*$ is a stable periodic orbit; if the modulus of at least one eigenvalue is larger than 1, then $\boldsymbol{q}^*$ is unstable (repelling). Possible behaviours of a periodic solution on Ω are shown in Fig.4.12. The continuous curves depicted are not trajectories since the map generates a sequence of points: they just indicate the union of an infinite number of possible intersection points of distinct orbits. Fig.4.12.a shows an example of *saddle cycle*, Fig.4.12.b of *spiral cycle* and Fig.4.12.c of *nodal cycle*, in analogy with the nomenclature of the fixed points of differential equations.

In general the multipliers and hence the stability vary with λ; it's useful to describe the mechanism of loosing stability reporting the eigenvalues of $\boldsymbol{M}$ in the Gauss plane, as shown in Fig.4.13 for three values of λ. The circle is the unit circle and one eigenvalue is unity for all λ; for λ=λ_1 the solution is stable since all the meaningful eigenvalues lie inside the unit circle, while for λ=λ_2 the periodic orbit is unstable, underlying the fact that for some λ_0 between λ_1 and λ_2 one multiplier crosses the circle and the stability is lost (or gained, depending on which is the direction of variation of λ).

Of great importance is *where* the critical multiplier crosses the unit circle (in Fig.4.13 it's assumed that this happens at -1), since depending on this different types of bifurcation occur; the three possible ways for the critical multiplier to leave the unit circle are shown in

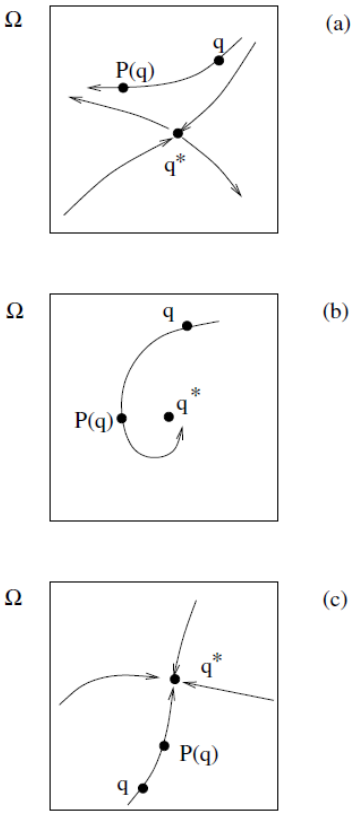

Fig. 4.12: Different behaviours of a periodic solution on the Poincaré section, from [104]

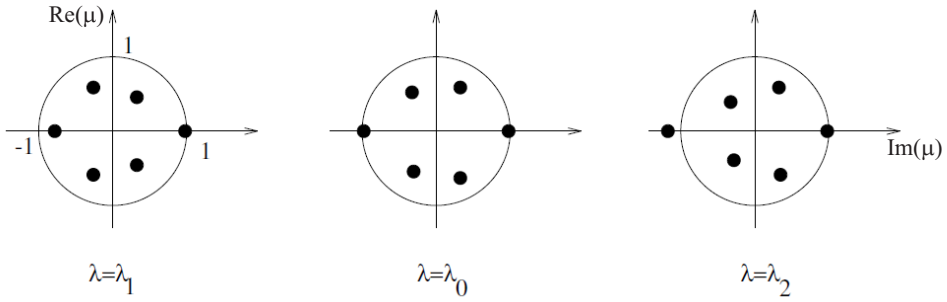

Fig. 4.13: Change in the position of the multipliers on the Gauss plane varying the parameter λ, from [104]

Fig.4.14.

In Fig.4.14.a the eigenvalue becomes unitary, $\mu(\lambda_0)= 1$ (*transcritical and cyclic-fold bifurcations*); in Fig.4.14.b the multiplier crosses the unit circle at the negative real axis, $\mu(\lambda_0)$=-1 *period doubling*: in Fig.4.14.c the monodromy matrix has a pair of complex conjugate eigen-

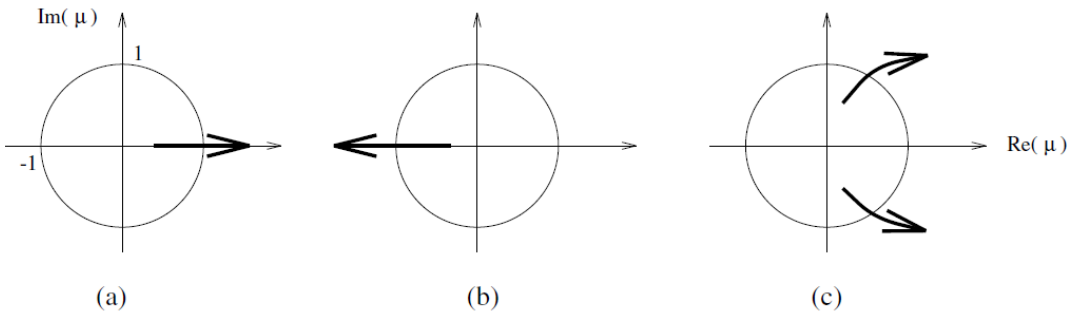

Fig. 4.14: Possible ways for the critical multiplier to leave the unit circle

values crossing the unit circle *secondary Hopf*.

The second case of loosing stability is here discussed, as is the one showing similarities with the behaviour of one of the configurations under investigations in this study. Recalling $\boldsymbol{P}$ as the Poincaré map defined in eq.(4.35), the study of periodic solutions brings to

$$\boldsymbol{P}(\boldsymbol{q}, \lambda) = \boldsymbol{q} \tag{4.37}$$

The fixed-point equation is equivalent to

$$\tilde{\boldsymbol{f}}(\boldsymbol{q}, \lambda) := \boldsymbol{P}(\boldsymbol{q}, \lambda) - \boldsymbol{q} = \boldsymbol{0} \tag{4.38}$$

which forms a system of n-1 scalar equations at whom the previously results valid for fixed points bifurcations can be applied; in particular the expression of the Jacobian of $\tilde{\boldsymbol{f}}$ should be exploited

$$\frac{\partial \tilde{\boldsymbol{f}}}{\partial \boldsymbol{q}} = \frac{\partial \boldsymbol{P}}{\partial \boldsymbol{q}} - \boldsymbol{I} \tag{4.39}$$

Assuming situation b in Fig.4.14, $\frac{\partial \tilde{\boldsymbol{f}}}{\partial \boldsymbol{q}}$ is non singular (the critical eigenvalue of $\frac{\partial \boldsymbol{P}}{\partial \boldsymbol{q}}$ is -1 and the others are smaller), consequently there is no bifurcation of fixed point for $\boldsymbol{P}$, as it would be the case when $\mu(\lambda_0)$= 1 leading the system to exhibits another or other fixed points on the Poincaré map (in a number depending on the multiplicity of the bifurcation), i.e. other periodic solutions (attractors).

To understand what happens to periodic oscillations in this situation, it can be observed that the chain rule implies

$$\frac{\partial \left[\boldsymbol{P}(\boldsymbol{P}(\boldsymbol{q}))\right]}{\partial \boldsymbol{q}} = \left(\frac{\partial \boldsymbol{P}(\boldsymbol{q})}{\partial \boldsymbol{q}}\right)^2 \tag{4.40}$$

Defining the map $\boldsymbol{P}^2$ as

$$\boldsymbol{P}^2(\boldsymbol{q}) = \boldsymbol{P}(\boldsymbol{P}(\boldsymbol{q})) \tag{4.41}$$

eq.(4.40) points out that when the monodromy matrix associated with the map $\boldsymbol{P}$ has -1 as an eigenvalue, $\boldsymbol{P}^2$ has an eigenvalue of value +1, that is the $\boldsymbol{P}^2$ fixed-point equation experiences a fixed point bifurcation: this means that there is no more the attracting fixed point of $\boldsymbol{P}$ (which has lost its stability) but there are two attracting fixed points of $\boldsymbol{P}^2$. This phenomenon, called *period doubling* or *flip bifurcation*, thus consists of an exchange of stability of period-one fixed point to period-two fixed point, as illustrated in Fig.4.15. As λ

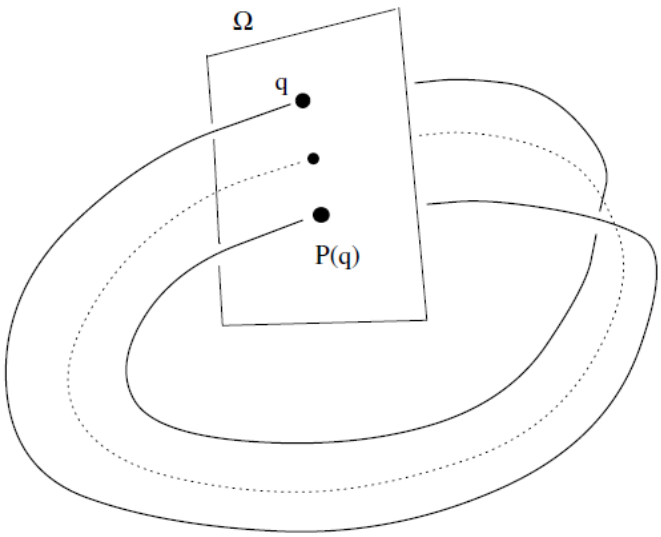

Fig. 4.15: Transition to period doubling, from [104]

approaches λ_0, the orbit of simple period represented by the dashed curve loses its stability and the new attractor is the heavy curve which depicts the stable orbit of double period; when the parameter is reversed and stability for the single period orbit is regained, what topologically happens is that the curve that winds twice shrinks to the curve that winds once. The term period when related to the Poincaré map is the integer that reflects how many iterations of $\boldsymbol{P}$ are required to reproduce the point from which iteration starts and so varying λ this integer remains constant if no further period doubling occurs. In contrast the period T referred to the periodic oscillation $\boldsymbol{y}(t)$ is affected by the variation of the parameter and so the period after the bifurcation is not varied exactly by a factor 2, attaining it as a limit as $\lambda \to \lambda_0$. The derivation of normal form for period doubling leads to a pitchfork shape, which explains why often the bifurcation diagram of period doublings have a square-root like shape.

This phenomenon is observed in many applications, as for example chemical reactions and

Navier-Stokes equations [37]. Moreover in many studies a sequence of period doubling occurs: after a first period doubling a second period doubling is more likely than other bifurcations and this routes can culminate in chaos [86]. The period-doubling sequence to chaos was first found in the context of one-dimensional maps [27] and studies have demonstrated it to occur in three-dimensional and higher continuous-time systems. The transition of period-doubling to chaos is also observed in experimental studies, for example on electric circuits [110] and chemical reactions [61].

The key role played by the monodromy matrix in ascertaining the nature of the stability of the periodic solution drove several strategies for its numerical evaluation. The solution of eq.(4.32) consists in the integration of n^2 differential equations and because the right-hand side depends on $\boldsymbol{y}^*$ and hence varies with t, the Jacobian is requested for each t, where $0 \leq t \leq T$; a way of providing it is to attach the system in eq.(4.1) to the one providing the monodromy matrix. This method requires that $n+n^2$ scalar differential equations are integrated simultaneously, bringing in this way storage issues. Other techniques try to reduce the size of the problem, but drawbacks related to computational cost or complexity of the algorithm rise up. Thus, even though there are different methods to compute this matrix, all of them are impractical for problems concerning systems with several degrees of freedom. An efficient approach (implicit Floquet Analysis) consists in the evaluation of just a limited number of eigenvalues of the monodromy matrix (the ones with the largest modulus) using Arnoldi's iterative algorithm and without requiring the explicit computation of the matrix [10]; this enormous simplification allowed its use for complex systems as rotorcraft stability analysis. This method, however, may lead to an erroneous estimation of the stability margins since there are spurious eigenvalues associated with algebraic constraints (when differential-algebraic equations are employed) which are meaningless for the analysis' purposes [94].

Using the result that the Floquet characteristic multipliers are perfectly equivalent to the eigenvalues of the Poincaré map, an empirical method [84] has been proposed to reconstruct a local Jacobian from data obtained by experiments; such an algorithm, based on a least-square identification of the Jacobian matrix, becomes impracticable with real systems. This technique is nevertheless feasible also for large systems if its provided an efficient way to condense the huge amount of data generated by numerical simulations, as the state vectors at each timestep. With this perspective, an approach to extract the dominant eigenvalues of the monodromy matrix based on the method of data analysis known as *Proper Orthogonal Decomposition* is proposed in [94], showing its application to the evaluation of ground

resonance stability of an helicopter model.

Chapter 5

Codes employed in the analysis

In this chapter the codes used to perform the analyses that will be presented in Cap. 7 are discussed, together with a brief presentation of the means by which they have been used. In the first section are described the dynamic time-domain aeroelastic codes developed in the present work, while later sections are devoted to the other in-house codes used as well (and sometimes slightly modified for clear needs).

5.1 Time-domain codes

In the present work three distinct solvers have been developed for dynamic analysis purposes. Each of them is characterized by using different options both on the pure aerodynamic side (always of course within the framework of potential flow) and on the aeroelastic coupling. Therefore description of the full aeroelastic model given in Cap. 2 will be here frequently recalled. The three solvers, called *Solver1*, *Solver2* and *Solver3* have increasingly computational cost.

5.1.1 Solver 1

This Solver adopts the Infinite Plate Spline as interface algorithm; as outlined in Sec. 3.1, this implies simplified hypothesis, inherent both to the limits of the algorithm itself (as the 2D assumption) and to simplifications needed to preserve low computational cost. As a consequence in this model the aerodynamic mesh doesn't follow the structure, i.e. the coordinates of the inducted control points where the boundary condition is imposed and the coordinates of the inducing rings employed in the evaluation of the coefficients of the

matrices $\boldsymbol{A}$ and $\boldsymbol{A}_{\mathrm{w}}$ in Secs. 2.3.2 and 2.3.3 are not updated during the deformation process of the body. However, body's deformation still influences the boundary condition (and thus the aerodynamic loads) with the terms $\boldsymbol{RHS}_2$ and $\boldsymbol{RHS}_3$ discussed in Sec. 2.4.1.
This choice implies that a prescribed wake model is adopted, as it appears not consistent to consider a free wake when the shedding aerodynamic mesh doesn't occupy the real position of the body, giving in any case a low accurate approximate shape for the wake.
On the other side, this model is still believed to capture the basic features of the aeroelastic problem allowing at the same time a relatively low computational cost also for big sized systems and refined meshes.

5.1.2 Solver 2

In Solver 2 the IPS is substituted with the Moving Least Square interpolation algorithm for everything is linked with the coupling of aerodynamic and structural fields. This allows to build up for each timestep the real aerodynamic mesh, because the simplifying assumptions of the previous interface algorithm are no more necessary (see Sec. 3.2). Nonetheless this Solver makes use of a mixed approach: the *velocity vectors* $\boldsymbol{V}_{\mathrm{SI}}$ and $\boldsymbol{V}_{\mathrm{WI}}$ used respectively for the coefficients of matrices $\boldsymbol{A}$ and $\boldsymbol{A}_{\mathrm{w}}$ are still evaluated ignoring the new position of the body, but the *aerodynamic coefficients* of these matrices (i.e. the normal components of these vectors) are partly updated at each timestep because in eqs.(2.52) and (2.54) is now considered the actual normal direction $\boldsymbol{n}_{\mathrm{k}}$ of the ring where the k-th control point is placed, while in *Solver 1* $\boldsymbol{n}_{\mathrm{k}}$ was the one relative to the undeformed configuration.
The reason of this choice is the assumption that for a correct esteem of the *velocity vector* the important thing is the relative distance between the vortex line and the induced point (see Biot-Savart law, eq.(2.50)) and this is considered still in good agreement with the initial one when the body is deformed. On the contrary, what mainly changes during the dynamic evolution, especially for very deformed configurations as the ones under investigations, is the direction along which the boundary condition should be written and so there is a lack of accuracy to keep projecting the induced velocity vector on the initial normal direction. Once this is ascertained, the assumption to consider the aerodynamic mesh still in the *undeformed* configuration provides a great advantage since it enables to avoid a free wake approach (with the consequent increase in computational cost), which would be mandatory once the shedding rings are moved with the body. Morevorer the *velocity vectors* $\boldsymbol{V}_{\mathrm{SI}}$ and $\boldsymbol{V}_{\mathrm{WI}}$ are not evaluated at each timestep, since just the change in their respective dot products is contemplated.

Thus this modification represents an improvement in the accuracy comparing to the previous Solver without an excessive drawback in simulation run time.
The normal of each ring in the deformed configuration is obtainable by mean of the evaluation of the updated rings position, a task performed applying eq.(3.17) to the 3D coordinates of all the vertices (it's worth to notice that this apparently easy task would have been less trivial and accurate adopting the IPS); as in this case the ring is no more planar, a medium plane is assumed and the vector product between the diagonals is used for the calculation of the direction.

Consistently with this modification, another improvement is employed: vector $\boldsymbol{r}_L^k$, which gives the direction of lift produced from the k-th ring as expressed in eq.(2.89) and shown in Fig.2.8, is updated during each timestep. This is accomplished by means of the evaluation of the actual position of points 4_L^k and 2_L^k. The aerodynamic load is thus *follower* both in direction and intensity.

5.1.3 Solver 3

Solver 3 adopts the MLS interpolation algorithm and considers the aerodynamic mesh in its actual (deformed) position, enabling the free wake model and the *correct* (in the sense that no further assumptions as the previous are made) expression of all the quantities involved in the evaluation of the external loads.
The main differences among the three Solvers are graphically presented in Fig. 5.1.

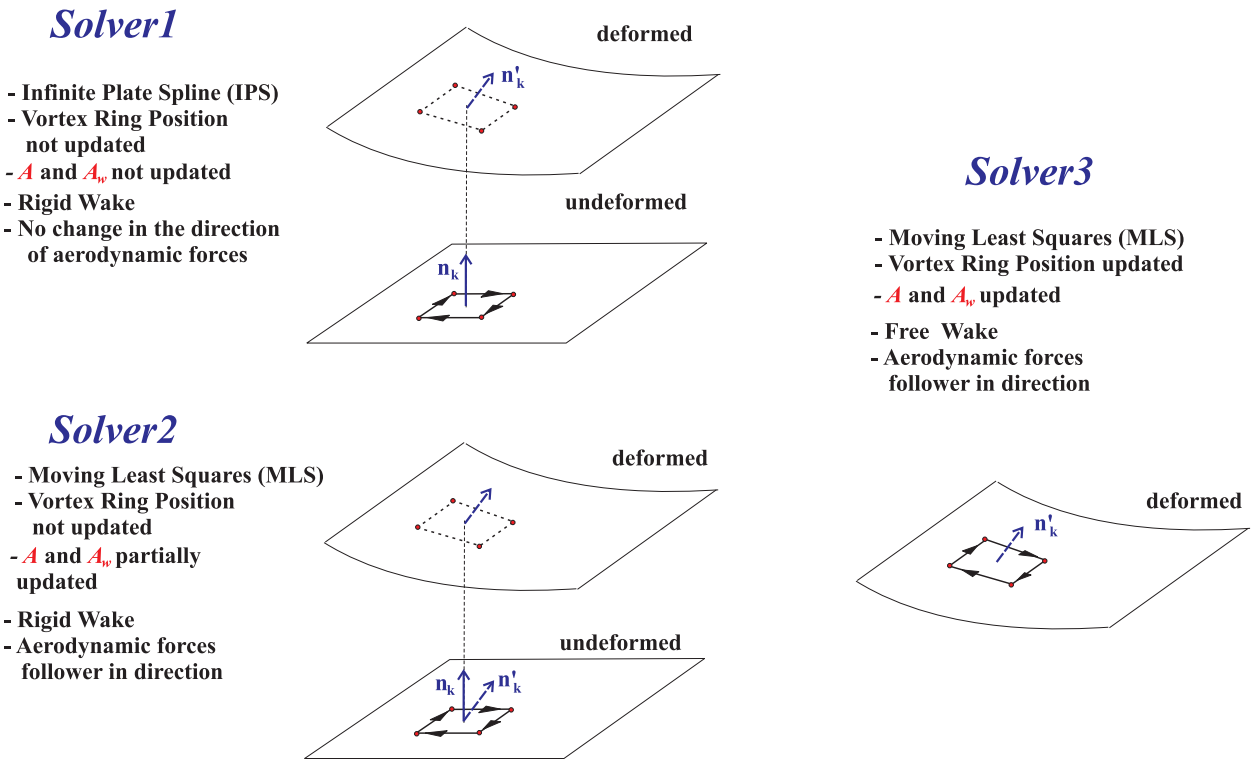

Fig. 5.1: Differences between the time-domain aeroelastic solvers

5.2 Static and frequency-domain codes

5.2.1 Nonlinear aeroelastic static tool and its employment in the analysis

In-house code for the investigation of the role of geometric structural nonlinearities in the detection of static aeroelastic instabilities (mainly, divergence speed) was presented and validated in [34]. This tool solves the static equilibrium equations in the presence of aerodynamic loads adopting iterative algorithms like the standard Newton-Raphson method and arc-length method; the latter is a continuation technique necessary both to ensure convergence in the neighborhood of critical points (prevented in the Newton-Raphson method from the bad conditioning of the tangent matrix) and to track the response in the postcritical region [3, 98, 100]. Since a nonlinear problem is solved, a parameter is introduced, called *load level*, which determines how much of the nominal (or final) load is being applied. Varying the value of this parameter (generally from 0 to 1) a curve is obtained where are reported the coordinates (or deformation) of each degree of freedom and the corresponding value of the load level.

This code can be regarded the static equivalent of *Solver 1*, in that the same interface algorithm (IPS) is employed and similar simplifying hypothesis on the aerodynamic coefficients and lift direction are made.

As it will be shown in Cap. 7, one of the strategies adopted to study the dynamic response of the Joined-Wings will consist in a re-start from a steady state reached by mean of static solution. The static code, in fact, provides a deformed configuration relative to the flow speed and the angle of attack assigned. Of course, this configuration can be assessed as a *stable* stationary equilibrium point of the system only by mean of a dynamic analysis. Therefore the deformed configuration, in equilibrium with the corresponding aerodynamic forces, is perturbed and the response is tracked.

Following this line of reasoning, when *Solver 2* is taken in consideration a modified static tool should be used since otherwise the mismatch would introduce an involuntary and not controllable source of errors which could lead to erroneous results. Therefore the static equivalent of *Solver 2* has been developed and, as a validation, its outcomes verified to fall not too far from those of the original static tool.

When *Solver 3* is considered, it is not so obvious on which kind of static equivalent tool it has to be favourably relied on. The main ambiguity concerns the shape to assign to the wake at the beginning of the dynamic simulation.

In fact for *Solver 1* and *Solver 2* the wake is prescribed, and consistently with that at the first timestep it is made of horseshoe vortices with an intensity related to the distribution of circulation present over the wing in the steady state being restarted. As the simulation goes on, this *horseshoe wake* moves back leaving space to the *ring wake* being shed (see Sec. 2.3.3).
This approach is no more pursuable when the time-domain capability employs a free wake approach because a clear mismatch rises; this consideration was confirmed by various attempts to start the dynamic simulation as made for the other two Solvers, showing how the outcome of the dynamic analysis (also when a stable range of velocities was considered) was a configuration considerably far from the static one.
In literature [62] a way to find a suitable steady state condition is presented, based on an iterative process on the shape of the wake starting from an initial guess of its geometry, which is then moved accordingly with the induced velocity components parallel to a plane perpendicular to the free-stream velocity (*wake relaxation*). This strategy is believed to surely improve the accuracy of a static analysis, without giving however a substantial contribution to the present issue.
An alternative way to proceed is just to start from a rest condition (undeformed wing and thus no wake in the flow domain) and follow the transient triggered by the onset flow having a nonzero angle of attack until a steady state is reached. Here, an approach similar to the second one is employed, where the angle of attack is not given impulsively, but rather slowly increased within the time since it reaches the sought value, to resemble as much as possible a quasi-static process.

5.2.2 DLM based code for flutter speed prediction

A doublet lattice method (DLM) is employed for the frequency-domain unsteady aerodynamic calculation in order to assess the flutter speed of the given configuration. A prediction of flutter velocity for the configurations investigated in the present work is desirable in order to have a comparison among the critical speeds sorting out from the analysis through the three time-domain Solvers. As reported in literature [118], whereas Computational Fluid Dynamics (CFD) had a great impact on steady-state aerodynamic analysis, the same cannot be said for the unsteady, especially when considering flutter analysis and thus DLM, based on the hypothesis of potential flow, still proves to be a valid tool. This method was firstly introduced in [2] and later on widely adopted from the aeronautical industry [101].
In literature however it is claimed [85] that DLM analysis could lack in precision when used

for cases in which wake roll-up plays an important role, or for cases in which the structural deformation is conspicuous. The first feature is possibly related to the fact that DLM makes use of the concept of acceleration potential (similar to the velocity potential but its derivative provides now the pressure instead of velocity) in order to satisfy the Laplace equation; this practically enables to non consider (and thus not model) the wake since as known it doesn't have pressure difference.

For what concerns the effect of high deformations on the accuracy of results, in this work nonlinear evaluations of flutter speed (in the sense shortly stressed out) are performed. A study concerning the reliability of linear and nonlinear tools when investigating Joined-Wing configurations was already pursued in [30, 34] for mechanical loading and static aeroelastic conditions, respectively. It was assessed that linear analysis may give unreliable and nonconservative predictions and in some cases linear tools were not even able to correctly evaluate trends when one or more parameters were varied.

This flutter solver requires the modes of the structures as an input; thus, evaluating the modal properties of the structure at different points on the static aeroelastic response (found with the static aeroelastic tool previusly described), it is possible to have a progressively more refined estimate of the flutter speed. The process of running different analyses with modes representative of the undeformed or deformed structure is the keypoint in which nonlinear effects are introduced. The predicted flutter speed $V_{\infty F}^{lin}$ is compared to the speed V_{∞}^{SS} at whom the linearization has been performed; in the critical condition these two velocities coincide.

Chapter 6

Validation

Validation of the codes developed in this study is here presented. Some components or even some full aeroelastic solvers used in the analyses have already been validated in previous works. For example, nonlinear structural finite element code, both in the static and dynamic versions, has been already employed in previous efforts, i.e. [19, 21, 30, 34]. Moreover, also the *DLM* capability has been already described and checked in references [31].

6.1 Validation of the Aerodynamic Solvers

In this section, validation of the aerodynamic part of the solver is considered. From a pure aerodynamic perspective, the differences between the codes concern the wake only, thus to validate the unsteady behavior the wake is treated both as rigid or deformable.

A common validation mean, popular as the *Wagner*'s test case, is usually adopted to verify the capabilities of an unsteady aerodynamic solver since it describes the effects of the starting vortex on the forces acting on an airfoil. There is an analytical expression [64] that describes the evolution of the lift coefficient in respect of τ, known as *reduced time*, which is the covered distance expressed in semi-chords of the airfoil, i.e. $\tau = 2\,V_\infty\,t/c$, where t represents the time and c the chord. If C_L is the lift coefficient, it holds that

$$C_L(\tau) = C_L(\infty)\,\Psi(\tau)$$

where:

$$\Psi(\tau) = 1 - 0.165\,e^{-0.0455\tau} - 0.335\,e^{-0.3\tau} \tag{6.1}$$

Since this testcase is a bi-dimensional one, to validate the code a wing with large aspect-ratio is considered ($AR = 30$) and the evaluation of the lift coefficient is done at its mid-station.

The simulation is run considering $\Delta t\, V_\infty/c = 1/8$. Results are shown in Fig. 6.1, where the lift coefficient normalized to the steady lift coefficient is plotted against the reduced time, for both the rigid and deformable wake approaches.

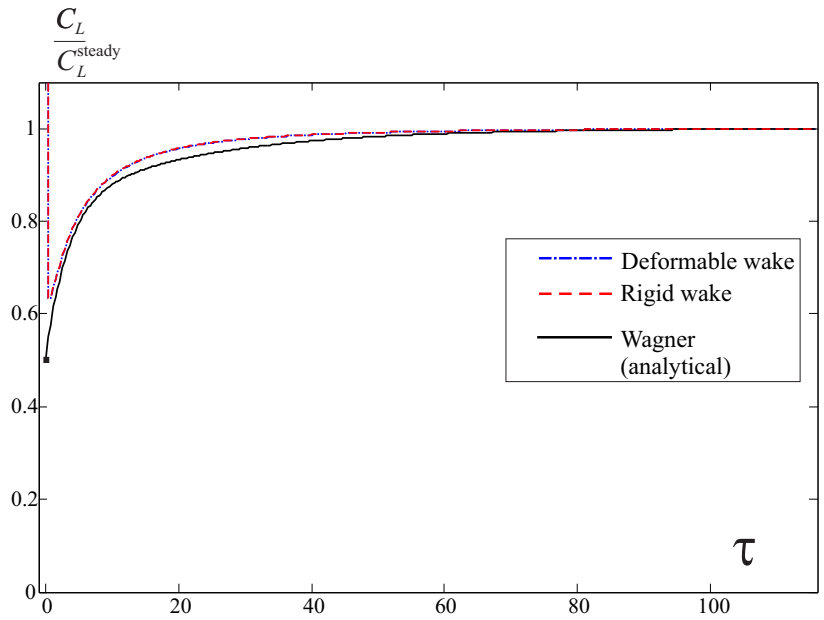

Fig. 6.1: Results of Wagner's test case using a rigid and a deformable wake: lift coefficient normalized to the steady lift coefficient plotted against the reduced time

It can be observed from eq.(6.1) as the Wagner function prescribes a value for the $C_L(0)$ which is half the steady state value; the difference between the computed curve and the classical results can be attributed to the finite acceleration rate during the first timestep (on the opposite in the Wagner case the acceleration time is zero): the effect is to increase the lift sharply during the transient phase and moderately later [63].

A 3D verification is then presented, because as noticed above the *Wagner* test is more suitable for the response of an airfoil than of a wing, though remaining a valid way to study the unsteadiness of the flow. In [29] it is proposed the analysis of the transient lift of a rigid wing in constant speed forward flight. The wing has the following parameters: unswept rectangular planform: angle of attack α=5°; V_∞=10$\frac{m}{s}$; chord of $1m$ and aspect ratio AR varying from 4 to 200 ($\simeq\infty$). The discretization is prescribed with 13 spanwise and 4 chordwise equally spaced panels; as before the timestep length is given as a function of the ratio $\Delta t\, V_\infty/c$: the suggested value here is 1/16. In Fig.(6.2) the variation of lift coefficient with time is reported for both the aerodynamic capabilities. Graphics show good agreement with the ones given in the reference (here not reported because non exactly

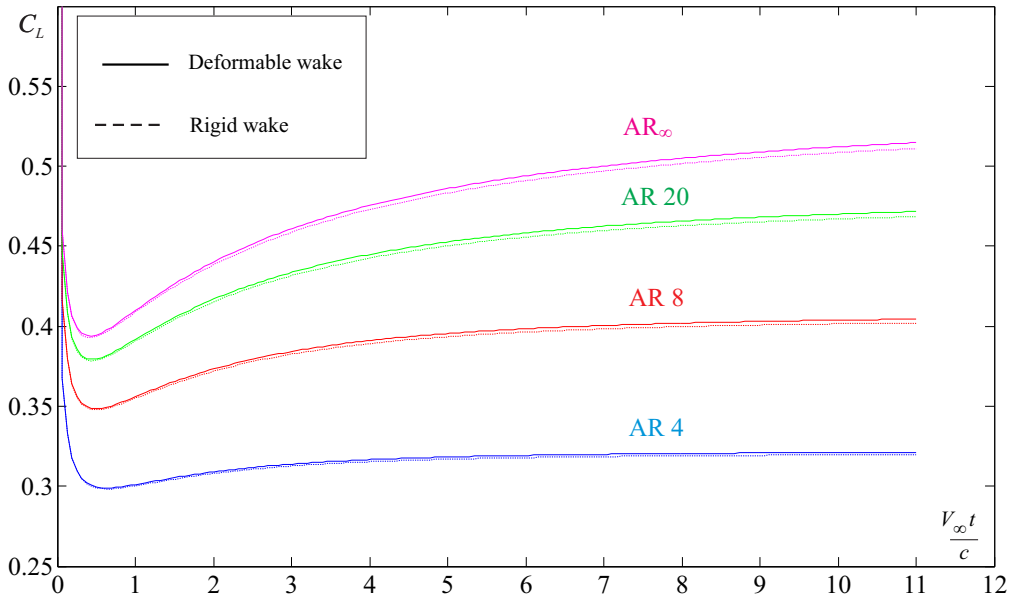

Fig. 6.2: Lift coefficient variation with time for an uncambered rectangular wing (impulsive start into a constant speed forward flight)

extrapolatable). The only difference concerns the earlier timesteps where the drop in the lift is slightly different; this is an issue encountered also by other authors [29], which proves to be very sensitive to the choice of the timestep. As remarked in the reference, the initial lift loss and the length of the transient seem to decrease with a reduction in the wing aspect ratio: this seems to suggest an influence of the trailing vortex wake in these features.
It can be observed how there are no big differences between the two wake models; this is showed also in [29], where this test is used to validate the aerodynamic UVLM code for nonlinear aeroelastic analyses and both the prescribed and free wake are taken into account.

6.2 Validation of the Meshless Transferring Capability

Validation of meshless capability has been first investigated starting from its basic features; known surfaces (given by analytical equations) have been reconstructed from a set of points scattered in the space. These cases, not reported here for brevity, give confidence just over a part of the algorithm, since its implementation in an aeroelastic framework can introduce new issues.

For this reason, another attempt to validate the coupling interface has been carried out. Since *Solver1* relies on IPS, a modified version of this solver has been implemented featuring

as differences just this new algorithm for the load and displacements transferring. This procedure rely of course on the the possibility to consider IPS just validated, proven by its use in previous works. The Joined-Wing configuration depicted in Fig. 6.3 (the same configuration will be study in this work) with a freestream speed of 55 m/s is considered, and the angle of attack α, measured in the symmetric xz plane, has the evolution shown in the same graph. The simulation starts from a steady equilibrium reached by means of static analysis (re-start technique introduced in Cap.5). The vertical displacement of the tip of the front wing is reported.
The results are in an excellent agreement.

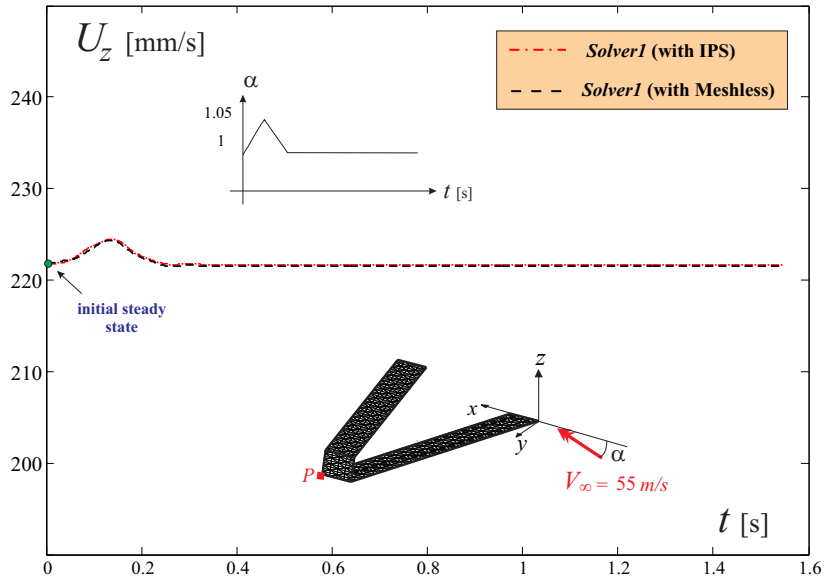

Fig. 6.3: Validation of meshless capability employing two versions of *Solver1*: the original performing IPS and a modified which made use of MLS transfer's method

6.3 Validation of the Time-Domain Aeroelastic Codes Capabilities

The three time-domain solvers are here validated against experimental results in a low-speed wind tunnel which are proposed in reference [7]. The test case consists of a delta wing plate model showing limit cycle oscillations, with a geometry detailed in the original work.
This experiment is performed numerically by the Solvers, and results are directly compared with the reference experiment, as well as computational results reported in [32].

6.3.1 Solver1

Numerical results obtained with *Solver1* are shown in Table 6.1. To favour the comparisons, the first two columns report references results, where the third and forth show the performances of *Solver1* with two different values of structural damping. In [7] the value of damping was not specified.

	Attar et Al.[7] (experimental)	Demasi et Al.[32]	*Solver1* ζ=3%	*Solver1* ζ=5%
Flutter velocity	24 m/s	22,7 (ζ= 1%)	24 m/s	24,5 m/s
$\dot{U}_{z_{\text{tip}}}$ (V_∞=25,5 m/s)	0,5 m/s		0,69 m/s	0,63 m/s
$\dot{U}_{z_{\text{tip}}}$ (V_∞=27 m/s)	1,36 m/s	1 m/s (ζ= 5%)	1,28 m/s	1,07 m/s
LCO frequency (V_∞=27 m/s)	14,5 Hz	14.92 Hz (ζ= 5%)	15,3 Hz	14,8 Hz
$\dot{U}_{z_{\text{tip}}}$ (V_∞=28 m/s)	1,85 m/s	1,55 m/s (ζ= 3%)	1,5 m/s	1,3 m/s

Table 6.1: Validation of *Solver1* with Delta Wing test case. $\dot{U}_{z_{\text{tip}}}$ is the maximum vertical speed of the tip of the wing

Maximum vertical speed of the tip for LCO established at different wind speed are also represented in Fig. 6.4.

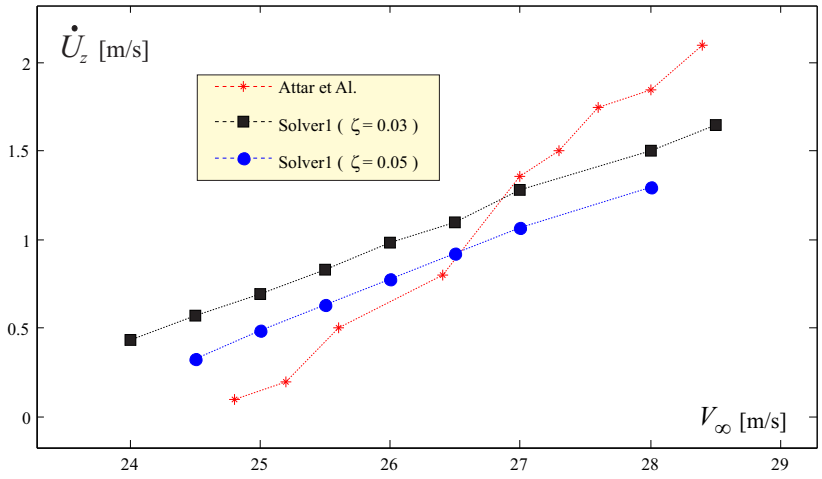

Fig. 6.4: Results of Delta Wing test case: experimental and *Solver1*. The maximum vertical speed of the wing's tip is plotted against the wind speed

6.3.2 Solver2

Numerical data for *Solver2* are now shown in Table 6.2. Maximum vertical speed of the tip

	Attar et Al.[7] (experimental)	Demasi et Al.[32]	*Solver2* ζ=3%	*Solver2* ζ=5%
Flutter velocity	24 m/s	22,7 (ζ= 1%)	23 m/s	23,5 m/s
$\dot{U}_{z_{\text{tip}}}$ (V_∞=25,5 m/s)	0,5 m/s		0,9 m/s	0,66 m/s
$\dot{U}_{z_{\text{tip}}}$ (V_∞=27 m/s)	1,36 m/s	1 m/s (ζ= 5%)	1,36 m/s	1,23 m/s
LCO frequency (V_∞=27 m/s)	14,5 Hz	14.92 Hz (ζ= 5%)	16 Hz	15,3 Hz
$\dot{U}_{z_{\text{tip}}}$ (V_∞=28 m/s)	1,85 m/s	1,55 m/s (ζ= 3%)	1,55 m/s	1,37 m/s

Table 6.2: Validation of *Solver2* with Delta Wing test case. $\dot{U}_{z_{\text{tip}}}$ is the maximum vertical speed of the tip of the wing

for LCO established at different wind speeds is also represented in Fig. 6.5.

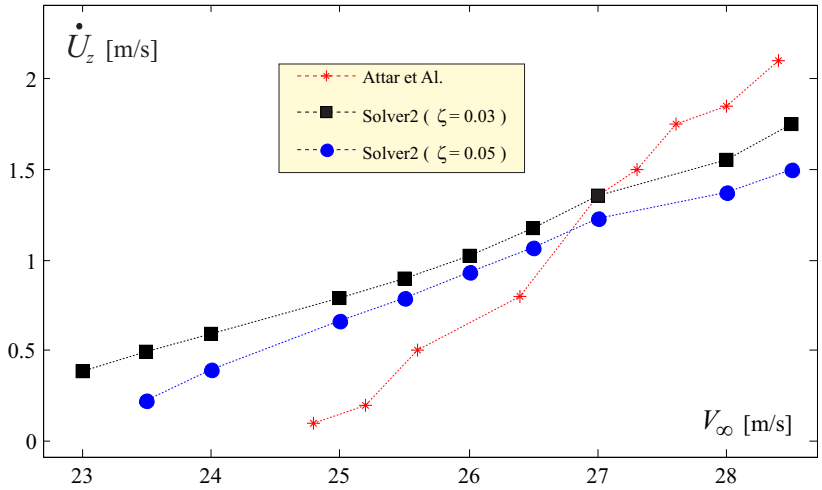

Fig. 6.5: Results of Delta Wing test case: experimental and *Solver2*. The maximum vertical speed of the wing's tip is plotted against the wind speed

6.3.3 Solver3

The same process is repeated for *Solver3*. See Table 6.3. Maximum vertical speed of the tip for LCO established at different wind speed are also represented in Fig. 6.6.

	Attar et Al.[7] (experimental)	Demasi et Al.[32]	*Solver3* ζ=3%	*Solver3* ζ=5%
Flutter velocity	24 m/s	22,7 (ζ= 1%)	24 m/s	24,5 m/s
$\dot{U}_{z_{\text{tip}}}$ (V_∞=25,5 m/s)	0,5 m/s		0,77 m/s	0,57 m/s
$\dot{U}_{z_{\text{tip}}}$ (V_∞=27 m/s)	1,36 m/s	1 m/s (ζ= 5%)	1,18 m/s	1 m/s
LCO frequency (V_∞=27 m/s)	14,5 Hz	14.92 Hz (ζ= 5%)	15,6 Hz	15,1 Hz
$\dot{U}_{z_{\text{tip}}}$ (V_∞=28 m/s)	1,85 m/s	1,55 m/s (ζ= 3%)	1,47 m/s	1,34 m/s

Table 6.3: Validation of *Solver3* with Delta Wing test case. $\dot{U}_{z_{\text{tip}}}$ is the maximum vertical speed of the tip of the wing

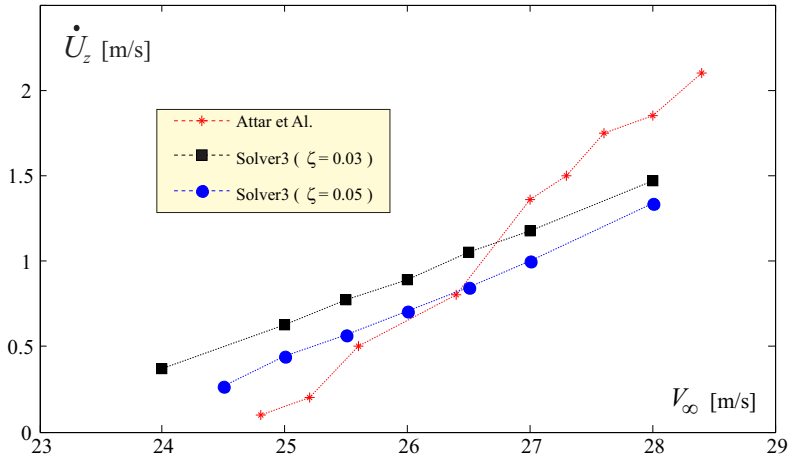

Fig. 6.6: Results of Delta Wing test case: experimental and *Solver3*. The maximum vertical speed of the wing's tip is plotted against the wind speed

Chapter 7

Results

7.1 Description of the Analyzed Joined-Wing Configurations

There are different configurations that will be analyzed in this paper. The first one, depicted in Fig. 7.1, is a Joined-Wing (named *JW70*) in which the joint is not located at the tip of both the wings. The thickness of the wings and the joint is $0.7\,mm$.

The second configuration (Fig. 7.2) is a PrandtlPlane-like [39] configuration featuring a swept-back lower wing and a swept-forward upper wing. It is designated *PrP40*. For this layout, the thickness of the wings is varied and specified case by case. Both *JW70* and the *PrP40* have been chosen for reference reasons, see [19, 21, 30, 34]. The models' dimensions are selected to be consistent with the ones corresponding to wind-tunnel scaled models.

The last layout (Fig. 7.3) is the typical *Sensorcraft* [79]. The geometrical details are taken from reference [90], a part from the thickness which has been set to $0.7\,mm$. In this configuration the aft wing is directly joined to the front wing, to act like a strut.

For all the layouts the adopted material is a typical Aluminium, featuring a Young's modulus $E = 6.9{\cdot}10^7\,\left[\frac{\mathrm{Kg}}{\mathrm{mm{\cdot}s^2}}\right]$, a Poisson's ratio $\nu = 0.33$ and a density $\rho_{\mathrm{mat}} = 0.69{\cdot}10^3\,\mathrm{kg/m^3}$.

For the aerodynamic analysis, the surface is discretized employing different (usually about 12) elements in the chordwise direction. The overall number of rectangular elements is then between approximately 600 and 3000 for the different cases.

The density of the air is chosen to be the standard air density ($\rho = 1.225\,\mathrm{kg/m^3}$).

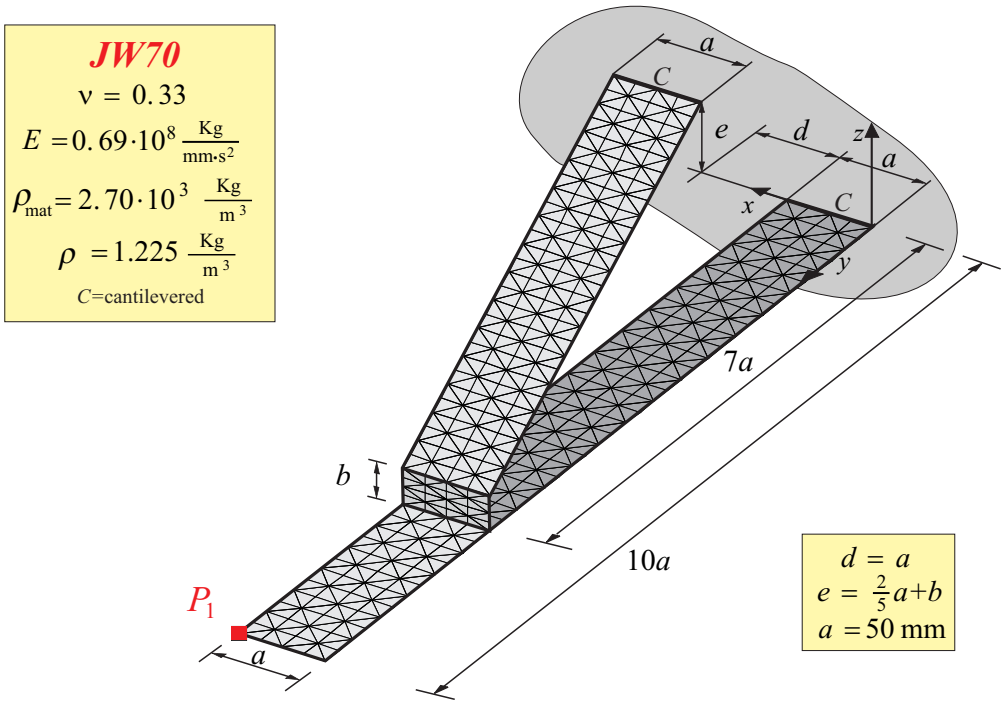

Fig. 7.1: JW70 model. The joint is located at 70% of the wing span. The thickness of the different parts of the structure is equal to 0.7 mm

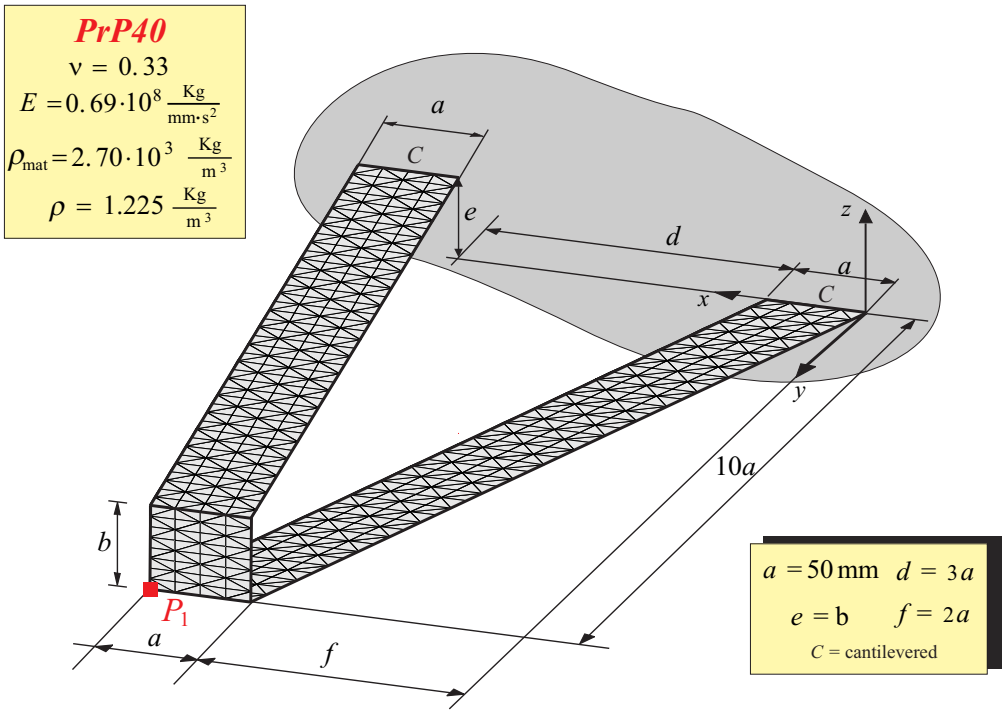

Fig. 7.2: PrandtlPlane Joined-Wing model PrP40. The joint is located at the tip of the wings. The thickness is specified later in the analyses because it is not only one

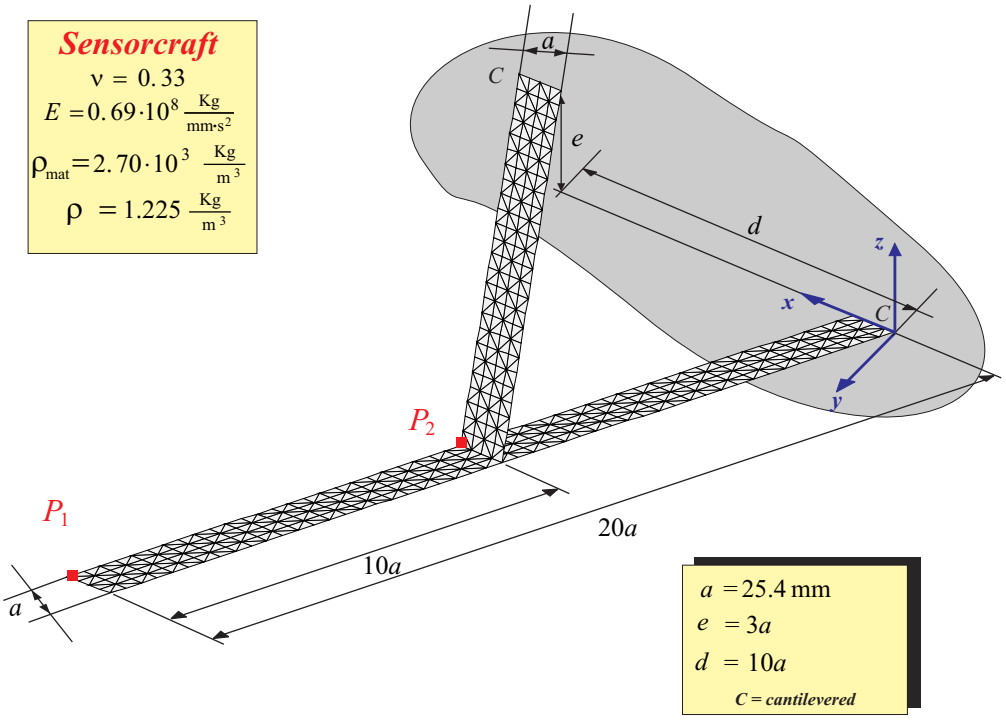

Fig. 7.3: *Sensorcraft.* The aft wing is connected to the front one at the midspan. The thickness of the wings is equal to 0.7 *mm*

7.2 Snap Divergence

The concept of *snap divergence* was first introduced in Ref.[34] and here is briefly summarized. The *pure structural case* represented by a structure subjected to conservative forces it is firstly considered. In that case it is possible to define a *buckling load* obtained via eigenvalue analysis. This investigation of the stability properties could be improved by linearizing about a steady state equilibrium obtained with a fully nonlinear static analysis. However, it is also possible to define (if exists for the case under investigation) the *snap-buckling load* as the one corresponding to the true critical point, defined as the state in which the structural tangent stiffness matrix $\boldsymbol{K}_{ST}$ becomes singular.

These definitions involve a precise mathematic event (singularity of a matrix). However, nonlinear analyses may also show responses with a progressive softening (see for example [20,30]). In some of these cases, very small load increments may lead to large displacements, being this in practice unacceptable. It may be then too restrictive and unsafe to base the buckling concept on the definitions above (singularity of the matrix).

These considerations can be extended to a system including aerodynamic forces, which are non-conservative in nature. Thus it is possible to define a matrix $\boldsymbol{K}_A$, the so-called aerodynamic tangent matrix. The *system* tangent matrix is now obtained by adding the structural and aerodynamic tangent matrices:

$$\boldsymbol{K}_T = \boldsymbol{K}_{ST} + \boldsymbol{K}_A \tag{7.1}$$

Similar to the buckling evaluated with nonlinear analysis, also the divergence may be defined as the condition in which $\boldsymbol{K}_T$ is singular. In Fig. 7.4 is depicted this scenario, where V_∞ is the velocity of the free stream, a measure of the external load acting on the structure, and U is a measure of the deformation (the vertical displacement of the tip, for example).

The *post-divergence* regime ($B - D$ branches in Fig. 7.4) deserves a depth investigation than what could be done by mean of an aeroelastic static analysis: after the snap-divergence instability is reached, the system would naturally experience a snap and try to reach a state on the stable post-critical branch. This sudden change is inherently a dynamic phenomenon and thus, inertial forces and time-dependent aerodynamic effects must be taken into consideration to properly model the response of the structure.

In Ref.[34] was studied the behaviour of configuration *JW70*; the results are here reported for point P_1 located at the tip of the lower wing, in Fig.7.5. A speed of $50\,m/s$ is chosen as nominal free stream speed and the angle of attack of the undeformed configuration is set to $1°$. The static aeroelastic response is obtained by gradually increasing the speed V_∞ since

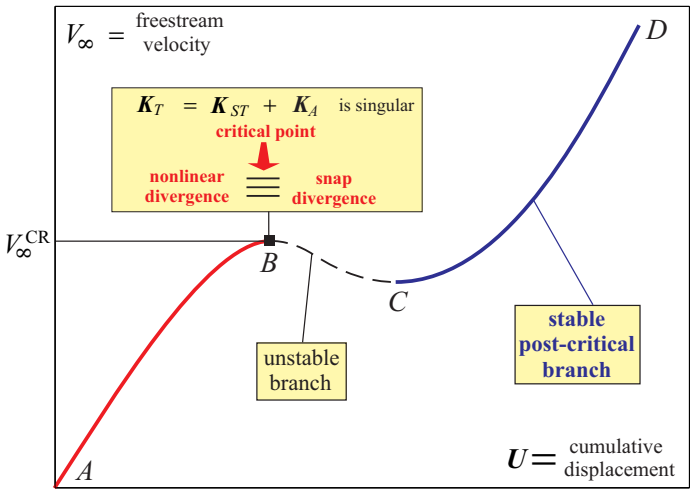

Fig. 7.4: Definition of snap divergence

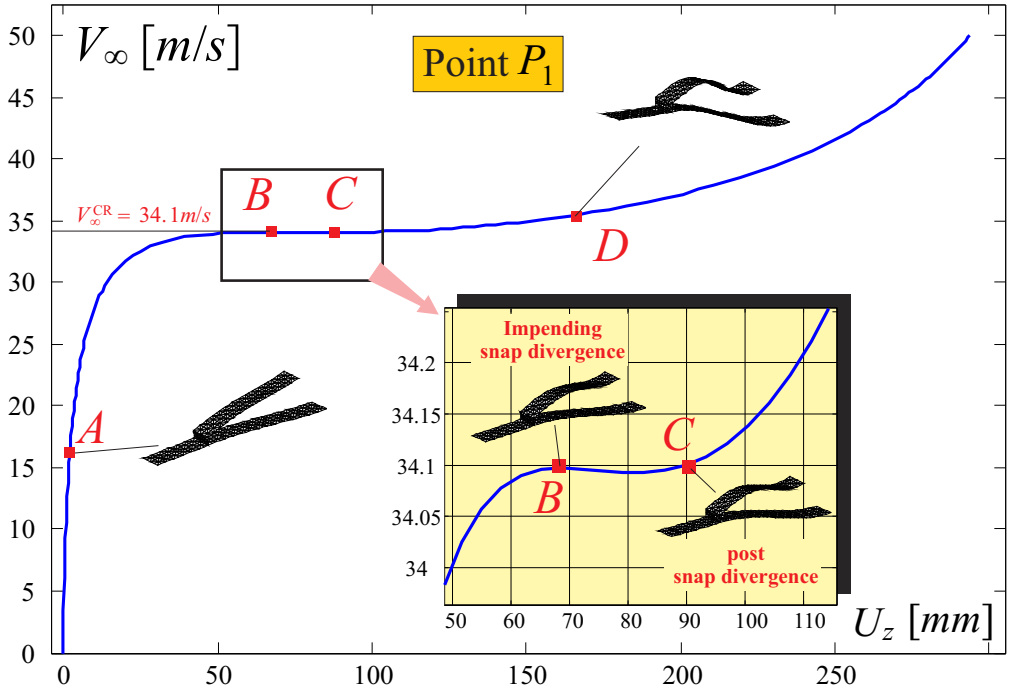

Fig. 7.5: Flow speed V_∞ (in m/s) versus displacement U_z (in mm) for lower wing's tip point P_1, with a zoom in the critical point area

a non linear analysis is employed. It appears clearly that a snap-divergence phenomenon occurs: an infinitesimal increment of speed at stage B would determine an impossibility to find a static equilibrium configuration continuously adjacent to the one in B. On the

contrary, the new equilibrium point would be C, configuration characterized by the same flow speed of state B. The snap-divergence speed V_∞^{CR} is equal for this case to $34.1\,m/s$. Notice that, at stage B the *system tangent matrix* is exactly singular, thus, the instability has a well defined mathematical characterization.

In this section the snap-divergence response will be shown from a dynamical perspective, in particular with *Solver1*. This choice is dictated by the necessity to keep the aeroelastic modelling consistent to the one used in the reference.

7.2.1 Time response on Snap divergence Occurence

The idea is to consider a steady state equilibrium slightly beneath the critical point and increase the velocity of the flow in a quasi-static way until a greater value of the *snap-divergence* speed is reached. In Fig. 7.6 the starting condition (state A, corresponding to a free-stream speed of $V_\infty = 33$ m/s) is shown; the flow speed is first increased to reach $V_\infty = 34.3$ m/s (state B), then decreased to its initial value with a law shown in the box of the same figure, where the wind speed in respect of time is plotted. Point P_1 is again used as an indicator of the global behaviour of the structure (in Ref.[34] was shown how other points of the structure exhibited qualitatively the same response).
It can be observed how tracking the dynamic response, as soon as the speed approaches values close to the critical one, there is an abrupt increase in the displacement of the wing tip. Comparing the displacements for the static and dynamic cases, it can be inferred that the dynamic response matches closely the static one. In the inverse path, where the speed is decreased to its initial value, similar trend is observed and the initial static equilibrium condition is gained at the end of the transient.

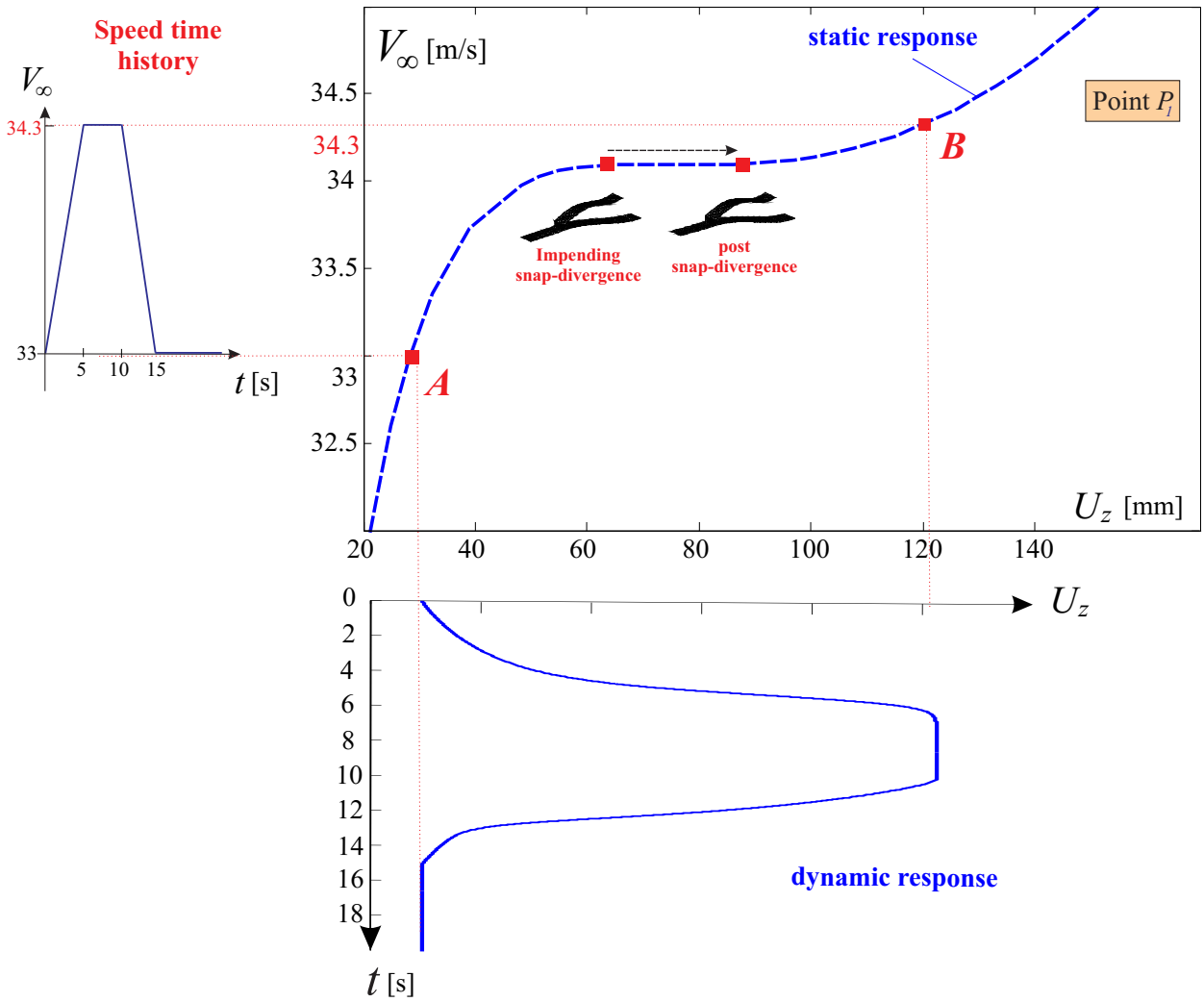

Fig. 7.6: Aeroelastic static response of *JW70* and dynamic response after the shown speed perturbation in time. U_z refers to the vertical displacement of the wing tip, point P_1

7.3 Postcritical Dynamic Aeroelastic Analysis

The aeroelastic solvers developed in the present work are used here to investigate the post-critical dynamic aeroelastic response of the baseline configurations. In particular, the focus is on the Limit Cycle Oscillations exhibited by Joined-Wings above the flutter speed.

7.3.1 Introduction to the Limit Cycle Oscillations

Flutter represents a critical condition for the design and optimization of aircraft structures, since the aeroelastic system, as the speed is increased, encounters a Hopf bifurcation point (see Sec. 4.5) and becomes dynamically unstable. This means that disturbances quickly grow unbounded and failure is reached.
However this growth may be attenuated in certain circumstances, ending up in self-sustained Limit Cycle Oscillations (LCOs). This response actually is not desirable since has as main consequences a shortening of the aircraft service life (speeding up failure by fatigue) and the risk to induce other critical instabilities making available new couplings among the flexible aircraft components. This limited amplitude motion occurs if nonlinearities inherently present in the dynamics of the system limit the exponential growth in amplitude predicted by the linear flutter analysis. Sources of nonlinearities are: inertia (with concentrated or distributed masses in particular locations, as connecting parts between primary components), aerodynamics (dynamic stall, flow separation, oscillating shock waves) and structures (large deflections, material, freeplay).

As a consequence it could be argued that an accurate prediction of a such inherently nonlinear phenomenon strongly depends on the ability to retain the meaningful nonlinearities of the full system, since wrong assumptions can lead to misleading results. The present capability considers only geometrical (structural) nonlinearities, relying on a fully linear aerodynamic model (if exception is made for the wake that, especially when the *roll up* model is considered, introduces a strong dependence on the history of the system).
This assumption is in compliance with the purpose to study configurations with low angles of attack and in the low subsonic regime. Moreover in literature [36] it has been stated that the most important nonlinearities in driving these kind of aeroelastic phenomena are of structural type. An insightful example about this controversial, and in general about some of the LCO main features, is provided by the Delta Wing configuration, often used for these kind of analyses, as for example in the works used for the validation of the present capabilities (see Sec. 6.3), where codes based on potential flow model were employed to investigate

Limit Cycle Oscillations.
Dynamic aeroelastic analyses on a Delta Wing configuration, with a slightly different geometry than the one in [7, 32], were pursued in [47] making use of a computational technique that implicitly couples, through subiterations, a Navier-Stokes solver (based on the Beam-Warming algorithm) to a linear structural solver. Results were compared to previous experiments [103], showing significantly higher amplitudes in the tip response. The proposed reason for this discrepancy was the lack in the consideration of nonlinear structural effects. A following study [46] favourable attempted to demonstrate this hypothesis: the linear modal structural solver was replaced by mean of a nonlinear one based on the Von Kármán plate equations coupled both with an Euler inviscid and a fully Navier-Stokes solver. The computations showed how the nonlinear structural terms played a fundamental role, decreasing the amplitudes to values closer to the experiments.
The two different aerodynamic solvers allowed to explore viscous effects. The outcome was that for these small deflections influence of viscosity was small, in contrast to the cases shown in [47]. Moreover further examination of the aerodynamics clarified the role played by the leading-edge vortex, which in the first study was the mechanism that limited the growth of the response, acting like an aerodynamic spring producing a normal force approximately 180° out of phase with the motion of the wing and yielding in this way to the limit cycle motion. Within this new framework, a well established leading-edge vortex didn't seem to appear until values of the dynamic pressure out of the range considered, thus proving it is the stiffening of the wing due to the development of the membrane stresses to provide the key mechanism by which diverging oscillations settle down to a pure harmonic response. This case and other studies [93] seem to suggest that, when studying configuration whose angle of attack can be considered sufficiently small, non-linear vortex flow phenomena may be important if structural nonlinearities are neglected or weak.

In the following, dynamic aeroelastic response of the different configurations using the three solvers is shown. The techniques adopted in the simulations are the ones described in Cap. 5.

7.3.2 JW70

Solver1

Fig. 7.7 shows the dynamic response of the *JW70* configuration when a vanishing perturbation in the angle of attack is given; in this way the stability of the static equilibrium (fixed point) represented by the main graph is verified. The perturbation consists in a linear increase in the angle formed by the onset flow direction and the x-axis, followed by a symmetric decrease to the unperturbed value (which is 1°). The peak is reached at 0.1 seconds and its value is $\alpha_x = 1.01$.

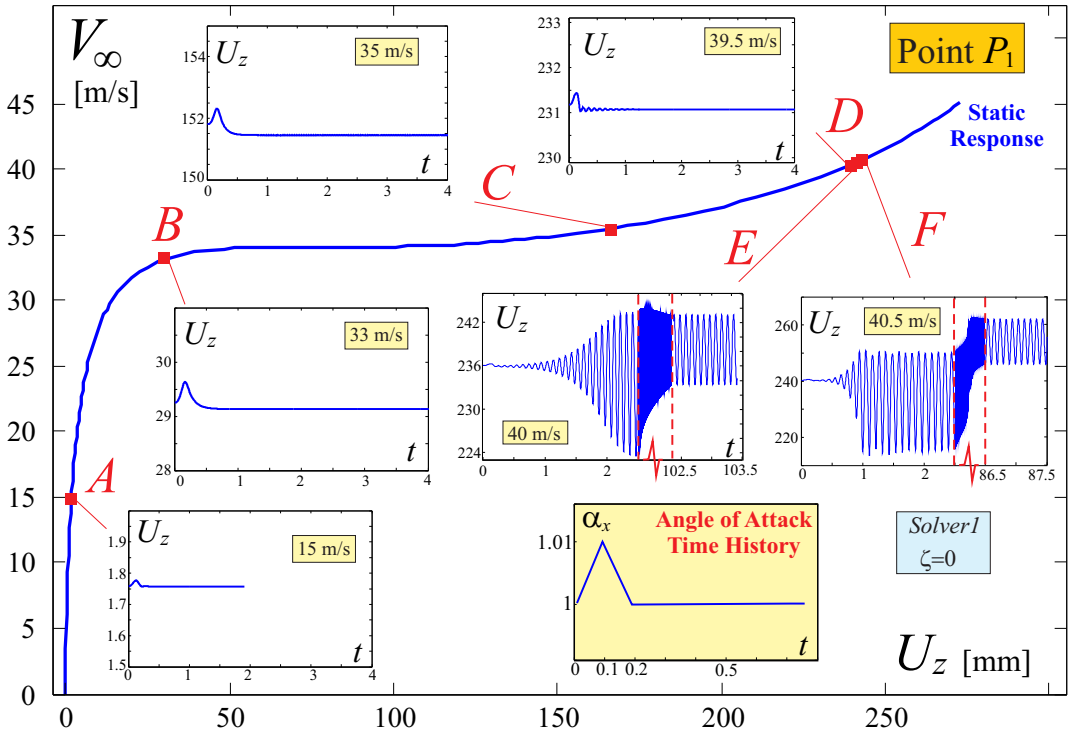

Fig. 7.7: *Solver1*. Aeroelastic dynamic response of *JW70* starting from steady states relative to different velocities when a vanishing perturbation in angle of attack of the onset flow is given. No structural damping is applied

The curves shown here have been obtained considering no structural damping. The simulations have been carried out for different speeds (corresponding to points A, B, C, D, E , F along the main curve). It can be observed how when the velocity is below $39,5$ m/s, the fixed points detected through the static nonlinear analysis are stable. In particular, with this approach, it is possible to define a small interval in which the flutter speed lies, meant

here as the smallest speed at whom the attractor of the dynamical system doesn't coincide (as instead happens for points A ,B , C ,D) with the attractor of the same system studied from a pure static perspective, i.e. the static equilibrium loses stability. For the present case, the flutter speed falls in the interval $39,5 \div 40$ m/s.

For speed larger than flutter, an LCO is observed. The properties of the LCOs are depicted in Fig. 7.8, making use of the *state plane* tool, common in the analysis of nonlinear dynamical systems (see Sec. 4.2) and consisting in the representation of two (or more, and in this case it is called *state space*) states of the system, in this case the displacement of a point of the structure and its time derivative.

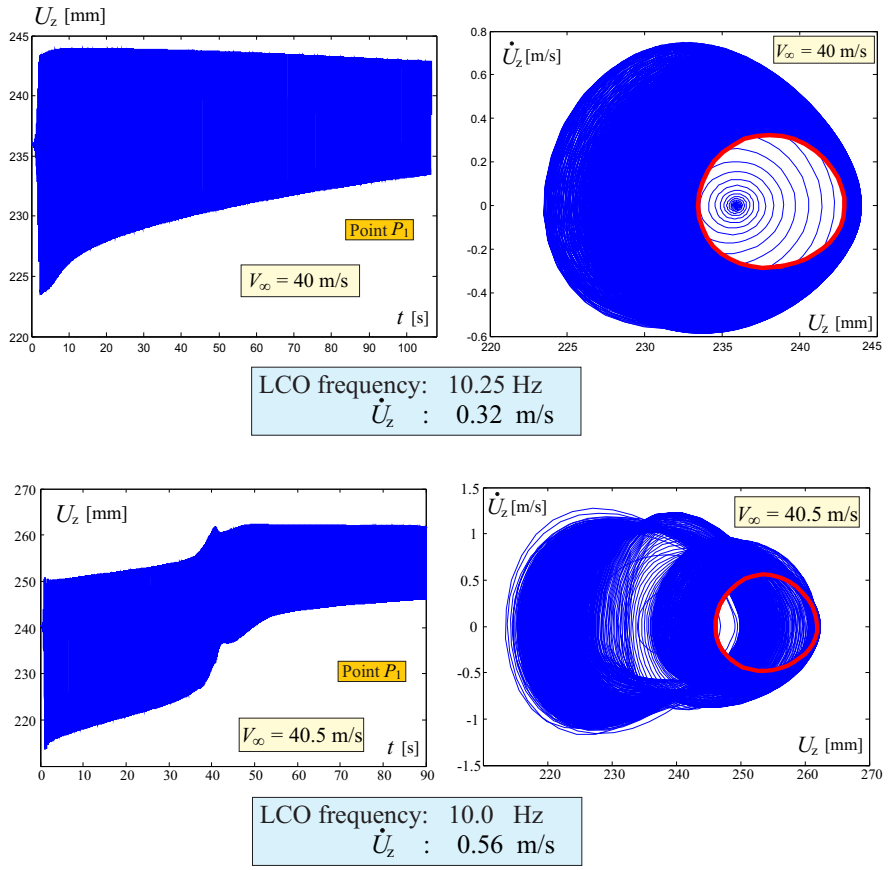

Fig. 7.8: Time response and state plane trajectory for *JW70* configuration, for different flow speeds. *Solver1* is employed. No structural damping is considered

Very interesting is the transient of system before settling to an LCO. The path described in the state plane is quite long (compared to other responses found in literature [32]) before

it is finally attracted from the LCO orbit; moreover, for a wind speed of $V_\infty = 40.5\,\mathrm{m/s}$ it has also an abrupt change in the oscillatory trend. It can be speculated that this behaviour is largely due to the overconstrained nature of the Joined-Wing layout. Responses of the other layouts will give more clues about that.

Solver2

The same process outlined previously is now repeated using *Solver2*. The static response used to start the simulation from a steady state condition is depicted in Fig. 7.9. This curve is obtained with a static aeroelastic tool consistent with the differences exhibited by this Solver in respect to the previous one (see discussion in Sec. 5.2). It may be well noticed that the snap-divergence has now a more pronounced connotation than the one shown in Fig.(7.5).

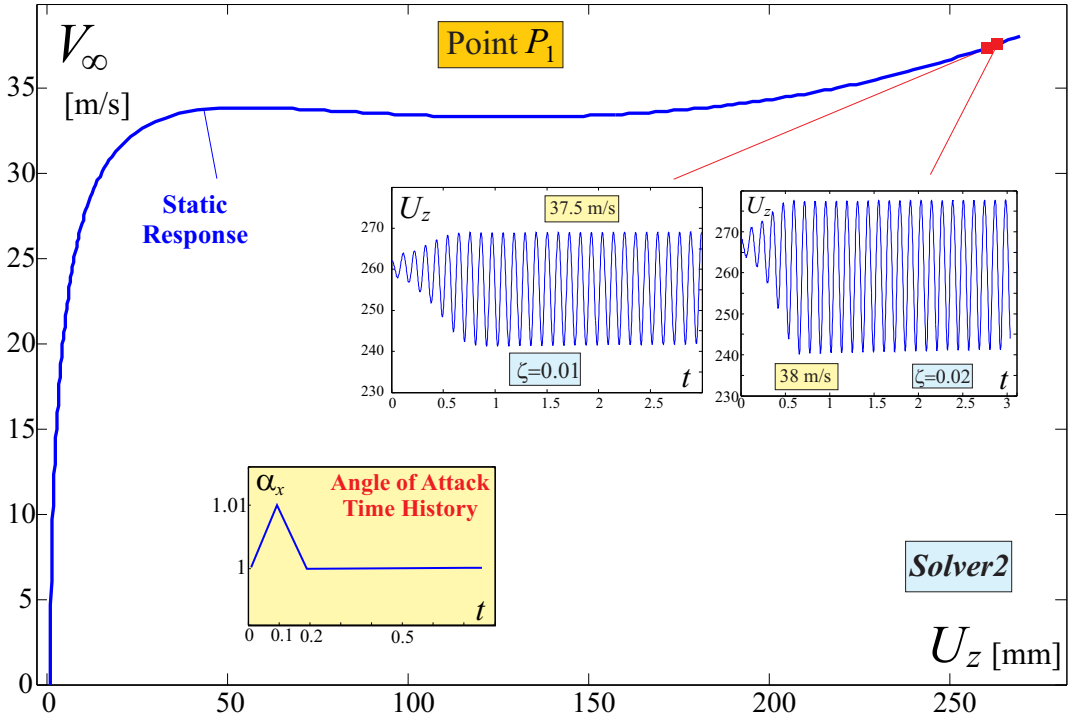

Fig. 7.9: *Solver2*. Aeroelastic dynamic response of *JW70* starting from steady states relative to different velocities when a vanishing perturbation in angle of attack of the onset flow is given. Different structural damping are considered

In the same figure and in Fig. 7.10, the dynamic responses obtained starting from different steady velocities and applying the above described perturbation are given. It may

be observed how the flutter speed decreases if compared with the outcome of the above analyses. In fact, even for structural damping ratio ζ different than zero, and speeds that were subcritical (in term of flutter) when the case was analyzed with the *Solver1*, an LCO is observed.

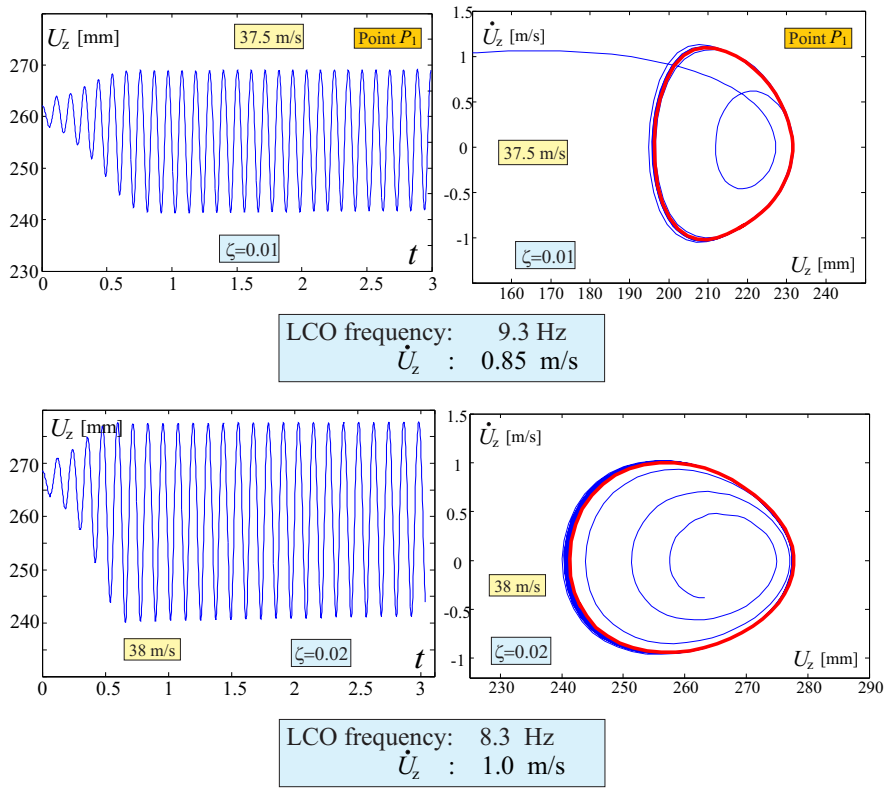

Fig. 7.10: Time response and state plane trajectory for *JW70* configuration, for different flow speeds. *Solver2* is employed

Solver3

Solver3 is now employed which has, among the new features, the capability to properly model the free wake. For reasons related to the need to consistently compare the results obtained with this Solver with the outcomes of the two other Solvers (see discussion in Sec. 5.2), an impulsive start is given to the configuration (no re-start from the static state), and the angle of attack is slowly increased until it reaches the sought value (in Fig. 7.11 is depicted the time history of the nominal angle of attack). In this way it is attempted to recreate an equivalent steady state condition to the one that would be possible to obtained with a static solver which correctly models the wake.

Actually when these simulations are carried out for speeds larger than the flutter one, then the response doesn't settle down to a stationary steady state, but an LCO is observed. Results are summarized in Fig. 7.11. The time histories suggest that the flutter speed is close to 38 m/s. In fact, the LCO observed at this speed has a very limited amplitude, indicating that the state is one immediately following a Hopf's bifurcation. With a small increase in speed, see $38,5$ m/s, the LCO has a larger amplitude. The LCO observed at a speed of $V_\infty = 38$ m/s has a frequency of 10.8 Hz. The one at $V_\infty = 38.5$ m/s has a frequency of 10.5 Hz. With a further increment of speed, the response does not seem to have any periodicity, suggesting a transition toward chaos. An in depth analysis is surely needed to affirm and demonstrate this possible chaotic behaviour.
It is anyhow very interesting to notice how a relatively small variation in speed significantly changes the kind of response.

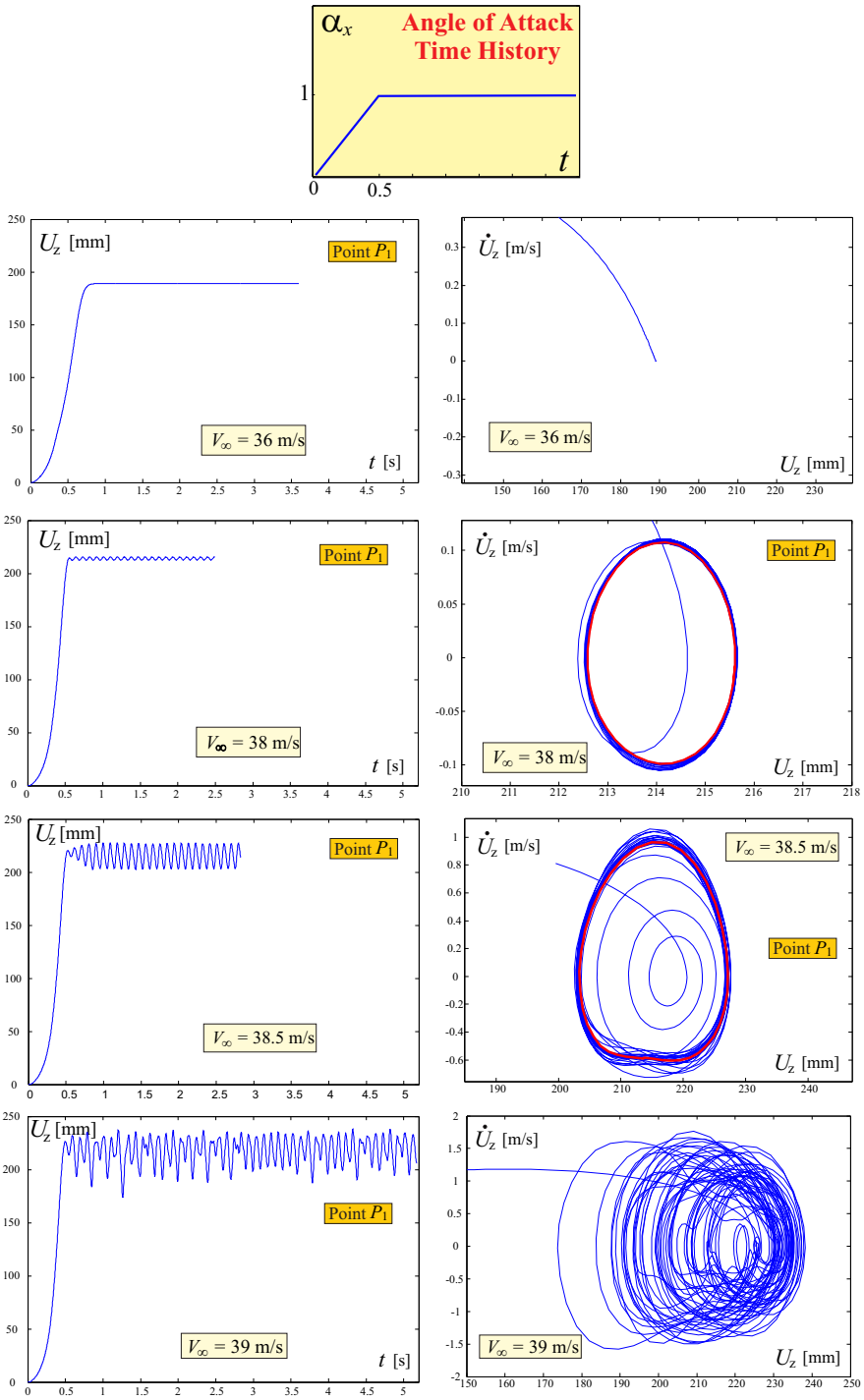

Fig. 7.11: Time response and state plane trajectory for *JW70* configuration, for different flow speeds. *Solver3* is employed. The angle of attack is increased linearly from 0° to 1° in 0.5 seconds. No structural damping is considered

7.3.3 PrP40

The configuration under examination is now the *PrP40*, where the thickness of the wings is set to $t = 1$ mm.

Solver1

Fig. 7.12 shows both the aeroelastic static response, and the time evolution of the *PrP40* configuration starting from an equilibrium state and experiencing a vanishing perturbation. This disturbance consists in a linear increase of the angle formed by the onset flow direction and the x-axis, followed by a symmetric decrease to the unperturbed value (which is 1°), the same used for the *JW70*.

The outcome of the simulations suggests that the flutter speed is in the range $58 \div 59$ m/s. Observing the response for speed larger than the flutter's one, it may be noticed how it is not settling to his final LCO with the complex pattern observed before for the *JW70*, in which the oscillating motion was very slowly cutting its amplitude and shifting its mean value before reaching the asymptotic behaviour.
This points out the importance, in addition to the overconstraining which again shows to have its influence in the lengthening of the transient needed to reach the steady state amplitude and mean value of the oscillation, of the specific layout of *JW70* which is characterized by a substantially different geometry of the lower wing (with a separate outer part).

Repeating the simulation with a value of the damping ratio $\zeta = 0.03$ the critical speed increases; however, the time response reminds the ones of the undamped system. Thus, this cases are not shown here for brevity.

Solver2

Results obtained using *Solver2* are shown in Fig. 7.14, whereas the LCOs in the state plane diagram are given in Fig. 7.15.

An interesting direct comparison of the LCO properties at a fixed speed (59 m/s) when choosing two different Solvers is shown in Fig. 7.16. Exploiting the geometrical follower nature of the aerodynamic forces (taken into account with *Solver2*) seems to have a meaningful effect on the amplitude of the LCO, and also on the frequency: both of them increase by a considerable extent. Although it is always difficult to rely on intuition when studying flutter, moreover when a nonlinear analysis is performed, the increase in amplitude can be interpreted with the fact that the follower force tends to exacerbate the deformation.

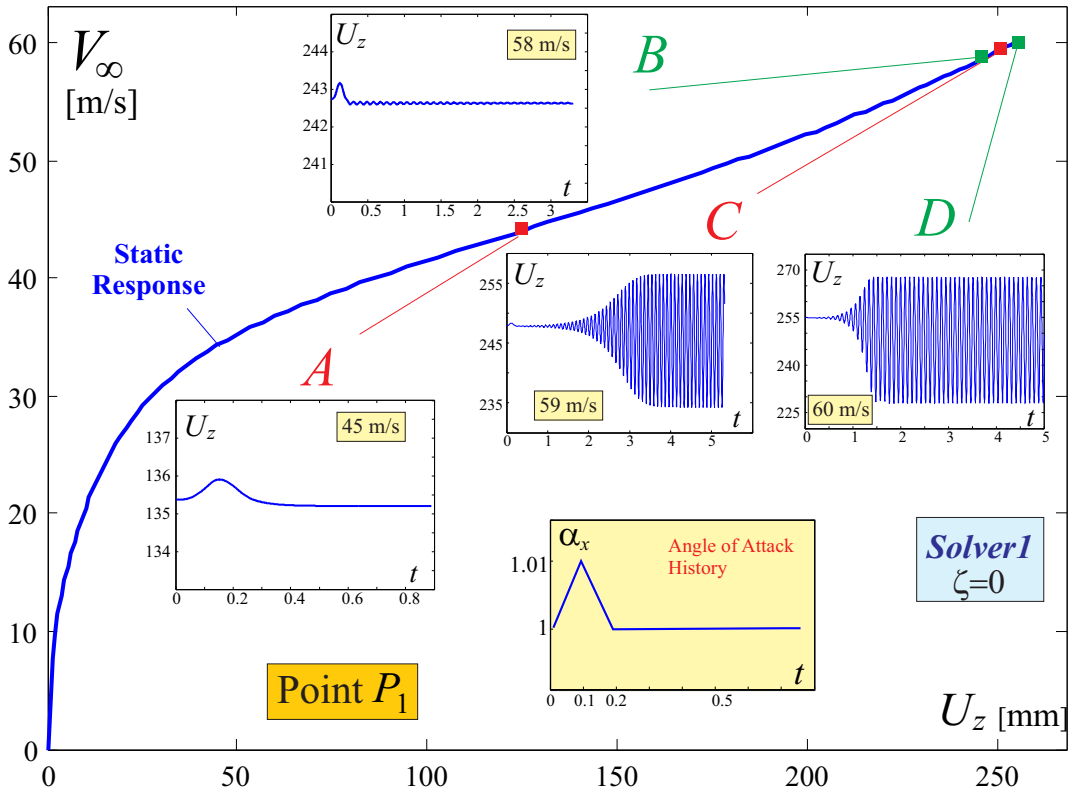

Fig. 7.12: *Solver1*. Aeroelastic dynamic response of *PrP40* starting from steady states relative to different velocities when a vanishing perturbation in angle of attack of the onset flow is given

Solver3

Time responses and state planes of the limit cycle oscillations found by means of the *Solver3* are not reported here. The performances of this tool in predicting flutter speed (lowest LCO speed) are analyzed in the next section.

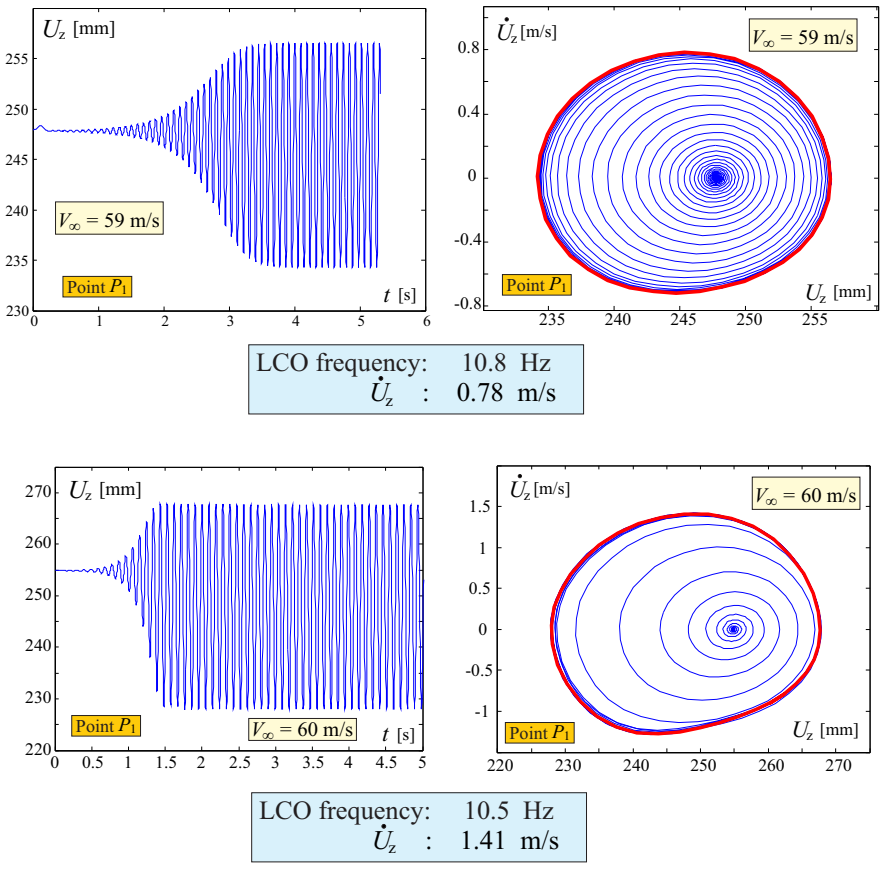

Fig. 7.13: Time response and state plane trajectory for *PrP40* configuration, for different flow speeds. *Solver1* is employed. No structural damping is considered

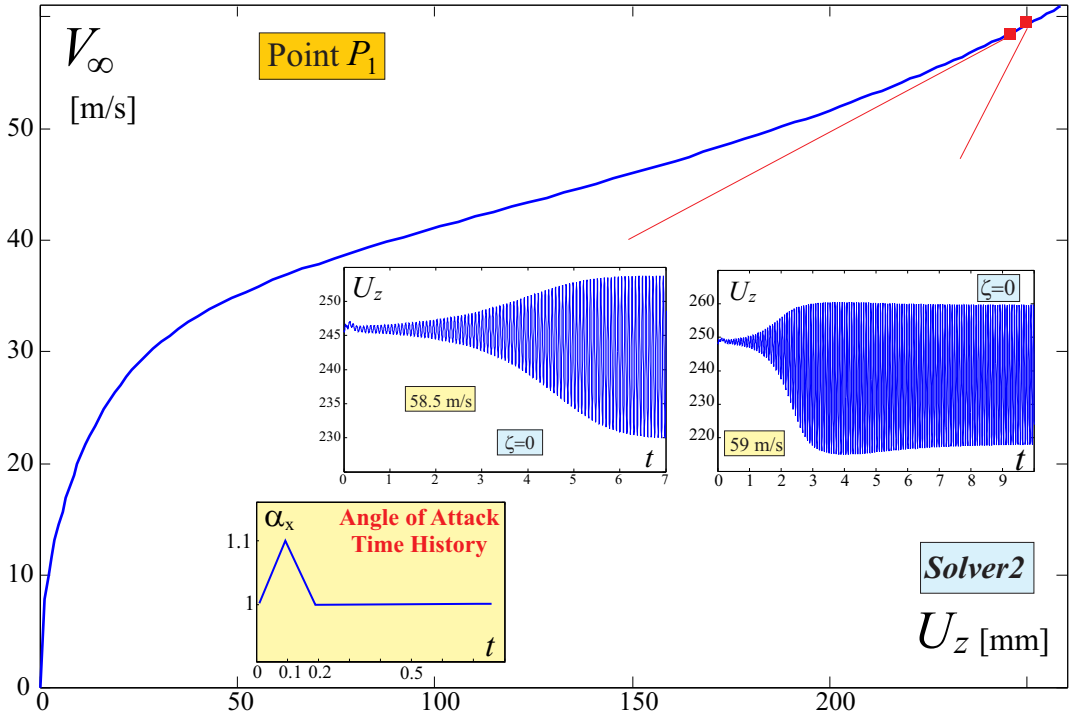

Fig. 7.14: *Solver2*. Aeroelastic dynamic response of *PrP40* starting from steady states relative to different velocities when a vanishing perturbation in angle of attack of the onset flow is given

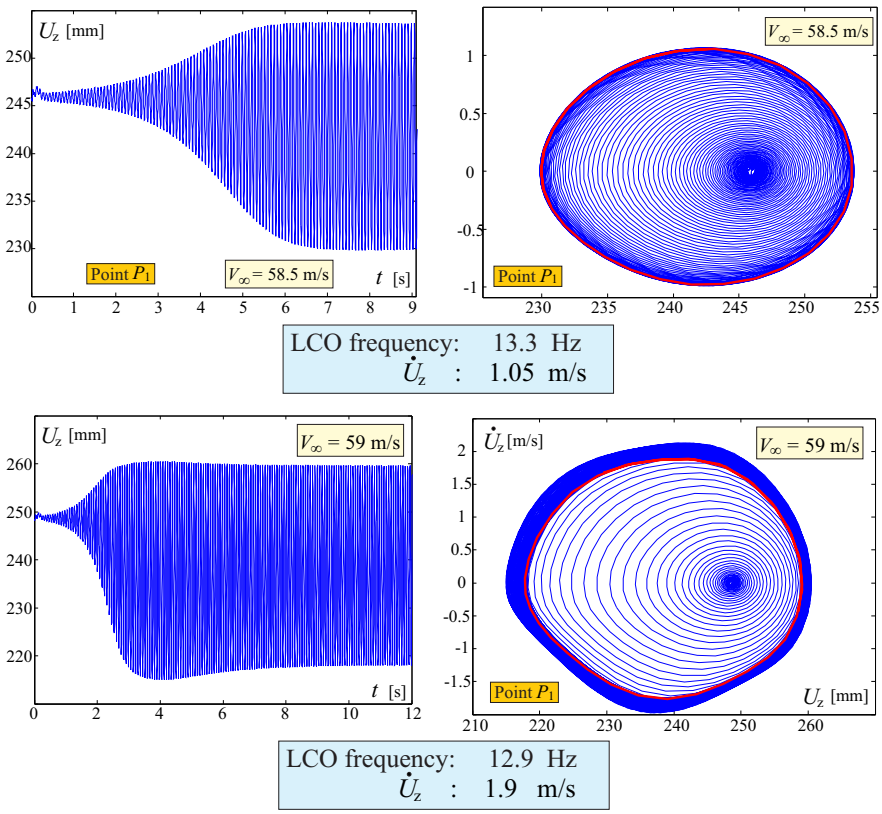

Fig. 7.15: Time response and state plane trajectory for *PrP40* configuration, for different flow speeds. *Solver2* is employed. No structural damping is considered

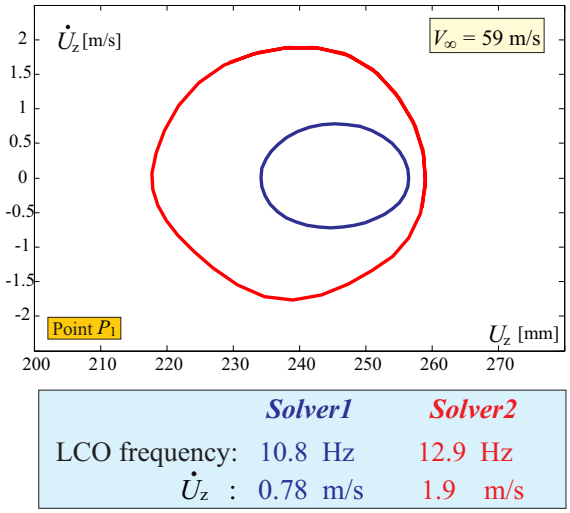

Fig. 7.16: Comparison in the state plane of LCOs of *PrP40* at a speed of $V_\infty = 59$ m/s as predicted by *Solver1* and *Solver2*

7.3.4 Sensorcraft

The *Sensorcraft* configuration is considered. The undisturbed flow forms with the x-axis an angle of 3°.

Solver1

The aeroelastic static response is tracked and reported in Fig. 7.17 where are represented the vertical displacements of both point $\boldsymbol{P}_1$, lying on the wing tip, and $\boldsymbol{P}_2$, at the midspan (as they are defined in Fig. 7.3). Before further proceedings, it is interesting to comment it.

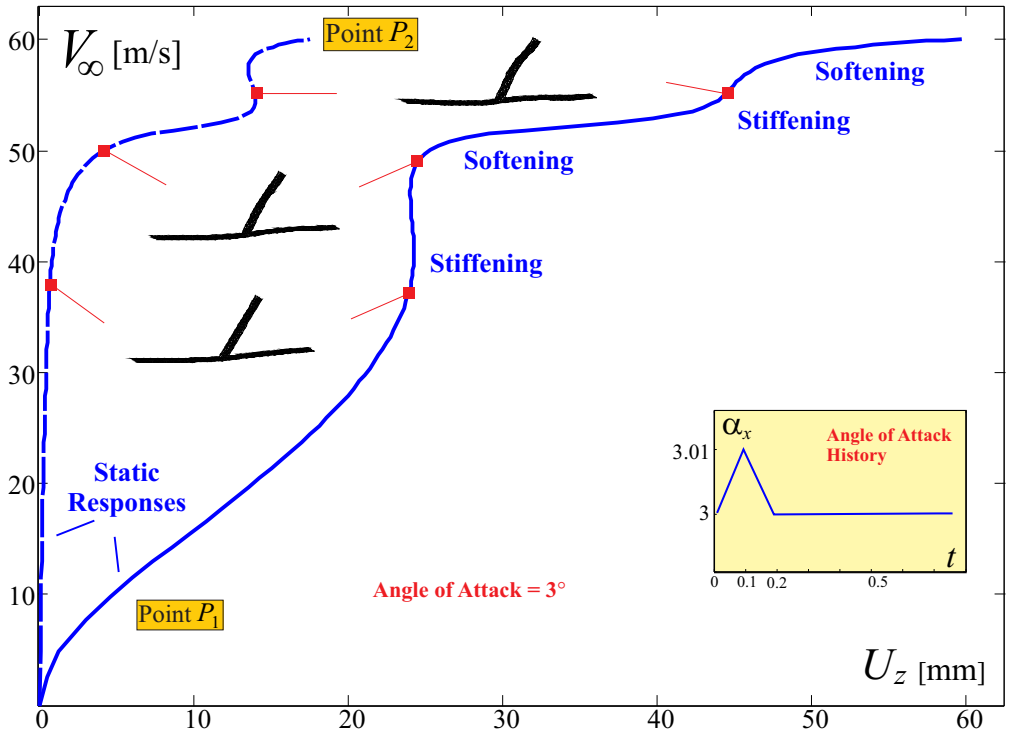

Fig. 7.17: Aeroelastic static response of *Sensorcraft*. Vertical displacements of points $\boldsymbol{P}_1$ and $\boldsymbol{P}_2$ are considered. Angle of attack is 3°. The vanishing perturbation that is applied to track the dynamic response is also represented

The response presents a sequence of softening and stiffening attitudes. To try to understand the complex exchange of loads involved in this response, videos of the deformation process obtained by sequences of *snapshots* like the ones reported in Fig. 7.17 are used. In the first stiffening region (for wing's tip), the deformation of the upper wing seems to produce a bending moment transmitted directly to the lower wing, such that the tip of the wing does not experience any vertical displacement for a big range of speeds.

Dynamic responses are presented in Fig. 7.18 for different flow velocities.

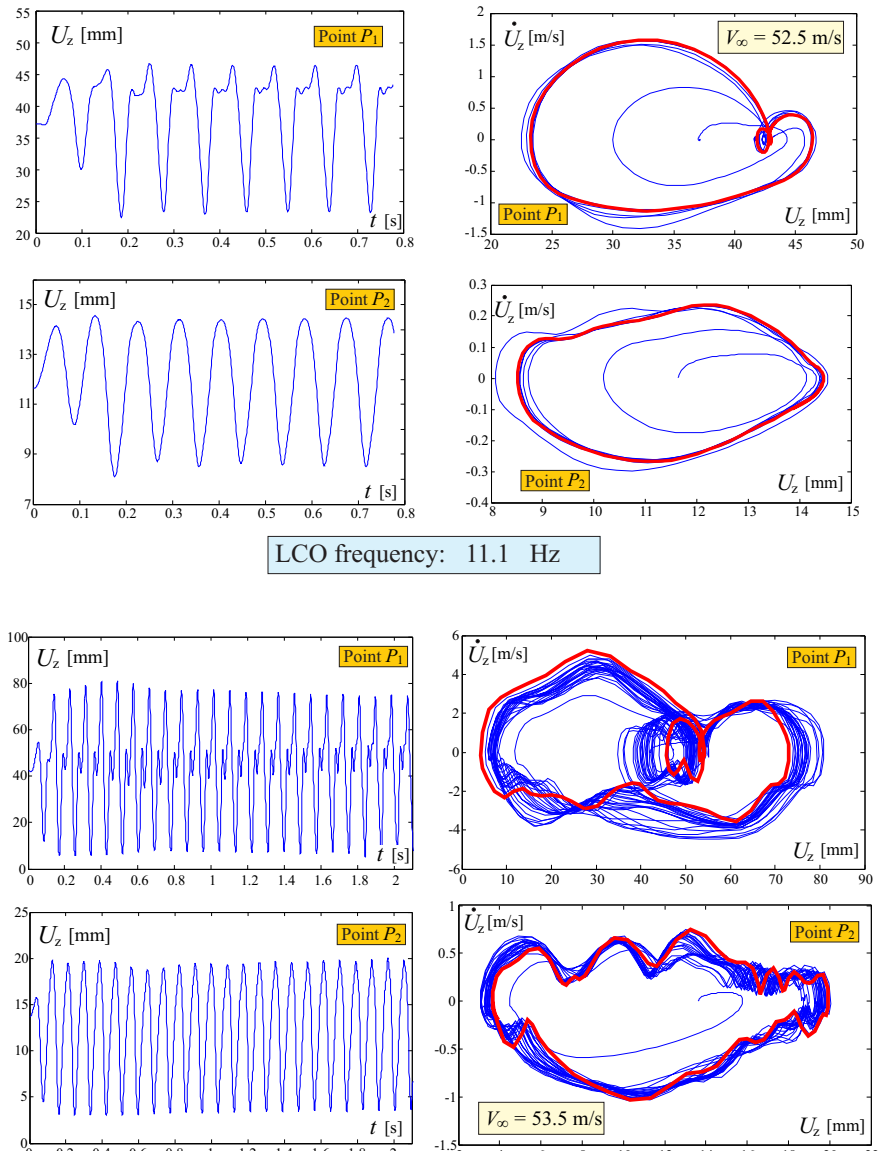

Fig. 7.18: Time response and state plane trajectory for *Sensorcraft* configuration, for different flow speeds. *Solver1* is employed. No structural damping is considered

Considering at first the case $V_\infty = 52.5$ m/s, the trajectory described by the midspan point $\boldsymbol{P}_2$ is the usual wave-like response. This does not hold for wing tip $\boldsymbol{P}_1$. In fact, considering a period, during the ascending part the motion is temporary reversed and some higher frequency oscillations of smaller amplitude establish before continuing again the ascending

motion. This pattern in the response has been observed also when structural damping was considered; moreover algorithmic damping (regulated as explained in Sec. 2.2.4 by the parameter ϱ_∞) has been varied in order to avoid influence of high frequencies modes in the simulation results.

If the speed is slightly increased to $V_\infty = 53.5$ m/s, the same pattern is observed, with the oscillation characterizing the ascending motion increasing its amplitude. It is natural then to repeat this process for higher speeds and observe what happens. A speed of $V_\infty = 59$ m/s is considered, and the response is depicted in Fig. 7.19. The response settles down to the

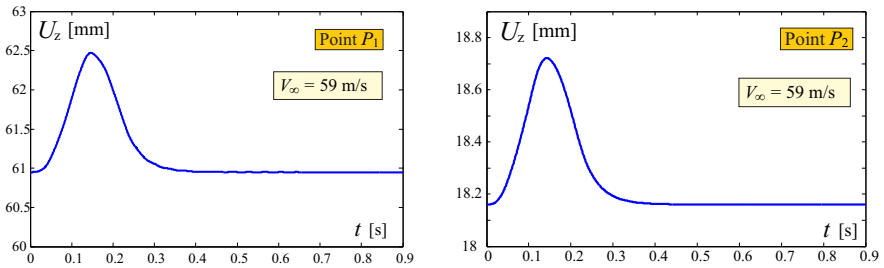

Fig. 7.19: Time response for *Sensorcraft* configuration, for $V_\infty = 59$ m/s. *Solver1* is employed

static equilibrium point, although the speed is increased from the previous cases showing LCOs (and so again instability would be expected). With the aid of Fig. 7.20 this strange behaviour is shown: starting from a stable condition ($V_\infty = 59$ m/s), the speed is slowly decreased to $V_\infty = 57$ m/s: the system loses its stability and an LCO is developed after the transient.

Solver2

Use of *Solver2* does not seem to give qualitatively differences from what previously observed. What can be noticed is a small decrease of the frequency, as shown in Fig. 7.21 when compared with the previous results.

Also the same oscillating pattern during the ascending motion is observed. In order to better visualize this phenomenon, it is interesting to plot the *snapshots* of the configuration during a period, Fig. 7.22. As it can be easily verified, the states c, d and e describe the small oscillation during the ascending motion. Focusing then on the upper wing, it can be observed a unique smooth wave-like pattern identified by a compression and an extension, whereas for the outer portion of the wing this does not hold.

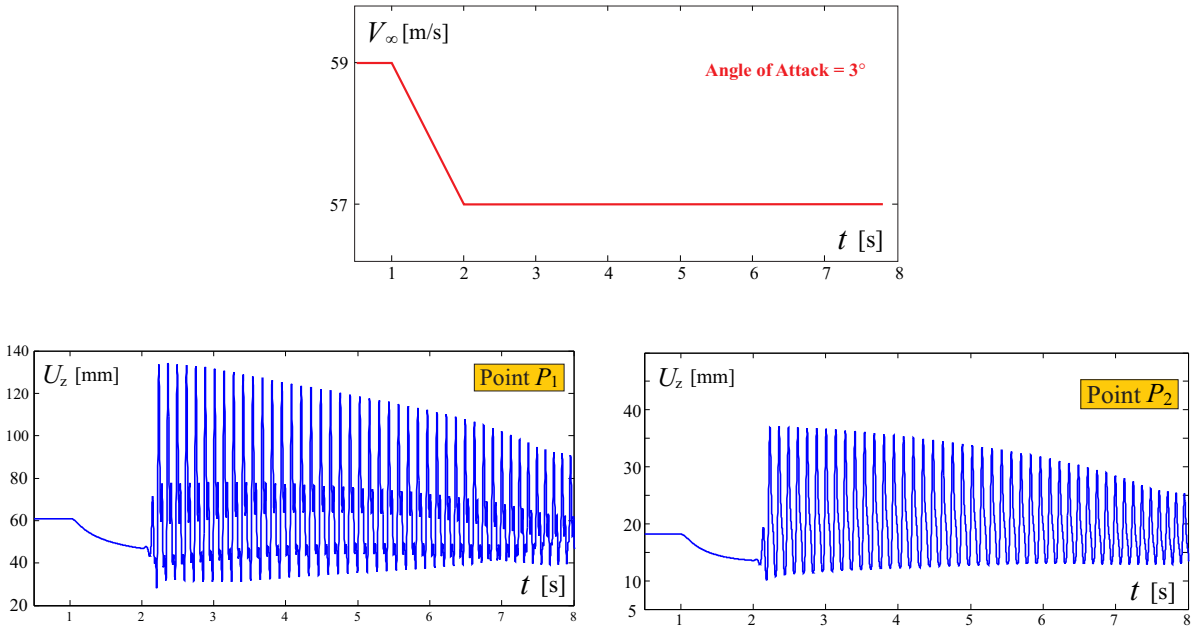

Fig. 7.20: Time response for *Sensorcraft* configuration, when the speed is decreased from $V_\infty = 59$ m/s to $V_\infty = 57$ m/s, and the angle of attack is maintained to 3°

Solver3

Results obtained with *Solver3* are presented in Fig. 7.23. The angle of attack is increased until the same value of 3° is obtained.

It is interesting to observe that the high frequency oscillation pattern earlier observed is now present in the descending portion of the LCO. The addition of a further source of nonlinearity (represented by wake roll up) seems to influence this pattern. Again *snapshots* in Fig. 7.24 are used to better visualize the response. States f, g and h describe the small oscillation during the descending motion.

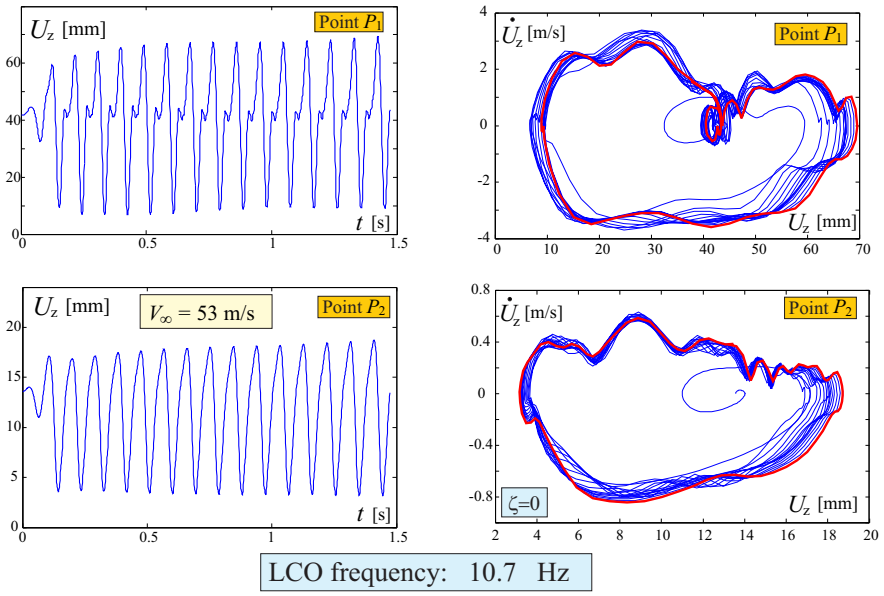

Fig. 7.21: Time response and state plane trajectory for *Sensorcraft* configuration at a speed $V_\infty = 53$ m/s. *Solver2* is employed. Vertical displacements of both points $\boldsymbol{P}_1$ and $\boldsymbol{P}_2$ are considered

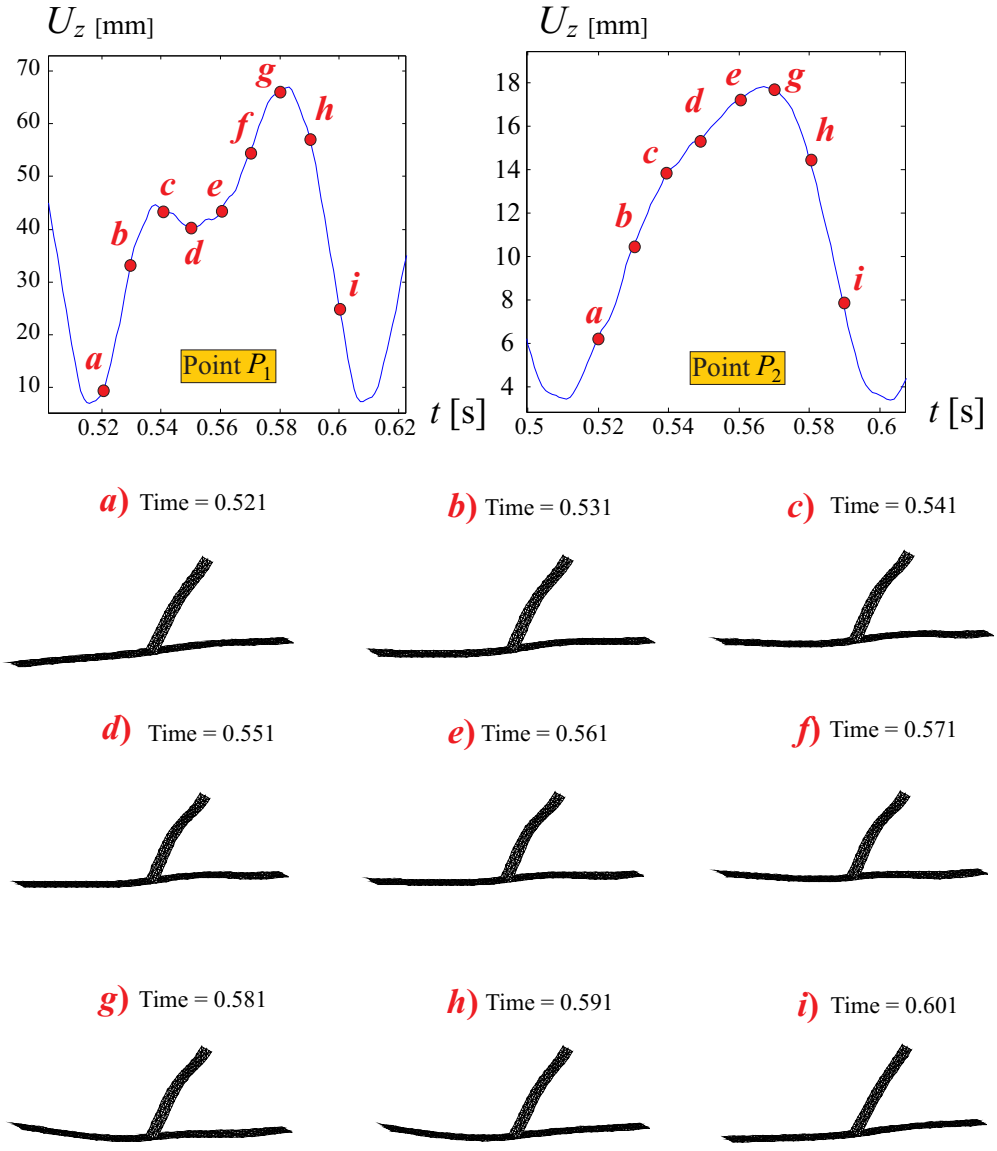

Fig. 7.22: Sequence of snapshots of the deformed configuration during one period. *Solver2* is employed and $V_\infty = 53$ m/s. The points c, d and e represent the small oscillation in the ascending motion

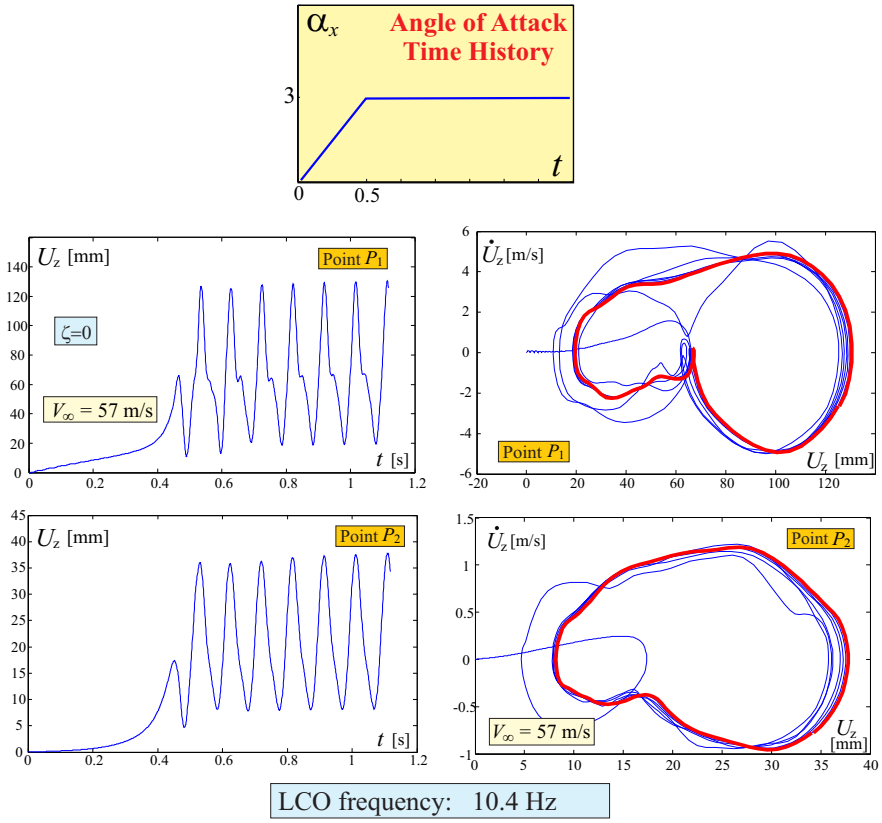

Fig. 7.23: Time response and state plane trajectory for *Sensorcraft* configuration, for $V_\infty =$ 57 m/s. *Solver3* is employed

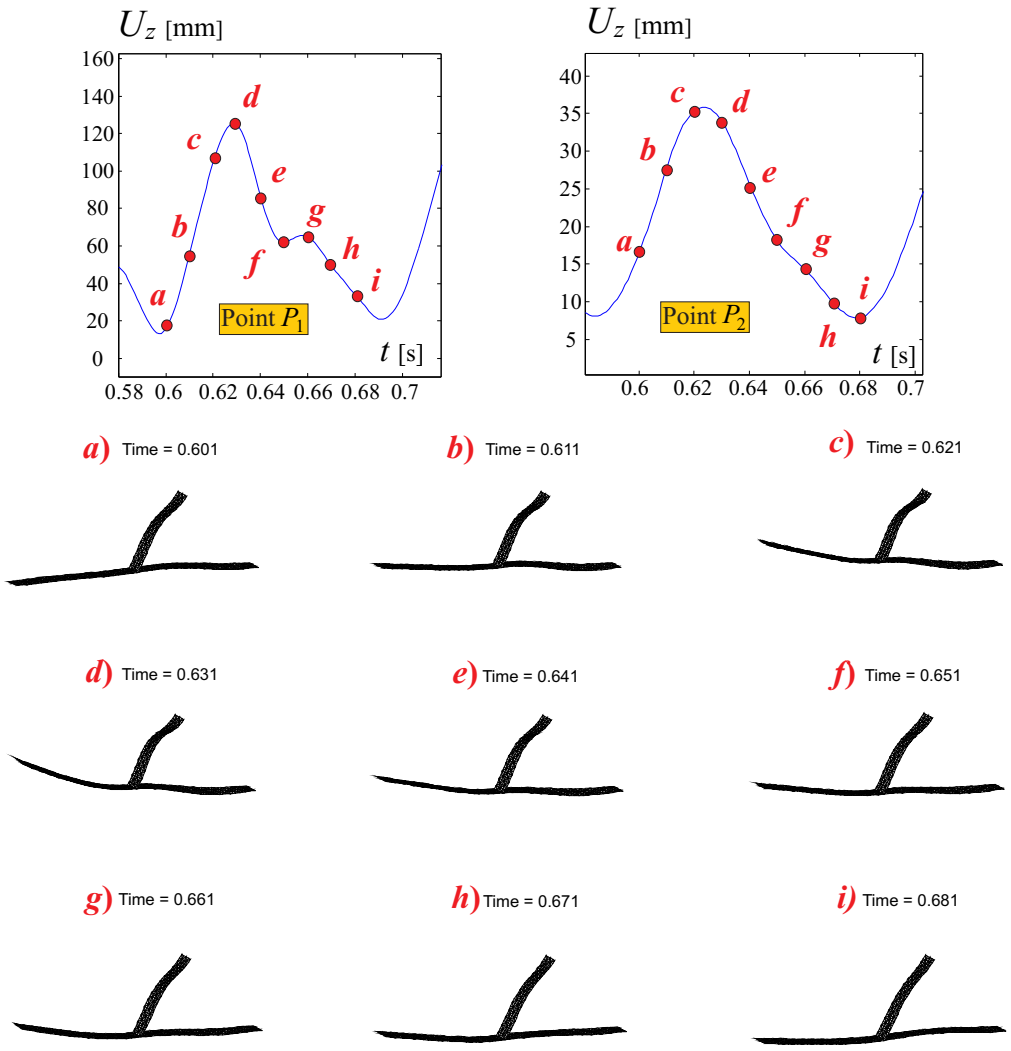

Fig. 7.24: Sequence of snapshots of the deformed configuration during one period. *Solver3* is employed and $V_\infty = 57$ m/s. The points f, g and h represent the small oscillation in the descending motion

7.4 Flutter evaluated with Linear and Nonlinear Analyses

Flutter velocities of the baseline configurations (in particular here are reported results relative to *PrP40* and *Sensorcraft*) are here reported, in order to have a comparison among the critical speeds sorting out from the analyses through the three time-domain solvers. The aim is in fact to attempt a comprehension of what are the basic features whose omission can bring to misleading results. This task is pursued through the DLM code (see discussion in Sec. 5.2), which also enables to investigate how linear and nonlinear tools may lead to notably different flutter speed predictions.

Two configurations are here considered: *PrP40* and *Sensorcraft*. They are thought to be representative of different deformations scenario: the first one exhibits quite large displacements and proves to be sensitive to the structural damping, while the second has small deformations and a quite insensitiveness of the flutter speed in respect of the structural damping (see post critical response in Sec. 7.3). In literature it is claimed [85] that DLM analysis lacks in precision when used for cases in which wake roll-up plays an important role, or for cases in which the structural deformation is conspicuous. This investigation will hopefully provide enlightenment about that.

7.4.1 PrP40

The configuration *PrP40* is first taken into consideration ($t = 1$ mm).
Results are relative to different values of structural damping ratio ζ. Flutter speeds are 51.5 m/s for the zero damping case, 52.2 m/s when $\zeta = 0.01$, 53.7 m/s when $\zeta = 0.02$ and 54.9 m/s when $\zeta = 0.03$.

Discrepancy of the flutter speed evaluated for the undeformed configuration and the real one is about 22%; in this case the discrepancy is in the nonconservative side (overprediction of the critical condition). Actually, increasing the linearization speed enhances this mismatch, at least for a large portion of the response. An overprediction of the divergence speed was also found when linear analyses were performed (see [34]).

7.4.2 Sensorcraft

Here the *Sensorcraft* is considered. Results are shown in Fig. 7.26. The interesting property of this configuration is the relatively smaller deformation consequences of the chosen geo-

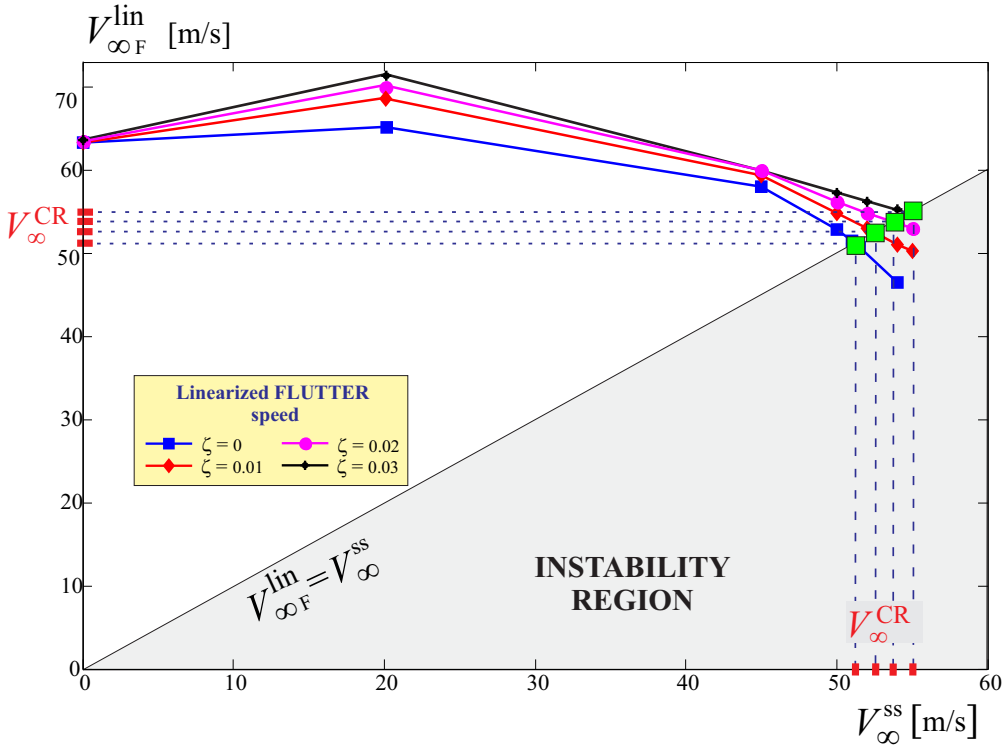

Fig. 7.25: Flutter speed predicted linearizing about steady state relative to different flow speeds for *PrP40*. The real critical condition (*nonlinear flutter*) occurs when these two speeds coincide

metric properties (this will be better characterized in next section). However, as it could be appreciated, there is still a non-negligible overprediction of the linear tool. In fact, considering the zero-damping case, the linear prediction gives 59.1 m/s against the 51.6 m/s, with a difference of approximately 15%. It is interesting to observe that, linearizing about a speed other than the fundamental (zero) one but still far from the critical, the flutter prediction instead of being more precise, may actually lead to larger errors. This was observed also for the *PrP40* case, suggesting that, evaluation done with immediate successive linearization may give misleading trends and even more inaccurate predictions, unless the linearization speed is close to the real critical one. These results seems to suggest the big role played by the nonlinearities in the evaluation of aeroelastic instability of Joined-Wing configurations.

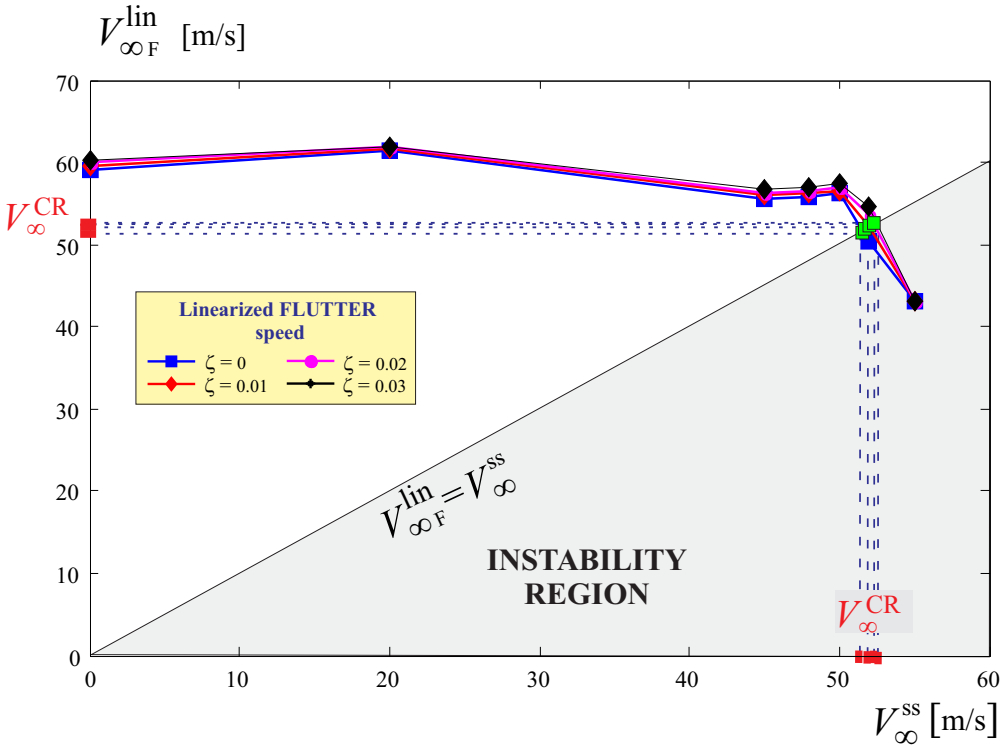

Fig. 7.26: Flutter speed predicted linearizing about steady state relative to different flow speeds for *Sensorcraft*. The real critical condition (*nonlinear flutter*) occurs when these two speeds coincide

7.5 Influence of Solver choice in the prediction of flutter speed

In this section it is investigated the effect of the features that discern the Solvers developed in this work on the determination of flutter speed. In-house DLM code results (reported in Sec. 7.4) are used as well as a comparison and as a further example of a different modelization (frequency-domain) of the aeroelastic problem, studying if and why this can bring to different results.

7.5.1 JW70

In Fig. 7.27 it is plotted the flutter speed with respect to the structural damping ratio.

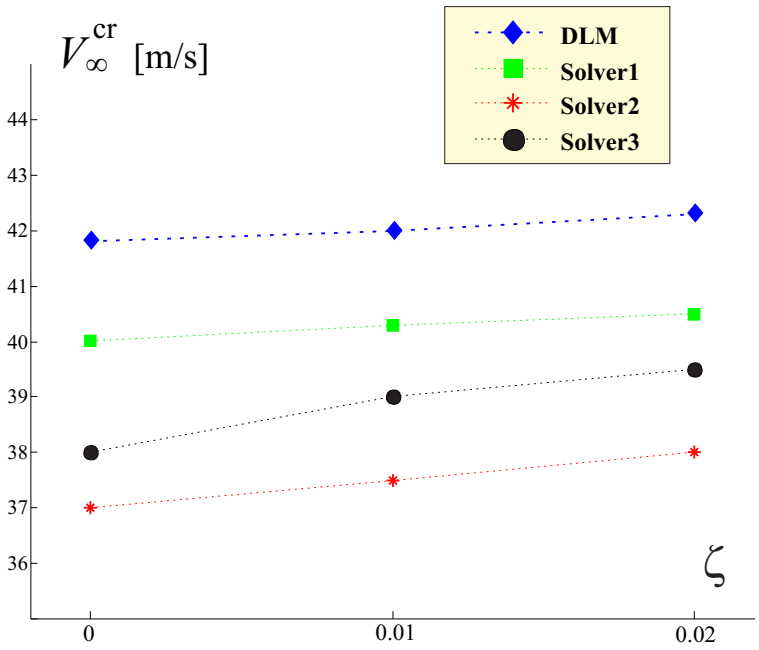

Fig. 7.27: Flutter speeds for *JW70* configuration, evaluated with the different solvers and for different values of structural damping ratio

The critical speeds evaluated with the three time-domain Solvers are obtained by considering the two successive speeds for which the response was showing and was no more showing an LCO. In this case, the DLM predicts the highest flutter speed in respect with all the other methods. *Solver2*, instead, gives the lowest. Employing correctly the lift direction can be considered detrimental for the deformation of the structure (as speculated by mean of Fig.

7.16), but this doesn't automatically lead to the conclusion that it has a decreasing effect on the prediction of the flutter speed. In fact, especially for configurations behaving nonlinearly, the aeroelastic instability is a result of the redistribution of stiffness (particularly of changing in stiffness ratios) and thus an increase in the overall deformation (due to follower nature of forces) doesn't have a clear consequence in that sense. For example, it will be shown for the *PrP40* layout that *Solver2* predictions have an opposite trend respect to this layout.

Solver3, which have singularities bound to the structure and the wake free to deform and evolve, is the most different among the adopted codes. The trend shown here, and confirmed also in the other layouts, is an overstimation of the critical speed with respect to *Solver2*, the one that more goes near to its modelization and so it is more appropriated for a comparison to catch the effect of its new features. The wake *roll up* seems in this sense to have a relevant role in increasing the critical speed, as will be later detailed.

7.5.2 PrP40

In Fig. 7.28 it is plotted the flutter speed, with respect to the structural damping ratio. Considering the undamped case, the DLM solver finds a flutter speed of approximately

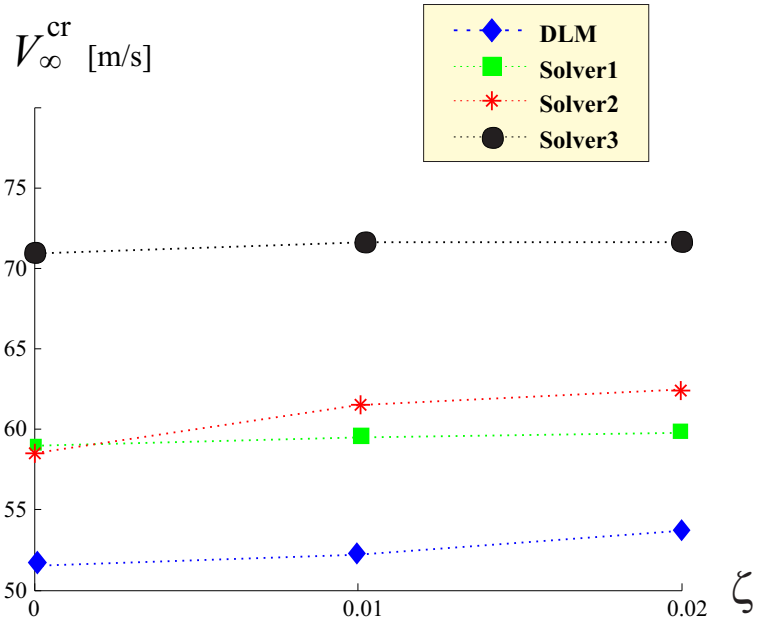

Fig. 7.28: Flutter speeds for *PrP40* configuration, evaluated with the different solvers and for different values of structural damping ratio

51.5 m/s, whereas, *Solver1* predicts a critical speed of 58.5 m/s. The relative error is in

the order of 12%, definitely larger than the discrepancy observed for the *JW70* case. The number of natural modes, aerodynamic panels and structural elements in the analyses have been verified to be enough to give convergent results.
Another difference from the *JW*70, earlier disclosed in the comments about effects of follower forces, is the higher flutter speeds predicted by *Solver2* when compared to *Solver1* for nonzero damping ratios.

However, the most relevant observation is the discrepancy of *Solver3* with all the other solvers. Since the greater improvement of this Solver lies in the wake model (especially if a direct comparison between *Solver3* with *Solver2* is considered), an explanation is tempted based on this physical argument. To isolate this effect, a pure aerodynamic analysis is introduced, that is the problem as stated in Sec. 2.3 (without the aeroelastic coupling) is solved and the loads acting on the rigid structure are evaluated.
The flow has an angle of attack of 5° and the lift coefficient evolution in time is depicted in Fig. 7.29. In the immediate transient there is a small difference between the lift coefficient which vanishes when evolving in time. The first result is thus that the net force acting on

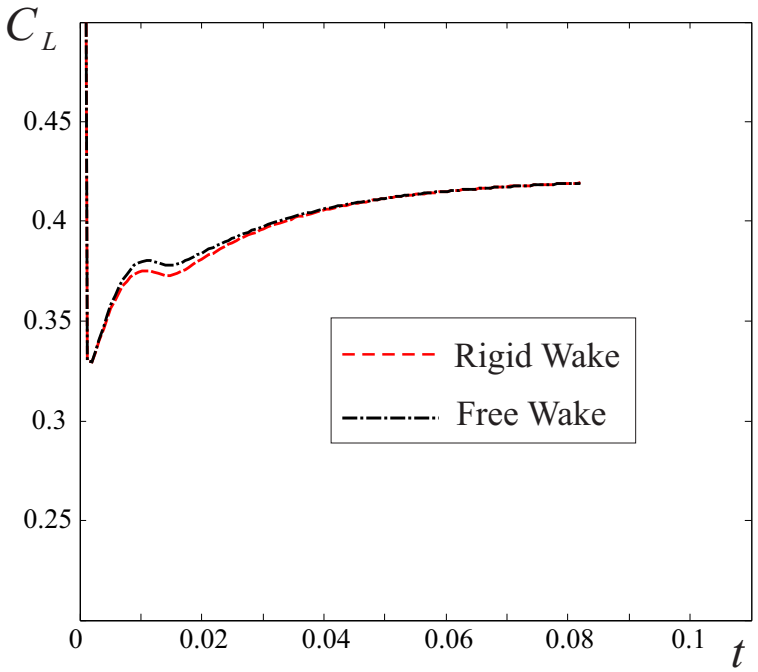

Fig. 7.29: Lift coefficient's variation with time for PrP40 configuration for both rigid and free wake models

the wings is not particularly affected by the wake model. In Fig. 7.30 are reported two *snapshots* of the free wake evolution for this case.

Then, the *distribution* of lift is considered. In Fig. 7.31 it is shown the distribution of local

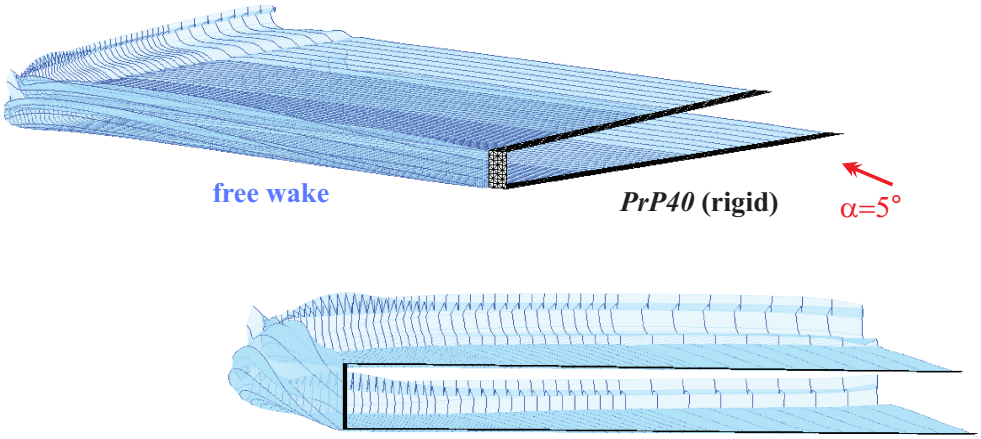

Fig. 7.30: Wake evolution after 0,08 s

lift coefficient (lift coefficient of a chordwise rows of panels) over the wingspan at a time in which the global lift coefficients are identical. Effects of the wake can now be appreciated.

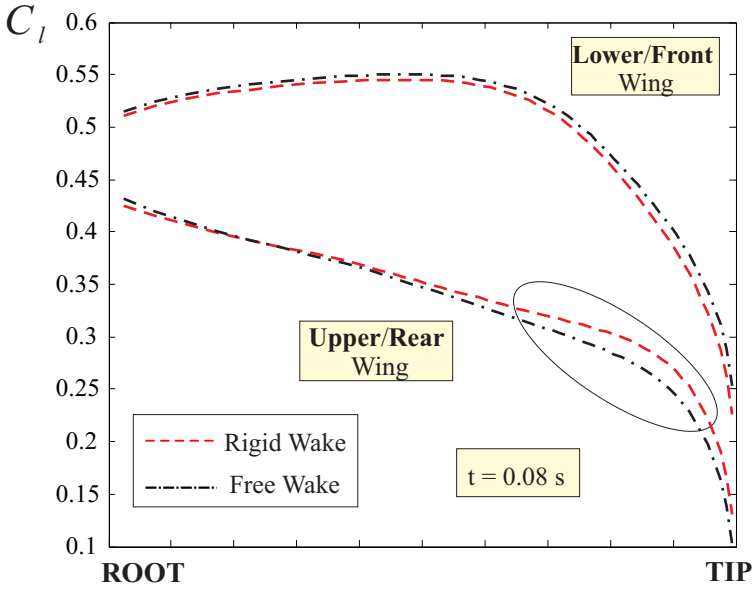

Fig. 7.31: Local lift coefficient span distribution for PrP40 configuration for both rigid and free wake models at $t = 0{,}08\ s$

When free wake is modeled, there is a significant decrease of the load on the outer part of

the upper wing; on the other hand on the front wing there is an almost uniformly distributed increase. A forward swept single wing is known to be prone to enhance divergence instability, the opposite for the backward [15]; on pure speculative basis, the redistribution of loads brought from the free wake model can thus be regarded as stabilizing because the upper wing sees decreased its load, particularly at the tip where the destabilizing bending-torsion coupling introduced by the sweep angle is stronger, and the opposite happens for the lower wing. The same trend is found considering a different time.

To investigate the reason of such a redistribution, similar analyses were carried out on different configurations, like the rectangular wing and the delta wing analyzed in Cap. 6. Results, not reported here for brevity, don't show such a big effect: maximum percentage difference is around 1%, against 15% or 20% reached by the *PrP40*.

A similar predominance of wake modelization influence for a Joined-Wing configuration respect to a standard one is in some way expected since this layout inherently provides a deep reciprocal influence body-wake, which can thus bring to different results if different models are adopted. It is not anyway so evident if the main cause has to be sought in the particular *PrP40* geometry (staggered and swept angle) or in general in the Joined-Wing layout itself.

Therefore a similar aerodynamic study was repeated for an unstaggered and with zero sweep angle *PrandtlPlane*-like configuration, the standard Wing Box shown in Fig.7.32.

The transient and variation of lift coefficient with time exhibits a similar behaviour to

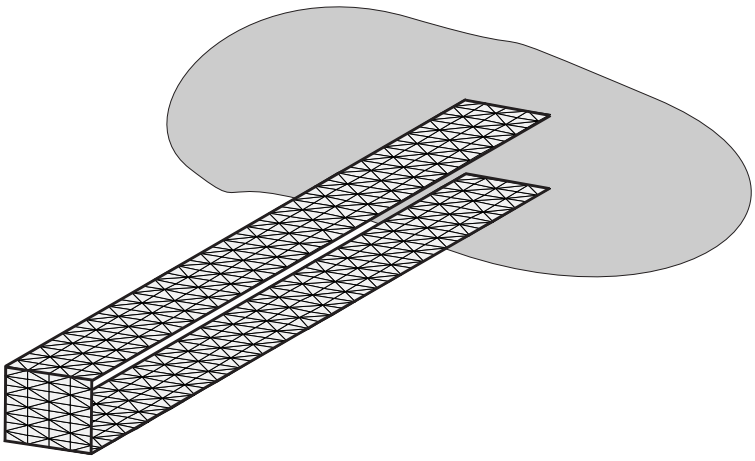

Fig. 7.32: Standard Wing Box layout for aerodynamic investigations

the one pointed out in Fig. 7.29 and it is thus here omitted. More interesting, instead, is the distribution of loads for this case, reported in Fig. 7.33. As can be seen, there is still

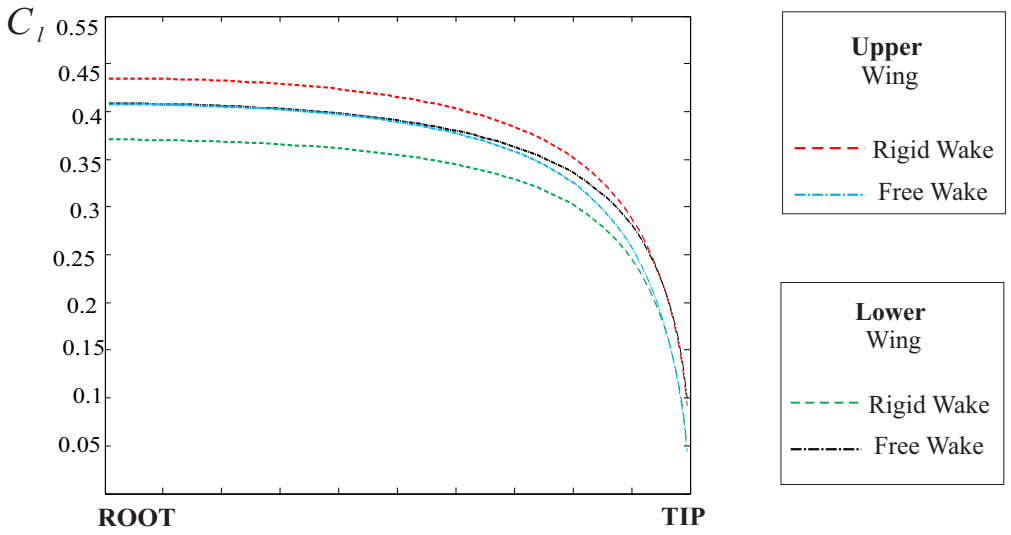

Fig. 7.33: Local lift coefficient span distribution for Wing Box layout for both rigid and free wake models

this changing in the distribution comparing the two cases, regarding this as a property of the Joined-Wing configuration and not a particular case of *PrP40*. A similar aerodynamic analysis of the *JW70*, which is showing as well a decrease in the flutter speed when *Solver3* is employed instead of *Solver2*, confirms this trend.

A further note about the role of the wake's model is that it can affect the induced drag of the configuration. This was already shown in reference [13], where a free-wake modelling was shown to predict a lower induced drag whereas the lift coefficient was not experiencing differences.

7.5.3 Sensorcraft

In Fig. 7.34, it is plotted the flutter speed, as evaluated with the different solvers, with respect to the structural damping ratio.

The predictions are now much closer, and the differences are negligible. This is thought to be strictly related to the smaller deformations involved, which do not enhance the modelling differences of the solvers.

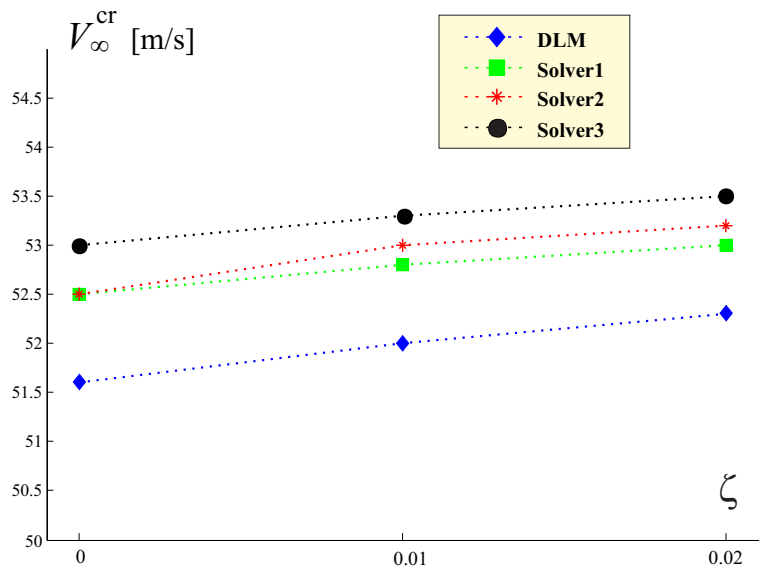

Fig. 7.34: Flutter speeds for *Sensorcraft* configuration, evaluated with the different solvers and for different values of structural damping ratio

7.6 Bifurcations and multistability

This section shows the complicate scenario that can arise when the aeroelastic nonlinear system represented by a Joined-Wing configuration is studied. Some of the concepts introduced in Cap. 4 are here characterized through a practical example.
The test case adopted is the *PrP40* shown in Fig. 7.2 where the thickness is now selected to be 0.6 mm. The freestream velocity is along the x axis, i.e. the configuration has angle of attack zero; the tools employed are *Solver1* for the dynamic response and the aeroelastic static solver (see Cap. 5).

Differently than what has been made in Sec. 7.3, the starting tool is directly the dynamic solver. In fact there is no more the intent to verify if the equilibrium point found through static analyses is dynamically stable. The goal here is to study what happens to the system when, starting from the undeformed configuration where no aerodynamic forces are acting (since angle of attack is zero), a vanishing disturbance is applied. The behaviour is expected to depend on parameters, recalling Sec. 4.5; in this analysis the speed of the free stream is varied, but this procedure could be employed for all the others meaningful parameters (as thickness, joint height).
Since the perturbation is vanishing, the undeformed configuration is a fixed point of the system for all velocities. With reference to the bifurcation diagram of Fig. 7.35, in which the vertical displacement of the tip of the lower wing (point P_1 in Fig. 7.2) has been chosen as representative state of the system, these fixed points lie on the ordinate axis. In Fig. 7.37 the state space of the system is reported; accordingly to the analysis of stability of dynamical systems, this graph is a useful tool to attempt the comprehension of what is happening to the system. Actually just two states of the system are represented, the vertical displacement of the lower wing tip and its time derivative, thus state plane would be a better definition. For each range of the parameter, this graph enables to detect the attractor (or attractors) of the systems looking at the behaviour of its states (see Sec. 4.5 for a more precise discussion). Until the speed is smaller than V^{sd}, only the main branch (undeformed) is present. This critical speed is associated with two *saddle node* bifurcations occurring on branches far from the fundamental one. What occurs is the inception of two new stable fixed points on each of the non-fundamental branches. That is, if the speed falls between V^{sd} and V^{bf}, there are *five possible equilibrium configurations*; three of them are *stable*. This property is demonstrated in Fig. 7.36 by giving different vanishing perturbations in angle of attack, and observing that after the transient the configuration can settle to the three different stationary equilibria.

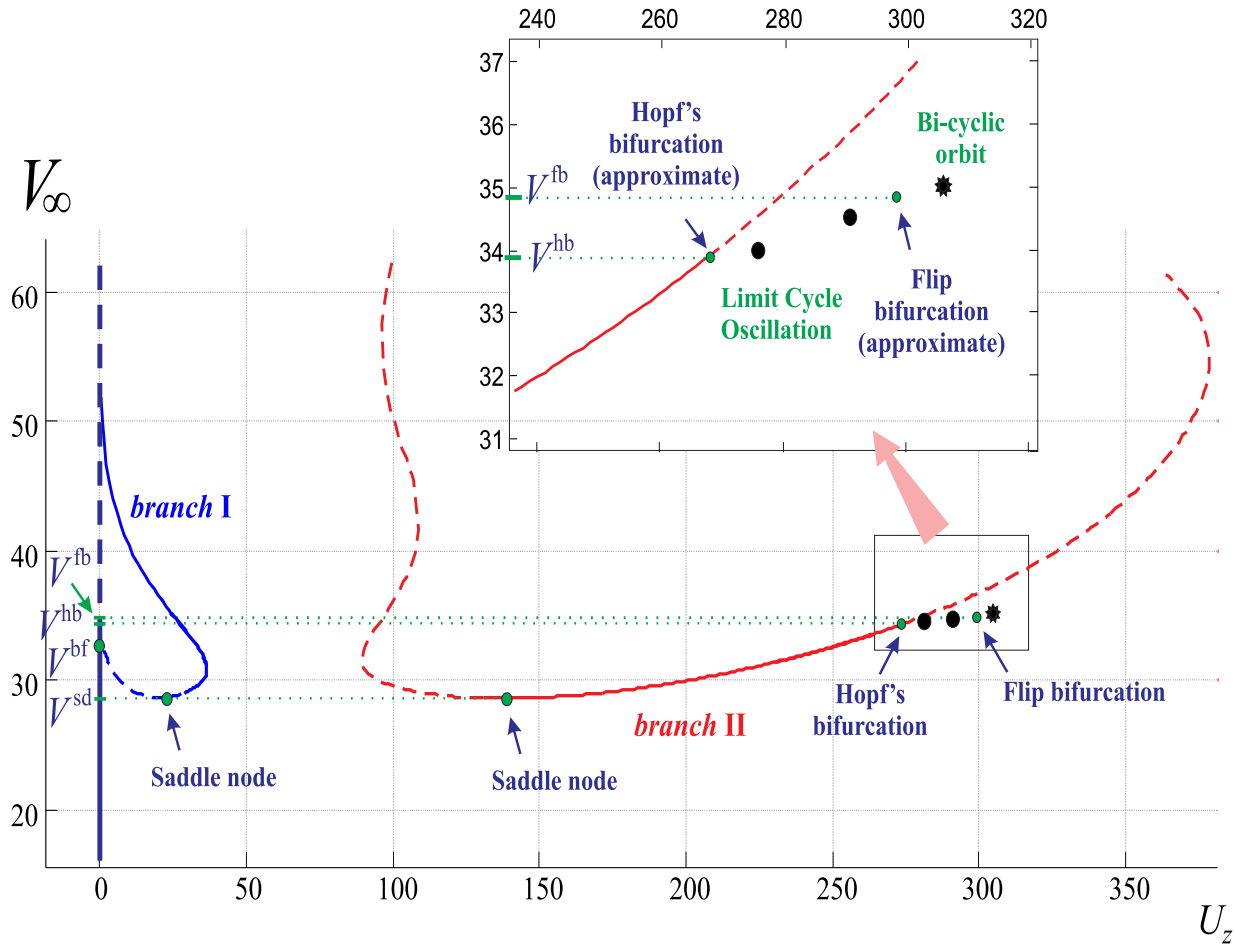

Fig. 7.35: Bifurcation diagram of the system. Solid (dashed) lines represent stable (unstable) fixed points, full circles stand for stable limit cycle oscillations and the full complex star stands for stable bi-cyclic periodic closed orbit

A so called *tri-stability* situation is in place.

Looking at Fig. 7.37, a speed in this range has been chosen, i.e. $V_\infty = 29.5$ m/s, and the equilibrium points are represented with small circles, full (empty) if they are stable (unstable). When speed approaches V^{bf}, there is a bifurcation that leads to a change in the stability of the main branch: the undeformed configuration looses its stability. Probably it is a *transcritical bifurcation*, since it seems that an exchange of stability has taken place among the equilibrium points of the system. The state plane diagram for $V_\infty = 33.7$ m/s, which is in the range $V^{bf} \div V^{hb}$ is depicted in Fig. 7.37. There is a bi-stability, being the stable states on the branch I and II. There are also two unstable poles, the first being on the undeformed configuration and the other one on the branch II. Responses showing this

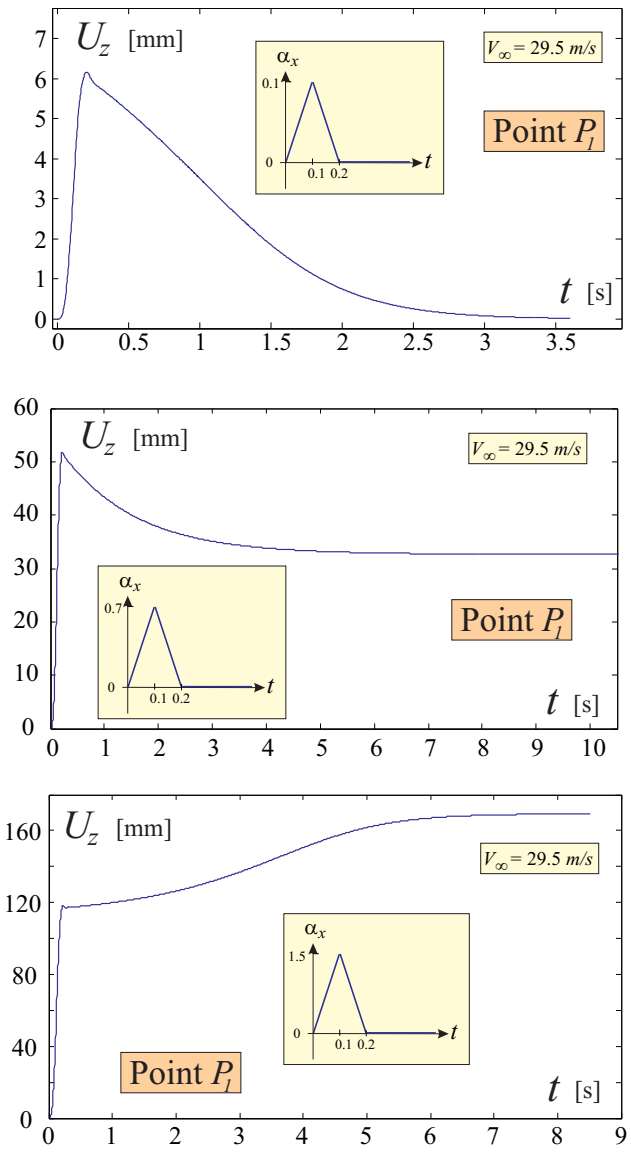

Fig. 7.36: Tri-stability region for $V_\infty = 29.5$ m/s. Starting from the initial undeformed configuration different vanishing perturbations in angle attack are given, and the response is tracked

behaviour are represented in Fig. 7.38.

Increasing the speed, in branch II it is encountered an Hopf bifurcation; this critical speed is V^{hb}. This bifurcation pertains to the loosing of stability of a stationary equilibrium, which ends up in periodic oscillations. On the contrary, the properties of the fixed points on the other branches do not change as again can be argued from Fig. 7.37 when range $V^{\text{hb}} \div V^{\text{fb}}$ is considered.

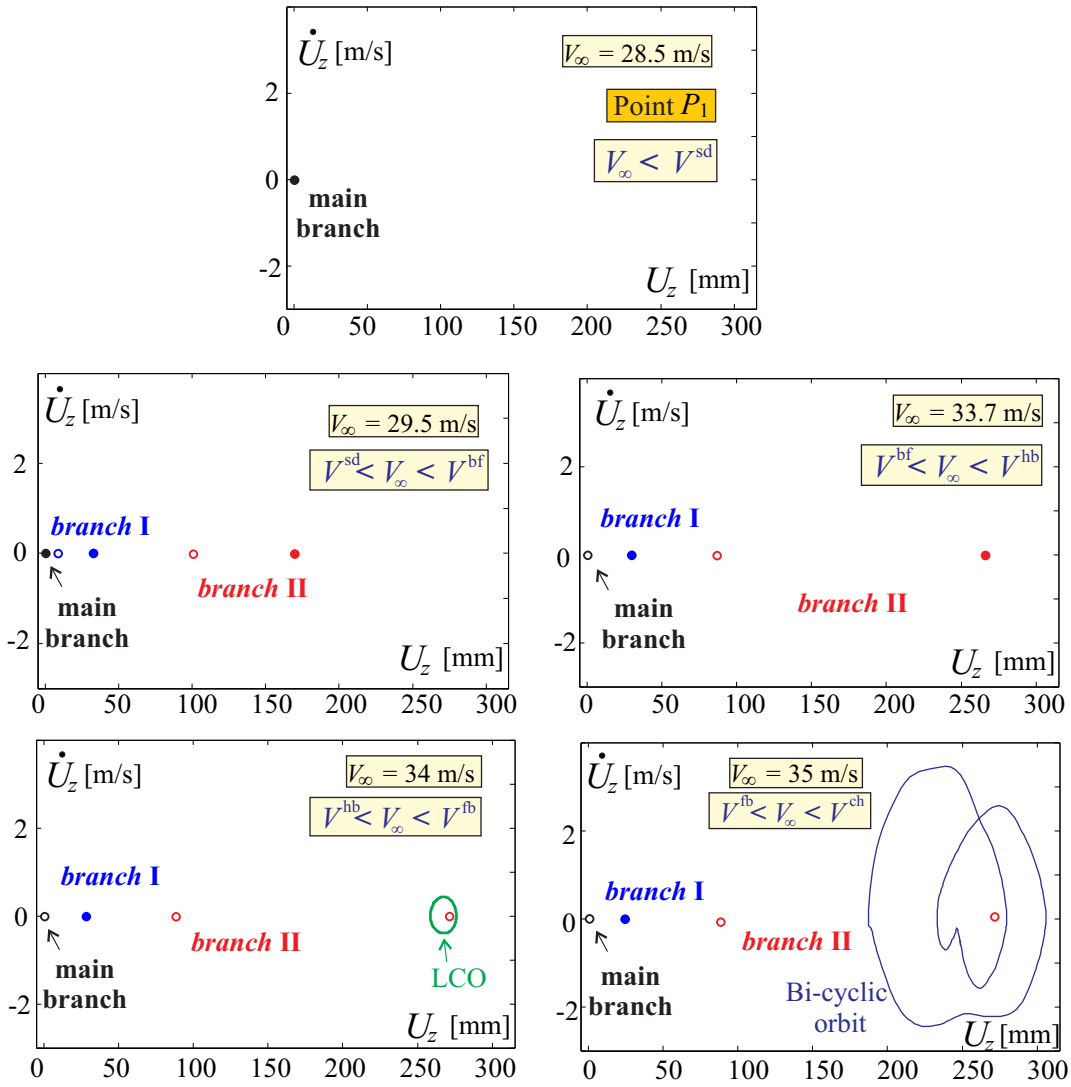

Fig. 7.37: State spaces for the different meaningful speed ranges. Equilibrium points are represented with small circles, full (empty) if they are stable (unstable)

Thus, as it is shown for a speed $V_\infty = 34.0$ m/s, different perturbations lead to the response shown in Fig. 7.39.

The largest distinguishing speed found in this analysis is V^{fb}, for which a flip bifurcation (also called *period doubling*) occurs. For speeds slightly larger than V^{fb}, considering that branch I has still stable fixed points, there is again a bi-stability region, similar to the one encountered in the previous range but of different type because on branch II a clear bifurcation took place. This is shown also in Fig. 7.40; the close orbit described after period doubling occurrence is here assessed to as bi-cyclic periodic orbit.

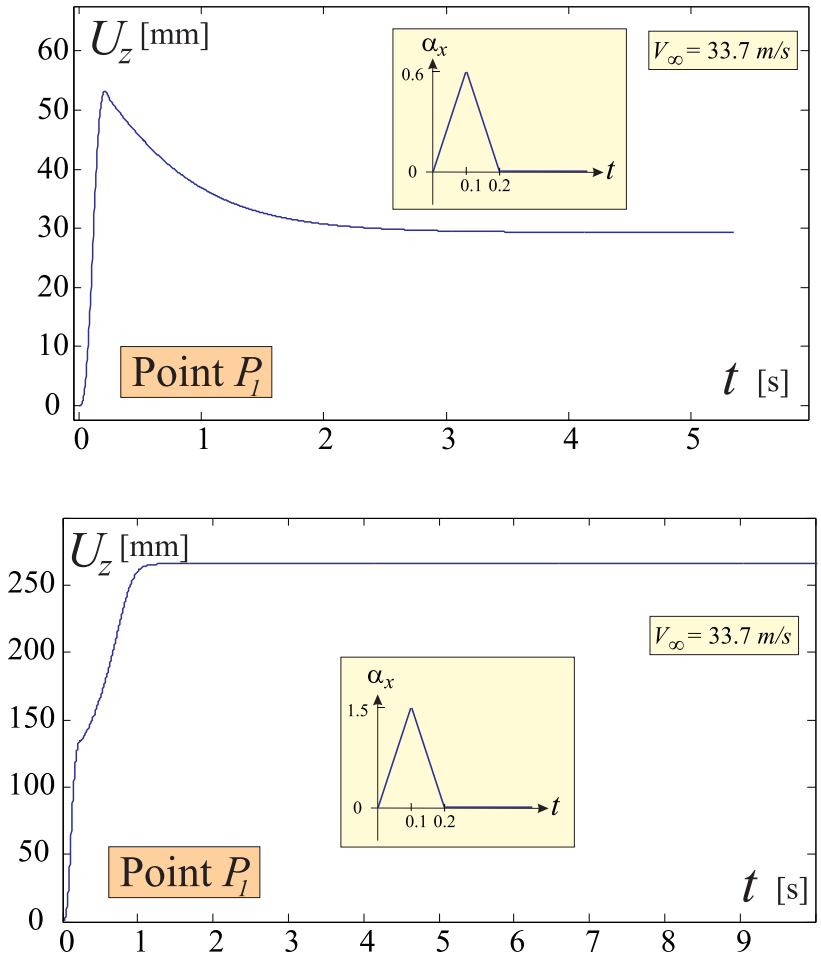

Fig. 7.38: Bi-stability region for $V_\infty = 33.7$ m/s. The system can settle down to both the static equilibrium points on branches I and II

As discussed in Sec. 4.5.3, periodic solutions, as for example the ones sorting out from a Hopf bifurcation, can lose stability, giving rise to different kind of phenomena. In this example it seems that the periodic orbits characterizing branch II in the range $V^{\text{hb}} \div V^{\text{fb}}$ become unstable through a period doubling. It has been stated that to correctly mathematical assess a flip-bifurcation occurrence the eigenvalues of the so called *Monodromy Matrix* (known also as Floquet characteristic multipliers) [94, 104] have to be studied. This was not pursued in this study; instead, period doubling was assessed noticing that, immediately after V^{fb}, the period of the orbit was exactly doubling compared to the one of the limit cycle oscillation established at a speed slightly lower than that critical speed. Fig. 7.41 clearly shows this event.

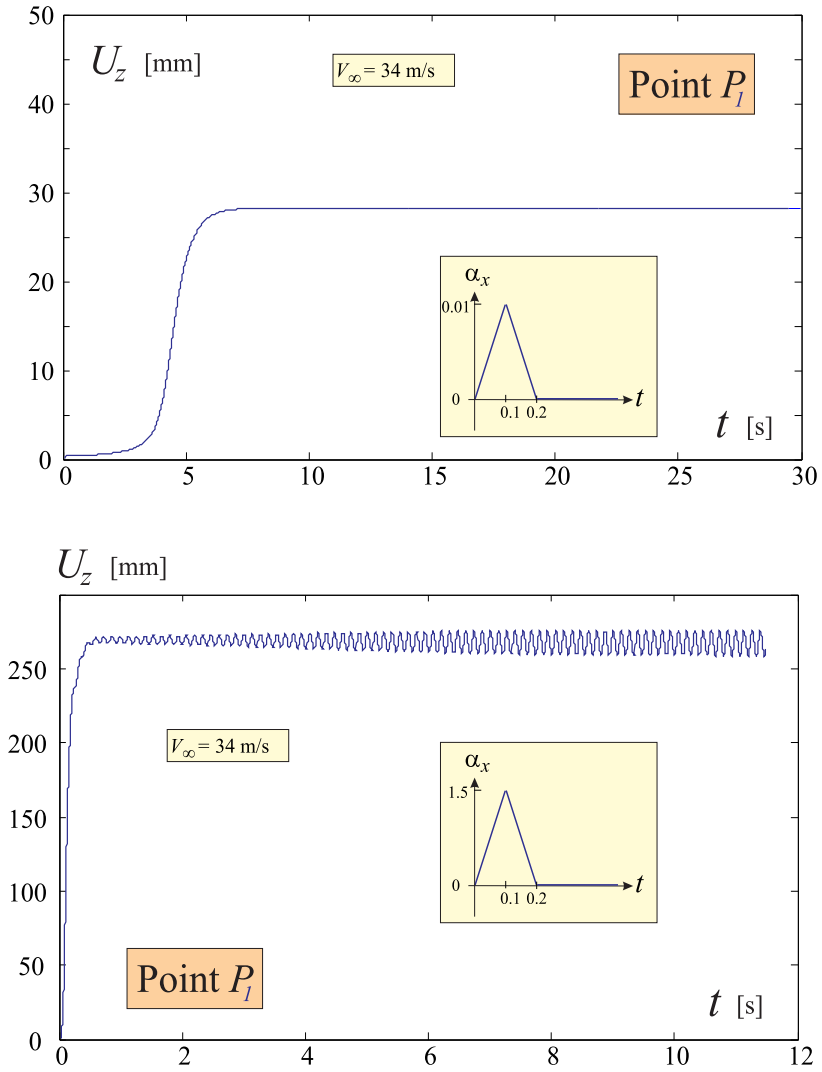

Fig. 7.39: Bi-stability region for $V_\infty = 34$ m/s. Either the static solution on branch I or the limit cycle oscillation are approached after a transient

To correctly describe how topologically changes the dynamic behaviour of a system, its response as a whole, i.e. looking simultaneously at the response of all its states in the state space, should be considered. For obvious reasons, when the dimension of the system enormously increases, as in this example, this is not more possible; anyway a better perspective is attempted in Fig. 7.42 where are plotted various combinations of the state plane starting from three degrees of freedom, the vertical displacements of points P_1, P_2 and P_3 (shown in Fig. 7.2).

When speed is further increased, the response associated with the branch detached from

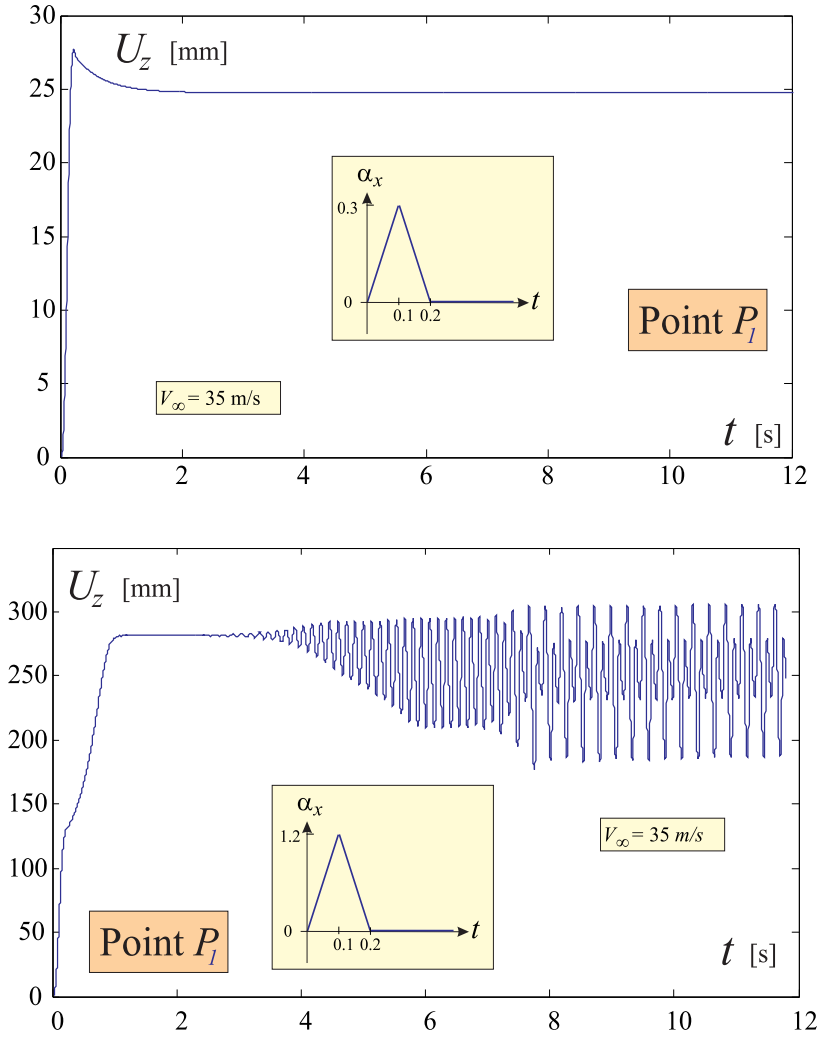

Fig. 7.40: Bi-stability region for $V_\infty = 35$ m/s. Either the stationary equilibrium points on branch I or the bi-cyclical closed orbit characterizing now branch II are approached after a transient

the period doubling bifurcation seems to have a chaotical response, as shown in Fig. 7.43. Even though in depth analyses are needed to confirm this conclusion, it has been noticed [86] that the period doubling bifurcation often triggers the transition to chaos; this has been found also in experimental studies, for example on electric circuits [110] and chemical reactions [61]. The bifurcation diagram shown in Fig.7.35 has been obtained, for what concerns solid and dashed lines representing stable and unstable fixed points, making use of the continuation capability of the nonlinear static tool (see Sec. 5.2). Considering for example Fig. 7.36, three distinct configurations sort out of the dynamic simulations. The first one corresponds

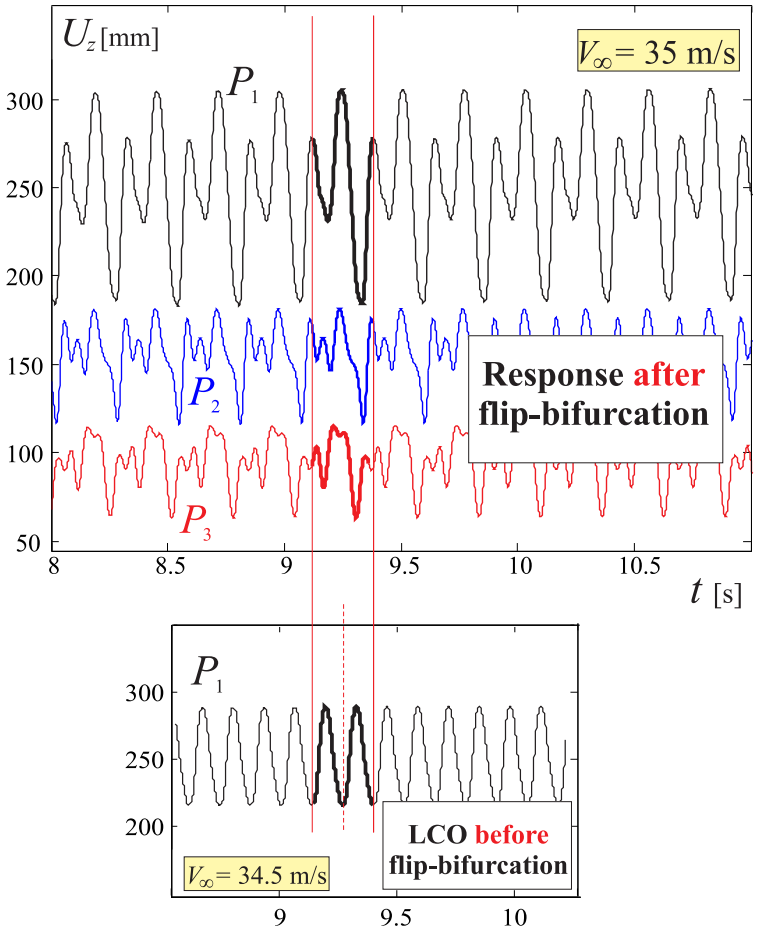

Fig. 7.41: Time responses for a speed higher than V^{fb}. They are compared to a subcritical one to assess the doubling of the period

to the undeformed condition; the other two, giving rise to branch I and II, can be considered starting points for a static analysis, in a reverse perspective if strategies employed in 7.3 are recalled.

In this way, starting for example from the two saddle nodes depicted in Fig.7.35 and increasing the load (that by mean of the *load level* parameter employed in this analysis has a straight relation with the velocity of the flow) it is possible to find the neighbours stationary points and so on to build the entire curve. Care, of course, has to be paid in the choice of the parameters governing arc-length scheme since the accuracy of the reproduced diagram mostly rely on the ability to track the effective behaviour of the system, which is not a trivial task considering its multistability nature.

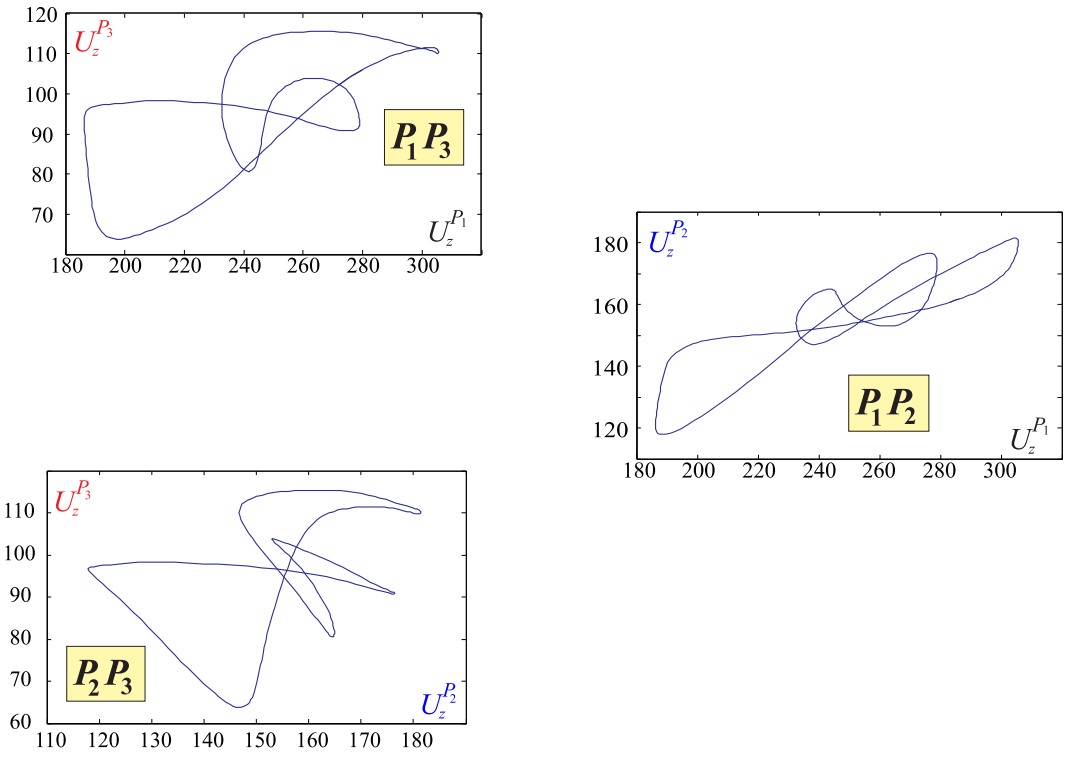

Fig. 7.42: State planes for points P_1, P_2, P_3. Differences in the response topology with respect to the one shown by a stable LCO orbit can be appreciated

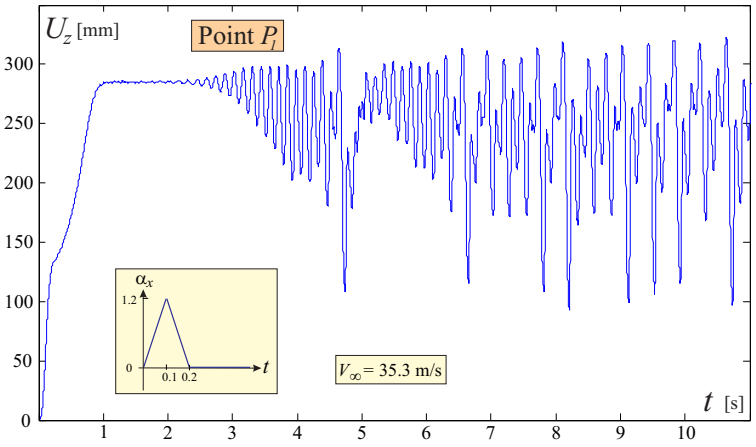

Fig. 7.43: Time response for $V_\infty = 35.3$ m/s when a vanishing perturbation in angle attack is given. No periodicity is shown

Chapter 8

Aerodynamic Tangent Matrix for the Unsteady Panel Method

In this section it is shown a methodology to obtain the aerodynamic tangent matrix, also called aerodynamic Jacobian, when an Unsteady Panel Method (UPM) is employed as aerodynamic solver. The role played by the aerodynamic tangent matrix in order to solve the dynamic equation with a Newton method has been pointed out in Sec. 2.2.3. The present effort is thought to provide a tool for future aeroelastic studies involving the UPM for analyses on wing box models.

8.1 Problem Statement

Recalling the definition of aerodynamic tangent matrix given in Sec. 2.2.3, it follows

$$\boldsymbol{K}_{\text{aero}} = \frac{\partial \boldsymbol{F}^S_{\text{aero}}}{\partial \boldsymbol{u}^S_{\text{g}}} \tag{8.1}$$

where $\boldsymbol{F}^S_{\text{aero}}$ represents the aerodynamic loads and $\boldsymbol{u}^S_{\text{g}}$ is the array with the global *generalized* displacements (translations and rotations) of the nodes obtained from the FE discretization. It is further assumed that the aerodynamic loads do not depend on the rotational degrees of freedom, thus the derivatives are just in respect to the translations $\boldsymbol{u}^S$. In Cap. 3 two methods to transfer the information from the aerodynamic to the structural mesh were presented, thus in the following $\boldsymbol{u}^S$ and $\boldsymbol{F}^S_{\text{aero}}$ can be substituted with $\boldsymbol{u}^A$ and $\boldsymbol{F}_{\text{aero}}$.
An explicit dependence of the external forces acting on the panels from the boundary displacements (vertices of the panels) is sought, in order to be able to perform the sought derivatives. This task can be pursued using the strategies of the sensitivity analysis employed in

the last decades in aerodynamic optimization, where the derivatives of aerodynamic quantities (like lift and drag, typically depending on both geometry and flow) with respect to some parametrization of the geometry are needed [60]. The concept of gradient-based optimization has similarities with the present goal: given a vector $\boldsymbol{I}$ of *objective functions* and a vector $\boldsymbol{v}$ of *design variables* which parametrize the problem, the aim is to evaluate $\frac{\partial \boldsymbol{I}}{\partial \boldsymbol{v}}$. The principle methods of sensitivity evaluation, apart from the obvious one consisting in the application of finite differences which though suffers of drawbacks on both the computational and accuracy point of view, can be divided into two broad categories [91] whose efficiency depend on the number of cost functions n_I and the number of variables n_v: *direct* and *adjoint* approach. It will be given here only a brief survey of the implicit gradient approach, which can be regarded as a simplified version of the *adjoint* approach [60].

Considering the flow about an aerodynamic body, the continuous governing equation R is a function of the flow-field variables (indicated as $\boldsymbol{w}$) and the physical location of the boundary (represented by the function $\boldsymbol{X}$)

$$R = R\left(\boldsymbol{w}, \boldsymbol{X}\right) = 0 \tag{8.2}$$

The properties that define the cost function depends as well on $\boldsymbol{w}$ and $\boldsymbol{X}$ such that

$$\boldsymbol{I} = \boldsymbol{I}\left(\boldsymbol{w}, \boldsymbol{X}\right) \tag{8.3}$$

Thus a change in the cost function $\boldsymbol{I}$ can be expressed as

$$\delta \boldsymbol{I} = \frac{\partial \boldsymbol{I}}{\partial \boldsymbol{w}} \delta \boldsymbol{w} + \frac{\partial \boldsymbol{I}}{\partial \boldsymbol{X}} \delta \boldsymbol{X} \tag{8.4}$$

A discrete approach is pursued, that is both the variables $\boldsymbol{w}$ and the shape $\boldsymbol{X}$ are defined in a finite number of points and so they have to be thought as arrays containing their values in the points arising from the discretization. The discrete governing equations of the flow field which express validity of eq.(8.2) in each node have in matrix form this expression

$$\boldsymbol{R} = \boldsymbol{R}\left(\boldsymbol{w}, \boldsymbol{X}\right) = \boldsymbol{0} \tag{8.5}$$

In order to eliminate $\delta \boldsymbol{w}$ from eq.(8.4), the governing equations of the flow field are used as constraints. From eq.(8.5) it holds

$$\delta \boldsymbol{R} = \frac{\partial \boldsymbol{R}}{\partial \boldsymbol{w}} \delta \boldsymbol{w} + \frac{\partial \boldsymbol{R}}{\partial \boldsymbol{X}} \delta \boldsymbol{X} = \boldsymbol{0} \tag{8.6}$$

which enables to determine $\delta \boldsymbol{w}$ and insert the result in eq.(8.4).

8.2 Application to the Unsteady Panel Method

This procedure can be followed to evaluate the aerodynamic tangent matrix, in the sense that though no optimization process is performed here, the aim is as well to evaluate derivatives of functions with respect to variables of the problem. $\boldsymbol{F}_{\text{aero}}$ can thus be interpreted as the cost function, while the boundary $\boldsymbol{X}$ is coincident with the design variables $\boldsymbol{u}^A$ (displacement of the vertices of the panels). For what concerns the flow-field variables, the governing equation for an unsteady panel method enforces the Dirichlet boundary condition of non penetration in the control points and have this expression

$$\boldsymbol{R} = \boldsymbol{A}^{BN} \cdot \boldsymbol{\mu} + \boldsymbol{A}^{W} \cdot \boldsymbol{\mu}^{W} - \boldsymbol{B} \cdot \boldsymbol{\sigma} = \boldsymbol{0} \tag{8.7}$$

where $\boldsymbol{\mu}$ represents the strength of doublets singularities, $\boldsymbol{A}^{BN}$ and $\boldsymbol{A}^{W}$ are the relative Aerodynamic Influence Coefficients matrices for the body-near wake and for the far wake respectively; $\boldsymbol{\sigma}$ represents the strength of sources singularities and $\boldsymbol{B}$ is the relative Aerodynamic Influence Coefficients matrix.

The unknown strength of the sources is known from the geometry (being related to the normal component of the free-stream) so the doublet strengths $\boldsymbol{\mu}$ it's a possible choice for the flow-field variables $\boldsymbol{w}$. Eq.(8.5) can thus be re-written as

$$\boldsymbol{R}\left(\boldsymbol{\mu}, \boldsymbol{u}^A\right) = \boldsymbol{0} \tag{8.8}$$

which enables to give a straight expression of eq.(8.6)

$$\begin{aligned} \delta\boldsymbol{R} =& \boldsymbol{A}^{BN}\delta\boldsymbol{\mu} + \boldsymbol{\mu}\frac{\partial \boldsymbol{A}^{BN}}{\partial \boldsymbol{u}^A}\delta\boldsymbol{u}^A + \boldsymbol{\mu}\frac{\partial \boldsymbol{A}^{W}}{\partial \boldsymbol{u}^A}\delta\boldsymbol{u}^A + \\ & -\boldsymbol{\sigma}\frac{\partial \boldsymbol{B}}{\partial \boldsymbol{u}^A}\delta\boldsymbol{u}^A - \boldsymbol{B}\frac{\partial \boldsymbol{\sigma}}{\partial \boldsymbol{u}^A}\delta\boldsymbol{u}^A = \boldsymbol{0} \end{aligned} \tag{8.9}$$

From eq.(8.9) can be then evaluated the term $\frac{\partial \boldsymbol{\mu}}{\partial \boldsymbol{u}^A}$ as follows

$$\frac{\partial \boldsymbol{\mu}}{\partial \boldsymbol{u}^A} = \left[\boldsymbol{A}^{BN}\right]^{-1}\left(\boldsymbol{\sigma}\frac{\partial \boldsymbol{B}}{\partial \boldsymbol{u}^A} + \boldsymbol{B}\frac{\partial \boldsymbol{\sigma}}{\partial \boldsymbol{u}^A} - \boldsymbol{\mu}\frac{\partial \boldsymbol{A}^{BN}}{\partial \boldsymbol{u}^A} - \boldsymbol{\mu}\frac{\partial \boldsymbol{A}^{W}}{\partial \boldsymbol{u}^A}\right) \tag{8.10}$$

Having in mind the aim to reduce as much as possible the computational cost of the entire procedure (since the evaluation of the tangent matrix will be probably required at each timestep of the dynamic simulation), it can be inferred that the last term is neglectable (as its physical meaning is the variation in the induction of a panel of the wake if a node in the body is perturbed) leading to the final expression for eq.(8.10)

$$\frac{\partial \boldsymbol{\mu}}{\partial \boldsymbol{u}^A} \simeq \left[\boldsymbol{A}^{BN}\right]^{-1}\left(\boldsymbol{\sigma}\frac{\partial \boldsymbol{B}}{\partial \boldsymbol{u}^A} + \boldsymbol{B}\cdot\frac{\partial \boldsymbol{\sigma}}{\partial \boldsymbol{u}^A} - \boldsymbol{\mu}\frac{\partial \boldsymbol{A}^{BN}}{\partial \boldsymbol{u}^A}\right) \tag{8.11}$$

The aerodynamic load $\boldsymbol{F}^j_{\text{aero}}$ acting over panel j can be written as

$$\boldsymbol{F}^j_{\text{aero}}\left(\boldsymbol{\mu}, \boldsymbol{u}^A\right) = p_j\left(\boldsymbol{\mu}\right) S_j\left(\boldsymbol{u}^A\right) \boldsymbol{n}_j\left(\boldsymbol{u}^A\right) \tag{8.12}$$

where p_j, S_j and $\boldsymbol{n}_j$ are respectively the pressure, the area and the normal vector of each panel j; the explicit dependence of the loads from the variables of the problem has been indicated. Eq.(8.4) specialized for this case leads to

$$\delta\boldsymbol{F}^j_{\text{aero}} = \left(\frac{\partial p_j}{\partial \mu_k} S_j \boldsymbol{n}_j\right)\delta\mu_k + \left(p_j \frac{\partial S_j}{\partial u_l}\boldsymbol{n}_j\right)\delta u^A_l + \left(p_j S_j \frac{\partial \boldsymbol{n}_j}{\partial u^A_l}\right)\delta u^A_l \tag{8.13}$$

where, using the results of eq.(8.11), the relation

$$\delta\mu_k = \frac{\partial \delta\mu_k}{\partial u^A_l}\delta u^A_l \tag{8.14}$$

can be employed. In this way the final expression for eq.(8.13) is

$$\delta\boldsymbol{F}^j_{\text{aero}} = \left(\frac{\partial p_j}{\partial \mu_k}\frac{\partial \mu_k}{\partial u^A_l} S_j \boldsymbol{n}_j\right)\delta u^A_l + \left(p_j \frac{\partial S_j}{\partial u_l}\boldsymbol{n}_j\right)\delta u^A_l + \left(p_j S_j \frac{\partial \boldsymbol{n}_j}{\partial u^A_l}\right)\delta u^A_l \tag{8.15}$$

8.3 Evaluation of the single terms

In order to give an operative form of the aerodynamic tangent matrix, the single terms in eq.(8.15) are stressed out. It consists of four main contributions: $\left(\frac{\partial \boldsymbol{\mu}}{\partial \boldsymbol{u}^A}\right)_{kl} = \frac{\partial \mu_k}{\partial u^A_l}$ which can be regarded as the sensitivity of doublet strength in respect to the boundary displacements; $\left(\frac{\partial \boldsymbol{p}}{\partial \boldsymbol{\mu}}\right)_{jk} = \frac{\partial p_j}{\partial \mu_k}$ which is the sensitivity of pressure in respect to doublet strength; $\left(\frac{\partial \boldsymbol{S}}{\partial \boldsymbol{u}^A}\right)_{kl} = \frac{\partial S_k}{\partial u^A_l}$ which is the variation of panel surface with respect to boundary displacements; $\left(\frac{\partial \boldsymbol{n}}{\partial \boldsymbol{u}^A}\right)_{kl,1} = \frac{\partial n^x_k}{\partial u^A_l}$, $\left(\frac{\partial \boldsymbol{n}}{\partial \boldsymbol{u}^A}\right)_{kl,2} = \frac{\partial n^y_k}{\partial u^A_l}$ and $\left(\frac{\partial \boldsymbol{n}}{\partial \boldsymbol{u}^A}\right)_{kl,3} = \frac{\partial n^z_k}{\partial u^A_l}$ which is the variation of the normal direction of the panel (in its three directions) with respect to boundary displacements.

8.3.1 Sensitivity of doublet strength in respect to displacements

The term $\frac{\partial \boldsymbol{\mu}}{\partial \boldsymbol{u}^A}$ is here investigated, recalling its definition from eq.(8.11). In reference [62] is provided a detailed treatise of the formulas that have to be used in order to evaluate the two involved influence matrices ($\boldsymbol{A}^{BN}$ and $\boldsymbol{B}$).

First the body-near wake Aerodynamic Influence Coefficients matrix $\boldsymbol{A}^{BN}$ is considered. The generic entry of this matrix C_{jk} represents the perturbation potential induced by the uniform unit doublet distribution on the panel k (*emitting panel*) over the control point

of panel j (*receiving panel*). The in-house panel method capability is organized such that the coordinates of the center of the receiving panel j (*receiving point*) are transformed from the global to the reference system local with the emitting panel k (which lies in a plane perpendicular to the local z-axis) in order to use the correct formulas for the induction (as the induction of a doublet depends on its orientation and so in this way formulas valid for a doublet aligned with the z-direction can be adopted). In Fig.8.1 is depicted the quadrilateral doublet element and the two previously defined reference systems: (X,Y,Z) is the global one (in which the perturbation $\delta\boldsymbol{u}^A$ is considered); (l,m,n) is the reference system local with the emitting panel. The coordinates of the 4 vertices of the emitting panel and of the center of

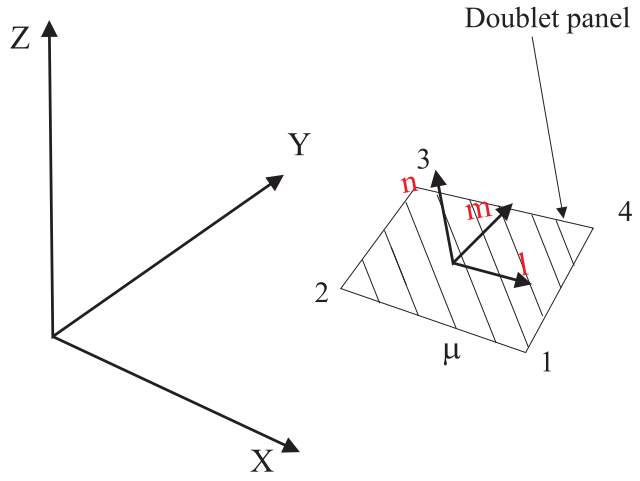

Fig. 8.1: Quadrilateral doublet element

the receiving panel, all expressed in the local reference (l,m,n), are indicated respectively with $(x_1,y_1,0)$, $(x_2,y_2,0)$, $(x_3,y_3,0)$, $(x_4,y_4,0)$ and (x,y,z). In this treatise, just the main equations are reported since the amount of mathematical relations involved in the whole procedure is quite big; the interested reader is referred to Appendix C for the complete list of equations and variables adopted in the algorithm.

The generic entry of the matrix $\boldsymbol{A}^{BN}$ can be evaluated applying the equation that gives the perturbation potential (for a unitary doublet strength)

$$\Phi^D = -\frac{1}{4\pi}\left\{ \tan^{-1}\left[\frac{zx_{21}(F_1r_2 - G_1r_1)}{z^2x_{21}^2r_1r_2 + F_1G_1}\right] + \tan^{-1}\left[\frac{zx_{32}(F_2r_3 - G_2r_2)}{z^2x_{32}^2r_2r_3 + F_2G_2}\right] \right.$$
$$\left. \tan^{-1}\left[\frac{zx_{43}(F_3r_4 - G_3r_3)}{z^2x_{43}^2r_3r_4 + F_3G_3}\right] + \tan^{-1}\left[\frac{zx_{14}(F_4r_1 - G_4r_4)}{z^2x_{14}^2r_4r_1 + F_4G_4}\right] \right\} \tag{8.16}$$

The constants involved in this calculation are reported in Appendix C. When $z \to 0$ and the receiving and emitting panel do not coincide $\Phi^D = \frac{1}{2}$, otherwise $\Phi^D = 0$.

For improved computational efficiency, when the receiving point is far from the center of the emitting panel, the influence of the quadrilateral element with area A can be approximated by a point doublet (far-field approximation)

$$\Phi^D = \frac{S}{4\pi} \frac{z}{\sqrt{(x^2+y^2+z^2)^3}} \tag{8.17}$$

The last contribution to this matrix comes from the near wake (the first row of wake panels shed from the trailing edge of the body). There is a relation between the doublet strength of the wake panel l ($\mu_{w,l}$) and the body surface doublet strengths at the trailing edge ($\mu_{Ute,l}$ and $\mu_{Lte,l}$ for the upper and lower correspondent trailing edge panels, respectively). Infact in order to satisfy the Kutta linear condition it has to be

$$\mu_{w,l} = \mu_{Ute,l} - \mu_{Lte,l} \tag{8.18}$$

Consequently the contribution of the panel l of the near wake to the boundary equation of element j can be written as

$$C_{jl}\mu_{w,l} = C_{jl}(\mu_{Ute,l} - \mu_{Lte,l}) \tag{8.19}$$

This means that in order to include this contribution within the strength of the doublets of the body (thus eliminating the strengths of the near wake doublets as unknowns of the problem), it's enough to express the influence of the panels of the first row of the wake on the generic j point in terms of the contribution of the two correspondent shedding panels at the trailing edge; this can be simply made modifying the influence term of the receiving point j when the emitting panel is on the trailing edge of the body. The final coefficients A^{BN}_{jk} of the matrix can thus be written as

$$\begin{aligned} A^{BN}_{jk} &= C_{jk} \text{ if panel k is not at the trailing edge} \\ A^{BN}_{jk} &= C_{jk} + C_{jl} \text{ if k = Ute,l} \\ A^{BN}_{jk} &= C_{jk} - C_{jl} \text{ if k = Lte,l} \end{aligned} \tag{8.20}$$

Now that the matrix $\boldsymbol{A}^{BN}$ has been completely defined, it's possible to evaluate the term $\frac{\partial \boldsymbol{A}^{BN}}{\partial \boldsymbol{u}}$ (apex A is omitted for clarity). The variation $\delta\boldsymbol{u}$ will produce two different effects depending if the perturbed vertex is thought as belonging to the receiving or the emitting panel.

The former case is first considered. If k is the ID of the panel where the perturbed vertex (that will have a global ID i while its local ID can just be 1,2,3 or 4 as illustrated in

Fig.8.1) is located, this first case consists in the building of row $\frac{\partial A^{BN}_{k,c}}{\partial u_i}$ with $c = 1, ..., N_{pan}$ where N_{pan} is the number of aerodynamic panels. Of course u_i is a vector since point i has three degrees of freedom which can be perturbed, i.e. there are $u_{i,x}$, $u_{i,y}$ and $u_{i,z}$; here $\frac{\partial}{\partial u_i}$ is used to stay more general and u_i has to be read as the displacement of point i in the selected direction. The generical term $\frac{\partial A^{BN}_{k,b}}{\partial u_i}$ (where b is the ID of the emitting panel) can be obtained considering eqs.(8.16) and (8.17). Since these relations are expressed in the local reference system, it's useful to consider first a perturbation of the 3 components of the receiving point which respectively leads to $(x,y,z) \rightarrow (x+\delta x,y,z)$, $(x,y,z) \rightarrow (x,y+\delta y,z)$, $(x,y,z) \rightarrow (x,y,z+\delta z)$. In case of validity of eq.(8.17), the derivatives of the perturbation velocity potential are easy to evaluate and are given by

$$\begin{aligned} \frac{\partial \Phi^D}{\partial x} &= -\frac{S}{4\pi}\frac{3zx}{d^5} \\ \frac{\partial \Phi^D}{\partial y} &= -\frac{S}{4\pi}\frac{3zy}{d^5} \\ \frac{\partial \Phi^D}{\partial z} &= \frac{S}{4\pi}\frac{d^2-3z^2}{d^5} \end{aligned} \tag{8.21}$$

where $d=\sqrt{x^2+y^2+z^2}$ is the distance between the centers of the two panels (the origin of the local reference coincides with the center of the emitting panel). The derivatives of eq.(8.16) with respect to the same variables are presented in Appendix C.
After the derivatives $\frac{\partial \Phi^D}{\partial x}, \frac{\partial \Phi^D}{\partial y}$ and $\frac{\partial \Phi^D}{\partial z}$ are evaluated, the term $\frac{\partial A^{BN}_{k,b}}{\partial u_i}$ can be obtained. In order to do that, it is first observed that $\frac{\partial}{\partial u_i}=\frac{\partial}{\partial s_i}$ where s_i is the coordinate of point i (i.e. it's identical to derive in respect to displacement or coordinate of the perturbed point); the evaluation of the derivative of the potential in respect of the displacement in global coordinate can be performed making use of the chain rule

$$\frac{\partial \Phi^D}{\partial u_i} = \frac{\partial \Phi^D}{\partial s_i} = \frac{1}{4}\left(\frac{\partial \Phi^D}{\partial x}\frac{\partial x}{\partial s_i} + \frac{\partial \Phi^D}{\partial y}\frac{\partial y}{\partial s_i} + \frac{\partial \Phi^D}{\partial z}\frac{\partial z}{\partial s_i}\right) \tag{8.22}$$

where everything is multiplied by $\frac{1}{4}$ because the receiving point is in the center of the panel (it's not coincident with the vertices being perturbed, which thus have an influence weighted by this factor). The terms $\frac{\partial x}{\partial s}$, $\frac{\partial y}{\partial s}$ and $\frac{\partial z}{\partial s}$ can be evaluated through the matrix $\boldsymbol{GL}^b$ which enables to shift the coordinates of the perturbed point i from the Global to the Local reference system of the emitting panel k. Defining $\boldsymbol{l},\boldsymbol{m},\boldsymbol{n}$ the unit vectors of this system, the following holds

$$\begin{bmatrix} x \\ y \\ z \end{bmatrix}^i = \begin{bmatrix} l_x & l_y & l_z \\ m_x & m_y & m_z \\ n_x & n_y & n_z \end{bmatrix}^k \begin{bmatrix} s_x \\ s_y \\ s_z \end{bmatrix}^i \tag{8.23}$$

Therefore, if for example it is performed the evaluation of the term $\frac{\partial A^{BN}_{k,b}}{\partial u_{20,x}}$ (point 20 belonging to panel k is perturbed in the direction x), from eq.(8.22) it follows

$$\frac{\partial A^{BN}_{k,b}}{\partial u_{20,x}} = \frac{1}{4}\left(\frac{\partial \Phi^D}{\partial x} l_x + \frac{\partial \Phi^D}{\partial y} m_x + \frac{\partial \Phi^D}{\partial z} n_x\right) \tag{8.24}$$

Of course other auxiliaries reference systems can be employed, as for example is the case for the in-house code, where body reference systems are contemplated for analyses involving more then a single body; in this cases if $\boldsymbol{l}$,$\boldsymbol{m}$,$\boldsymbol{n}$ describes the local reference system in the body frame (and not in the global one as previously assumed), $\boldsymbol{GL}^b$ has not the expression in eq.(8.23) since an additional transformation is needed to shift from the body reference to the global one. Therefore if body and global systems are not coincident, this difference must be contemplated.

Last effort to completely carry out this first case is due to the near wake; recalling eq.(8.20), when b is a trailing edge panel the term $\frac{\partial A^{BN}_{k,b}}{\partial u_i}$ has to contain two terms: the first, the standard one, due to variation of C_{kb}; the second one due to $\pm C_{kl}$ (+ or - depending on the upper or lower position of panel b) which can be obtained in the way just shown, of course considering now the induction of the wake panel l (and not of the body panel b) on point k.

Now it is considered the case of perturbed vertex belonging to the the emitting panel, that is the column $\frac{\partial A^{BN}_{c,k}}{\partial u_i}$ with $c = 1, ..., N_{pan}$ is built. The generical term b of $\frac{\partial A^{BN}_{b,k}}{\partial u_i}$ (where b is now the ID of the receiving panel) can be obtained always considering eqs.(8.16) and (8.17) but now the variation concerns one of the 4 vertices of the panel and thus the derivatives are made with respect to their coordinates. As an example, here is reported the case when eq.(8.17) is applicable

$$\begin{aligned}
\frac{\partial \Phi^D}{\partial x_1} &= \frac{\partial S}{\partial x_1}\frac{z}{4\pi d^3} \qquad & \frac{\partial \Phi^D}{\partial y_1} &= \frac{\partial S}{\partial y_1}\frac{z}{4\pi d^3} \\
\frac{\partial \Phi^D}{\partial x_2} &= \frac{\partial S}{\partial x_2}\frac{z}{4\pi d^3} \qquad & \frac{\partial \Phi^D}{\partial y_2} &= \frac{\partial S}{\partial y_2}\frac{z}{4\pi d^3} \\
\frac{\partial \Phi^D}{\partial x_3} &= \frac{\partial S}{\partial x_3}\frac{z}{4\pi d^3} \qquad & \frac{\partial \Phi^D}{\partial y_3} &= \frac{\partial S}{\partial y_3}\frac{z}{4\pi d^3} \\
\frac{\partial \Phi^D}{\partial x_4} &= \frac{\partial S}{\partial x_4}\frac{z}{4\pi d^3} \qquad & \frac{\partial \Phi^D}{\partial y_4} &= \frac{\partial S}{\partial y_4}\frac{z}{4\pi d^3}
\end{aligned}$$

Again the chain rule is applied to evaluate the derivative in respect to the global displacement; if for example the *local* ID of vertex i is 2, it reads

$$\frac{\partial \Phi^D}{\partial u_i} = \frac{\partial \Phi^D}{\partial x_2}\frac{\partial x_2}{\partial s_i} + \frac{\partial \Phi^D}{\partial y_2}\frac{\partial y_2}{\partial s_i} \tag{8.25}$$

where now the terms $\frac{\partial x_2}{\partial s_i}$ and $\frac{\partial y_2}{\partial s_i}$ can be evaluated through the matrix $\boldsymbol{GL}^k$ which enables to shift the coordinates of the perturbed vertex i from the Global to the Local reference system of the emitting panel k. Defining as before $\boldsymbol{l}$,$\boldsymbol{m}$,$\boldsymbol{n}$ the unit vectors of this system, the following holds

$$\begin{bmatrix} x_1 \\ y_1 \\ 0 \end{bmatrix}^i = \begin{bmatrix} l_x & l_y & l_z \\ m_x & m_y & m_z \\ n_x & n_y & n_z \end{bmatrix}^k \begin{bmatrix} s_x \\ s_y \\ s_z \end{bmatrix}^i \tag{8.26}$$

Therefore, when it is performed the evaluation of term $\frac{\partial A^{BN}_{b,k}}{\partial u_{6,z}}$ (point 6 is perturbed in the direction z), it's first necessary to define which is its local ID (in order to establish which of the local derivatives have to be considered); assuming point 6 is the local vertex 2 of panel k, the first contribution to this term can be expressed as

$$\frac{\partial A^{BN}_{b,6}}{\partial u_{6,z}} \leftarrow \frac{\partial \Phi^D}{\partial x_2} l_z + \frac{\partial \Phi^D}{\partial y_2} m_z \tag{8.27}$$

Eqs.(8.16) and (8.17) represent the influence of a doublet (distribution or point) with normal z in the reference system where the influence is evaluated; when the perturbation concerns the vertex of the emitting panel, as is the case now considered, the local system exhibits a change in its orientation (being the unit vectors $\boldsymbol{l}$ and $\boldsymbol{m}$ by their definition on the doublet plane). To take this into account, it can be noticed that the resulting effect is a change in the matrix $\boldsymbol{GL}^k$ which enables to shift the coordinates of the receiving point of panel b from the Global to the Local reference system of the inducing panel k, affecting the terms x, y and z in eqs.(8.16) and (8.17). Simplifying, in the relation

$$\begin{bmatrix} x \\ y \\ z \end{bmatrix}^b = \begin{bmatrix} l_x & l_y & l_z \\ m_x & m_y & m_z \\ n_x & n_y & n_z \end{bmatrix}^k \begin{bmatrix} s_x \\ s_y \\ s_z \end{bmatrix}^b \tag{8.28}$$

used to find the local coordinates $(x, y, z)^b$ of the receiving point from the global ones $(s_x, s_y, s_z)^b$, the unit vectors $\boldsymbol{l}$,$\boldsymbol{m}$,$\boldsymbol{n}$ have changed and so a further variation is exhibited by the term $A^{BN}_{b,k}$. This thus implies that there is a variation of the *local* position of the receiving point of panel b and so again the derivatives $\frac{\partial \Phi^D}{\partial x}$,$\frac{\partial \Phi^D}{\partial y}$ and $\frac{\partial \Phi^D}{\partial z}$ are performed. As before it holds

$$\frac{\partial \Phi^D}{\partial u_i} = \frac{\partial \Phi^D}{\partial s_i} = \frac{\partial \Phi^D}{\partial x}\frac{\partial x}{\partial s_i} + \frac{\partial \Phi^D}{\partial y}\frac{\partial y}{\partial s_i} + \frac{\partial \Phi^D}{\partial z}\frac{\partial z}{\partial s_i} \tag{8.29}$$

However now $\frac{\partial x}{\partial s_i}$, $\frac{\partial y}{\partial s_i}$ and $\frac{\partial z}{\partial s_i}$ have a different meaning: coordinates (x, y, z) are not changing because their global coordinates have been moved, but because the rotation matrix has

changed. To stress out these derivatives, eq.(8.28) is considered and the derivatives of the terms of the rotation matrix with respect to the global coordinate of the perturbed vertex is performed

$$\begin{aligned}\frac{\partial x}{\partial s_i} &= \frac{\partial l_x}{\partial s_i}s_x^b + \frac{\partial l_y}{\partial s_i}s_y^b + \frac{\partial l_z}{\partial s_i}s_z^b \\ \frac{\partial y}{\partial s_i} &= \frac{\partial m_x}{\partial s_i}s_x^b + \frac{\partial m_y}{\partial s_i}s_y^b + \frac{\partial m_z}{\partial s_i}s_z^b \\ \frac{\partial z}{\partial s_i} &= \frac{\partial n_x}{\partial s_i}s_x^b + \frac{\partial n_y}{\partial s_i}s_y^b + \frac{\partial n_z}{\partial s_i}s_z^b\end{aligned} \tag{8.30}$$

Moreover, in eq.(8.28) also the vector $(s_x, s_y, s_z)^b$ exhibits a changing. This happens since the local frame where the receiving point has to be projected has the origin in the center of the emitting panel; $(s_x, s_y, s_z)^b$ is then created subtracting the coordinates of the center of the emitting panel $\boldsymbol{P}^k$ to the coordinates of the receiving point $\boldsymbol{P}^b$

$$\boldsymbol{s}^b = \boldsymbol{P}^b - \boldsymbol{P}^k \tag{8.31}$$

A perturbation of a vertex of panel k surely affects the position of its center, i.e. the vector $\boldsymbol{P}^k$=(P_1^k,P_2^k,P_3^k), leading to

$$\frac{\partial P_j^k}{\partial s_i} = \frac{1}{4}\delta_{ij} \tag{8.32}$$

where δ_{ij} is the Kronecker delta. In eq.(8.32) it has been assumed that global and body reference coincides; if this is not true, eq.(8.32) it is valid for a perturbation of the vertices described in the body frame and the chain rule has to be used to express the derivatives with respect to global coordinates (this is not shown here to not further complicate the treatise). The final expression for the term $\frac{\partial A_{b,6}^{BN}}{\partial u_{6,z}}$ is then

$$\begin{aligned}\frac{\partial A_{b,6}^{BN}}{\partial u_{6,z}} =& \frac{\partial \Phi^D}{\partial x_2}l_z + \frac{\partial \Phi^D}{\partial y_2}m_z + \frac{\partial \Phi^D}{\partial x}\left(\frac{\partial l_x}{\partial s_{z,6}}s_x^b + \frac{\partial l_y}{\partial s_{z,6}}s_y^b + \frac{\partial l_z}{\partial s_{z,6}}s_z^b - \frac{1}{4}l_z\right) + \\ &+ \frac{\partial \Phi^D}{\partial y}\left(\frac{\partial m_x}{\partial s_{z,6}}s_x^b + \frac{\partial m_y}{\partial s_{z,6}}s_y^b + \frac{\partial m_z}{\partial s_{z,6}}s_z^b - \frac{1}{4}m_z\right) + \\ &+ \frac{\partial \Phi^D}{\partial z}\left(\frac{\partial n_x}{\partial s_{z,6}}s_x^b + \frac{\partial n_y}{\partial s_{z,6}}s_y^b + \frac{\partial n_z}{\partial s_{z,6}}s_z^b - \frac{1}{4}n_z\right)\end{aligned} \tag{8.33}$$

In Appendix can be found the derivatives involved in eq.(8.33). In this case the near-wake gives no contribution since as stated by eq.(8.20), the wake provides just an *inducing* coefficients, being not *induced* from the body's panels, thus its influence coefficient it is not affected if an emitting body panel changes its coordinates.

The algorithm shown to build $\frac{\partial \boldsymbol{A}^{BN}}{\partial \boldsymbol{u}}$ would lead to a three-dimensional array, because for each perturbed displacement u (again for each displacement, each direction has to be

separately considered), there is a square matrix $\frac{\partial \boldsymbol{A}^{BN}}{\partial u}$ with dimensions $N_{pan} \times N_{pan}$. Since in eq.(8.11) it is stated that the required quantity is $\frac{\partial \boldsymbol{A}^{BN}}{\partial \boldsymbol{u}}\boldsymbol{\mu}$ an not $\frac{\partial \boldsymbol{A}^{BN}}{\partial \boldsymbol{u}}$ itself, it is better for storage reasons to directly perform during the calculation the product $\frac{\partial \boldsymbol{A}^{BN}}{\partial \boldsymbol{u}}\boldsymbol{\mu}$ which leads, for each vertex perturbation, to a one dimensional array with N_{pan} elements. Calling again k the panel whose vertices are perturbed, when first case is examined (perturbed vertex belongs to the receiving panel) this consists in multiplying $\frac{\partial A^{BN}_{k,b}}{\partial u}\mu_b$ for each considered emitting panel b ; in the second case $\frac{\partial A^{BN}_{b,k}}{\partial u}\mu_k$ is evaluated, and so on for each perturbation δu.
$\frac{\partial \boldsymbol{A}^{BN}}{\partial \boldsymbol{u}} \cdot \boldsymbol{\mu}$ can thus finally be assembled leading to the required matrix $N_{pan} \times 3N_{vert}$ where N_{vert} is the number of vertices of the aerodynamic grid.

Now the Aerodynamic Influence Coefficients matrix $\boldsymbol{B}$ for the source distribution is considered. The generical entry of this matrix B_{jk} represents the perturbation potential influence coefficient for a constant unitary source distribution on the panel k (*emitting panel*) over the control point of panel j (*receiving panel*). In analogy with what said about source induction, the coordinates of the receiving point j are transformed from the global to the reference system local with the emitting panel k in order to correctly define the influence (as it will be shortly highlight, a part of the source induction is related to the doublet one and so it is recommended to express everything in the same frame). As a consequence, the same nomenclature is used to call the local frame and the points defined within it (Fig.8.1). The generical entry for the matrix $\boldsymbol{B}$ can be evaluated applying the equation that gives the perturbation potential Φ^S (for a unitary source strength)

$$\begin{aligned}\Phi^S = -\frac{1}{4\pi}\Bigg[&\frac{(x-x_1)y_{21}-(y-y_1)x_{21}}{d_{12}}\log\left(\frac{r_1+r_2+d_{12}}{r_1+r_2-d_{12}}\right)+\\ &+\frac{(x-x_2)y_{32}-(y-y_2)x_{32}}{d_{23}}\log\left(\frac{r_3+r_2+d_{23}}{r_3+r_2-d_{23}}\right)+\\ &+\frac{(x-x_3)y_{43}-(y-y_3)x_{43}}{d_{34}}\log\left(\frac{r_3+r_4+d_{34}}{r_3+r_4-d_{34}}\right)+\\ &+\frac{(x-x_4)y_{14}-(y-y_4)x_{14}}{d_{41}}\log\left(\frac{r_4+r_1+d_{41}}{r_4+r_1-d_{41}}\right)\Bigg]-z\Phi^D\end{aligned} \tag{8.34}$$

where Φ^D is the potential of a constant doublet distribution described in eq.(8.16). The far-field approximation, consisting in the approximation of a quadrilateral element with a point source, leads to

$$\Phi^S = \frac{S}{4\pi\sqrt{x^2+y^2+z^2}} \tag{8.35}$$

Having defined matrix $\boldsymbol{B}$, the evaluation of the term $\frac{\partial \boldsymbol{B}}{\partial \boldsymbol{u}}$ closely follows the steps used for

$\frac{\partial \boldsymbol{A}^{BN}}{\partial \boldsymbol{u}}$. The derivatives of the potential when the perturbed vertex belongs to the receiving panel are now given by (when eq.(8.35) is assumed valid)

$$\begin{aligned}
\frac{\partial \Phi^S}{\partial x} &= -\frac{S}{4\pi}\frac{(x-x_0)}{d^3} \\
\frac{\partial \Phi^S}{\partial y} &= -\frac{S}{4\pi}\frac{(y-y_0)}{d^3} \\
\frac{\partial \Phi^S}{\partial z} &= -\frac{S}{4\pi}\frac{z}{d^3}
\end{aligned} \tag{8.36}$$

while when the perturbed vertex belongs to the emitting panel it is

$$\begin{aligned}
\frac{\partial \Phi^S}{\partial x_1} &= \frac{\partial S}{\partial x_1}\frac{1}{4\pi d} & \frac{\partial \Phi^S}{\partial y_1} &= \frac{\partial S}{\partial y_1}\frac{1}{4\pi d} \\
\frac{\partial \Phi^S}{\partial x_2} &= \frac{\partial S}{\partial x_2}\frac{1}{4\pi d} & \frac{\partial \Phi^S}{\partial y_2} &= \frac{\partial S}{\partial y_2}\frac{1}{4\pi d} \\
\frac{\partial \Phi^S}{\partial x_3} &= \frac{\partial S}{\partial x_3}\frac{1}{4\pi d} & \frac{\partial \Phi^S}{\partial y_3} &= \frac{\partial S}{\partial y_3}\frac{1}{4\pi d} \\
\frac{\partial \Phi^S}{\partial x_4} &= \frac{\partial S}{\partial x_4}\frac{1}{4\pi d} & \frac{\partial \Phi^S}{\partial y_4} &= \frac{\partial S}{\partial y_4}\frac{1}{4\pi d}
\end{aligned} \tag{8.37}$$

The same algorithm performed for $\frac{\partial \boldsymbol{A}^{BN}}{\partial \boldsymbol{u}}\boldsymbol{\mu}$ finally leads to $\frac{\partial \boldsymbol{B}}{\partial \boldsymbol{u}}\boldsymbol{\sigma}$.

The last contribution to $\frac{\partial \boldsymbol{\mu}}{\partial \boldsymbol{u}}$, recalling eq.(8.11), is given by $\frac{\partial \boldsymbol{\sigma}}{\partial \boldsymbol{u}}$. By definition, the strength of the source of the general panel k, named σ_k, is given by

$$\sigma_k = -(\boldsymbol{V}_{wind} - \boldsymbol{V}_{trasc,k}) \cdot \boldsymbol{n}_k \tag{8.38}$$

In eq.(8.38) $\boldsymbol{V}_{wind}$ is the speed of the free stream, $\boldsymbol{V}_{trasc,k}$ is the speed of the control point of panel k due to the motion of the body q where it is located (for example a rotating blade) and is given by

$$\boldsymbol{V}_{trasc,k} = \boldsymbol{V}_{tr,q} + \boldsymbol{\Omega}_q \cdot \boldsymbol{s}_k \tag{8.39}$$

where $\boldsymbol{V}_{tr,q}$ and $\boldsymbol{\Omega}_q$ describe the motion of body q in the global reference system and $\boldsymbol{s}_k$ contains the global coordinates of the center of the panel; $\boldsymbol{n}_k$ is the unity vector normal to the panel, expressed now in the global reference system (to be consistent with the definition of $\boldsymbol{V}_{wind}$ and $\boldsymbol{V}_{trasc,k}$). When a vertex i of panel k is perturbed, two are the effects in terms of variation of σ_k: the normal direction changes, giving a contribution related to $\frac{\partial \boldsymbol{n}_k}{\partial u_i}$; it is different the position of the point where $\boldsymbol{V}_{trasc,k}$ is considered ($\boldsymbol{s}_k \rightarrow \boldsymbol{s}_k + \delta\boldsymbol{u}$).

The first contribution, named $\left(\frac{\partial \sigma_k}{\partial u_i}\right)_1$, is first considered; in Appendix C the derivatives of $\boldsymbol{n}$ with respect to the global coordinates of the panel have been performed in order to be

able to calculate eq.(8.33) and here they can be re-used, leading to

$$\left(\frac{\partial \sigma_k}{\partial u_i}\right)_1 = -(\boldsymbol{V}_{wind} - \boldsymbol{V}_{trasc,k}) \cdot \frac{\partial \boldsymbol{n}_k}{\partial u_i} = -(\boldsymbol{V}_{wind} - \boldsymbol{V}_{trasc,k}) \cdot \left(\boldsymbol{B}\boldsymbol{G}^q \cdot \frac{\partial \boldsymbol{n}_k}{\partial u_i}\right) \tag{8.40}$$

To show an example, it is assumed a variation of component y of vertex 15 of panel 10 (which belongs to body 1)

$$\begin{aligned}\frac{\partial \sigma_{10}}{\partial u_{15,y\,1}} =& -(\boldsymbol{V}_{wind,x} - \boldsymbol{V}_{trasc,x,10})\frac{\partial n_{10,x}}{\partial u_{15,y}} - (\boldsymbol{V}_{wind,y} - \boldsymbol{V}_{trasc,y,10})\frac{\partial n_{10,y}}{\partial u_{15,y}} + \\ &- (\boldsymbol{V}_{wind,z} - \boldsymbol{V}_{trasc,z,10})\frac{\partial n_{10,z}}{\partial u_{15,y}}\end{aligned} \tag{8.41}$$

and so on for all the other possible perturbations.

The second contribution, named $\left(\frac{\partial \sigma_k}{\partial u_i}\right)_2$, is now considered; from eq.(8.39) it can be inferred that

$$\frac{\partial \boldsymbol{V}_{trasc,k}}{\partial u_i} = \boldsymbol{\Omega}_q \cdot \frac{\partial \boldsymbol{s}_k}{\partial u_i} \tag{8.42}$$

$\boldsymbol{s}_k$ is the vector with the coordinates of the center of the panel ($s_{k,x}$,$s_{k,y}$,$s_{k,z}$); making use of eq.(8.32) to perform the derivatives of the coordinates of the center in respect to those of the vertices (which should be done using the chain rule if body and global frames don't coincide) and recalling eq.(8.38) it holds

$$\left(\frac{\partial \sigma_k}{\partial u_i}\right)_2 = \frac{\partial \boldsymbol{V}_{trasc,k}}{\partial u_i} \cdot \boldsymbol{n}_k \tag{8.43}$$

Finally the term $\frac{\partial \sigma_k}{\partial u_i}$ is computed

$$\frac{\partial \sigma_k}{\partial u_i} = \left(\frac{\partial \sigma_k}{\partial u_i}\right)_1 + \left(\frac{\partial \sigma_k}{\partial u_i}\right)_2 = -(\boldsymbol{V}_{wind} - \boldsymbol{V}_{trasc,k}) \cdot \frac{\partial \boldsymbol{n}_k}{\partial u_i} + \frac{\partial \boldsymbol{V}_{trasc,k}}{\partial u_i} \cdot \boldsymbol{n}_k \tag{8.44}$$

The algorithm employed to build $\frac{\partial \boldsymbol{\sigma}}{\partial \boldsymbol{u}}$ leads to a matrix $N_{pan} \times 3N_{vert}$ (each coordinate of each vertex has a column where the variation of the σ of the panel is put in its row); to avoid this expensive and useless storing passage, the final matrix $\boldsymbol{B}\frac{\partial \boldsymbol{\sigma}}{\partial \boldsymbol{u}}$ with dimensions $N_{pan} \times 3N_{vert}$ is directly built while the effect of perturbed vertex i on its panel k is investigated

$$\left(\boldsymbol{B} \cdot \frac{\partial \boldsymbol{\sigma}}{\partial \boldsymbol{u}}\right)_{ki} = \boldsymbol{B}_{kk}\frac{\partial \sigma_k}{\partial u_i} \tag{8.45}$$

8.3.2 Sensitivity of pressure in respect to doublet strength

The sensitivity of the pressure acting on the panel in respect to the doublet strength, indicated as $\frac{\partial \boldsymbol{p}}{\partial \boldsymbol{\mu}}$, is here investigated. The starting point is the Bernoulli theorem which enables to calculate the pressure when a potential flow is studied. In its general form, when an unsteady flow is considered, it states

$$k_\infty + \frac{1}{2}\rho V_\infty^2 = k + \frac{1}{2}\rho V^2 + \rho\frac{\partial \phi}{\partial t} \tag{8.46}$$

where ρ is the density of the flow (uniform for the hypothesis underlying this model), p_∞ and V_∞ are reference values of pressure and velocity (undisturbed flow), p and V are the local pressure and speed and ϕ is the perturbation velocity potential. The speed vector $\boldsymbol{V}$ can be expressed as

$$\boldsymbol{V} = \boldsymbol{V}_\infty + \boldsymbol{v} \tag{8.47}$$

where $\boldsymbol{V}_\infty$ is the free-stream (undisturbed) velocity and $\boldsymbol{v}$ is the perturbation velocity; therefore by definition of ϕ, $\boldsymbol{V}$ can also be expressed as

$$\boldsymbol{V} = \boldsymbol{V}_\infty + \nabla\phi \tag{8.48}$$

Eq.(8.46) can thus be rearranged in the following way

$$\begin{aligned} \Delta p = p - p_\infty =& -\frac{1}{2}\rho\left(|\nabla\phi + \boldsymbol{V}_\infty|\right)^2 + \frac{1}{2}\rho V_\infty^2 - \rho\frac{\partial\phi}{\partial t} \\ =& -\frac{1}{2}\rho|\nabla\phi|^2 - \rho\boldsymbol{V}_\infty\cdot\nabla\phi - \rho\frac{\partial\phi}{\partial t} \end{aligned} \tag{8.49}$$

In the collocation points (centers of the panel body), where eq.(8.49) is evaluated , it holds

$$\phi = \mu \tag{8.50}$$

Making use of this, the sought derivative can be written as

$$\begin{aligned} \frac{\partial \Delta p_k}{\partial \mu_i} =& -\frac{1}{2}\rho\frac{\partial|\nabla\phi_k|^2}{\partial\mu_i} - \rho\frac{\partial\left(\boldsymbol{V}_\infty\cdot\nabla\phi_k\right)}{\partial\mu_i} - \rho\frac{\partial\left(\frac{\partial\phi_k}{\partial t}\right)}{\partial\mu_i} \\ =& -\frac{1}{2}\rho\frac{\partial|\nabla\mu_k|^2}{\partial\mu_i} - \rho\frac{\partial\left(\boldsymbol{V}_\infty\cdot\nabla\mu_k\right)}{\partial\mu_i} - \rho\frac{\partial\left(\frac{\partial\mu_k}{\partial t}\right)}{\partial\mu_i} \\ =& -\rho\nabla\mu_k\cdot\frac{\partial\nabla\mu_k}{\partial\mu_i} - \rho\boldsymbol{V}_\infty\cdot\frac{\partial\nabla\mu_k}{\partial\mu_i} - \rho\frac{\partial\left(\frac{\partial\mu_k}{\partial t}\right)}{\partial\mu_i} \end{aligned} \tag{8.51}$$

From eq.(8.51) can be noticed that to evaluate the sensitivity it is enough to calculate $\frac{\partial\left(\frac{\partial\mu_k}{\partial t}\right)}{\partial\mu_i}$ and $\frac{\partial\nabla\mu_k}{\partial\mu_i}$.

The term $\frac{\partial\left(\frac{\partial \mu_k}{\partial t}\right)}{\partial \mu_i}$ can be performed making use for convenience of a first order finite difference scheme

$$\frac{\partial \mu_k}{\partial t} = \frac{\mu_k^T - \mu_k^{T-\Delta T}}{\Delta T} \tag{8.52}$$

leading to

$$\frac{\partial\left(\frac{\partial \mu_k}{\partial t}\right)}{\partial \mu_i} = \frac{1}{\Delta T}\delta_{ki} \tag{8.53}$$

The first contribute thus is non zero just when the variation concerns the doublet of the considered panel k (diagonal term). The term $\frac{\partial \nabla \mu_k}{\partial \mu_i}$ is constructed using a spatial finite difference scheme for

$$\nabla \mu_k = \left(\frac{\partial \mu_k}{\partial x}, \frac{\partial \mu_k}{\partial y}\right) \tag{8.54}$$

where the derivatives are performed with respect to the local reference system (that's why it doesn't appear the z derivative). In Appendix C the different schemes used are presented: they vary from a first to a second order, centered forward and backward, depending on the number of neighbours at disposal for the control point k. Here an example is reported for the centered second order scheme just to give an idea of the strategy; in Fig.(8.2) b,c,d,e are the neighbours of k along the two local directions.

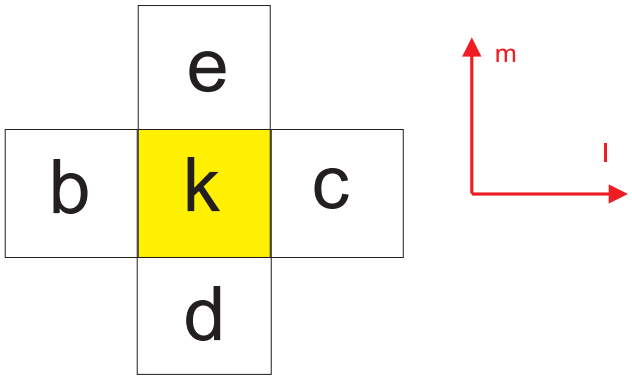

Fig. 8.2: Centered 2^{nd} order scheme for finite difference discretization of $\nabla \mu_k$

$$\begin{aligned}
\frac{\partial \mu_k}{\partial x} &= \left(\frac{\mu_c - \mu_k}{kc} kb + \frac{\mu_k - \mu_b}{kb} kc\right) \frac{1}{bc} \\
\frac{\partial \mu_k}{\partial y} &= \left(\frac{\mu_d - \mu_k}{kd} ek + \frac{\mu_k - \mu_e}{ek} kd\right) \frac{1}{de}
\end{aligned} \tag{8.55}$$

kc, kb, kc, ek, ce, bc are the distances among the correspondent panels. From eq.(8.55) it

follows

$$\begin{aligned}
\frac{\partial \nabla \mu_k}{\partial \mu_k} &= \left[\left(-\frac{kb}{kc}+\frac{kc}{kb}\right)\frac{1}{bc};\left(-\frac{ek}{kd}+\frac{kd}{ek}\right)\frac{1}{de}\right] \\
\frac{\partial \nabla \mu_k}{\partial \mu_b} &= \left[-\frac{kc}{kb}\frac{1}{bc};0\right] \\
\frac{\partial \nabla \mu_k}{\partial \mu_d} &= \left[\frac{kb}{kc}\frac{1}{bc};0\right] \\
\frac{\partial \nabla \mu_k}{\partial \mu_c} &= \left[0;\frac{ek}{kd}\frac{1}{de}\right] \\
\frac{\partial \nabla \mu_k}{\partial \mu_e} &= \left[0;-\frac{kd}{ek}\frac{1}{de}\right]
\end{aligned} \tag{8.56}$$

Eqs.(8.56) and (8.53) permits to calculate eq.(8.51), that is how varies the pressure on panel k when the intensity of the doublet i changes; in the most general case maximum 5 terms can influence the pressure, i.e. the square matrix $\frac{\partial \boldsymbol{p}}{\partial \boldsymbol{\mu}}$ with dimension $N_{pan} \times N_{pan}$ in its k-row can just have five non-zero terms. Depending on the number of neighbours, this number can reduce as other scheme than the one shown in Fig.(8.2) are employed.

8.3.3 Sensitivity of area in respect to displacements

The term $\frac{\partial \boldsymbol{S}}{\partial \boldsymbol{u}}$ represents the variation of the surface of panel when one of its vertices is moved. This contribution can easily be provided by calculations made previously to allow the definition of terms $\frac{\partial \boldsymbol{A}^{BN}}{\partial \boldsymbol{u}}$ and $\frac{\partial \boldsymbol{B}}{\partial \boldsymbol{u}}$. In fact, as explained in more detail in Appendix C, in the definition of the properties of the panel a mean plane is assumed (since the quadrilaterals are not planar in general); starting from the four corner points, the two diagonals $\boldsymbol{d}_1$ and $\boldsymbol{d}_2$ are first defined; the half modulus of their vector product (which leads to the normal vector $\boldsymbol{n}$) represents the area of the mean plane. Thus the derivatives of this modulus, just calculated to correctly asses the contributions related to the far-field approximation (eqs.(8.36) and (8.37) for example), are the sought sensitivities. Defining $\boldsymbol{N}_k$ the vector normal to panel k

$$\boldsymbol{N}_k = \boldsymbol{d}_{1,k} \times \boldsymbol{d}_{1,k}$$

it follows

$$\frac{\partial S_k}{\partial u_i} = \frac{1}{2}\frac{\partial |\boldsymbol{N}_k|}{\partial u_i} \tag{8.57}$$

8.3.4 Sensitivity of normal direction in respect to displacements

The term $\frac{\partial \boldsymbol{n}}{\partial \boldsymbol{u}}$ represents the variation in the direction of the unity vector $\boldsymbol{n}$ normal to the panel k when one of its vertices are moved. This contribution can be performed by calculations made previously to allow the definition of terms $\frac{\partial \boldsymbol{A}^{BN}}{\partial \boldsymbol{u}}$ and $\frac{\partial \boldsymbol{B}}{\partial \boldsymbol{u}}$ when the contribution due to the changing in the orientation of the plane following the doublet was considered eq.(8.30).

Chapter 9

Conclusions

In the present work nonlinear aeroelastic response of Joined-Wings has been investigated, with focus on the development of solvers for the detection of postcritical dynamic phenomena.

Tools employed ranged from pure aerodynamic, to static and dynamic, frequency-domain (flutter eigenvalues) and time-domain. The aerodynamic solver relied upon the hypothesis of potential flow, consistently with the considered conditions of small angles of attack, attached flow and subsonic speeds. For the structure was employed a geometrically nonlinear finite element based on the linear membrane constant strain triangle (CST) and the flat plate discrete Kirchoff triangle (DKT).
In order to keep the computational cost of the nonlinear analysis under practical limits, three different time-domain codes with increasing accuracy have been considered. In this way, an attempt to earn confidence in the basic aeroelastic features to retain was pursued. In particular different coupling algorithms (Infinite Plate Spline and Moving Least Square shape functions), way of distributing the aerodynamic singularities (on an undeformable reference plane or attached to the body during the deformation process) and wake modelization (rigid or free) were considered.

The main results gained by this work are here briefly summarized

- a dynamic characterization of the *snap-divergence* concept was achieved. Its occurrence was first found in a previous work and examinated by means of an aeroelastic static analysis. The question was then to assess its existence by mean of a dynamic study. Results showed that the static predictions were correct, and the characteristic *snap* was observed

- flutter analysis undergone with a linear frequency-domain tool was compared to a

nonlinear one, obtained as a sequence of linearizations performed about deformed configurations. It was found that the linear tools were giving nonconservative predictions. Discrepancies, ranging from 25% to 15%, were observed also for the less deformed configuration (Sensorcraft-like)

- the impact of different modelling of the aeroelastic problem on flutter speed was assessed for time-domain solvers. Comparisons with the above frequency-domain capability were also given. It was shown that solvers implementing different assumptions may lead to considerably different results.

- dynamic postcritical regime was explored and limit cycle oscillations were found. For some combinations of solvers and layouts, the response evolution to the LCO showed unusual trends: phase-space trajectories took time to resemble the final periodic orbit, being the transient relatively long. Moreover, for the Sensorcraft-like configuration, at certain speeds the LCO was showing within a period different patterns between the outer and inner parts of the wing system.

- the complex scenario arising from the aeroelastic response of a Joined-Wing became evident when different kind of perturbations were given to the system. Multistability and different bifurcations (stationary and relative to periodic orbits), along with transition to chaos, were detected.

When the use of the tools gave different results, a physical interpretation of the possible reasons was attempted. In particular the free-wake modelling proved to increase the flutter speed (at least for the configurations under examination) and this was put in relation with a redistribution of lift over the span which has stabilizing effect. Other differences in the prediction were harder to be motivated. For example the follower nature of the aerodynamic loads in *direction* (contemplated only in *Solver 2* and *Solver 3*) showed an influence on the detection of flutter speed. The updating at each timestep of the actual direction of the external load can be considered detrimental for the deformation of the structure (and results agreed with that), but this doesn't automatically lead to the conclusion that it has a decreasing effect on the prediction of the critical speed. In fact, especially for configurations behaving nonlinearly, the aeroelastic instability is a result of the redistribution of stiffness and thus the increase in the deformation (due to follower nature of forces) can be favourable in that sense.

A contribution that this study aims to give is also represented by the extended treatise of theory and implementation of the aeroelastic solvers. This has been accomplished

describing problems inherent to the time discretization of the dynamic equation and presenting in detail the aeroelastic coupling. For example emphasis has been placed on the different contributions giving rise to the aerodynamic unsteady forces and on the investigations of different interface algorithms, examining possible advantages and drawbacks of two significantly different approaches.

The investigations performed in this work merged in the article "Phenomenology of Nonlinear Aeroelastic Responses of Highly Deformable Joined-wings Configurations" presented at the 55th AIAA/ASMe/ASCE/AHS/SC Structures, Structural Dynamics, and Materials Conference at National Harbor, Maryland.

Future improvements can concern different aspects.

While here conceptual investigations on wind-tunnel-like models are pursued, analyses can be carried out within the same framework on *realistic* aircraft, i.e. inertial and stiffness distributions are assessed considering operative conditions, as well as sizing dimensions.

New sources of nonlinearity can be added to the system, as for example free-play of control surfaces. In literature it has been shown that this feature has a great influence in the aeroelastic response of the wing, leading to a big variety of ways the system can loose its stability.

The wing box can be employed instead of shells to model the structure; this would allow to use a panel method as aerodynamic code, which takes into account the influence of thickness in the evaluation of the pressure acting on the wing. In this perspective can be considered the evaluation of the aerodynamic tangent matrix described in Cap.8.

The aeroelastic problem can be generalized considering the flight dynamic ("free flying" configuration): the wing is no more clamped to the fuselage and the dynamic of the aircraft as a whole with its own degrees of freedom coupled with the deformation of the lifting surfaces is studied.

List of Figures

Appendices

Appendix A

Infinite Plate Spline Interface Algorithm

The mathematical procedure to establish the interface algorithm between aerodynamic and structural field using the Infinite Plate Spline method is reported in this section.

Considering a plate that extends to infinity in both directions, deforms just normal to its plane and has bending stiffness only, the governing equation is

$$D_{11}\frac{\partial^4 w}{\partial x^4} + 2\left(D_{12} + 2D_{66}\right)\frac{\partial^4 w}{\partial x^2 \partial y^2} + D_{22}\frac{\partial^4 w}{\partial y^4} = p \tag{A.1}$$

where p is the applied pressure. Assuming isotropic material, the following relations are valid:

$$\begin{aligned} D_{11} &= \frac{Eh^3}{12\left(1-\upsilon^2\right)} \\ D_{12} &= \upsilon D_{11} = \frac{\upsilon E h^3}{12\left(1-\upsilon^2\right)} \\ D_{22} &= D_{11} = \frac{Eh^3}{12\left(1-\upsilon^2\right)} \\ D_{66} &= \frac{1-\upsilon}{2} D_{11} = \frac{1-\upsilon}{2}\frac{Eh^3}{12\left(1-\upsilon^2\right)} \end{aligned} \tag{A.2}$$

Substituting these into eq.(A.1), it holds:

$$\frac{Eh^3}{12\left(1-\upsilon^2\right)}\left[\frac{\partial^4 w}{\partial x^4} + 2\frac{\partial^4 w}{\partial x^2 \partial y^2} + \frac{\partial^4 w}{\partial y^4}\right] = p \tag{A.3}$$

Calling $D = \frac{Eh^3}{12(1-\upsilon^2)}$ and assuming that there is a radial symmetry which means that only

derivatives with respect to r are not zero, eq.(A.3) assumes the form

$$D\frac{1}{r}\frac{\mathrm{d}}{\mathrm{d}r}\left(r\frac{\mathrm{d}}{\mathrm{d}r}\left[\frac{1}{r}\frac{\mathrm{d}}{\mathrm{d}r}\left(r\frac{\mathrm{d}w}{\mathrm{d}r}\right)\right]\right) = p \tag{A.4}$$

Dividing by D both sides of the equation, multiplying by r and separating the variables, eq.(A.4) becomes:

$$\mathrm{d}\left(r\frac{\mathrm{d}}{\mathrm{d}r}\left[\frac{1}{r}\frac{\mathrm{d}}{\mathrm{d}r}\left(r\frac{\mathrm{d}w}{\mathrm{d}r}\right)\right]\right) = \frac{rp\,\mathrm{d}r}{D} \tag{A.5}$$

As the purpose is to find the displacement field produced by the load applied in the generical structural node, a concentrated force P is considered in the origin ($r = 0$). Multiplying and dividing the right hand side of eq.(A.5) by 2π, it is:

$$\mathrm{d}\left(r\frac{\mathrm{d}}{\mathrm{d}r}\left[\frac{1}{r}\frac{\mathrm{d}}{\mathrm{d}r}\left(r\frac{\mathrm{d}w}{\mathrm{d}r}\right)\right]\right) = \frac{2\pi rp\,\mathrm{d}r}{2\pi D} \tag{A.6}$$

Actually there's no applied pressure p acting over the plate except for the presence of the concentrated load at $r = 0$, so if eq.(A.6) is integrated it can be inferred that the only non-zero contribution of the integral on the r.h.s. is very close to the origin and that

$$\lim_{\epsilon\to 0}\int_0^{\epsilon} 2\pi pr\,dr = P$$

with these arguments, it is possible to write

$$r\frac{\mathrm{d}}{\mathrm{d}r}\left[\frac{1}{r}\frac{\mathrm{d}}{\mathrm{d}r}\left(r\frac{\mathrm{d}w}{\mathrm{d}r}\right)\right] = \frac{P}{2\pi D} \tag{A.7}$$

Separating the variables and integrating, eq.(A.7) can be solved giving

$$w = \frac{P}{2\pi D}\left(\frac{1}{2}\left(\frac{1}{2}r^2\ln r - \frac{1}{4}r^2\right) - \frac{1}{8}r^2\right) + C_1\frac{r^2}{4} + C_2\ln r + C_3 \tag{A.8}$$

that with some algebra takes to:

$$w = \frac{P}{16\pi D}r^2\ln r^2 + \left(\frac{C_1}{4} - \frac{P}{8\pi D}\right)r^2 + C_2\ln r + C_3 \tag{A.9}$$

where C_1, C_2 and C_3 are arbitrary constants. In order to not have a singularity when $r \to 0$, the constant C_2 has to be zero. Defining $\left(\frac{C_1}{4} - \frac{P}{8\pi D}\right) = B$ and $C_3 = A$, eq.(A.9) becomes

$$w\,(r) = \frac{P}{16\pi D}r^2\ln r^2 + Br^2 + A \tag{A.10}$$

which express the displacement field of an infinite thin plate provoked by the concentrated load P; if N concentrated loads are applied, by the superimposition of eq.(A.10) it is possible to obtain the deflection as

$$w\left(x,y\right)=\sum_{i=1}^{N}\left(\frac{P_i}{16\pi D}r_i^2\ln r_i^2+B_i r_i^2+A_i\right) \tag{A.11}$$

where

$$r_i^2=\left(x-x_i\right)^2+\left(y-y_i\right)^2=x^2-2xx_i+x_i^2+y^2-2yy_i+y_i^2 \tag{A.12}$$

expresses the square distance between the point where the load is applied (x_i,y_i) and the point where the deflection is evaluated (x,y).

In order to avoid oscillations, the condition that at infinity the radial lines from loaded points appear to be straight lines is imposed. This requirement can be satisfied forcing all terms that go to infinity with higher order than the linear one to be zero. Eq.(A.11) can be written, posing $F_i=\frac{P_i}{16\pi D}$, as:

$$\begin{aligned}w=\sum_{i=1}^{N}\Big(&F_i\left[\left(x-x_i\right)^2+\left(y-y_i\right)^2\right]\ln\left[\left(x-x_i\right)^2+\left(y-y_i\right)^2\right]+\\&+B_i\left[\left(x-x_i\right)^2+\left(y-y_i\right)^2\right]+A_i\Big)\end{aligned} \tag{A.13}$$

that using polar coordinates ($x=r\cos\vartheta$, $y=r\sin\vartheta$), becomes:

$$\begin{aligned}w\left(r,\vartheta\right)=&\sum_{i=1}^{N}F_i r^2\ln\left[r^2-2r\left(x_i\cos\vartheta+y_i\sin\vartheta\right)+x_i^2+y_i^2\right]+\\&-\sum_{i=1}^{N}2rF_i\left(x_i\cos\vartheta+y_i\sin\vartheta\right)\ln\left[r^2-2r\left(x_i\cos\vartheta+y_i\sin\vartheta\right)+x_i^2+y_i^2\right]+\\&+\sum_{i=1}^{N}F_i\left(x_i^2+y_i^2\right)\ln\left[r^2-2r\left(x_i\cos\vartheta+y_i\sin\vartheta\right)+x_i^2+y_i^2\right]+\\&+\sum_{i=1}^{N}B_i\left[r^2-2r\left(x_i\cos\vartheta+y_i\sin\vartheta\right)+x_i^2+y_i^2\right]+\sum_{i=1}^{N}A_i\end{aligned} \tag{A.14}$$

To give an expression of the the displacement $w\left(r,\vartheta\right)$ for large values of r ($r\to\infty$), this observation is made

$$\ln\left(r^2-2r\left(x_i\cos\vartheta+y_i\sin\vartheta\right)+x_i^2+y_i^2\right)\approx\ln r^2-\frac{2}{r}\left(x_i\cos\vartheta+y_i\sin\vartheta\right)+\frac{x_i^2+y_i^2}{r^2} \tag{A.15}$$

which allows to conclude that, for large values of r, the displacement is

$$\begin{aligned} w(r,\vartheta) = r^2 \ln r^2 \sum_{i=1}^{N} F_i + r^2 \sum_{i=1}^{N} B_i - 2r \ln r^2 \sum_{i=1}^{N} F_i \left(x_i \cos\vartheta + y_i \sin\vartheta\right) + \\ + \ \ln r^2 \sum_{i=1}^{N} F_i \left(x_i^2 + y_i^2\right) - 2r \sum_{i=1}^{N} \left(x_i \cos\vartheta + y_i \sin\vartheta\right)\left(B_i + F_i\right) + ... \end{aligned} \tag{A.16}$$

The deletion of higher order terms (order $r^2 \ln r^2$, $r \ln r^2$ and r^2) than the linear one, in order to satisfy the earlier prescription of avoiding oscillations, is accomplished imposing that

$$\begin{aligned} \sum_{i=1}^{N} F_i &= 0 \\ \sum_{i=1}^{N} F_i x_i &= 0 \\ \sum_{i=1}^{N} F_i y_i &= 0 \\ \sum_{i=1}^{N} B_i &= 0 \end{aligned} \tag{A.17}$$

Finally an expression of eq.(A.13) which satisfy eq.(A.17) can be written as

$$\begin{aligned} w(x,y) = \sum_{i=1}^{N} \left[A_i + B_i \left(x_i^2 + y_i^2\right)\right] + x \left(-2 \sum_{i=1}^{N} B_i x_i\right) + \\ + y \left(-2 \sum_{i=1}^{N} B_i y_i\right) + \sum_{i=1}^{N} F_i r_i^2 \ln r_i^2 \end{aligned} \tag{A.18}$$

or

$$w(x,y) = a_0 + a_1 x + a_2 y + \sum_{i=1}^{N} F_i r_i^2 \ln r_i^2 \tag{A.19}$$

where these definitions have been given

$$\begin{aligned} a_0 &= \sum_{i=1}^{N} \left[A_i + B_i \left(x_i^2 + y_i^2\right)\right] \\ a_1 &= -2 \sum_{i=1}^{N} B_i x_i \\ a_2 &= -2 \sum_{i=1}^{N} B_i y_i \end{aligned} \tag{A.20}$$

Eq.(A.19) shows how using IPS it's possible to evaluate the displacement of a point along the normal direction to the local plane where it is lying, i.e. its $Z_{i\,\mathrm{loc}}$ coordinate, once its position through the local coordinates $x_{i\,\mathrm{loc}}$ and $y_{i\,\mathrm{loc}}$ is given and the coefficients in eq.(A.20) are evaluated. In order to provide a relation between the degrees of freedom of the structural nodes and their derivatives with the analogous aerodynamic quantities, eq.(A.19) can be applied to the i^{th} structural node

$$Z_{i\,\mathrm{loc}}\left(x_{i\,\mathrm{loc}}, y_{i\,\mathrm{loc}}\right) = a_0 + a_1 x_{i\,\mathrm{loc}} + a_2 y_{i\,\mathrm{loc}} + \sum_{j=1}^{N} F_j K_{ij} \tag{A.21}$$

where N is the number of *structural nodes* lying in the same plane of point i (consequently belonging to the same spline's plane) and the matrix $\boldsymbol{K}$ has been introduced, defined as

$$K_{ij} = \left(r_{ij\,\mathrm{loc}}\right)^2 \ln\left(r_{ij\,\mathrm{loc}}\right)^2 \tag{A.22}$$

with

$$\left(r_{ij\,\mathrm{loc}}\right)^2 = \left(x_{i\,\mathrm{loc}} - x_{j\,\mathrm{loc}}\right)^2 + \left(y_{i\,\mathrm{loc}} - y_{j\,\mathrm{loc}}\right)^2 \tag{A.23}$$

and

$$\left(r_{ij\,\mathrm{loc}}\right)^2 \ln\left(r_{ij\,\mathrm{loc}}\right)^2 = 0 \qquad \text{if } i = j \tag{A.24}$$

Remembering that the conditions in eq.(A.17) have to be satisfied, eq.(A.21) can be rewritten in matrix form in this way

$$\begin{bmatrix} 0 \\ 0 \\ 0 \\ Z_{1\,\mathrm{loc}} \\ Z_{2\,\mathrm{loc}} \\ Z_{3\,\mathrm{loc}} \\ \dots \\ Z_{N\,\mathrm{loc}} \end{bmatrix} = \begin{bmatrix} 0 & 0 & 0 & 1 & 1 & 1 & \dots & 1 \\ 0 & 0 & 0 & x_{1\,\mathrm{loc}} & x_{2\,\mathrm{loc}} & x_{3\,\mathrm{loc}} & \dots & x_{N\,\mathrm{loc}} \\ 0 & 0 & 0 & y_{1\,\mathrm{loc}} & y_{2\,\mathrm{loc}} & y_{3\,\mathrm{loc}} & \dots & y_{N\,\mathrm{loc}} \\ 1 & x_{1\,\mathrm{loc}} & y_{1\,\mathrm{loc}} & 0 & K_{12} & K_{13} & \dots & K_{1\,N} \\ 1 & x_{2\,\mathrm{loc}} & y_{2\,\mathrm{loc}} & K_{21} & 0 & K_{23} & \dots & K_{2\,N} \\ 1 & x_{3\,\mathrm{loc}} & y_{3\,\mathrm{loc}} & K_{31} & K_{32} & 0 & \dots & K_{3\,N} \\ \dots & \dots & \dots & \dots & \dots & \dots & \dots & \dots \\ 1 & x_{N\,\mathrm{loc}} & y_{N\,\mathrm{loc}} & K_{N1} & K_{N2} & K_{N3} & \dots & 0 \end{bmatrix} \begin{bmatrix} a_0 \\ a_1 \\ a_2 \\ F_1 \\ F_2 \\ F_3 \\ \dots \\ F_N \end{bmatrix} \tag{A.25}$$

Setting

$$\boldsymbol{Z}_{\mathrm{loc}} = \begin{bmatrix} 0 & 0 & 0 & Z_{1\,\mathrm{loc}} & Z_{2\,\mathrm{loc}} & Z_{3\,\mathrm{loc}} & \ldots & Z_{N\,\mathrm{loc}} \end{bmatrix}^T$$

$$\boldsymbol{F} = \begin{bmatrix} a_0 & a_1 & a_2 & F_1 & F_2 & F_3 & \ldots & F_N \end{bmatrix}^T$$

$$\boldsymbol{R} = \begin{bmatrix} 1 & 1 & 1 & \ldots & 1 \\ x_{1\,\mathrm{loc}} & x_{2\,\mathrm{loc}} & x_{3\,\mathrm{loc}} & \ldots & x_{N\,\mathrm{loc}} \\ y_{1\,\mathrm{loc}} & y_{2\,\mathrm{loc}} & y_{3\,\mathrm{loc}} & \ldots & y_{N\,\mathrm{loc}} \end{bmatrix} \qquad \boldsymbol{K} = \begin{bmatrix} 0 & K_{12} & K_{13} & \ldots & K_{1\,N} \\ K_{21} & 0 & K_{23} & \ldots & K_{2\,N} \\ K_{31} & K_{32} & 0 & \ldots & K_{3\,N} \\ \ldots & \ldots & \ldots & \ldots & \ldots \\ K_{N1} & K_{N2} & K_{N3} & \ldots & 0 \end{bmatrix} \tag{A.26}$$

Eq.(A.21) can be written as

$$\boldsymbol{Z}_{\mathrm{loc}} = \begin{bmatrix} \boldsymbol{0} & \boldsymbol{R} \\ \boldsymbol{R} & \boldsymbol{K} \end{bmatrix} \boldsymbol{F} \tag{A.27}$$

or, defining

$$\boldsymbol{G} = \begin{bmatrix} \boldsymbol{0} & \boldsymbol{R} \\ \boldsymbol{R} & \boldsymbol{K} \end{bmatrix} \tag{A.28}$$

as

$$\boldsymbol{Z}_{\mathrm{loc}} = \boldsymbol{G}\boldsymbol{F} \tag{A.29}$$

In eq.(A.29) $\boldsymbol{F}$ is the array of *fictitious* concentrated loads acting at the known set of points which enable to rebuild the deflection associated with the local vertical displacements stored in $\boldsymbol{Z}_{\mathrm{loc}}$. Since $\boldsymbol{G}$ is a known matrix once the set of points and the geometry has been fixed, eq.(A.29) can be advantageously used to get an expression of the unknown array with a matrix inversion

$$\boldsymbol{F} = \boldsymbol{G}^{-1}\boldsymbol{Z}_{\mathrm{loc}} \tag{A.30}$$

Now the coefficients that have to be used for the spline interpolation are known and eq.(A.19) can be used for whatever set of points. In order to avoid the time consuming task of updating the vector $\boldsymbol{F}$ at each timestep, the assumption that during the deformation process the original local coordinates $x_{i\,\mathrm{loc}}$ and $y_{i\,\mathrm{loc}}$ of the generical point i do not change has to be made, i.e. the vertical projection is always corresponding (or at least in good approximation) to the initial position of the structural point considered. If this hypothesis fail, $\boldsymbol{G}$ changes during the simulation and eq.(A.30) has to be continuously evaluated.

The expression of the aerodynamic loads is given starting from the boundary condition applied on the *control points* of the aerodynamic mesh; the involved quantities are thus related to the derivative of the vertical displacement $\frac{\mathrm{d}\mathcal{Z}_{\mathrm{loc}}}{\mathrm{d}x^S}$ with respect to the x^S axis (local x direction of the plate, assumed parallel to the free stream direction), the speed $\dot{\mathcal{Z}}_{\mathrm{loc}}$ and the acceleration $\ddot{\mathcal{Z}}_{\mathrm{loc}}$ of this set of points. In order to carry out this task, let at first indicate with $\mathcal{X}_{i\,\mathrm{loc}}$ and $\mathcal{Y}_{i\,\mathrm{loc}}$ the *local* coordinates of the i^{th} control point; the coordinate $\mathcal{Z}_{i\,\mathrm{loc}}$ of this point can be calculated using eq.(A.19)

$$\mathcal{Z}_{i\,\mathrm{loc}}\left(\mathcal{X}_{i\,\mathrm{loc}}, \mathcal{Y}_{i\,\mathrm{loc}}\right) = a_0 + a_1\mathcal{X}_{i\,\mathrm{loc}} + a_2\mathcal{Y}_{i\,\mathrm{loc}} + \sum_{j=1}^{N} F_j\mathcal{K}_{ij} \tag{A.31}$$

where N is always the number of structural nodes because these are the points where the *fictitious* concentrated forces are applied; on the other hand now it's used $\mathcal{K}_{ij}$ instead of K_{ij} in order to show that also the control points are involved in the calculation of such matrix, with

$$\mathcal{K}_{ij} = \left(\mathcal{R}_{ij\,\mathrm{loc}}\right)^2 \ln\left(\mathcal{R}_{ij\,\mathrm{loc}}\right)^2 \tag{A.32}$$

and

$$\begin{aligned} \left(\mathcal{R}_{ij\,\mathrm{loc}}\right)^2 &= \left(\mathcal{X}_{i\,\mathrm{loc}} - x_{j\,\mathrm{loc}}\right)^2 + \left(\mathcal{Y}_{i\,\mathrm{loc}} - y_{j\,\mathrm{loc}}\right)^2 \\ \left(\mathcal{R}_{ij\,\mathrm{loc}}\right)^2 &= 0 \qquad \text{if } i = j \end{aligned} \tag{A.33}$$

For eq.(A.31) a similar matrix representation of eq.(A.29) can be given, such that

$$\boldsymbol{\mathcal{Z}}_{\mathrm{loc}} = \boldsymbol{C}\boldsymbol{F} \tag{A.34}$$

where $\boldsymbol{C}$ has a similar expression of $\boldsymbol{G}$ but with the difference about $\mathcal{K}_{ij}$ just stressed out and $\boldsymbol{Z}_{\mathrm{loc}}$ is the array containing the local vertical displacements of control poins; substituting in it eq.(A.30), it is finally

$$\boldsymbol{\mathcal{Z}}_{\mathrm{loc}} = \boldsymbol{C}\boldsymbol{G}^{-1}\boldsymbol{Z}_{\mathrm{loc}} \tag{A.35}$$

that enables the transfer of the information about velocity and acceleration between structure and aerodynamic mesh, since for the fixed expression (earlier motivated) of the spline's matrices $\boldsymbol{G}$ and $\boldsymbol{C}$, it holds

$$\begin{aligned} \dot{\boldsymbol{\mathcal{Z}}}_{\mathrm{loc}} &= \boldsymbol{H}\dot{\boldsymbol{Z}}_{\mathrm{loc}} \\ \ddot{\boldsymbol{\mathcal{Z}}}_{\mathrm{loc}} &= \boldsymbol{H}\ddot{\boldsymbol{Z}}_{\mathrm{loc}} \end{aligned} \tag{A.36}$$

where $\boldsymbol{H} = \boldsymbol{C}\boldsymbol{G}^{-1}$ is the interface matrix for the displacement field.

In order to calculate the derivative of the vertical displacement is necessary to differentiate the spline equation specialized for the control points, shown in eq.(A.31), respect to x^S, that

is the generical term $\mathcal{K}_{ij}$ has to be derived with respect to the local x direction; in matrix form, it is

$$\begin{bmatrix} \dfrac{\mathrm{d}\mathcal{Z}_{1\,\mathrm{loc}}}{\mathrm{d}x^S} \\ \dfrac{\mathrm{d}\mathcal{Z}_{2\,\mathrm{loc}}}{\mathrm{d}x^S} \\ \dfrac{\mathrm{d}\mathcal{Z}_{3\,\mathrm{loc}}}{\mathrm{d}x^S} \\ \cdots \\ \dfrac{\mathrm{d}\mathcal{Z}_{N\mathrm{loc}}}{\mathrm{d}x^S} \end{bmatrix} = \begin{bmatrix} 0 & 1 & 0 & \dfrac{\mathrm{d}\mathcal{K}_{11}}{\mathrm{d}x^S} & \dfrac{\mathrm{d}\mathcal{K}_{12}}{\mathrm{d}x^S} & \dfrac{\mathrm{d}\mathcal{K}_{13}}{\mathrm{d}x^S} & \cdots & \dfrac{\mathrm{d}\mathcal{K}^S_{1\,N}}{\mathrm{d}x^S} \\ 0 & 1 & 0 & \dfrac{\mathrm{d}\mathcal{K}_{21}}{\mathrm{d}x^S} & \dfrac{\mathrm{d}\mathcal{K}_{22}}{\mathrm{d}x^S} & \dfrac{\mathrm{d}\mathcal{K}_{23}}{\mathrm{d}x^S} & \cdots & \dfrac{\mathrm{d}\mathcal{K}^S_{2\,N}}{\mathrm{d}x^S} \\ 0 & 1 & 0 & \dfrac{\mathrm{d}\mathcal{K}_{31}}{\mathrm{d}x^S} & \dfrac{\mathrm{d}\mathcal{K}_{32}}{\mathrm{d}x^S} & \dfrac{\mathrm{d}\mathcal{K}_{33}}{\mathrm{d}x^S} & \cdots & \dfrac{\mathrm{d}\mathcal{K}^S_{3\,N}}{\mathrm{d}x^S} \\ \cdots & \cdots & \cdots & \cdots & \cdots & \cdots & \cdots & \cdots \\ 0 & 1 & 0 & \dfrac{\mathrm{d}\mathcal{K}_{N1}}{\mathrm{d}x^S} & \dfrac{\mathrm{d}\mathcal{K}_{N2}}{\mathrm{d}x^S} & \dfrac{\mathrm{d}\mathcal{K}_{N3}}{\mathrm{d}x^S} & \cdots & \dfrac{\mathrm{d}\mathcal{K}_{NN}}{\mathrm{d}x^S} \end{bmatrix} \begin{bmatrix} a_0 \\ a_1 \\ a_2 \\ F_1 \\ F_2 \\ F_3 \\ \cdots \\ F_{N_n} \end{bmatrix} \tag{A.37}$$

Using eqs.(A.32) and (A.33) it holds

$$\mathcal{K}_{ij} = \left[(\mathcal{X}_{i\,\mathrm{loc}} - x_{j\,\mathrm{loc}})^2 + (\mathcal{Y}_{i\,\mathrm{loc}} - y_{j\,\mathrm{loc}})^2\right] \ln\left[(\mathcal{X}_{i\,\mathrm{loc}} - x_{j\,\mathrm{loc}})^2 + (\mathcal{Y}_{i\,\mathrm{loc}} - y_{j\,\mathrm{loc}})^2\right] \tag{A.38}$$

Differentiating the previous relation (this operation has to be done replacing the coordinates $\mathcal{X}_{i\,\mathrm{loc}}$ and $\mathcal{Y}_{i\,\mathrm{loc}}$ with the generic coordinates x^S and y^S and differentiating with respect to x^S) and calculating the derivatives in the local coordinates of the i^{th} control point, the generical term of eq.(A.37) is as follows:

$$\frac{\mathrm{d}\mathcal{K}_{ij}}{\mathrm{d}x^S} = 2\,(\mathcal{X}_{i\,\mathrm{loc}} - x_{j\,\mathrm{loc}})\left\{\ln\left[(\mathcal{X}_{i\,\mathrm{loc}} - x_{j\,\mathrm{loc}})^2 + (\mathcal{Y}_{i\,\mathrm{loc}} - y_{j\,\mathrm{loc}})^2\right] + 1\right\} \tag{A.39}$$

or

$$\frac{\mathrm{d}\mathcal{K}_{ij}}{\mathrm{d}x^S} = 2\,(\mathcal{X}_{i\,\mathrm{loc}} - x_{j\,\mathrm{loc}})\left[\ln(\mathcal{R}_{ij\,\mathrm{loc}})^2 + 1\right] \tag{A.40}$$

where if the j^{th} structural point is exactly coincident with the i^{th} control point then $\dfrac{\mathrm{d}\mathcal{K}_{ij}}{\mathrm{d}x^S} = 0$.

Finally, a relation similar to eq.(A.34) is obtained

$$\frac{\mathrm{d}\boldsymbol{\mathcal{Z}}_{\mathrm{loc}}}{\mathrm{d}x^S} = \boldsymbol{\mathcal{D}}\boldsymbol{F} \tag{A.41}$$

which finally takes to the relation sought

$$\frac{\mathrm{d}\boldsymbol{\mathcal{Z}}_{\mathrm{loc}}}{\mathrm{d}x^S} = \boldsymbol{H}^D\boldsymbol{Z}_{\mathrm{loc}} \tag{A.42}$$

where $\boldsymbol{H}^D = \boldsymbol{D}\boldsymbol{G}^{-1}$ is the interface matrix for the spatial derivative displacement field.

Once the rotation matrices are built to shift from the local reference system of the spline to the global coordinate system (this choice can be performed considering the wing as piecewise-planar and assuming a local reference for every section that has a different normal), eqs.(A.36) and (A.42) allow to completely define the aerodynamic loads providing the sought interface matrices.

The last step to completely define the present interface algorithm for the aerodynamic-structural coupling is the transfer of the aerodynamic load applied in the aerodynamic mesh (load point) to the structural nodes. After each load point has been associated with a structural element through an algorithm that can determine whether a point (the load point in this case) is inside a triangle or not, the goal is to find the nodal forces equivalent to the given concentrated load applied in an internal point P, as depicted in Fig.A.1. The problem

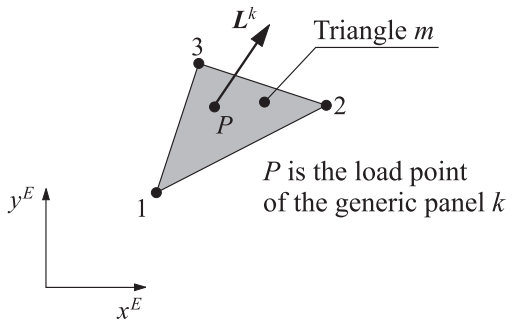

Fig. A.1: Applied load in a triangular element

can be solved imposing that the work done by the external force is equal to the work done by the nodal forces of the element. In order to do that it's necessary to express the displacement in the point where the load is applied as a combination of the nodal displacements, i.e. some shape functions have to be chosen. A reference coordinate system is adopted, such that the axes x^E and y^E are on the plane of the element and the axis z^E is perpendicular to it. The shape functions relative to the nodes 1,2 and 3 of the triangle m are indicated respectively as $h_1^m\left(x^E, y^E\right)$, $h_2^m\left(x^E, y^E\right)$ and $h_3^m\left(x^E, y^E\right)$. By definition of shape functions, the virtual displacement at point $P\left(x_P^E, y_P^E\right)$ can be calculated as combination of the above shape functions:

$$\begin{aligned}
\delta u_P &= h_1^m\left(x_P^E, y_P^E\right)\delta u_1 + h_2^m\left(x_P^E, y_P^E\right)\delta u_2 + h_3^m\left(x_P^E, y_P^E\right)\delta u_3 \\
\delta v_P &= h_1^m\left(x_P^E, y_P^E\right)\delta v_1 + h_2^m\left(x_P^E, y_P^E\right)\delta v_2 + h_3^m\left(x_P^E, y_P^E\right)\delta v_3 \\
\delta w_P &= h_1^m\left(x_P^E, y_P^E\right)\delta w_1 + h_2^m\left(x_P^E, y_P^E\right)\delta w_2 + h_3^m\left(x_P^E, y_P^E\right)\delta w_3
\end{aligned} \tag{A.43}$$

Imposing that the work done by the external force is the same as the work done by the nodal forces, it can be written that

$$\begin{aligned} L^k_{x^E}\delta u_P &= L^m_{1\,x^E}\delta u_1 + L^m_{2\,x^E}\delta u_2 + L^m_{3\,x^E}\delta u_3 \\ L^k_{y^E}\delta v_P &= L^m_{1\,y^E}\delta v_1 + L^m_{2\,y^E}\delta v_2 + L^m_{3\,y^E}\delta v_3 \\ L^k_{z^E}\delta w_P &= L^m_{1\,z^E}\delta w_1 + L^m_{2\,z^E}\delta w_2 + L^m_{3\,z^E}\delta w_3 \end{aligned} \tag{A.44}$$

where $L^k_{x^E}$, $L^k_{y^E}$ and $L^k_{z^E}$ are the components (in the coordinate system represented by x^E, y^E and z^E) of the vector $\boldsymbol{L}^k$ with the force acting on the load point k, while $L^m_{1\,x^E}$, $L^m_{1\,y^E}$ and $L^m_{1\,z^E}$ are the components of the nodal force relative to the node 1 of the element m and so forth. From eq.(A.44) it can be deduced for the node 1, using eq.(A.43), that

$$\begin{bmatrix} L^m_{1\,x^E} \\ L^m_{1\,y^E} \\ L^m_{1\,z^E} \end{bmatrix} = h^m_1\left(x^E_P, y^E_P\right) \cdot \begin{bmatrix} L^k_{x^E} \\ L^k_{y^E} \\ L^k_{z^E} \end{bmatrix} \tag{A.45}$$

and similarly, for nodes 2 and 3:

$$\begin{bmatrix} L^m_{2\,x^E} \\ L^m_{2\,y^E} \\ L^m_{2\,z^E} \end{bmatrix} = h^m_2\left(x^E_P, y^E_P\right) \cdot \begin{bmatrix} L^k_{x^E} \\ L^k_{y^E} \\ L^k_{z^E} \end{bmatrix} \qquad \begin{bmatrix} L^m_{3\,x^E} \\ L^m_{3\,y^E} \\ L^m_{3\,z^E} \end{bmatrix} = h^m_3\left(x^E_P, y^E_P\right) \cdot \begin{bmatrix} L^k_{x^E} \\ L^k_{y^E} \\ L^k_{z^E} \end{bmatrix} \tag{A.46}$$

It can be demonstrated [9] that the area coordinates defined by the triangle m and the load point k allow to define the coefficients of the shape functions for a constant strain triangle, and so it holds

$$\begin{aligned} h^m_1\left(x^E, y^E\right) &= \tfrac{1}{2S}\left(a_1 + b_1 x^E + c_1 y^E\right) \\ h^m_2\left(x^E, y^E\right) &= \tfrac{1}{2S}\left(a_2 + b_2 x^E + c_2 y^E\right) \\ h^m_3\left(x^E, y^E\right) &= \tfrac{1}{2S}\left(a_3 + b_1 x^E + c_3 y^E\right) \end{aligned} \tag{A.47}$$

where

$$\begin{aligned} 2S &= x^E_1 y^E_2 + x^E_2 y^E_3 + x^E_3 y^E_1 - y^E_1 x^E_2 - y^E_2 x^E_3 - y^E_3 x^E_1 \\ a_1 &= x^E_2 y^E_3 - x^E_3 y^E_2 \qquad b_1 = y^E_2 - y^E_3 \qquad c_1 = x^E_3 - x^E_2 \\ a_2 &= x^E_3 y^E_1 - x^E_1 y^E_3 \qquad b_2 = y^E_3 - y^E_1 \qquad c_2 = x^E_1 - x^E_3 \\ a_3 &= x^E_1 y^E_2 - x^E_2 y^E_1 \qquad b_3 = y^E_1 - y^E_2 \qquad c_3 = x^E_2 - x^E_1 \end{aligned} \tag{A.48}$$

Including this choice in eqs.(A.45) and (A.46) it can be seen that the translational and rotational equilibriums on the element are satisfied, and so the load equivalence is obtained. The sought result is summarized in a vectorial form

$$\begin{aligned} \boldsymbol{L}_1^m &= h_1^m \left(x_P^E, y_P^E\right) \boldsymbol{L}^k \\ \boldsymbol{L}_2^m &= h_2^m \left(x_P^E, y_P^E\right) \boldsymbol{L}^k \\ \boldsymbol{L}_3^m &= h_3^m \left(x_P^E, y_P^E\right) \boldsymbol{L}^k \end{aligned} \tag{A.49}$$

which show how the transfer of the load from load points to the vertices of the triangle considered can be easily performed.

Appendix B

Moving Least Square (Meshless) Interface Algorithm

The procedure of constructing shape functions using Moving Least Square approximation and the way to apply them in order to obtain the coupling between aerodynamic and structural field with the desired properties is here presented.

The values of the function $\hat{u}(\boldsymbol{x})$ on a set of nodes $\{\boldsymbol{\eta}_1, \boldsymbol{\eta}_2, ..., \boldsymbol{\eta}_{\hat{n}}\}$ are obtained from its values $\hat{u}(\boldsymbol{\xi}_1)$,$\hat{u}(\boldsymbol{\xi}_2)$,...,$\hat{u}(\boldsymbol{\xi}_{\hat{n}})$ on scattered centers (or sources) $\{\boldsymbol{\xi}_1, \boldsymbol{\xi}_2, ..., \boldsymbol{\xi}_{\hat{n}}\}$ without deriving an analytical expression. This extrapolation is denoted by $\hat{u}^h(\boldsymbol{\eta})$ and is built as a sum of $\hat{m}$ basis functions $\hat{p}_i(\boldsymbol{\eta})$

$$\hat{u}^h(\boldsymbol{\eta}) = \sum_{i=1}^{\hat{m}} \hat{p}_i(\boldsymbol{\eta})\, a_i^{\boldsymbol{\xi}}(\boldsymbol{\eta}) = \hat{\boldsymbol{p}}(\boldsymbol{\eta}) \cdot \boldsymbol{a}^{\boldsymbol{\xi}}(\boldsymbol{\eta}) \tag{B.1}$$

where a_i are the unknown coefficients of the basis functions which depend on the point $\boldsymbol{\eta}$ where the value is sought; the vector $\hat{\boldsymbol{p}}$ of basis functions consists often of monomials of the lowest order such to form polynomial basis with minimum completeness but particular functions can be added to reproduce a particular behaviour of the variables investigated. In the present study linear and quadratic polynomials are adopted:

$$\begin{aligned} \hat{\boldsymbol{p}} &= \{1, x, y, z\} \\ \hat{\boldsymbol{p}} &= \{1, x, y, z, x^2, xy, y^2, yz, z^2, zx\} \end{aligned} \tag{B.2}$$

The $\hat{m}$ coefficients a_i describing (as shown in eq.(B.1)) the function in the point $\boldsymbol{\eta}$ are obtained minimizing the weighted residual functional (a weighted discrete L_2 norm) $J(\boldsymbol{\eta})$

$$J(\boldsymbol{\eta}) = \sum_{i=1}^{\hat{n}} W(\boldsymbol{\eta} - \boldsymbol{\xi}_i)\, [\tilde{u}(\boldsymbol{\xi}_i, \boldsymbol{\eta}) - \hat{u}(\boldsymbol{\xi}_i)]^2 \tag{B.3}$$

where

$$\tilde{u}(\boldsymbol{\xi}_i, \boldsymbol{\eta}) = \hat{\boldsymbol{p}}(\boldsymbol{\xi}_i) \cdot \boldsymbol{a}(\boldsymbol{\eta}) \tag{B.4}$$

is the approximated value of the the field function in the generical center of the set $\boldsymbol{\xi}$ obtained by means of the same extrapolation process pointed out in eq.(B.1). A useful matrix form of eq.(B.3) can be given as follow:

$$J(\boldsymbol{\eta}) = (\hat{\boldsymbol{P}}\,\boldsymbol{a}(\boldsymbol{\eta}) - \hat{\boldsymbol{u}}) \cdot \Big(\boldsymbol{W}\,(\hat{\boldsymbol{P}}\,\boldsymbol{a}(\boldsymbol{\eta}) - \hat{\boldsymbol{u}}) \Big) \tag{B.5}$$

where the following vectors and matrices are introduced:

$$\hat{\boldsymbol{u}} = \{\hat{u}(\boldsymbol{\xi}_1), \hat{u}(\boldsymbol{\xi}_2), ..., \hat{u}(\boldsymbol{\xi}_{\hat{n}})\}$$

$$\hat{\boldsymbol{P}} = \begin{bmatrix} \hat{p}_1(\boldsymbol{\xi}_1) & \hat{p}_2(\boldsymbol{\xi}_1) & ... & \hat{p}_{\hat{m}}(\boldsymbol{\xi}_1) \\ \hat{p}_1(\boldsymbol{\xi}_2) & \hat{p}_2(\boldsymbol{\xi}_2) & ... & \hat{p}_{\hat{m}}(\boldsymbol{\xi}_2) \\ ... & ... & ... & ... \\ \hat{p}_1(\boldsymbol{\xi}_{\hat{n}}) & \hat{p}_2(\boldsymbol{\xi}_{\hat{n}}) & ... & \hat{p}_{\hat{m}}(\boldsymbol{\xi}_{\hat{n}}) \end{bmatrix} \tag{B.6}$$

$$\boldsymbol{W} = \begin{bmatrix} W(\boldsymbol{\eta} - \boldsymbol{\xi}_1) & 0 & ... & 0 \\ 0 & W(\boldsymbol{\eta} - \boldsymbol{\xi}_2) & ... & 0 \\ ... & ... & ... & ... \\ 0 & 0 & ... & W(\boldsymbol{\eta} - \boldsymbol{\xi}_{\hat{n}})) \end{bmatrix} \tag{B.7}$$

Solving the minimization problem

$$\frac{\partial J(\boldsymbol{\eta})}{\partial \boldsymbol{a}} = \boldsymbol{0} \tag{B.8}$$

an expression for the coefficient vector $\boldsymbol{a}(\boldsymbol{\eta})$ is obtained

$$\boldsymbol{a}(\boldsymbol{\eta}) = \hat{\boldsymbol{A}}^{-1} \hat{\boldsymbol{B}}\,\hat{\boldsymbol{u}} \tag{B.9}$$

where $\hat{\boldsymbol{A}}$ is called the *moment matrix* and is given by

$$\hat{\boldsymbol{A}} = \hat{\boldsymbol{P}}^T\,\boldsymbol{W}\,\hat{\boldsymbol{P}} \tag{B.10}$$

and $\hat{\boldsymbol{B}}$ is given by

$$\hat{\boldsymbol{B}} = \hat{\boldsymbol{P}}^T\,\boldsymbol{W} \tag{B.11}$$

It is now possible to give a definitive expression of eq.(B.1) as:

$$\hat{u}^h(\boldsymbol{\eta}) = \sum_{i=1}^{\hat{n}} \Phi_i(\boldsymbol{\eta})\,\hat{u}_i \tag{B.12}$$

where $\Phi_i(\boldsymbol{\eta})$ is the coefficient of the MLS shape function of node $\boldsymbol{\eta}$ corresponding to the center i, which is given by

$$\Phi_i(\boldsymbol{\eta}) = \sum_{j=1}^{\hat{m}} \hat{p}_j(\boldsymbol{\eta}) \left[\hat{\boldsymbol{A}}^{-1}\hat{\boldsymbol{B}}\right]_{ji} \tag{B.13}$$

Eq.(B.12) can also be written in the following matrix form, suitable for applications to the aeroelastic model

$$\hat{u}^h(\boldsymbol{\eta}) = \boldsymbol{\Phi}(\boldsymbol{\eta}) \cdot \hat{\boldsymbol{u}} \tag{B.14}$$

where $\boldsymbol{\Phi}(\boldsymbol{\eta})$ is the array containing the coefficients of the MLS shape function of node $\boldsymbol{\eta}$.

The Radial Basis Functions (RBF) that can be adopted for the three-dimensional cases [112] are

$$\begin{aligned}
&W^0(r) = (1-r)^2 && \mathcal{C}^0 \\
&W^2(r) = (1-r)^4(4\,r+1) && \mathcal{C}^2 \\
&W^4(r) = (1-r)^6(\frac{35}{3}r^2 + \frac{18}{3}r + 1) && \mathcal{C}^4 \\
&W^6(r) = (1-r)^8(32\,r^3 + 25\,r^2 + 8r + 1) && \mathcal{C}^6
\end{aligned} \tag{B.15}$$

where r represents the Euclidean distance between the two considered points. The degree of smoothness $\mathcal{C}^n$ of the RBF bounds the maximum number of continuous derivatives of the approximant function $\hat{\boldsymbol{u}}^h$, as can be argued from the expression of the shape functions in eq.(B.13). Usually the weight functions in eq.(B.15) are written using as independent variable r/δ instead of r, where δ is a scaling factor that allows one to change the function support for different centers, making more appropriate the determination of the local support dimension in those cases where there is a great variation in the data density or when it is requested to exactly enforce structural constraints on the aerodynamic mesh.

The final issue is the conservation of energy [95]. To present the problem and its solution in the most general way, the following coupling conditions are considered

$$\begin{aligned}
&\boldsymbol{\sigma}^s\,\boldsymbol{n} = -p\,\boldsymbol{n} + \boldsymbol{\sigma}^f\,\boldsymbol{n} \\
&\boldsymbol{\eta}^s = \boldsymbol{\eta}^f \\
&\dot{\boldsymbol{\eta}}^s = \dot{\boldsymbol{\eta}}^f \quad \text{or} \quad \frac{\partial \dot{\boldsymbol{\eta}}^s}{\partial n} = \frac{\partial \dot{\boldsymbol{\eta}}^f}{\partial n}
\end{aligned} \tag{B.16}$$

where $\boldsymbol{\eta}^s$ denotes the structural boundary position, $\boldsymbol{\eta}^f$ is the aerodynamic counterpart, p is the pressure, $\boldsymbol{\sigma}^s$ and $\boldsymbol{\sigma}^f$ are respectively the structure stress tensor and the fluid viscous stress tensor, and $\boldsymbol{n}$ is the normal vector to either a newly defined virtual interface surface or the surface of the fluid. The first relation expresses the dynamic equilibrium between stresses

on the two fields, whereas the others are kinematic compatibility conditions on displacement and speed; for the latter one, just the normal component can be used if an inviscid flows is considered (wall tangency condition). As these conditions are valid for continuous systems and the two fields are discretized to solve the problem, conservation properties have to be assured: the change of energy in the fluid-structure system need to be equal to the energy supplied by external forces. In the following it is demonstrated how this property can be retained enforcing the coupling conditions in a weak sense through the use of Virtual Work. Calling $\delta\boldsymbol{\eta}^f$ and $\delta\boldsymbol{\eta}^s$ the admissible displacements for the two respective fields, the relation between nodal quantities (i and j are respectively the generical aerodynamic and structural node) is

$$\delta\boldsymbol{\eta}_i^f = \sum_{j=1}^{j_s} \Phi_j(\boldsymbol{\eta}_i^f)\, \delta\boldsymbol{\eta}_j^s \tag{B.17}$$

where i^f and j^f are respectively the number of aerodynamic and structural nodes considered. The resulting virtual displacement of the aerodynamic surface Γ^f is obtained assuming N_i base functions belonging to the aerodynamic field discretization space corresponding to the i^f nodes of the same surface; in this way, the following relation holds

$$\delta\boldsymbol{\eta}^f = \sum_{i=1}^{i_f} N_i \sum_{j=1}^{j_s} \Phi_j(\boldsymbol{\eta}_i^f)\, \delta\boldsymbol{\eta}_j^s \tag{B.18}$$

The virtual work of the aerodynamic load is equal to

$$\delta W^f = \int_{\Gamma^f} (-p\boldsymbol{n} + \boldsymbol{\sigma^f n}) \cdot \delta\boldsymbol{\eta}^f \, d\Gamma \tag{B.19}$$

Calling $\boldsymbol{f}_j$ the load on the structural node j induced by the fluid, the virtual work of the forces acting on the structure is

$$\delta W^s = \sum_{j=1}^{j^s} \boldsymbol{f}_j\, \delta\boldsymbol{\eta}_j^s \tag{B.20}$$

Imposing equivalence of the virtual works and rearranging eq.(B.19) through eq.(B.17) and eq.(B.18) the following holds

$$\boldsymbol{f}_j = \sum_{i=1}^{i^f} \boldsymbol{F}_i\, \Phi_j(\boldsymbol{\eta}_i^f) \tag{B.21}$$

where $\mathbf{F}_i$ is given by

$$\boldsymbol{F}_i = \int_{\Gamma^f} (-p\,\boldsymbol{n} + \boldsymbol{\sigma^f n})\, N_i \, d\Gamma \tag{B.22}$$

Consider now $\boldsymbol{f}$ ($\boldsymbol{F}$) to be the matrix whose rows are the forces evaluated at the generic aerodynamic (structural) j-th (i-th) node, $\boldsymbol{f}_j$ ($\boldsymbol{F}_i$). Thus eq.(B.21) may be written in the matrix form:

$$\boldsymbol{f} = \boldsymbol{\Psi}^T \boldsymbol{F} \tag{B.23}$$

being $\boldsymbol{\Psi}$ the interpolation matrix that matches the two displacement's fields, i.e., Ψ_{ij}=$\Phi_j(\boldsymbol{\eta}_i^f)$. Eq.(B.23) shows the sought result: to ensure the balance of the energy exchanged between fluid and structure, the loads on the structural nodes $\boldsymbol{f}$ have to be evaluated multiplying the loads $\boldsymbol{F}$ on the aerodynamic grid by the transpose of the interpolation matrix.

Appendix C

Aerodynamic Tangent Matrix (UPM)

In this section are reported in details all the formulas used in the evaluation of the various terms of the aerodynamic tangent matrix for an Unsteady Panel Method. Refer to Cap.8 for the nomenclature and the problem statement.

C.1 Sensitivity of doublet strength in respect to displacements

In this first part the term $\frac{\partial \boldsymbol{A}^{BN}}{\partial \boldsymbol{u}}$ is considered. The equation that gives the perturbation potential for a unitary doublet strength is

$$\begin{aligned}\Phi^D = -\frac{1}{4\pi}\Bigg\{ &\tan^{-1}\left[\frac{zx_{21}(F_1r_2 - G_1r_1)}{z^2x_{21}^2r_1r_2 + F_1G_1}\right] + \tan^{-1}\left[\frac{zx_{32}(F_2r_3 - G_2r_2)}{z^2x_{32}^2r_2r_3 + F_2G_2}\right] \\ &\tan^{-1}\left[\frac{zx_{43}(F_3r_4 - G_3r_3)}{z^2x_{43}^2r_3r_4 + F_3G_3}\right] + \tan^{-1}\left[\frac{zx_{14}(F_4r_1 - G_4r_4)}{z^2x_{14}^2r_4r_1 + F_4G_4}\right]\Bigg\}\end{aligned} \tag{C.1}$$

When the receiving point is far from the center of the emitting panel and thus the far-field approximation is possible, the influence of the quadrilateral element with area S can be approximated by a point doublet (far-field approximation)

$$\Phi^D = \frac{S}{4\pi}\frac{z}{\sqrt{(x^2+y^2+z^2)^3}} \tag{C.2}$$

Constants adopted in the definitions of the potential and its derivatives are reported in the following.

$$
\begin{aligned}
x_{21} &= (x_2 - x_1) & m_{12} &= \frac{y_{21}}{x_{21}} & e_3 &= (x - x_3)^2 + z^2 \\
x_{32} &= (x_3 - x_2) & m_{23} &= \frac{y_{32}}{x_{32}} & e_4 &= (x - x_4)^2 + z^2 \\
x_{43} &= (x_4 - x_3) & m_{34} &= \frac{y_{43}}{x_{43}} & h_1 &= (x - x_1)(y - y_1) \\
x_{14} &= (x_1 - x_4) & m_{41} &= \frac{y_{14}}{x_{14}} & h_2 &= (x - x_2)(y - y_2) \\
y_{21} &= (y_2 - y_1) & r_1 &= \sqrt{(x - x_1)^2 + (y - y_1)^2 + z^2} & h_3 &= (x - x_3)(y - y_3) \\
y_{32} &= (y_3 - y_2) & r_2 &= \sqrt{(x - x_2)^2 + (y - y_2)^2 + z^2} & h_4 &= (x - x_4)(y - y_4) \\
y_{43} &= (y_4 - y_3) & r_3 &= \sqrt{(x - x_3)^2 + (y - y_3)^2 + z^2} & F_1 &= y_{21}e_1 - x_{21}h1 \\
y_{14} &= (y_1 - y_4) & r_4 &= \sqrt{(x - x_4)^2 + (y - y_4)^2 + z^2} & F_2 &= y_{32}e_2 - x_{32}h2 \\
d_{12} &= \sqrt{x_{21}^2 + y_{21}^2} & e_1 &= (x - x_1)^2 + z^2 & F_3 &= y_{43}e_3 - x_{43}h3 \\
d_{23} &= \sqrt{x_{32}^2 + y_{32}^2} & e_2 &= (x - x_2)^2 + z^2 & F_4 &= y_{14}e_4 - x_{14}h4 \\
d_{34} &= \sqrt{x_{43}^2 + y_{43}^2} & & & G_1 &= y_{21}e_2 - x_{21}h2 \\
d_{41} &= \sqrt{x_{14}^2 + y_{14}^2} & & & G_2 &= y_{32}e_3 - x_{32}h3 \\
& & & & G_3 &= y_{43}e_4 - x_{43}h4 \\
& & & & G_4 &= y_{14}e_1 - x_{14}h1
\end{aligned}
\tag{C.3}
$$

The case of perturbed vertex thought as belonging to the receiving panel is first presented. The derivatives of the potential Φ^D with respect to the coordinates of the receiving point when eq.(C.2) is valid are given by

$$
\begin{aligned}
\frac{\partial \Phi^D}{\partial x} &= -\frac{S}{4\pi}\frac{3zx}{d^5} \\
\frac{\partial \Phi^D}{\partial y} &= -\frac{S}{4\pi}\frac{3zy}{d^5} \\
\frac{\partial \Phi^D}{\partial z} &= \frac{S}{4\pi}\frac{d^2 - 3z^2}{d^5}
\end{aligned}
\tag{C.4}
$$

where $d=\sqrt{x^2+y^2+z^2}$ is the distance between the centers of the two panels. The derivatives in the general case (close-field) are given by

$$\begin{aligned}\frac{\partial\Phi^D}{\partial x} = -\frac{1}{4\pi}\Bigg\{ & \frac{zx_{21}(F_1^x r_2 + F_1 r_2^x - G_1^x r_1 - G_1 r_1^x)(z^2x_{21}^2 r_1 r_2 + F_1 G_1)}{(z^2x_{21}^2 r_1 r_2 + F_1 G_1)^2 + [zx_{21}(F_1 r_2 - G_1 r_1)]^2} + \\ & - \frac{zx_{21}(F_1 r_2 - G_1 r_1)[z^2x_{21}^2(r_1^x r_2 + r_1 r_2^x) + F_1^x G_1 + F_1 G_1^x]}{(z^2x_{21}^2 r_1 r_2 + F_1 G_1)^2 + [zx_{21}(F_1 r_2 - G_1 r_1)]^2} + \\ & + \frac{zx_{32}(F_2^x r_3 + F_2 r_3^x - G_2^x r_2 - G_2 r_2^x)(z^2x_{32}^2 r_3 r_2 + F_2 G_2)}{(z^2x_{32}^2 r_3 r_2 + F_2 G_2)^2 + [zx_{32}(F_2 r_3 - G_2 r_2)]^2} + \\ & - \frac{zx_{32}(F_2 r_3 - G_2 r_2)[z^2x_{32}^2(r_2^x r_3 + r_2 r_3^x) + F_2^x G_2 + F_2 G_2^x]}{(z^2x_{32}^2 r_3 r_2 + F_2 G_2)^2 + [zx_{32}(F_2 r_3 - G_2 r_2)]^2} + \\ & + \frac{zx_{43}(F_3^x r_4 + F_3 r_4^x - G_3^x r_3 - G_3 r_3^x)(z^2x_{43}^2 r_3 r_4 + F_3 G_3)}{(z^2x_{43}^2 r_3 r_4 + F_3 G_3)^2 + [zx_{43}(F_3 r_4 - G_3 r_3)]^2} + \\ & - \frac{zx_{43}(F_3 r_4 - G_3 r_3)[z^2x_{43}^2(r_3^x r_4 + r_3 r_4^x) + F_3^x G_3 + F_3 G_3^x]}{(z^2x_{43}^2 r_3 r_4 + F_3 G_3)^2 + [zx_{43}(F_3 r_4 - G_3 r_3)]^2} + \\ & + \frac{zx_{14}(F_4^x r_1 + F_4 r_1^x - G_4^x r_4 - G_4 r_4^x)(z^2x_{14}^2 r_3 r_4 + F_4 G_4)}{(z^2x_{14}^2 r_1 r_4 + F_4 G_4)^2 + [zx_{14}(F_4 r_1 - G_4 r_4)]^2} + \\ & - \frac{zx_{14}(F_4 r_1 - G_4 r_4)[z^2x_{14}^2(r_4^x r_1 + r_4 r_1^x) + F_4^x G_4 + F_4 G_4^x]}{(z^2x_{14}^2 r_1 r_4 + F_4 G_4)^2 + [zx_{14}(F_4 r_1 - G_4 r_4)]^2} \Bigg\}\end{aligned} \tag{C.5}$$

$$\begin{aligned}\frac{\partial\Phi^D}{\partial y} = -\frac{1}{4\pi}\Bigg\{ & \frac{zx_{21}(F_1^y r_2 + F_1 r_2^y - G_1^y r_1 - G_1 r_1^y)(z^2x_{21}^2 r_1 r_2 + F_1 G_1)}{(z^2x_{21}^2 r_1 r_2 + F_1 G_1)^2 + [zx_{21}(F_1 r_2 - G_1 r_1)]^2} + \\ & - \frac{zx_{21}(F_1 r_2 - G_1 r_1)[z^2x_{21}^2(r_1^y r_2 + r_1 r_2^y) + F_1^y G_1 + F_1 G_1^y]}{(z^2x_{21}^2 r_1 r_2 + F_1 G_1)^2 + [zx_{21}(F_1 r_2 - G_1 r_1)]^2} + \\ & + \frac{zx_{32}(F_2^y r_3 + F_2 r_3^y - G_2^y r_2 - G_2 r_2^y)(z^2x_{32}^2 r_3 r_2 + F_2 G_2)}{(z^2x_{32}^2 r_3 r_2 + F_2 G_2)^2 + [zx_{32}(F_2 r_3 - G_2 r_2)]^2} + \\ & - \frac{zx_{32}(F_2 r_3 - G_2 r_2)[z^2x_{32}^2(r_2^y r_3 + r_2 r_3^y) + F_2^y G_2 + F_2 G_2^y]}{(z^2x_{32}^2 r_3 r_2 + F_2 G_2)^2 + [zx_{32}(F_2 r_3 - G_2 r_2)]^2} + \\ & + \frac{zx_{43}(F_3^y r_4 + F_3 r_4^y - G_3^y r_3 - G_3 r_3^y)(z^2x_{43}^2 r_3 r_4 + F_3 G_3)}{(z^2x_{43}^2 r_3 r_4 + F_3 G_3)^2 + [zx_{43}(F_3 r_4 - G_3 r_3)]^2} + \\ & - \frac{zx_{43}(F_3 r_4 - G_3 r_3)[z^2x_{43}^2(r_3^y r_4 + r_3 r_4^y) + F_3^y G_3 + F_3 G_3^y]}{(z^2x_{43}^2 r_3 r_4 + F_3 G_3)^2 + [zx_{43}(F_3 r_4 - G_3 r_3)]^2} + \\ & + \frac{zx_{14}(F_4^y r_1 + F_4 r_1^y - G_4^y r_4 - G_4 r_4^y)(z^2x_{14}^2 r_3 r_4 + F_4 G_4)}{(z^2x_{14}^2 r_1 r_4 + F_4 G_4)^2 + [zx_{14}(F_4 r_1 - G_4 r_4)]^2} + \\ & - \frac{zx_{14}(F_4 r_1 - G_4 r_4)[z^2x_{14}^2(r_4^y r_1 + r_4 r_1^y) + F_4^y G_4 + F_4 G_4^y]}{(z^2x_{14}^2 r_1 r_4 + F_4 G_4)^2 + [zx_{14}(F_4 r_1 - G_4 r_4)]^2} \Bigg\}\end{aligned} \tag{C.6}$$

$$\frac{\partial \Phi^D}{\partial z} = -\frac{1}{4\pi}\Bigg\{ \frac{x_{21}(F_1 r_2 - G_1 r_1) + z x_{21}(F_1^z r_2 + F_1 r_2^z - G_1^z r_1 - G_1 r_1^z)(z^2 x_{21}^2 r_1 r_2 + F_1 G_1)}{(z^2 x_{21}^2 r_1 r_2 + F_1 G_1)^2 + [z x_{21}(F_1 r_2 - G_1 r_1)]^2} + \\ - \frac{z x_{21}(F_1 r_2 - G_1 r_1)[2 z x_{21}^2 r1 r2 + z^2 x_{21}^2 (r_1^z r_2 + r_1 r_2^z) + F_1^z G_1 + F_1 G_1^z]}{(z^2 x_{21}^2 r_1 r_2 + F_1 G_1)^2 + [z x_{21}(F_1 r_2 - G_1 r_1)]^2} + \\ + \frac{x_{32}(F_2 r_3 - G_2 r_2) + z x_{32}(F_2^z r_3 + F_2 r_3^z - G_2^z r_2 - G_2 r_2^z)(z^2 x_{32}^2 r_3 r_2 + F_2 G_2)}{(z^2 x_{32}^2 r_3 r_2 + F_2 G_2)^2 + [z x_{32}(F_2 r_3 - G_2 r_2)]^2} + \\ - \frac{z x_{32}(F_2 r_3 - G_2 r_2)[2 z x_{32}^2 r3 r2 + z^2 x_{32}^2 (r_2^z r_3 + r_2 r_3^z) + F_2^z G_2 + F_2 G_2^z]}{(z^2 x_{32}^2 r_3 r_2 + F_2 G_2)^2 + [z x_{32}(F_2 r_3 - G_2 r_2)]^2} + \\ + \frac{x_{43}(F_3 r_4 - G_3 r_3) + z x_{43}(F_3^z r_4 + F_3 r_4^z - G_3^z r_3 - G_3 r_3^z)(z^2 x_{43}^2 r_3 r_4 + F_3 G_3)}{(z^2 x_{43}^2 r_3 r_4 + F_3 G_3)^2 + [z x_{43}(F_3 r_4 - G_3 r_3)]^2} + \\ - \frac{z x_{43}(F_3 r_4 - G_3 r_3)[2 z x_{43}^2 r3 r4 + z^2 x_{43}^2 (r_3^z r_4 + r_3 r_4^z) + F_3^z G_3 + F_3 G_3^z]}{(z^2 x_{43}^2 r_3 r_4 + F_3 G_3)^2 + [z x_{43}(F_3 r_4 - G_3 r_3)]^2} + \\ + \frac{x_{14}(F_4 r_1 - G_4 r_4) + z x_{14}(F_4^z r_1 + F_4 r_1^z - G_4^z r_4 - G_4 r_4^z)(z^2 x_{14}^2 r_3 r_4 + F_4 G_4)}{(z^2 x_{14}^2 r_1 r_4 + F_4 G_4)^2 + [z x_{14}(F_4 r_1 - G_4 r_4)]^2} + \\ - \frac{z x_{14}(F_4 r_1 - G_4 r_4)[2 z x_{14}^2 r1 r4 + z^2 x_{14}^2 (r_4^z r_1 + r_4 r_1^z) + F_4^z G_4 + F_4 G_4^z]}{(z^2 x_{14}^2 r_1 r_4 + F_4 G_4)^2 + [z x_{14}(F_4 r_1 - G_4 r_4)]^2} \Bigg\} \tag{C.7}$$

Where the following quantities are defined

$$r_1^x = \frac{\partial r_1}{\partial x} = \frac{(x-x_1)}{\sqrt{(x-x_1)^2+(y-y_1)^2+z^2}} \qquad r_1^y = \frac{\partial r_1}{\partial y} = \frac{(y-y_1)}{\sqrt{(y-y_1)^2+(y-y_1)^2+z^2}}$$

$$r_2^x = \frac{\partial r_2}{\partial x} = \frac{(x-x_2)}{\sqrt{(x-x_2)^2+(y-y_2)^2+z^2}} \qquad r_2^y = \frac{\partial r_2}{\partial y} = \frac{(y-y_2)}{\sqrt{(y-y_2)^2+(y-y_2)^2+z^2}}$$

$$r_3^x = \frac{\partial r_3}{\partial x} = \frac{(x-x_3)}{\sqrt{(x-x_3)^2+(y-y_3)^2+z^2}} \qquad r_3^y = \frac{\partial r_3}{\partial y} = \frac{(y-y_3)}{\sqrt{(y-y_3)^2+(y-y_3)^2+z^2}}$$

$$r_4^x = \frac{\partial r_4}{\partial x} = \frac{(x-x_4)}{\sqrt{(x-x_4)^2+(y-y_4)^2+z^2}} \qquad r_4^y = \frac{\partial r_4}{\partial y} = \frac{(y-y_4)}{\sqrt{(y-y_4)^2+(y-y_4)^2+z^2}}$$

$$F_1^x = \frac{\partial F_1}{\partial x} = 2y_{21}(x-x1) - x_{21}(y-y_1) \qquad F_1^y = \frac{\partial F_1}{\partial y} = -x_{21}(x-x_1)$$

$$F_2^x = \frac{\partial F_2}{\partial x} = 2y_{32}(x-x2) - x_{32}(y-y_2) \qquad F_2^y = \frac{\partial F_2}{\partial y} = -x_{32}(x-x_2)$$

$$F_3^x = \frac{\partial F_3}{\partial x} = 2y_{43}(x-x3) - x_{43}(y-y_3) \qquad F_3^y = \frac{\partial F_3}{\partial y} = -x_{43}(x-x_3)$$

$$F_4^x = \frac{\partial F_4}{\partial x} = 2y_{14}(x-x4) - x_{14}(y-y_4) \qquad F_4^y = \frac{\partial F_4}{\partial y} = -x_{14}(x-x_4)$$

$$G_1^x = \frac{\partial G_1}{\partial x} = 2y_{21}(x-x2) - x_{21}(y-y_2) \qquad G_1^y = \frac{\partial G_1}{\partial y} = -x_{21}(x-x_2)$$

$$G_2^x = \frac{\partial G_2}{\partial x} = 2y_{32}(x-x3) - x_{32}(y-y_3) \qquad G_2^y = \frac{\partial G_2}{\partial y} = -x_{32}(x-x_3)$$

$$G_3^x = \frac{\partial G_3}{\partial x} = 2y_{43}(x-x4) - x_{43}(y-y_4) \qquad G_3^y = \frac{\partial G_3}{\partial y} = -x_{43}(x-x_4)$$

$$G_4^x = \frac{\partial G_4}{\partial x} = 2y_{14}(x-x1) - x_{14}(y-y_1) \qquad G_4^y = \frac{\partial G_4}{\partial y} = -x_{14}(x-x_1)$$

$$r_1^z = \frac{\partial r_1}{\partial z} = \frac{(z-z_1)}{\sqrt{(z-z_1)^2+(y-y_1)^2+z^2}} \qquad F_3^z = \frac{\partial F_3}{\partial z} = 2zy_{43}$$

$$r_2^z = \frac{\partial r_2}{\partial z} = \frac{(z-z_2)}{\sqrt{(z-z_2)^2+(y-y_2)^2+z^2}} \qquad F_4^z = \frac{\partial F_4}{\partial z} = 2zy_{14}$$

$$r_3^z = \frac{\partial r_3}{\partial z} = \frac{(z-z_3)}{\sqrt{(z-z_3)^2+(y-y_3)^2+z^2}} \qquad G_1^z = \frac{\partial G_1}{\partial z} = F_1^z$$

$$r_4^z = \frac{\partial r_4}{\partial z} = \frac{(z-z_4)}{\sqrt{(z-z_4)^2+(y-y_4)^2+z^2}} \qquad G_2^z = \frac{\partial G_2}{\partial z} = F_2^z$$

$$F_1^z = \frac{\partial F_1}{\partial z} = 2xy_{21} \qquad G_3^z = \frac{\partial G_3}{\partial z} = F_3^z$$

$$F_2^z = \frac{\partial F_2}{\partial z} = 2zy_{32} \qquad G_4^z = \frac{\partial G_4}{\partial z} = F_4^z$$

The case of perturbed vertex thought as belonging to the emitting panel is here taken in consideration. In case of validity of eq.(C.2), the derivatives of the perturbation potential are

$$\begin{aligned}
\frac{\partial \Phi^D}{\partial x_1} &= \frac{\partial S}{\partial x_1}\frac{z}{4\pi d^3} \qquad & \frac{\partial \Phi^D}{\partial y_1} &= \frac{\partial S}{\partial y_1}\frac{z}{4\pi d^3} \\
\frac{\partial \Phi^D}{\partial x_2} &= \frac{\partial S}{\partial x_2}\frac{z}{4\pi d^3} \qquad & \frac{\partial \Phi^D}{\partial y_2} &= \frac{\partial S}{\partial y_2}\frac{z}{4\pi d^3} \\
\frac{\partial \Phi^D}{\partial x_3} &= \frac{\partial S}{\partial x_3}\frac{z}{4\pi d^3} \qquad & \frac{\partial \Phi^D}{\partial y_3} &= \frac{\partial S}{\partial y_3}\frac{z}{4\pi d^3} \\
\frac{\partial \Phi^D}{\partial x_4} &= \frac{\partial S}{\partial x_4}\frac{z}{4\pi d^3} \qquad & \frac{\partial \Phi^D}{\partial y_4} &= \frac{\partial S}{\partial y_4}\frac{z}{4\pi d^3}
\end{aligned}$$

The derivatives of eq.(C.1) with respect to the same variables are here presented

$$\begin{aligned}
\frac{\partial \Phi^D}{\partial x_1} = -\frac{1}{4\pi}\Bigg\{ & \frac{[-z(F_1r_2 - G_1r_1) + zx_{21}(F_1^{x_1}r_2 - G_1^{x_1}r_1 - G_1r_1^{x_1})](z^2x_{21}^2r_1r_2 + F_1G_1)}{(z^2x_{21}^2r_1r_2 + F_1G_1)^2 + [zx_{21}(F_1r_2 - G_1r_1)]^2} \\
& - \frac{zx_{21}(F_1r_2 - G_1r_1)[-2x_{21}z^2r_1r_2 + z^2x_{21}^2r_1^{x_1}r_2 + F_1^{x_1}G_1 + F_1G_1^{x_1}]}{(z^2x_{21}^2r_1r_2 + F_1G_1)^2 + [zx_{21}(F_1r_2 - G_1r_1)]^2} + \\
& + \frac{[z(F_4r_1 - G_4r_4) + zx_{14}(F_4^{x_1}r_1 + F_4r_1^{x_1} - G_4^{x_1}r_4](z^2x_{14}^2r_1r_4 + F_4G_4)}{(z^2x_{14}^2r_1r_4 + F_4G_4)^2 + [zx_{14}(F_4r_1 - G_4r_4)]^2} + \\
& - \frac{zx_{14}(F_4r_1 - G_4r_4)[2x_{14}z^2r_1r_4 + z^2x_{14}^2r_1^{x_1}r_4 + F_4^{x_1}G_4 + F_4G_4^{x_1}]}{(z^2x_{14}^2r_1r_4 + F_4G_4)^2 + [zx_{14}(F_4r_1 - G_4r_4)]^2}\Bigg\}
\end{aligned}$$

$$\begin{aligned}
\frac{\partial \Phi^D}{\partial x_2} = -\frac{1}{4\pi}\Bigg\{ & \frac{[z(F_1r_2 - G_1r_1) + zx_{21}(F_1^{x_2}r_2 + F_1r_2^{x_2} - G_1^{x_2}r_1)](z^2x_{21}^2r_1r_2 + F_1G_1)}{(z^2x_{21}^2r_1r_2 + F_1G_1)^2 + [zx_{21}(F_1r_2 - G_1r_1)]^2} \\
& - \frac{zx_{21}(F_1r_2 - G_1r_1)[2x_{21}z^2r_1r_2 + z^2x_{21}^2r_1r_2^{x_2} + F_1^{x_2}G_1 + F_1G_1^{x_2}]}{(z^2x_{21}^2r_1r_2 + F_1G_1)^2 + [zx_{21}(F_1r_2 - G_1r_1)]^2} + \\
& + \frac{[-z(F_2r_3 - G_2r_2) + zx_{32}(F_2^{x_2}r_3 - G_2^{x_2}r_2 - G_2r_2^{x_2}](z^2x_{32}^2r_2r_3 + F_2G_2)}{(z^2x_{32}^2r_2r_3 + F_2G_2)^2 + [zx_{32}(F_2r_3 - G_2r_3)]^2} + \\
& - \frac{zx_{32}(F_2r_3 - G_2r_2)[-2x_{32}z^2r_3r_2 + z^2x_{32}^2r_2^{x_2}r_3 + F_2^{x_2}G_2 + F_2G_2^{x_2}]}{(z^2x_{32}^2r_2r_3 + F_2G_2)^2 + [zx_{32}(F_2r_3 - G_2r_3)]^2}\Bigg\}
\end{aligned}$$

$$\begin{aligned}
\frac{\partial \Phi^D}{\partial x_3} = -\frac{1}{4\pi}\Bigg\{ & \frac{[-z(F_3r_4 - G_3r_3) + zx_{43}(F_3^{x_3}r_4 - G_3^{x_3}r_3 - G_3r_3^{x_3})](z^2x_{43}^2r_3r_4 + F_3G_3)}{(z^2x_{43}^2r_3r_4 + F_3G_3)^2 + [zx_{43}(F_3r_4 - G_3r_3)]^2} \\
& - \frac{zx_{43}(F_3r_4 - G_3r_3)[-2x_{43}z^2r_3r_4 + z^2x_{43}^2r_4r_3^{x_3} + F_3^{x_3}G_3 + F_3G_3^{x_3}]}{(z^2x_{43}^2r_3r_4 + F_3G_3)^2 + [zx_{43}(F_3r_4 - G_3r_3)]^2} + \\
& + \frac{[z(F_2r_3 - G_2r_2) + zx_{32}(F_2^{x_3}r_3 + F_2r_3^{x_3} - G_2^{x_3}r_2](z^2x_{32}^2r_2r_3 + F_2G_2)}{(z^2x_{32}^2r_2r_3 + F_2G_2)^2 + [zx_{32}(F_2r_3 - G_2r_3)]^2} + \\
& - \frac{zx_{32}(F_2r_3 - G_2r_2)[2x_{32}z^2r_3r_2 + z^2x_{32}^2r_3^{x_3}r_2 + F_2^{x_3}G_2 + F_2G_2^{x_3}]}{(z^2x_{32}^2r_2r_3 + F_2G_2)^2 + [zx_{32}(F_2r_3 - G_2r_3)]^2}\Bigg\}
\end{aligned}$$

$$\frac{\partial\Phi^D}{\partial x_4}=-\frac{1}{4\pi}\Bigg\{\frac{[z(F_3r_4-G_3r_3)+zx_{43}(F_3^{x_4}r_4+F_3r_4^{x_4}-G_3^{x_4}r_3)](z^2x_{43}^2r_3r_4+F_3G_3)}{(z^2x_{43}^2r_3r_4+F_3G_3)^2+[zx_{43}(F_3r_4-G_3r_3)]^2}$$
$$-\frac{zx_{43}(F_3r_4-G_3r_3)[2x_{43}z^2r_3r_4+z^2x_{43}^2r_4^{x_4}r_3+F_3^{x_4}G_3+F_3G_3^{x_4}]}{(z^2x_{43}^2r_3r_4+F_3G_3)^2+[zx_{43}(F_3r_4-G_3r_3)]^2}+$$
$$+\frac{[-z(F_4r_1-G_4r_4)+zx_{14}(F_4^{x_4}r_1-G_4^{x_4}r_4-G_4r_4^{x_4}](z^2x_{14}^2r_1r_4+F_4G_4)}{(z^2x_{14}^2r_1r_4+F_4G_4)^2+[zx_{14}(F_4r_1-G_4r_4)]^2}+$$
$$-\frac{zx_{14}(F_4r_1-G_4r_4)[-2x_{14}z^2r_1r_4+z^2x_{14}^2r_4^{x_4}r_1+F_4^{x_4}G_4+F_4G_4^{x_4}]}{(z^2x_{14}^2r_1r_4+F_4G_4)^2+[zx_{14}(F_4r_1-G_4r_4)]^2}\Bigg\}$$

$$\frac{\partial\Phi^D}{\partial y_1}=-\frac{1}{4\pi}\Bigg\{\frac{[zx_{21}(F_1^{x_1}r_2-G_1^{y_1}r_1-G_1r_1^{x_1})](z^2x_{21}^2r_1r_2+F_1G_1)}{(z^2x_{21}^2r_1r_2+F_1G_1)^2+[zx_{21}(F_1r_2-G_1r_1)]^2}$$
$$-\frac{zx_{21}(F_1r_2-G_1r_1)[z^2x_{21}^2r_1^{y_1}r_2+F_1^{y_1}G_1+F_1G_1^{y_1}]}{(z^2x_{21}^2r_1r_2+F_1G_1)^2+[zx_{21}(F_1r_2-G_1r_1)]^2}+$$
$$+\frac{[zx_{14}(F_4^{y_1}r_1+F_4r_1^{y_1}-G_4^{y_1}r_4](z^2x_{14}^2r_1r_4+F_4G_4)}{(z^2x_{14}^2r_1r_4+F_4G_4)^2+[zx_{14}(F_4r_1-G_4r_4)]^2}+$$
$$-\frac{zx_{14}(F_4r_1-G_4r_4)[z^2x_{14}^2r_1^{y_1}r_4+F_4^{y_1}G_4+F_4G_4^{y_1}]}{(z^2x_{14}^2r_1r_4+F_4G_4)^2+[zx_{14}(F_4r_1-G_4r_4)]^2}\Bigg\}$$

$$\frac{\partial\Phi^D}{\partial y_2}=-\frac{1}{4\pi}\Bigg\{\frac{[zx_{21}(F_1^{x_2}r_2+F_1r_2^{y_2}-G_1^{y_2}r_1)](z^2x_{21}^2r_1r_2+F_1G_1)}{(z^2x_{21}^2r_1r_2+F_1G_1)^2+[zx_{21}(F_1r_2-G_1r_1)]^2}$$
$$-\frac{zx_{21}(F_1r_2-G_1r_1)[z^2x_{21}^2r_1r_2^{y_2}+F_1^{y_2}G_1+F_1G_1^{y_2}]}{(z^2x_{21}^2r_1r_2+F_1G_1)^2+[zx_{21}(F_1r_2-G_1r_1)]^2}+$$
$$+\frac{[zx_{32}(F_2^{y_2}r_3-G_2^{y_2}r_2-G_2r_2^{y_2}](z^2x_{32}^2r_2r_3+F_2G_2)}{(z^2x_{32}^2r_2r_3+F_2G_2)^2+[zx_{32}(F_2r_3-G_2r_3)]^2}+$$
$$-\frac{zx_{32}(F_2r_3-G_2r_2)[z^2x_{32}^2r_2^{y_2}r_3+F_2^{y_2}G_2+F_2G_2^{y_2}]}{(z^2x_{32}^2r_2r_3+F_2G_2)^2+[zx_{32}(F_2r_3-G_2r_3)]^2}\Bigg\}$$

$$\frac{\partial\Phi^D}{\partial y_3}=-\frac{1}{4\pi}\Bigg\{\frac{[zx_{43}(F_3^{x_3}r_4-G_3^{y_3}r_3-G_3r_3^{y_3})](z^2x_{43}^2r_3r_4+F_3G_3)}{(z^2x_{43}^2r_3r_4+F_3G_3)^2+[zx_{43}(F_3r_4-G_3r_3)]^2}$$
$$-\frac{zx_{43}(F_3r_4-G_3r_3)[z^2x_{43}^2r_4r_3^{y_3}+F_3^{y_3}G_3+F_3G_3^{y_3}]}{(z^2x_{43}^2r_3r_4+F_3G_3)^2+[zx_{43}(F_3r_4-G_3r_3)]^2}+$$
$$+\frac{[zx_{32}(F_2^{y_3}r_3+F_2r_3^{y_3}-G_2^{y_3}r_2](z^2x_{32}^2r_2r_3+F_2G_2)}{(z^2x_{32}^2r_2r_3+F_2G_2)^2+[zx_{32}(F_2r_3-G_2r_3)]^2}+$$
$$-\frac{zx_{32}(F_2r_3-G_2r_2)[z^2x_{32}^2r_3^{y_3}r_2+F_2^{y_3}G_2+F_2G_2^{y_3}]}{(z^2x_{32}^2r_2r_3+F_2G_2)^2+[zx_{32}(F_2r_3-G_2r_3)]^2}\Bigg\}$$

$$\frac{\partial \Phi^D}{\partial y_4} = -\frac{1}{4\pi}\left\{ \frac{[zx_{43}(F_3^{x_4} r_4 + F_3 r_4^{y_4} - G_3^{y_4} r_3)](z^2 x_{43}^2 r_3 r_4 + F_3 G_3)}{(z^2 x_{43}^2 r_3 r_4 + F_3 G_3)^2 + [zx_{43}(F_3 r_4 - G_3 r_3)]^2} \right.$$
$$- \frac{zx_{43}(F_3 r_4 - G_3 r_3)[z^2 x_{43}^2 r_4^{y_4} r_3 + F_3^{y_4} G_3 + F_3 G_3^{y_4}]}{(z^2 x_{43}^2 r_3 r_4 + F_3 G_3)^2 + [zx_{43}(F_3 r_4 - G_3 r_3)]^2} +$$
$$+ \frac{[zx_{14}(F_4^{y_4} r_1 - G_4^{y_4} r_4 - G_4 r_4^{y_4}](z^2 x_{14}^2 r_1 r_4 + F_4 G_4)}{(z^2 x_{14}^2 r_1 r_4 + F_4 G_4)^2 + [zx_{14}(F_4 r_1 - G_4 r_4)]^2} +$$
$$\left. - \frac{zx_{14}(F_4 r_1 - G_4 r_4)[z^2 x_{14}^2 r_4^{y_4} r_1 + F_4^{y_4} G_4 + F_4 G_4^{y_4}]}{(z^2 x_{14}^2 r_1 r_4 + F_4 G_4)^2 + [zx_{14}(F_4 r_1 - G_4 r_4)]^2} \right\}$$

Where the following quantities are defined

$$G_1^{x_1} = \frac{\partial G_1}{\partial x_1} = h_2 \qquad r_1^{x_1} = \frac{\partial r_1}{\partial x_1} = -\frac{(x - x_1)}{\sqrt{(x - x_1)^2 + (y - y_1)^2 + z^2}}$$

$$F_4^{x_1} = \frac{\partial F_4}{\partial x_1} = -h_4 \qquad r_2^{x_2} = \frac{\partial r_2}{\partial x_2} = -\frac{(x - x_2)}{\sqrt{(x - x_2)^2 + (y - y_2)^2 + z^2}}$$

$$G_4^{x_4} = \frac{\partial G_4}{\partial x_3} = h_1 \qquad F_1^{x_1} = \frac{\partial F_1}{\partial x_1} = -2(x - x_1)y_{21} + h_1 + x_{21}(y - y_1)$$

$$F_3^{x_4} = \frac{\partial F_3}{\partial x_3} = -h_3 \qquad G_1^{x_2} = \frac{\partial G_1}{\partial x_2} = -2(x - x_2)y_{21} - h_2 + x_{21}(y - y_1)$$

$$G_2^{x_2} = \frac{\partial G_2}{\partial x_2} = h_3 \qquad G_4^{x_1} = \frac{\partial G_4}{\partial x_1} = -2(x - x_1)y_{14} - h_1 + x_{14}(y - y_1)$$

$$F_1^{x_2} = \frac{\partial F_1}{\partial x_2} = -h_1 \qquad F_2^{x_2} = \frac{\partial F_2}{\partial x_2} = -2(x - x_2)(y_{32} + h_2 + x_{32}(y - y_2)$$

$$G_3^{x_3} = \frac{\partial G_3}{\partial x_3} = h_4 \qquad r_3^{x_3} = \frac{\partial r_3}{\partial x_3} = -\frac{(x - x_3)}{\sqrt{(x - x_3)^2 + (y - y_3)^2 + z^2}}$$

$$F_2^{x_3} = \frac{\partial F_2}{\partial x_3} = -h_2 \qquad r_4^{x_4} = \frac{\partial r_4}{\partial x_4} = -\frac{(x - x_4)}{\sqrt{(x - x_4)^2 + (y - y_4)^2 + z^2}}$$

$$G_3^{y_3} = \frac{\partial G_3}{\partial y_3} = -e_4 \qquad F_3^{x_3} = \frac{\partial F_3}{\partial x_3} = -2(x - x_3)y_{43} + h_3 + y_{43}(y - y_3)$$

$$F_2^{y_3} = \frac{\partial F_2}{\partial y_3} = e_2 \qquad G_2^{x_3} = \frac{\partial G_2}{\partial x_3} = -2(x - x_3)y_{32} - h_3 + x_{32}(y - y_3)$$

$$G_1^{y_2} = \frac{\partial G_1}{\partial y_2} = e_2 + x_{21}(x - x_2) \qquad F_4^{x_4} = \frac{\partial F_4}{\partial x_3} = -2(x - x_4)y_{14} + h_4 + x_{14}(y - y_4)$$

$$F_2^{y_2} = \frac{\partial F_2}{\partial y_2} = -e_2 + x_{32}(x - x_2) \qquad G_3^{x_4} = \frac{\partial G_3}{\partial x_3} = -2(x - x_4)y_{43} - h_4 + x_{43}(y - y_4)$$

$$
\begin{aligned}
F_1^{y_1} &= \frac{\partial F_1}{\partial y_1} = -e_1 + x_{21}(x - x_1) & r_3^{y_3} &= \frac{\partial r_3}{\partial y_3} = -\frac{(y - y_3)}{\sqrt{(x - x_3)^2 + (y - y_3)^2 + z^2}} \\
G_1^{y_1} &= \frac{\partial G_1}{\partial y_1} = -e_2 & r_4^{y_4} &= \frac{\partial r_4}{\partial y_4} = -\frac{(y - y_4)}{\sqrt{(x - x_4)^2 + (y - y_4)^2 + z^2}} \\
F_4^{y_1} &= \frac{\partial F_4}{\partial y_1} = e_4 & F_3^{y_3} &= \frac{\partial F_3}{\partial y_3} = -e_3 + x_{43}(x - x_3) \\
G_4^{y_1} &= \frac{\partial G_4}{\partial y_1} = e_1 + (x - x_1)x_{14} & G_2^{y_3} &= \frac{\partial G_2}{\partial y_3} = e_3 + (x - x_3)x_{32} \\
G_2^{y_2} &= \frac{\partial G_2}{\partial y_2} = -e_3 & F_4^{y_4} &= \frac{\partial F_4}{\partial y_4} = -e_3 + x_{14}(x - x_4) \\
F_1^{y_2} &= \frac{\partial F_1}{\partial y_2} = e_1 & r_1^{y_1} &= \frac{\partial r_1}{\partial y_1} = -\frac{(y - y_1)}{\sqrt{(x - x_1)^2 + (y - y_1)^2 + z^2}} \\
G_4^{y_4} &= \frac{\partial G_4}{\partial y_4} = -e_1 & r_2^{y_2} &= \frac{\partial r_2}{\partial y_2} = -\frac{(y - y_2)}{\sqrt{(x - x_2)^2 + (y - y_2)^2 + z^2}} \\
F_3^{y_4} &= \frac{\partial F_3}{\partial y_4} = e_3 & G_3^{y_4} &= \frac{\partial G_3}{\partial y_4} = e_4 + x_{43}(x - x_4)
\end{aligned}
$$

As shown in eq.(8.33), here for clarity recalled,

$$
\begin{aligned}
\frac{\partial A_{b,6}^{*BN}}{\partial u_{6,z}} =& \frac{\partial \Phi^D}{\partial x_2} l_z + \frac{\partial \Phi^D}{\partial y_2} m_z + \frac{\partial \Phi^D}{\partial x} \left(\frac{\partial l_x}{\partial s_{z,6}} s_x^b + \frac{\partial l_y}{\partial s_{z,6}} s_y^b + \frac{\partial l_z}{\partial s_{z,6}} s_z^b - \frac{1}{4} \right) + \\
&+ \frac{\partial \Phi^D}{\partial y} \left(\frac{\partial m_x}{\partial s_{z,6}} s_x^b + \frac{\partial m_y}{\partial s_{z,6}} s_y^b + \frac{\partial m_z}{\partial s_{z,6}} s_z^b - \frac{1}{4} \right) + \\
&+ \frac{\partial \Phi^D}{\partial z} \left(\frac{\partial n_x}{\partial s_{z,6}} s_x^b + \frac{\partial n_y}{\partial s_{z,6}} s_y^b + \frac{\partial n_z}{\partial s_{z,6}} s_z^b - \frac{1}{4} \right)
\end{aligned}
\tag{C.8}
$$

to correctly assess the contribution $\frac{\partial A_{b,k}^{BN}}{\partial u_i}$ (where b is the ID of the receiving point and k is the the perturbed vertex belonging to the emitting panel) the derivatives of the matrix $\boldsymbol{GL}^k$ which enables to shift the coordinates of the receiving point from the Global to the Local reference system of the emitting panel in respect with the global coordinates of the perturbed vertex are needed.

In order to visualize the three unit vectors $\boldsymbol{l}$,$\boldsymbol{m}$ and $\boldsymbol{n}$, Fig.C.1 is presented. Starting from the four corner points, the two diagonals $\boldsymbol{d}_1$ and $\boldsymbol{d}_2$ are first defined. The vector product of this diagonals (normalized by its modulus) gives the unity vector $\boldsymbol{n}$ normal to the mean plane of the quadrilateral (as the quadrilaterals are not planar in general, the singularity distributions are thought to be distributed on an average flat panel)

$$
\boldsymbol{n} = \frac{\boldsymbol{d}_1 \times \boldsymbol{d}_2}{|\boldsymbol{d}_1 \wedge \boldsymbol{d}_2|} \tag{C.9}
$$

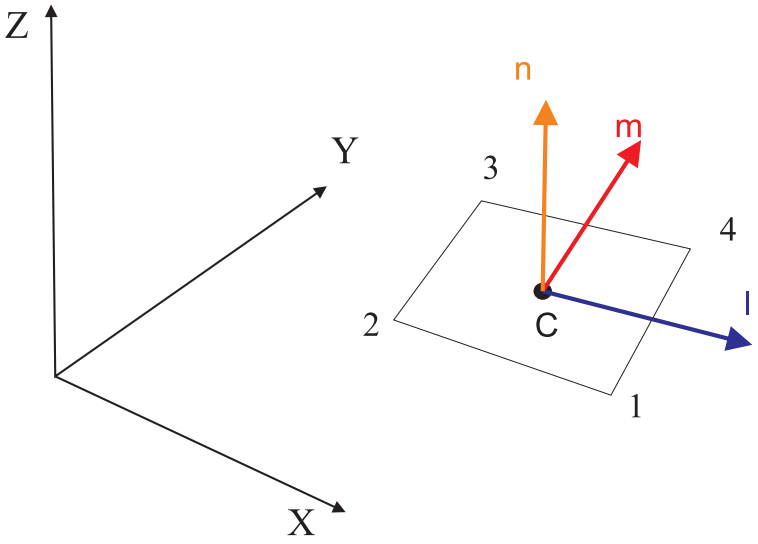

Fig. C.1: Local reference system defined by unit vectors l,m,n

The order of the corner gives the direction of the normal; thus to be consistent with the sign given to the perturbation potential in eqs.(8.16),(8.17),(8.34) and (8.35) $\boldsymbol{d}_1$ runs from point 1 to point 3 and $\boldsymbol{d}_2$ runs from point 2 to point 4. The area of the panel moreover is given by

$$S = \frac{|\boldsymbol{d}_1 \wedge \boldsymbol{d}_2|}{2} \tag{C.10}$$

The control point where the boundary condition is imposed coincides with the center of the panel C, defined as the mean of the four corner points

$$\boldsymbol{C} = \frac{1}{4}\sum_{i=1}^{4} \boldsymbol{R_i} \tag{C.11}$$

The origin of the local coordinate system is coincident with C and the unity vector is directed from it to the mid-point of the edge lying between vertices 3 and 4

$$\boldsymbol{m} = \frac{\frac{\boldsymbol{R_3}+\boldsymbol{R_4}}{2} - \boldsymbol{C}}{\left|\frac{\boldsymbol{R_3}+\boldsymbol{R_4}}{2} - \boldsymbol{C}\right|} \tag{C.12}$$

Finally the other vector lying in the mean plane is given by

$$\boldsymbol{l} = \boldsymbol{m} \times \boldsymbol{n} \tag{C.13}$$

In order to perform the derivatives in respect with the *global* coordinates of the 4 vertices of

the panel, the previous variables are defined in the global reference ($\boldsymbol{x}$,$\boldsymbol{y}$,$\boldsymbol{z}$) of Fig.C.1

$$
\begin{aligned}
&\boldsymbol{d_{13}} = (d_{13x}, d_{13y}, d_{13z}) = (x_3 - x_1, y_3 - y_1, z_3 - z_1) \\
&\boldsymbol{d_{24}} = (d_{24x}, d_{24y}, d_{24z}) = (x_4 - x_2, y_4 - y_2, z_4 - z_2) \\
&\boldsymbol{n} = (n_x, n_y, n_z) = \frac{1}{n}(d_{13y}d_{24z} - d_{13z}d_{24y}, d_{24x}d_{13z} - d_{13x}d_{24z}, d_{13x}d_{24y} - d_{13y}d_{24x}) \\
&n = |\boldsymbol{d}_1 \wedge \boldsymbol{d}_2| = \sqrt{(d_{13y}d_{24z} - d_{13z}d_{24y})^2 + (d_{24x}d_{13z} - d_{13x}d_{24z})^2 + (d_{13x}d_{24y} - d_{13y}d_{24x})^2} \\
&\boldsymbol{C} = (C_x, C_y, C_z) = \left(\frac{x_1 + x_2 + x_3 + x_4}{4}, \frac{y_1 + y_2 + y_3 + y_4}{4}, \frac{z_1 + z_2 + z_3 + z_4}{4}\right) \\
&\frac{\boldsymbol{R_3} + \boldsymbol{R_4}}{2} = \left(\frac{x_3 + x_4}{2}, \frac{y_3 + y_4}{2}, \frac{z_3 + z_4}{2}\right) \\
&\boldsymbol{m} = (m_x, m_y, m_z) = \frac{1}{m}\left(\frac{x_3 + x_4 - x_1 - x_2}{4}, \frac{y_3 + y_4 - y_1 - y_2}{4}, \frac{z_3 + z_4 - z_1 - z_2}{4}\right) \\
&m = \frac{1}{4}\sqrt{(x_3 + x_4 - x_1 - x_2)^2 + (y_3 + y_4 - y_1 - y_2)^2 + (z_3 + z_4 - z_1 - z_2)^2} \\
&\boldsymbol{l} = (l_x, l_y, l_z) = (m_y n_z - m_z n_y, n_x m_z - m_x n_z, m_x n_y - m_y n_x)
\end{aligned}
\tag{C.14}
$$

Following the definitions of eq.(C.14) it's now possible to perform the required derivatives. It's here reminded that the following represent the derivatives in respect of the global coordinates of the unit vectors defined in the *body* reference system (that depending on the

particular case can be different from the global one). Firstly the unit vector $\boldsymbol{n}$ is considered

$$
\begin{aligned}
\frac{\partial n_x}{\partial x_1} &= -\frac{n^{x_1}}{n^2} n_x & \frac{\partial n_x}{\partial y_1} &= \frac{-d_{24z} n - n^{y_1} n_x}{n^2} \\
\frac{\partial n_y}{\partial x_1} &= \frac{d_{24z} n - n^{x_1} n_y}{n^2} & \frac{\partial n_y}{\partial y_1} &= -\frac{n^{y_1}}{n^2} n_y \\
\frac{\partial n_z}{\partial x_1} &= \frac{-d_{24y} n - n^{x_1} n_z}{n^2} & \frac{\partial n_z}{\partial y_1} &= \frac{d_{24x} n - n^{y_1} n_z}{n^2} \\
\frac{\partial n_x}{\partial x_2} &= -\frac{n^{x_2}}{n^2} n_x & \frac{\partial n_x}{\partial y_2} &= \frac{d_{13z} n - n^{y_2} n_x}{n^2} \\
\frac{\partial n_y}{\partial x_2} &= \frac{-d_{13z} n - n^{x_2} n_y}{n^2} & \frac{\partial n_y}{\partial y_2} &= -\frac{-n^{y_2}}{n^2} n_y \\
\frac{\partial n_z}{\partial x_2} &= \frac{d_{13y} n - n^{x_2} n_z}{n^2} & \frac{\partial n_z}{\partial y_2} &= \frac{-d_{13x} n - n^{y_2} n_z}{n^2} \\
\frac{\partial n_x}{\partial x_3} &= -\frac{\partial n_x}{\partial x_1} & \frac{\partial n_x}{\partial y_3} &= -\frac{\partial n_x}{\partial y_1} \\
\frac{\partial n_y}{\partial x_3} &= -\frac{\partial n_y}{\partial x_1} & \frac{\partial n_y}{\partial y_3} &= -\frac{\partial n_y}{\partial y_1} \\
\frac{\partial n_z}{\partial x_3} &= -\frac{\partial n_z}{\partial x_1} & \frac{\partial n_z}{\partial y_3} &= -\frac{\partial n_z}{\partial y_1} \\
\frac{\partial n_x}{\partial x_4} &= -\frac{\partial n_x}{\partial x_2} & \frac{\partial n_x}{\partial y_4} &= -\frac{\partial n_x}{\partial y_2} \\
\frac{\partial n_y}{\partial x_4} &= -\frac{\partial n_y}{\partial x_2} & \frac{\partial n_y}{\partial y_4} &= -\frac{\partial n_y}{\partial y_2} \\
\frac{\partial n_z}{\partial x_4} &= -\frac{\partial n_z}{\partial x_2} & \frac{\partial n_z}{\partial y_4} &= -\frac{\partial n_z}{\partial y_2} \\
\frac{\partial n_x}{\partial z_1} &= \frac{d_{24y} n - n^{z_1} n_x}{n^2} & \frac{\partial n_x}{\partial z_3} &= -\frac{\partial n_x}{\partial z_1} \\
\frac{\partial n_y}{\partial z_1} &= \frac{-d_{24x} n - n^{z_1} n_y}{n^2} & \frac{\partial n_y}{\partial z_3} &= -\frac{\partial n_y}{\partial z_1} \\
\frac{\partial n_z}{\partial z_1} &= -\frac{n^{z_1}}{n^2} n_z & \frac{\partial n_z}{\partial z_3} &= -\frac{\partial n_z}{\partial z_1} \\
\frac{\partial n_x}{\partial z_2} &= \frac{-d_{13y} n - n^{z_2} n_x}{n^2} & \frac{\partial n_x}{\partial z_4} &= -\frac{\partial n_x}{\partial z_2} \\
\frac{\partial n_y}{\partial z_2} &= \frac{d_{13x} n - n^{z_2} n_y}{n^2} & \frac{\partial n_y}{\partial z_4} &= -\frac{\partial n_y}{\partial z_2} \\
\frac{\partial n_z}{\partial z_2} &= -\frac{n^{z_2}}{n^2} n_z & \frac{\partial n_z}{\partial z_4} &= -\frac{\partial n_z}{\partial z_2}
\end{aligned}
$$

where the following quantities have been defined

$$
\begin{aligned}
n^{x_1} &= \frac{\partial n}{\partial x_1} = \frac{d_{24z}n_y - d_{24y}n_z}{n} = -\frac{\partial n}{\partial x_3} \\
n^{x_2} &= \frac{\partial n}{\partial x_2} = \frac{-d_{13z}n_y + d_{13y}n_z}{n} = -\frac{\partial n}{\partial x_4} \\
n^{y_1} &= \frac{\partial n}{\partial y_1} = \frac{-d_{24z}n_x + d_{24x}n_z}{n} = -\frac{\partial n}{\partial y_3} \\
n^{y_2} &= \frac{\partial n}{\partial y_2} = \frac{d_{13z}n_x - d_{13x}n_z}{n} = -\frac{\partial n}{\partial y_4} \\
n^{z_1} &= \frac{\partial n}{\partial z_1} = \frac{-d_{13y}n_x + d_{13x}n_y}{n} = -\frac{\partial n}{\partial z_3} \\
n^{z_2} &= \frac{\partial n}{\partial z_2} = \frac{d_{24y}n_x - d_{24x}n_y}{n} = -\frac{\partial n}{\partial z_4}
\end{aligned}
$$

This relations, representing the derivatives of the modulus of the vector product of the diagonals of the panel, are also useful in the evaluation of the derivatives of the area S when far-field equations are used (see eq.C.10).

Derivatives of unit vector $\boldsymbol{m}$ are now listed

$$\frac{\partial m_x}{\partial x_1} = -\frac{\frac{1}{4} + m_x m^{x_1}}{m} = \frac{\partial m_x}{\partial x_2}$$
$$\frac{\partial m_y}{\partial x_1} = -\frac{m_y m^{x_1}}{m} = \frac{\partial m_y}{\partial x_2}$$
$$\frac{\partial m_z}{\partial x_1} = -\frac{m_z m^{x_1}}{m} = \frac{\partial m_z}{\partial x_2}$$
$$\frac{\partial m_x}{\partial x_3} = -\frac{\partial m_x}{\partial x_1} = \frac{\partial m_x}{\partial x_4}$$
$$\frac{\partial m_y}{\partial x_3} = -\frac{\partial m_y}{\partial x_1} = \frac{\partial m_y}{\partial x_4}$$
$$\frac{\partial m_z}{\partial x_3} = -\frac{\partial m_z}{\partial x_1} = \frac{\partial m_z}{\partial x_4}$$
$$\frac{\partial m_x}{\partial z_1} = -\frac{m_x m^{z_1}}{m} = \frac{\partial m_y}{\partial z_2}$$
$$\frac{\partial m_y}{\partial z_1} = -\frac{m_y m^{z_1}}{m} = \frac{\partial m_y}{\partial z_2}$$
$$\frac{\partial m_z}{\partial z_1} = -\frac{\frac{1}{4} + m_z m^{z_1}}{m} = \frac{\partial m_z}{\partial z_2}$$
$$\frac{\partial m_x}{\partial y_1} = -\frac{m_x m^{y_1}}{m} = \frac{\partial m_y}{\partial y_2}$$
$$\frac{\partial m_y}{\partial y_1} = -\frac{\frac{1}{4} + m_y m^{y_1}}{m} = \frac{\partial m_y}{\partial y_2}$$
$$\frac{\partial m_z}{\partial y_1} = -\frac{m_z m^{y_1}}{m} = \frac{\partial m_z}{\partial y_2}$$
$$\frac{\partial m_x}{\partial y_3} = -\frac{\partial m_x}{\partial y_1} = \frac{\partial m_x}{\partial y_4}$$
$$\frac{\partial m_y}{\partial y_3} = -\frac{\partial m_y}{\partial y_1} = \frac{\partial m_y}{\partial y_4}$$
$$\frac{\partial m_z}{\partial y_3} = -\frac{\partial m_z}{\partial y_1} = \frac{\partial m_z}{\partial y_4}$$
$$\frac{\partial m_x}{\partial z_3} = -\frac{\partial m_x}{\partial z_1} = \frac{\partial m_x}{\partial z_4}$$
$$\frac{\partial m_y}{\partial z_3} = -\frac{\partial m_y}{\partial z_1} = \frac{\partial m_y}{\partial z_4}$$
$$\frac{\partial m_z}{\partial z_3} = -\frac{\partial m_z}{\partial z_1} = \frac{\partial m_z}{\partial z_4}$$

where

$$
\begin{aligned}
m^{x_1} &= \frac{\partial m}{\partial x_1} = -\frac{1}{4} m_x \\
m^{y_1} &= \frac{\partial m}{\partial y_1} = -\frac{1}{4} m_y \\
m^{z_1} &= \frac{\partial m}{\partial z_1} = -\frac{1}{4} m_z
\end{aligned}
$$

For the derivatives of unit vector $\boldsymbol{l}$ it holds

$$
\begin{aligned}
\frac{\partial l_x}{\partial x_1} &= \frac{\partial m_y}{\partial x_1} n_z + m_y \frac{\partial n_z}{\partial x_1} - \frac{\partial m_z}{\partial x_1} n_y - \frac{\partial n_y}{\partial x_1} m_z \\
\frac{\partial l_y}{\partial x_1} &= \frac{\partial n_x}{\partial x_1} m_z + n_x \frac{\partial m_z}{\partial x_1} - \frac{\partial m_x}{\partial x_1} n_z - \frac{\partial n_z}{\partial x_1} m_x \\
\frac{\partial l_z}{\partial x_1} &= \frac{\partial m_x}{\partial x_1} n_y + m_x \frac{\partial n_y}{\partial x_1} - \frac{\partial m_y}{\partial x_1} n_x - \frac{\partial n_x}{\partial x_1} m_y \\
\frac{\partial l_x}{\partial x_2} &= \frac{\partial m_y}{\partial x_2} n_z + m_y \frac{\partial n_z}{\partial x_2} - \frac{\partial m_z}{\partial x_2} n_y - \frac{\partial n_y}{\partial x_2} m_z \\
\frac{\partial l_y}{\partial x_2} &= \frac{\partial n_x}{\partial x_2} m_z + n_x \frac{\partial m_z}{\partial x_2} - \frac{\partial m_x}{\partial x_2} n_z - \frac{\partial n_z}{\partial x_2} m_x \\
\frac{\partial l_z}{\partial x_2} &= \frac{\partial m_x}{\partial x_2} n_y + m_x \frac{\partial n_y}{\partial x_2} - \frac{\partial m_y}{\partial x_2} n_x - \frac{\partial n_x}{\partial x_2} m_y \\
\frac{\partial l_x}{\partial x_3} &= \frac{\partial m_y}{\partial x_3} n_z + m_y \frac{\partial n_z}{\partial x_3} - \frac{\partial m_z}{\partial x_3} n_y - \frac{\partial n_y}{\partial x_3} m_z \\
\frac{\partial l_y}{\partial x_3} &= \frac{\partial n_x}{\partial x_3} m_z + n_x \frac{\partial m_z}{\partial x_3} - \frac{\partial m_x}{\partial x_3} n_z - \frac{\partial n_z}{\partial x_3} m_x \\
\frac{\partial l_z}{\partial x_3} &= \frac{\partial m_x}{\partial x_3} n_y + m_x \frac{\partial n_y}{\partial x_3} - \frac{\partial m_y}{\partial x_3} n_x - \frac{\partial n_x}{\partial x_3} m_y \\
\frac{\partial l_x}{\partial x_4} &= \frac{\partial m_y}{\partial x_4} n_z + m_y \frac{\partial n_z}{\partial x_4} - \frac{\partial m_z}{\partial x_4} n_y - \frac{\partial n_y}{\partial x_4} m_z \\
\frac{\partial l_y}{\partial x_4} &= \frac{\partial n_x}{\partial x_4} m_z + n_x \frac{\partial m_z}{\partial x_4} - \frac{\partial m_x}{\partial x_4} n_z - \frac{\partial n_z}{\partial x_4} m_x \\
\frac{\partial l_z}{\partial x_4} &= \frac{\partial m_x}{\partial x_4} n_y + m_x \frac{\partial n_y}{\partial x_4} - \frac{\partial m_y}{\partial x_4} n_x - \frac{\partial n_x}{\partial x_4} m_y
\end{aligned}
$$

$$
\begin{aligned}
\frac{\partial l_x}{\partial y_1} &= \frac{\partial m_y}{\partial x_1} n_z + m_y \frac{\partial n_z}{\partial y_1} - \frac{\partial m_z}{\partial y_1} n_y - \frac{\partial n_y}{\partial y_1} m_z \\
\frac{\partial l_y}{\partial y_1} &= \frac{\partial n_x}{\partial y_1} m_z + n_x \frac{\partial m_z}{\partial y_1} - \frac{\partial m_x}{\partial y_1} n_z - \frac{\partial n_z}{\partial y_1} m_x \\
\frac{\partial l_z}{\partial y_1} &= \frac{\partial m_x}{\partial y_1} n_y + m_x \frac{\partial n_y}{\partial y_1} - \frac{\partial m_y}{\partial y_1} n_x - \frac{\partial n_x}{\partial y_1} m_y \\
\frac{\partial l_x}{\partial y_2} &= \frac{\partial m_y}{\partial y_2} n_z + m_y \frac{\partial n_z}{\partial y_2} - \frac{\partial m_z}{\partial y_2} n_y - \frac{\partial n_y}{\partial y_2} m_z \\
\frac{\partial l_y}{\partial y_2} &= \frac{\partial n_x}{\partial y_2} m_z + n_x \frac{\partial m_z}{\partial y_2} - \frac{\partial m_x}{\partial y_2} n_z - \frac{\partial n_z}{\partial y_2} m_x \\
\frac{\partial l_z}{\partial y_2} &= \frac{\partial m_x}{\partial y_2} n_y + m_x \frac{\partial n_y}{\partial y_2} - \frac{\partial m_y}{\partial y_2} n_x - \frac{\partial n_x}{\partial y_2} m_y \\
\frac{\partial l_x}{\partial y_3} &= \frac{\partial m_y}{\partial y_3} n_z + m_y \frac{\partial n_z}{\partial y_3} - \frac{\partial m_z}{\partial y_3} n_y - \frac{\partial n_y}{\partial y_3} m_z \\
\frac{\partial l_y}{\partial y_3} &= \frac{\partial n_x}{\partial y_3} m_z + n_x \frac{\partial m_z}{\partial y_3} - \frac{\partial m_x}{\partial y_3} n_z - \frac{\partial n_z}{\partial y_3} m_x \\
\frac{\partial l_z}{\partial y_3} &= \frac{\partial m_x}{\partial y_3} n_y + m_x \frac{\partial n_y}{\partial y_3} - \frac{\partial m_y}{\partial y_3} n_x - \frac{\partial n_x}{\partial y_3} m_y \\
\frac{\partial l_x}{\partial y_4} &= \frac{\partial m_y}{\partial y_4} n_z + m_y \frac{\partial n_z}{\partial y_4} - \frac{\partial m_z}{\partial y_4} n_y - \frac{\partial n_y}{\partial y_4} m_z \\
\frac{\partial l_y}{\partial y_4} &= \frac{\partial n_x}{\partial y_4} m_z + n_x \frac{\partial m_z}{\partial y_4} - \frac{\partial m_x}{\partial y_4} n_z - \frac{\partial n_z}{\partial y_4} m_x \\
\frac{\partial l_z}{\partial y_4} &= \frac{\partial m_x}{\partial y_4} n_y + m_x \frac{\partial n_y}{\partial y_4} - \frac{\partial m_y}{\partial y_4} n_x - \frac{\partial n_x}{\partial y_4} m_y
\end{aligned}
$$

$$
\begin{aligned}
\frac{\partial l_x}{\partial z_1} &= \frac{\partial m_y}{\partial x_1} n_z + m_y \frac{\partial n_z}{\partial z_1} - \frac{\partial m_z}{\partial z_1} n_y - \frac{\partial n_y}{\partial z_1} m_z \\
\frac{\partial l_y}{\partial z_1} &= \frac{\partial n_x}{\partial z_1} m_z + n_x \frac{\partial m_z}{\partial z_1} - \frac{\partial m_x}{\partial z_1} n_z - \frac{\partial n_z}{\partial z_1} m_x \\
\frac{\partial l_z}{\partial z_1} &= \frac{\partial m_x}{\partial z_1} n_y + m_x \frac{\partial n_y}{\partial z_1} - \frac{\partial m_y}{\partial z_1} n_x - \frac{\partial n_x}{\partial z_1} m_y \\
\frac{\partial l_x}{\partial z_2} &= \frac{\partial m_y}{\partial z_2} n_z + m_y \frac{\partial n_z}{\partial z_2} - \frac{\partial m_z}{\partial z_2} n_y - \frac{\partial n_y}{\partial z_2} m_z \\
\frac{\partial l_y}{\partial z_2} &= \frac{\partial n_x}{\partial z_2} m_z + n_x \frac{\partial m_z}{\partial z_2} - \frac{\partial m_x}{\partial z_2} n_z - \frac{\partial n_z}{\partial z_2} m_x \\
\frac{\partial l_z}{\partial z_2} &= \frac{\partial m_x}{\partial z_2} n_y + m_x \frac{\partial n_y}{\partial z_2} - \frac{\partial m_y}{\partial z_2} n_x - \frac{\partial n_x}{\partial z_2} m_y \\
\frac{\partial l_x}{\partial z_3} &= \frac{\partial m_y}{\partial z_3} n_z + m_y \frac{\partial n_z}{\partial z_3} - \frac{\partial m_z}{\partial z_3} n_y - \frac{\partial n_y}{\partial z_3} m_z \\
\frac{\partial l_y}{\partial z_3} &= \frac{\partial n_x}{\partial z_3} m_z + n_x \frac{\partial m_z}{\partial z_3} - \frac{\partial m_x}{\partial z_3} n_z - \frac{\partial n_z}{\partial z_3} m_x \\
\frac{\partial l_z}{\partial z_3} &= \frac{\partial m_x}{\partial z_3} n_y + m_x \frac{\partial n_y}{\partial z_3} - \frac{\partial m_y}{\partial z_3} n_x - \frac{\partial n_x}{\partial z_3} m_y \\
\frac{\partial l_x}{\partial z_4} &= \frac{\partial m_y}{\partial z_4} n_z + m_y \frac{\partial n_z}{\partial z_4} - \frac{\partial m_z}{\partial z_4} n_y - \frac{\partial n_y}{\partial z_4} m_z \\
\frac{\partial l_y}{\partial z_4} &= \frac{\partial n_x}{\partial z_4} m_z + n_x \frac{\partial m_z}{\partial z_4} - \frac{\partial m_x}{\partial z_4} n_z - \frac{\partial n_z}{\partial z_4} m_x \\
\frac{\partial l_z}{\partial z_4} &= \frac{\partial m_x}{\partial z_4} n_y + m_x \frac{\partial n_y}{\partial z_4} - \frac{\partial m_y}{\partial z_4} n_x - \frac{\partial n_x}{\partial z_4} m_y
\end{aligned}
$$

Now $\frac{\partial \boldsymbol{B}}{\partial \boldsymbol{u}} \cdot \boldsymbol{\sigma}$ is considered. The equation that gives the perturbation potential for a source distribution of unitary strength is

$$
\begin{aligned}
\Phi^S = -\frac{1}{4\pi} \Bigg[& \frac{(x-x_1)y_{21} - (y-y_1)x_{21}}{d_{12}} \log\left(\frac{r_1 + r_2 + d_{12}}{r_1 + r_2 - d_{12}}\right) + \\
& + \frac{(x-x_2)y_{32} - (y-y_2)x_{32}}{d_{23}} \log\left(\frac{r_3 + r_2 + d_{23}}{r_3 + r_2 - d_{23}}\right) + \\
& + \frac{(x-x_3)y_{43} - (y-y_3)x_{43}}{d_{34}} \log\left(\frac{r_3 + r_4 + d_{34}}{r_3 + r_4 - d_{34}}\right) + \\
& + \frac{(x-x_4)y_{14} - (y-y_4)x_{14}}{d_{41}} \log\left(\frac{r_4 + r_1 + d_{41}}{r_4 + r_1 - d_{41}}\right) \Bigg] - z\Phi^D
\end{aligned}
\tag{C.15}
$$

When the receiving point is far from the center of the receiving panel (x_0,y_0,0) and thus the far-field approximation is possible, the influence of the quadrilateral element with area S can

be approximated by a point source

$$\Phi^S = \frac{S}{4\pi\sqrt{x^2+y^2+z^2}} \tag{C.16}$$

The constants here adopted are the same of eq.(C.3).

The case of perturbed vertex thought as belonging to the receiving panel is first presented. The derivatives of the potential Φ^S with respect to the coordinates of the receiving point when eq.(C.16) is valid are given by

$$\begin{aligned}
\frac{\partial\Phi^S}{\partial x} &= -\frac{S}{4\pi}\frac{(x-x_0)}{d^3} \\
\frac{\partial\Phi^S}{\partial y} &= -\frac{S}{4\pi}\frac{(y-y_0)}{d^3} \\
\frac{\partial\Phi^S}{\partial z} &= -\frac{S}{4\pi}\frac{z}{d^3}
\end{aligned} \tag{C.17}$$

The derivatives in the general case (close-field) are given by

$$\begin{aligned}
\frac{\partial\Phi^S}{\partial x} = \frac{1}{4\pi}\Bigg\{ & \frac{y_{21}}{d_{12}}\log\frac{r_1+r_2+d_{12}}{r_1+r_2-d_{12}} - \frac{2[(x-x_1)y_{21}-(y-y_1)x_{21}](r_1^x+r_2^x)}{(r_1+r_2+d_{12})(r_1+r_2-d_{12})} + \\
& + \frac{y_{32}}{d_{23}}\log\frac{r_3+r_2+d_{23}}{r_3+r_2-d_{23}} - \frac{2[(x-x_2)y_{32}-(y-y_2)x_{32}](r_2^x+r_3^x)}{(r_3+r_2+d_{23})(r_3+r_2-d_{23})} \\
& + \frac{y_{43}}{d_{34}}\log\frac{r_3+r_4+d_{34}}{r_3+r_4-d_{34}} - \frac{2[(x-x_3)y_{43}-(y-y_3)x_{43}](r_4^x+r_3^x)}{(r_3+r_4+d_{34})(r_3+r_4-d_{34})} \\
& + \frac{y_{14}}{d_{41}}\log\frac{r_1+r_4+d_{41}}{r_1+r_4-d_{41}} - \frac{2[(x-x_4)y_{14}-(y-y_4)x_{14}](r_4^x+r_1^x)}{(r_1+r_4+d_{41})(r_1+r_4-d_{41})}\Bigg\} + \\
& -z\frac{\partial\Phi^D}{\partial x}
\end{aligned}$$

$$\begin{aligned}
\frac{\partial\Phi^S}{\partial y} = -\frac{1}{4\pi}\Bigg\{ & \frac{x_{21}}{d_{12}}\log\frac{r_1+r_2+d_{12}}{r_1+r_2-d_{12}} + \frac{2[(x-x_1)y_{21}-(y-y_1)x_{21}](r_1^y+r_2^y)}{(r_1+r_2+d_{12})(r_1+r_2-d_{12})} + \\
& + \frac{x_{32}}{d_{23}}\log\frac{r_3+r_2+d_{23}}{r_3+r_2-d_{23}} + \frac{2[(x-x_2)y_{32}-(y-y_2)x_{32}](r_2^y+r_3^y)}{(r_3+r_2+d_{23})(r_3+r_2-d_{23})} \\
& + \frac{x_{43}}{d_{34}}\log\frac{r_3+r_4+d_{34}}{r_3+r_4-d_{34}} + \frac{2[(x-x_3)y_{43}-(y-y_3)x_{43}](r_4^y+r_3^y)}{(r_3+r_4+d_{34})(r_3+r_4-d_{34})} \\
& + \frac{x_{14}}{d_{41}}\log\frac{r_1+r_4+d_{41}}{r_1+r_4-d_{41}} + \frac{2[(x-x_4)y_{14}-(y-y_4)x_{14}](r_4^y+r_1^y)}{(r_1+r_4+d_{41})(r_1+r_4-d_{41})}\Bigg\} + \\
& -z\frac{\partial\Phi^D}{\partial y}
\end{aligned}$$

$$\frac{\partial\Phi^S}{\partial z} = -\frac{1}{2\pi}\left\{\frac{[(x-x_1)y_{21}-(y-y_1)x_{21}](r_1^z+r_2^z)}{(r_1+r_2+d_{12})(r_1+r_2-d_{12})}+\frac{[(x-x_2)y_{32}-(y-y_2)x_{32}](r_2^z+r_3^z)}{(r_3+r_2+d_{23})(r_3+r_2-d_{23})}+\right.$$
$$\left.+\frac{[(x-x_3)y_{43}-(y-y_3)x_{43}](r_4^z+r_3^z)}{(r_3+r_4+d_{34})(r_3+r_4-d_{34})}+\frac{[(x-x_4)y_{14}-(y-y_4)x_{14}](r_4^z+r_1^z)}{(r_1+r_4+d_{41})(r_1+r_4-d_{41})}\right\}+$$
$$-\Phi^D - z\frac{\partial\Phi^D}{\partial z}$$

The case of perturbed vertex thought as belonging to the emitting panel is now considered. In case of validity of eq.(C.16), the derivatives of the perturbation potential are

$$\frac{\partial\Phi^S}{\partial x_1} = \frac{\partial S}{\partial x_1}\frac{1}{4\pi d} \qquad \frac{\partial\Phi^S}{\partial y_1} = \frac{\partial S}{\partial y_1}\frac{1}{4\pi d}$$
$$\frac{\partial\Phi^S}{\partial x_2} = \frac{\partial S}{\partial x_2}\frac{1}{4\pi d} \qquad \frac{\partial\Phi^S}{\partial y_2} = \frac{\partial S}{\partial y_2}\frac{1}{4\pi d}$$
$$\frac{\partial\Phi^S}{\partial x_3} = \frac{\partial S}{\partial x_3}\frac{1}{4\pi d} \qquad \frac{\partial\Phi^S}{\partial y_3} = \frac{\partial S}{\partial y_3}\frac{1}{4\pi d}$$
$$\frac{\partial\Phi^S}{\partial x_4} = \frac{\partial S}{\partial x_4}\frac{1}{4\pi d} \qquad \frac{\partial\Phi^S}{\partial y_4} = \frac{\partial S}{\partial y_4}\frac{1}{4\pi d}$$

For the general case when just close-field relations are adopted, the derivatives with respect to the x coordinates are

$$\frac{\partial\Phi^S}{\partial x_1} = -\frac{1}{4\pi}\left\{\frac{[-y_{21}+(y-y_1)]d_{12}-[(x-x_1)y_{21}-(y-y_1)x_{21}]d_{12}^{x_1}}{d_{12}^2}\log\left(\frac{r_1+r_2+d_{12}}{r_1+r_2-d_{12}}\right)+\right.$$
$$+\frac{[y_{21}(x-x_1)-(y-y_1)x_{21}][(r_1^{x_1}+d_{12}^{x_1})(r_1+r_2-d_{12})-(r_1^{x_1}-d_{12}^{x_1})(r_1+r_2+d_{12})]}{d_{12}(r_1+r_2+d_{12})(r_1+r_2-d_{12})}+$$
$$+\frac{-(y-y_4)d_{41}-[(x-x_4)y_{14}-(y-y_4)x_{14}]d_{41}^{x_1}}{d_{41}^2}\log\left(\frac{r_1+r_4+d_{41}}{r_1+r_4-d_{41}}\right)+$$
$$\left.+\frac{[y_{14}(x-x_4)-(y-y_4)x_{14}][(r_1^{x_1}+d_{41}^{x_1})(r_1+r_4-d_{41})-(r_1^{x_1}-d_{41}^{x_1})(r_1+r_4+d_{41})]}{d_{41}(r_1+r_4+d_{41})(r_1+r_4-d_{41})}\right\}+$$
$$-z\frac{\partial\Phi^D}{\partial x_1}$$

$$\frac{\partial\Phi^S}{\partial x_2} = -\frac{1}{4\pi}\left\{\frac{-(y-y_1)d_{12}-[(x-x_1)y_{21}-(y-y_1)x_{21}]d_{12}^{x_2}}{d_{12}^2}\log\left(\frac{r_1+r_2+d_{12}}{r_1+r_2-d_{12}}\right)+\right.$$
$$+\frac{[y_{21}(x-x_1)-(y-y_1)x_{21}][(r_2^{x_2}+d_{12}^{x_2})(r_1+r_2-d_{12})-(r_2^{x_2}-d_{12}^{x_2})(r_1+r_2+d_{12})]}{d_{12}(r_1+r_2+d_{12})(r_1+r_2-d_{12})}+$$
$$+\frac{[-y_{32}+(y-y_2)]d_{23}-[(x-x_2)y_{32}-(y-y_2)x_{32}]d_{23}^{x_2}}{d_{23}^2}\log\left(\frac{r_3+r_2+d_{23}}{r_3+r_2-d_{23}}\right)+$$
$$\left.+\frac{[y_{32}(x-x_2)-(y-y_2)x_{32}][(r_2^{x_2}+d_{23}^{x_2})(r_2+r_3-d_{23})-(r_2^{x_2}-d_{23}^{x_2})(r_2+r_3+d_{23})]}{d_{23}(r_2+r_3+d_{23})(r_2+r_3-d_{23})}\right\}+$$
$$-z\frac{\partial\Phi^D}{\partial x_2}$$

$$\frac{\partial \Phi^S}{\partial x_3} = -\frac{1}{4\pi}\Bigg\{\frac{-(y-y_2)d_{23}-[(x-x_2)y_{32}-(y-y_2)x_{32}]d_{23}^{x_3}}{d_{23}^2}\log\left(\frac{r_3+r_2+d_{23}}{r_3+r_2-d_{23}}\right)+$$
$$+\frac{[y_{32}(x-x_2)-(y-y_2)x_{32}][(r_3^{x_3}+d_{23}^{x_3})(r_2+r_3-d_{23})-(r_3^{x_3}-d_{23}^{x_3})(r_2+r_3+d_{23})]}{d_{23}(r_2+r_3+d_{23})(r_2+r_3-d_{23})}+$$
$$+\frac{[-y_{43}+(y-y_3)]d_{34}-[(x-x_3)y_{43}-(y-y_3)x_{43}]d_{34}^{x_3}}{d_{34}^2}\log\left(\frac{r_3+r_4+d_{34}}{r_3+r_4-d_{34}}\right)+$$
$$+\frac{[y_{43}(x-x_3)-(y-y_3)x_{43}][(r_3^{x_3}+d_{34}^{x_3})(r_4+r_3-d_{34})-(r_3^{x_3}-d_{34}^{x_3})(r_4+r_3+d_{34})]}{d_{34}(r_4+r_3+d_{34})(r_4+r_3-d_{34})}\Bigg\}+$$
$$-z\frac{\partial \Phi^D}{\partial x_3}$$

$$\frac{\partial \Phi^S}{\partial x_4} = -\frac{1}{4\pi}\Bigg\{\frac{-(y-y_3)d_{34}-[(x-x_3)y_{43}-(y-y_3)x_{43}]d_{34}^{x_4}}{d_{34}^2}\log\left(\frac{r_3+r_4+d_{34}}{r_3+r_4-d_{34}}\right)+$$
$$+\frac{[y_{43}(x-x_3)-(y-y_3)x_{43}][(r_4^{x_4}+d_{34}^{x_4})(r_4+r_3-d_{34})-(r_4^{x_4}-d_{34}^{x_4})(r_4+r_3+d_{34})]}{d_{34}(r_4+r_3+d_{34})(r_4+r_3-d_{34})}+$$
$$+\frac{[-y_{14}+(y-y_4)]d_{41}-[(x-x_4)y_{14}-(y-y_4)x_{14}]d_{41}^{x_4}}{d_{41}^2}\log\left(\frac{r_1+r_4+d_{41}}{r_1+r_4-d_{41}}\right)+$$
$$+\frac{[y_{14}(x-x_4)-(y-y_4)x_{14}][(r_4^{x_4}+d_{41}^{x_4})(r_4+r_1-d_{41})-(r_4^{x_4}-d_{41}^{x_4})(r_4+r_1+d_{41})]}{d_{41}(r_4+r_1+d_{41})(r_4+r_1-d_{41})}\Bigg\}+$$
$$-z\frac{\partial \Phi^D}{\partial x_4}$$

The derivatives with respect to the y coordinates are

$$\frac{\partial \Phi^S}{\partial y_1} = -\frac{1}{4\pi}\Bigg\{\frac{[x_{21}-(x-x_1)]d_{12}-[(x-x_1)y_{21}-(y-y_1)x_{21}]d_{12}^{y_1}}{d_{12}^2}\log\left(\frac{r_1+r_2+d_{12}}{r_1+r_2-d_{12}}\right)+$$
$$+\frac{[y_{21}(x-x_1)-(y-y_1)x_{21}][(r_1^{y_1}+d_{12}^{y_1})(r_1+r_2-d_{12})-(r_1^{y_1}-d_{12}^{y_1})(r_1+r_2+d_{12})]}{d_{12}(r_1+r_2+d_{12})(r_1+r_2-d_{12})}+$$
$$+\frac{(x-x_4)d_{41}-[(x-x_4)y_{14}-(y-y_4)x_{14}]d_{41}^{y_1}}{d_{41}^2}\log\left(\frac{r_1+r_4+d_{41}}{r_1+r_4-d_{41}}\right)+$$
$$+\frac{[y_{14}(x-x_4)-(y-y_4)x_{14}][(r_1^{y_1}+d_{41}^{y_1})(r_1+r_4-d_{41})-(r_1^{y_1}-d_{41}^{y_1})(r_1+r_4+d_{41})]}{d_{41}(r_1+r_4+d_{41})(r_1+r_4-d_{41})}\Bigg\}+$$
$$-z\frac{\partial \Phi^D}{\partial y_1}$$

$$\frac{\partial \Phi^S}{\partial y_2} = -\frac{1}{4\pi}\Bigg\{\frac{(x-x_1)d_{12}-[(x-x_1)y_{21}-(y-y_1)x_{21}]d_{12}^{y_2}}{d_{12}^2}\log\left(\frac{r_1+r_2+d_{12}}{r_1+r_2-d_{12}}\right)+$$
$$+\frac{[y_{21}(x-x_1)-(y-y_1)x_{21}][(r_2^{y_2}+d_{12}^{y_2})(r_1+r_2-d_{12})-(r_2^{y_2}-d_{12}^{y_2})(r_1+r_2+d_{12})]}{d_{12}(r_1+r_2+d_{12})(r_1+r_2-d_{12})}+$$
$$+\frac{[-x_{32}+(x-x_2)]d_{23}-[(x-x_2)y_{32}-(y-y_2)x_{32}]d_{23}^{y_2}}{d_{23}^2}\log\left(\frac{r_3+r_2+d_{23}}{r_3+r_2-d_{23}}\right)+$$
$$+\frac{[y_{32}(x-x_2)-(y-y_2)x_{32}][(r_2^{y_2}+d_{23}^{y_2})(r_2+r_3-d_{23})-(r_2^{y_2}-d_{23}^{y_2})(r_2+r_3+d_{23})]}{d_{23}(r_2+r_3+d_{23})(r_2+r_3-d_{23})}\Bigg\}+$$
$$-z\frac{\partial \Phi^D}{\partial y_2}$$

$$\frac{\partial \Phi^S}{\partial y_3} = -\frac{1}{4\pi}\Bigg\{\frac{(x-x_2)d_{23}-[(x-x_2)y_{32}-(y-y_2)x_{32}]d_{23}^{y_3}}{d_{23}^2}\log\left(\frac{r_3+r_2+d_{23}}{r_3+r_2-d_{23}}\right)+$$
$$+\frac{[y_{32}(x-x_2)-(y-y_2)x_{32}][(r_3^{y_3}+d_{23}^{y_3})(r_2+r_3-d_{23})-(r_3^{y_3}-d_{23}^{y_3})(r_2+r_3+d_{23})]}{d_{23}(r_2+r_3+d_{23})(r_2+r_3-d_{23})}+$$
$$+\frac{[x_{43}+(x-x_3)]d_{34}-[(x-x_3)y_{43}-(y-y_3)x_{43}]d_{34}^{y_3}}{d_{34}^2}\log\left(\frac{r_3+r_4+d_{34}}{r_3+r_4-d_{34}}\right)+$$
$$+\frac{[y_{43}(x-x_3)-(y-y_3)x_{43}][(r_3^{y_3}+d_{34}^{y_3})(r_4+r_3-d_{34})-(r_3^{y_3}-d_{34}^{y_3})(r_4+r_3+d_{34})]}{d_{34}(r_4+r_3+d_{34})(r_4+r_3-d_{34})}\Bigg\}+$$
$$-z\frac{\partial \Phi^D}{\partial y_3}$$

$$\frac{\partial \Phi^S}{\partial y_4} = -\frac{1}{4\pi}\Bigg\{\frac{-(x-x_3)d_{34}-[(x-x_3)y_{43}-(y-y_3)x_{43}]d_{34}^{y_4}}{d_{34}^2}\log\left(\frac{r_3+r_4+d_{34}}{r_3+r_4-d_{34}}\right)+$$
$$+\frac{[y_{43}(x-x_3)-(y-y_3)x_{43}][(r_4^{y_4}+d_{34}^{y_4})(r_4+r_3-d_{34})-(r_4^{y_4}-d_{34}^{y_4})(r_4+r_3+d_{34})]}{d_{34}(r_4+r_3+d_{34})(r_4+r_3-d_{34})}+$$
$$+\frac{[x_{14}-(x-x_4)]d_{41}-[(x-x_4)y_{14}-(y-y_4)x_{14}]d_{41}^{y_4}}{d_{41}^2}\log\left(\frac{r_1+r_4+d_{41}}{r_1+r_4-d_{41}}\right)+$$
$$+\frac{[x_{14}(y-y_4)-(y-y_4)x_{14}][(r_4^{y_4}+d_{41}^{y_4})(r_4+r_1-d_{41})-(r_4^{y_4}-d_{41}^{y_4})(r_4+r_1+d_{41})]}{d_{41}(r_4+r_1+d_{41})(r_4+r_1-d_{41})}\Bigg\}+$$
$$-z\frac{\partial \Phi^D}{\partial y_4}$$

The following constants have been defined

$$
\begin{aligned}
d_{12}^{x_1} &= \frac{\partial d_{12}}{\partial x_1} = -\frac{x_{21}}{\sqrt{x_{21}^2 + y_{21}^2}} & \qquad d_{12}^{y_1} &= \frac{\partial d_{12}}{\partial y_1} = -\frac{y_{21}}{\sqrt{x_{21}^2 + y_{21}^2}} \\
d_{41}^{x_1} &= \frac{\partial d_{41}}{\partial x_1} = -\frac{x_{14}}{\sqrt{x_{14}^2 + y_{14}^2}} & \qquad d_{41}^{y_1} &= \frac{\partial d_{41}}{\partial y_1} = -\frac{y_{14}}{\sqrt{x_{14}^2 + y_{14}^2}} \\
d_{12}^{x_2} &= \frac{\partial d_{12}}{\partial x_2} = -d_{12}^{x_1} & \qquad d_{12}^{y_2} &= \frac{\partial d_{12}}{\partial y_2} = -d_{12}^{y_1} \\
d_{23}^{x_2} &= \frac{\partial d_{23}}{\partial x_2} = -\frac{x_{32}}{\sqrt{x_{32}^2 + y_{32}^2}} & \qquad d_{23}^{y_2} &= \frac{\partial d_{23}}{\partial y_2} = -\frac{y_{32}}{\sqrt{x_{32}^2 + y_{32}^2}} \\
d_{23}^{x_3} &= \frac{\partial d_{23}}{\partial x_3} = -d_{23}^{x_2} & \qquad d_{23}^{y_3} &= \frac{\partial d_{23}}{\partial y_3} = -d_{23}^{y_2} \\
d_{34}^{x_3} &= \frac{\partial d_{34}}{\partial x_3} = -\frac{x_{43}}{\sqrt{x_{43}^2 + y_{43}^2}} & \qquad d_{34}^{y_3} &= \frac{\partial d_{34}}{\partial y_3} = -\frac{y_{43}}{\sqrt{x_{43}^2 + y_{43}^2}} \\
d_{34}^{x_4} &= \frac{\partial d_{34}}{\partial x_4} = -d_{34}^{x_3} & \qquad d_{34}^{y_4} &= \frac{\partial d_{34}}{\partial y_4} = -d_{34}^{y_3} \\
d_{41}^{x_4} &= \frac{\partial d_{41}}{\partial x_4} = -d_{41}^{x_1} & \qquad d_{41}^{y_4} &= \frac{\partial d_{41}}{\partial y_4} = -d_{41}^{y_1}
\end{aligned}
$$

C.2 Sensitivity of pressure in respect to doublet strength

The term $\left(\frac{\partial \boldsymbol{p}}{\partial \boldsymbol{\mu}}\right)$, where $\left(\frac{\partial p_k}{\partial \mu}{}_i\right)$ representing the variation of pressure on panel k when the intensity of the doublet i changes, can be performed starting from the Bernoulli theorem for the unsteady case, which leads to

$$
\begin{aligned}
\Delta p = p - p_\infty &= -\frac{1}{2}\rho\left(|\nabla\phi + \rho \boldsymbol{V}_\infty|\right)^2 - \rho\frac{\partial\phi}{\partial t} \\
&= -\frac{1}{2}\rho|\nabla\phi|^2 - \rho\boldsymbol{V}_\infty \cdot \nabla\phi - \rho\frac{\partial\phi}{\partial t}
\end{aligned}
\tag{C.18}
$$

Since in the collocation points of the body it holds

$$
\phi = \mu \tag{C.19}
$$

eq.(C.18), applied to panel k, can be derivated with respect to μ_i

$$
\begin{aligned}
\frac{\partial \Delta p_k}{\partial \mu_i} &= -\frac{1}{2}\rho\frac{\partial|\nabla\phi_k|^2}{\partial\mu_i} - \rho\frac{\partial\left(\boldsymbol{V}_\infty \cdot \nabla\phi_k\right)}{\partial\mu_i} - \rho\frac{\partial\left(\frac{\partial\phi_k}{\partial t}\right)}{\partial\mu_i} \\
&= -\frac{1}{2}\rho\nabla\mu_k \cdot \frac{\partial\nabla\mu_k}{\partial\mu_i} - \rho\boldsymbol{V}_\infty \cdot \frac{\partial\nabla\mu_k}{\partial\mu_i} - \rho\frac{\partial\left(\frac{\partial\mu_k}{\partial t}\right)}{\partial\mu_i}
\end{aligned}
\tag{C.20}
$$

The term $\frac{\partial\left(\frac{\partial \mu_k}{\partial t}\right)}{\partial \mu_i}$ is evaluated discretizing the time derivative with a first order backward finite difference scheme

$$\frac{\partial \mu_k}{\partial t} = \frac{\mu_k^T - \mu_k^{T-\Delta T}}{\Delta T} \tag{C.21}$$

leading to

$$\frac{\partial\left(\frac{\partial \mu_k}{\partial t}\right)}{\partial \mu_i} = \frac{1}{\Delta T}\delta_{ki} \tag{C.22}$$

The term $\frac{\partial \nabla \mu_k}{\partial \mu_i}$ is constructed using a finite difference scheme for

$$\nabla \mu_k = \left(\frac{\partial \mu_k}{\partial x}, \frac{\partial \mu_k}{\partial y}\right) \tag{C.23}$$

In eq.(C.23) it is not reported the derivative with respect to z because the gradient is performed along the local directions and therefore, when considering a variation along the direction perpendicular to the doublet plane, it is not more true that $\phi = \mu$. The notation $\frac{\partial \mu_k}{\partial z}$ would not be consistent with the rest of the treatise. This, however, is not a big deal because it holds

$$\frac{\partial \phi_k}{\partial z} = -\sigma_k \tag{C.24}$$

and thus this derivative does not give a contribution in eq.(C.20). The schemes adopted vary depending on the position of panel k, since it doesn't always have the same number of neighbours in the specified direction. In Fig.(C.2) are presented the different possible cases. In the following l is assumed as direction of derivation (local x axis); of course same strategy is applied for direction m.

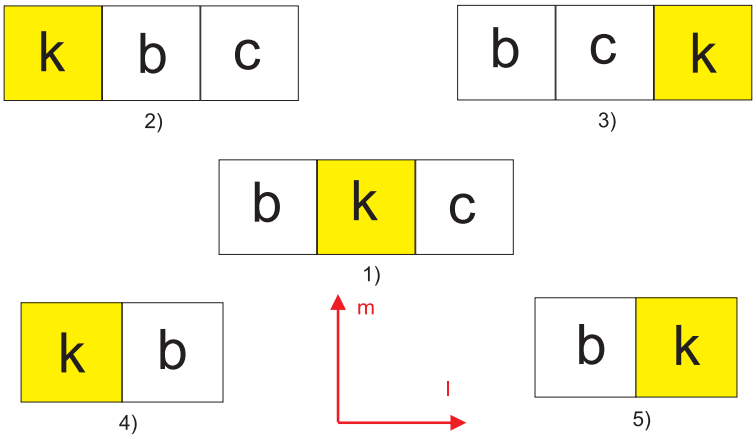

Fig. C.2: Schemes for finite difference discretization of $\nabla \mu_k$

In the following equations kc, kb, kc, ek, ce, bc are the distances among the correspondent panels. Scheme 1 is centered 2^{nd} order and is used whenever panel k has a neighbour on both sides.

$$\frac{\partial \mu_k}{\partial x} = \left(\frac{\mu_c - \mu_k}{kc} kb + \frac{\mu_k - \mu_b}{kb} kc \right) \frac{1}{bc} \tag{C.25}$$

Scheme 2 is forward 2^{nd} order and is used when panel k has no neighbour on left side but two on the other

$$\begin{aligned} \frac{\partial \mu_k}{\partial x} =& -2ab \left[-\frac{\mu_b - \mu_k}{kb^2} + \left(\frac{\mu_b - \mu_k}{kb} bc + \frac{\mu_c - \mu_b}{bc} kb \right) \frac{1}{kc \cdot kb} \right] + \\ &+ \left(\frac{\mu_b - \mu_k}{kb} bc + \frac{\mu_c - \mu_b}{bc} kb \right) \frac{1}{kc} \end{aligned} \tag{C.26}$$

Scheme 3 is back 2^{nd} order and is used when panel k has no neighbour on right side but two on the other

$$\begin{aligned} \frac{\partial \mu_k}{\partial x} =& 2ab \left[-\frac{\mu_b - \mu_k}{bc^2} + \left(\frac{\mu_b - \mu_c}{cb} kb + \frac{\mu_k - \mu_b}{kb} bc \right) \frac{1}{kc \cdot bc} \right] \\ &+ \left(\frac{\mu_b - \mu_c}{bc} kb + \frac{\mu_k - \mu_b}{kb} bc \right) \frac{1}{kc} \end{aligned} \tag{C.27}$$

Scheme 4 is forward 1^{st} order and is used when panel k has no neighbour on left side and just on the other

$$\frac{\partial \mu_k}{\partial x} = \frac{\mu_b - \mu_k}{kb} \tag{C.28}$$

Scheme 5 is backword 1^{st} order and is used when panel k has no neighbour on right side and just on the other

$$\frac{\partial \mu_k}{\partial x} = \frac{\mu_k - \mu_b}{kb} \tag{C.29}$$

The square matrix $\left(\frac{\partial \boldsymbol{p}}{\partial \boldsymbol{\mu}} \right)$ with dimension $N_{pan} \cdot N_{pan}$ can finally be evaluated. When assembling its k-row $\left(\frac{\partial \boldsymbol{p}}{\partial \boldsymbol{\mu}} \right)_{k,:}$, an algorithm provide the case under investigation and one of the previously equation is used. Depending on the scheme, this row will have a different number of non-zero elements: the diagonal term is always present (with both contributions from eq.(C.22) and from eq.(C.23)), while the extra-diagonal terms will vary from 2 to 4.

Bibliography

[1] Vision 2020: Strategic research agenda, October 2002.

[2] E. Albano and W.P. Rodden. A doublet lattice method for calculating lift distributions on oscillating surfaces in subsonic flows. *American Institute of Aeronautics and Astronautics*, 7:279–285, 1968.

[3] Eugene L. Allgower and Kurt Georg. Continuation and path following. *Acta Numerica*, 2:1–64, 1993.

[4] T. D. AlMomani, S. C. Vigmostad, and L. A. Alzube. A sharp-interface fluid-structure interaction algorithm for modeling red blood cells. *Jordan Journal of Mechanical & Industrial Engineering*, 6(2):193 – 198, 2012.

[5] S. Ananthan, J. G. Leishman, and M. Ramasamy. The role of filament stretching in the free-vortex modeling of rotor wakes. 58th Annual Forum and Technology Display of the american Helicopter Society International, Montreal, Canada, 11-13 June 2002.

[6] Sunil Arya, David M. Mount, Nathan S. Netanyahu, Ruth Silverman, and Angela Y. Wu. An optimal algorithm for approximate nearest neighbor searching fixed dimensions. *J. ACM*, 45(6):891–923, November 1998.

[7] Peter J. Attar, Earl H. Dowell, and J.R. White. Modeling the lco of a delta wing using a high fidelity structural model. volume 3, pages 1986 – 2000, 2004.

[8] J. C. A. Barata and M. S. Hussein. The moore-penrose pseudoinverse. a tutorial review of the theory. 2011.

[9] K. J. Bathe. Finite element procedures. 1996. Prentice Hall, Englewood Cliffs, NJ, USA.

[10] Olivier A. Bauchau and YuriG. Nikishkov. An implicit transition matrix approach to stability analysis of flexible multi-body systems. *Multibody System Dynamics*, 5(3):279–301, 2001.

[11] T. Belytschko, W.K. Liu, and B. Moran. *Nonlinear finite elements for continua and structures*. Wiley, 2000.

[12] T. Belytschko and D. F. Schoeberle. On the unconditional stability of an implicit algorithm for nonlinear structural dynamics. *Journal of Applied Mechanics*, 42(4):865–869, 1975.

[13] G. Bernardini. *Problematiche Aerodinamiche Relative alla Progettazione di Configurazioni Innovative*. PhD thesis, Politecnico di Milano, Nov 1999.

[14] J.J. Bertin and M.L. Smith. *Aerodynamics for engineers*. Prentice-Hall, 1979.

[15] R.L. Bisplinghoff and H. Ashley. *Principles of Aeroelasticity*. Dover Phoenix Editions. Dover Publications, 2002.

[16] Michael P. Brenner, Shang-You Tee, David A. Weitz, and Boris I. Shraiman. A model for velocity fluctuations in sedimentation. *Journal of Fluid Mechanics*, 501:71–104, 2004.

[17] R.L. Campbell and E.G. Paterson. Fluid structure interaction analysis of flexible turbomachinery. *Journal of Fluids and Structures*, 27(8):1376 – 1391, 2011.

[18] J. Carr. *Applications of Centre Manifold Theory*. Number v. 35 in Applied Mathematical Sciences Series. Springer-Verlag, 1981.

[19] Rauno Cavallaro, Luciano Demasi, and Federica Bertuccelli. Risks of linear design of Joined Wings: a nonlinear dynamic perspective in the presence of follower forces. Number AIAA 2013-1558. 54rd AIAA/ASME/ASCE/AHS/ASC Structures, Structural Dynamics, and Materials Conference, Boston, Massachusetts, American Institute of Aeronautics and Astronautics, 8-11 April 2013.

[20] Rauno Cavallaro, Luciano Demasi, and Andrea Passariello. Nonlinear analysis of PrandtlPlane Joined Wings - part ii: Effects of anisotropy. Number AIAA 2012-1462. 53rd AIAA/ASME/ASCE/AHS/ASC Structures, Structural Dynamics, and Materials Conference, Honolulu, Hawaii, 23-26 April 2012.

[21] Rauno Cavallaro, Luciano Demasi, and Andrea Passariello. Nonlinear analysis of PrandtlPlane Joined Wings: Effects of anisotropy. *AIAA Journal*, 2014. In press.

[22] Juan Raul Cebral and Rainald Lohner. Conservative load projection and tracking for fluid-structure problems. *AIAA Journal*, Vol. 35(No. 4):pp. 687–692, 1997.

[23] George Celniker and Dave Gossard. Deformable curve and surface finite-elements for free-form shape design. *SIGGRAPH Comput. Graph.*, 25(4):257–266, July 1991.

[24] J. R. Chambers. *Innovation in Flight: Research of the NASA Langley Research Center on Revolutionary Advanced Concepts for Aeronautics*. Number 39 in Monograph in Aerospace History. NASA, November 2005. NASA SP 2005-4539.

[25] J. Chung and G. M. Hulbert. A time integration algorithm for structural dynamics with improved numerical dissipation: The generalized-alpha method. *Journal of Applied Mechanics*, 60(2):371–375, 1993.

[26] Vittorio Cipolla and Aldo Frediani. Design of solar powered unmanned biplanes for hale missions. In Giuseppe Buttazzo and Aldo Frediani, editors, *Variational Analysis and Aerospace Engineering: Mathematical Challenges for Aerospace Design*, volume 66 of *Springer Optimization and Its Applications*, pages 141–177. Springer US, 2012. 10.1007/978-1-4614-2435-2_7.

[27] P. Collet and J.P. Eckmann. *Iterated Maps on the Interval as Dynamical Systems*. Modern Birkhäuser Classics. Birkhäuser Boston, 2009.

[28] M.A. Crisfield. *Non Linear Finite Element Analysis of Solid and Structures*, volume 2. John Wiley & Sons, 1991.

[29] C. De Souza, R.G. Da Silva, and C. Cesnik. Nonlinear aeroelastic framework based on vortex-lattice method and corotational shell finite element. Number AIAA 2012-1976. 53rd, AIAA/ASME/ASME/ASCE/AHS/ASC Structures, structural dynamics and materials, Honolulu, Hawaii, American Institute of Aeronautics and Astronautics, 23-26 April 2012.

[30] L. Demasi, R. Cavallaro, and A.M Razon. Post-critical analysis of PrandtlPlane joined-wing configurations. *AIAA Journal*, 51(1):161–177, 2013.

[31] L. Demasi and E. Livne. Aeroelastic coupling of geometrically nonlinear structures and linear unsteady aerodynamics: Two formulations. *Journal of Fluids and Structures*, 25(5):918 – 935, 2009.

[32] L. Demasi and E. Livne. Dynamic Aeroelasticity of Structurally Nonlinear Configurations Using Linear Modally Reduced Aerodynamic Generalized Forces. *AIAA Journal*, 47:71–90, 2009.

[33] L. Demasi and A. Palacios. A Reduced Order Nonlinear Aeroelastic Analysis of Joined Wings Based on the Proper Orthogonal Decomposition. 2010. Presented at the 51st AIAA/ASME/ASCE/AHS/ASC Structures, Structural Dynamics & Materials Conference, Orlando, Florida, 12-15 April 2010.

[34] Luciano Demasi, Rauno Cavallaro, and Federica Bertuccelli. Post-critical analysis of Joined Wings: the concept of snap-divergence as a characterization of the instability. Number AIAA 2013-1559. 54rd AIAA/ASME/ASCE/AHS/ASC Structures, Structural Dynamics, and Materials Conference, Boston, Massachusetts, American Institute of Aeronautics and Astronautics, 8-11 April 2013.

[35] S. Dong. Bdf-like methods for nonlinear dynamic analysis. *Journal of Computational Physics*, 229(8):3019 – 3045, 2010.

[36] Earl Dowell, John Edwards, and Thomas Strganac. Nonlinear aeroelasticity. *Journal of Aircraft*, 40(5):857–874, September 2003.

[37] Valter Franceschini and Claudio Tebaldi. Sequences of infinite bifurcations and turbulence in a five-mode truncation of the navier-stokes equations. *Journal of Statistical Physics*, 21(6):707–726, 1979.

[38] A. Frediani. Velivolo biplano ad ali contrapposte. 2003. Italian Patent FI 2003A000043, 19 February 2003.

[39] Aldo Frediani, Vittorio Cipolla, and Emanuele Rizzo. The PrandtlPlane configuration: Overview on possible applications to civil aviation. In Giuseppe Buttazzo and Aldo Frediani, editors, *Variational Analysis and Aerospace Engineering: Mathematical Challenges for Aerospace Design*, volume 66 of *Springer Optimization and Its Applications*, pages 179–210. Springer US, 2012. 10.1007/978-1-4614-2435-2_8.

[40] Aldo Frediani and Guido Montanari. Best wing system: an exact solution of the prandtl's problem. In *Variational Analysis and Aerospace Engineering*, volume 33 of *Springer Optimization and Its Applications*, pages 183–211. Springer New York, 2009.

[41] Aldo Frediani, Flavio Quattrone, and Francesco Contini. The lifting system of a PrandtlPlane, part 3: Structures made in composites. In Giuseppe Buttazzo and Aldo Frediani, editors, *Variational Analysis and Aerospace Engineering: Mathematical Challenges for Aerospace Design*, volume 66 of *Springer Optimization and Its Applications*, pages 269–288. Springer US, 2012. 10.1007/978-1-4614-2435-2_11.

[42] E. Gal and R. Levy. The geometric stiffness of triangular composite-materials shell elements. *Computers and Structures*, 83:2318–2333, 2005.

[43] E. Gal, R. Levy, H. Abramovich, and P. Pavsner. Buckling analysis of composite panels. *Composite Structures*, 73(2):179 – 185, 2006. International Conference on Buckling and Postbuckling Behavior of Composite Laminated Shell Structures.

[44] F. H. Gern, A. Ko, E. Sulaeman, J. Gundlach, R. H. Kapania, and R. T. Haftka. Multidisciplinary Design Optimization of a Transonic Commerical Transport with Strut-Braced Wing. *Journal of Aircraft*, 38(No. 6):1006–1014, November 2001.

[45] J.H. Ginsberg. *Mechanical and Structural Vibrations: Theory and Applications*. Wiley, 2001.

[46] Raymond E. Gordnier. Computation of limit-cycle oscillations of a delta wing. *Journal of Aircraft*, 40(6):1206–1208, 2003.

[47] Raymond E. Gordnier and Reid B. Melville. Numerical simulation of limit-cycle oscillations of a cropped delta wing using the full navier-stokes equations. *International Journal of Computational Fluid Dynamics*, 14(3):211–224, 2001.

[48] D.G.E. Grigoriadis, S.C. Kassinos, and E.V. Votyakov. Immersed boundary method for the mhd flows of liquid metals. *Journal of Computational Physics*, 228(3):903 – 920, 2009.

[49] J. Guckenheimer and P. Holmes. *Nonlinear Oscillations, Dynamical Systems, and Bifurcations of Vector Fields*. Number v. 42 in Applied Mathematical Sciences. Springer, 1983.

[50] Ohad Gur, Manav Bhatia, Joseph A Schetz, William H Mason, Rakesh K Kapania, and Dimitri N Mavris. Design optimization of a truss-braced-wing transonic transport aircraft. *Journal of Aircraft*, 47(6):1907–1917, 2010.

[51] G.P. Guruswamy. Ensaero - a multidisciplinary program for fluid/structural interaction studies of aerospace vehicles. *Computing Systems in Engineering*, 1:237 – 256, 1990. Computational Technology for Flight Vehicles.

[52] R. L. Harder and R. N. Desmarais. Interpolation using surface splines. *Journal of Aircraft*, 9(2):189–191, 1972.

[53] P. Hartman. *Ordinary Differentil Equatons*. Wiley, New York, 1964.

[54] J. Hess and M. Smith. Calculation of Potential Flows about Arbitrary Bodies. 1967.

[55] Hans M. Hilber, Thomas J. R. Hughes, and Robert L. Taylor. Improved numerical dissipation for time integration algorithms in structural dynamics. *Earthquake Engineering & Structural Dynamics*, 5(3):283–292, 1977.

[56] Gene Hou, Jin Wang, and Anita Layton. Numerical methods for fluid-structure interaction - a review. *Communications in Computational Physics*, 12(2):337–377, August 2012.

[57] T J R Hughes. *The Finite Element Method: Linear Static and Dynamic Finite Element Analysis*. Prentice-Hall, 1987.

[58] Thomas J. R. Hughes. A note on the stability of newmark's algorithm in nonlinear structural dynamics. *International Journal for Numerical Methods in Engineering*, 11(2):383–386, 1977.

[59] Thomas J.R. Hughes. Stability, convergence and growth and decay of energy of the average acceleration method in nonlinear structural dynamics. *Computers & Structures*, 6(45):313 – 324, 1976.

[60] Antony Jameson. Computational methods for aerodynamic design. In SureshM. Deshpande, ShivarajS. Desai, and Roddam Narasimha, editors, *Fourteenth International Conference on Numerical Methods in Fluid Dynamics*, volume 453 of *Lecture Notes in Physics*, pages 71–85. Springer Berlin Heidelberg, 1995.

[61] D.V. Jorgensen and A. Rutherford. On the dynamics of a stirred tank with consecutive reactions. *Chem. Eng. Sci*, 38:4553, 1983.

[62] J. Katz and A. Plotkin. *Low-Speed Aerodynamics*. Cambridge Aerospace Series. Cambridge University Press, 2001.

[63] J. Katz and D. Weihs. The effect of chordwise flexibility on the lift of a rapidly accelerated airfoil. *Aeronautical Quart*, pages 360–369–40, 1979.

[64] M. Thiemo Kier. Comparison of unsteady aerodynamic modelling methodologies with respect to flight loads analysis. In *AIAA Atmospheric Flight Mechanics Conference and Exhibit Guidance, Navigation, and Control and Co-located Conferences*, number AIAA 2005-6027, August 2005.

[65] Y. I. Kim, G. J. Park, R. M. Kolonay, M. Blair, and R. A. Canfield. Nonlinear Response Structural Optimization of a Joined Wing Using Equivalent Loads. *AIAA Journal*, 46, 2008.

[66] D. Kuhl and M. A. Crisfield. Energy-conserving and decaying algorithms in non-linear structural dynamics. *International Journal for Numerical Methods in Engineering*, 45(5):569–599, 1999.

[67] Detlef Kuhl and Ekkehard Ramm. Constraint energy momentum algorithm and its application to non-linear dynamics of shells. *Computer Methods in Applied Mechanics and Engineering*, 136(34):293 – 315, 1996.

[68] Detlef Kuhl and Ekkehard Ramm. Generalized energymomentum method for non-linear adaptive shell dynamics. *Computer Methods in Applied Mechanics and Engineering*, 178(34):343 – 366, 1999.

[69] H. Lamb. *Hydrodynamics*. Dover Publications, 1945.

[70] P. Lancaster and K. Salkauskas. Surfaces Generated by Moving Least Squares Methods. *Mathematics of Computation*, 37(155):141–158, 1981.

[71] R. H. Lange, J. F. Cahill, E. S. Bradley, R. R. Eudaily, C. M. Jenness, and D. G. Macwilkinson. Feasibility Study of the Transonic Biplane Concept for Transport Aircraft Applications. 1974. NASA CR–132462, Lockheed–Georgia Company.

[72] J. G. Leishman, M. J. Bhagwat, and A. J. Coyne. Investigation into the rollup and diffusion of rotor tip vortices using laser doppler velocimetry. 53rd Annual Forum of the American Helicopter Society, Virginia Beach, VA, April 28-May 1 1997.

[73] J. Gordon Leishman. *Principles of helicopter aerodynamics*. Cambridge aerospace series. Cambridge University Press, Cambridge, New York, 2000.

[74] J. Gordon Leishman and Mahendra J. Bhagwat. Generalized viscous vortex model for application to free-vortex wake and aeroacoustic calculations. 58th Annual Forum and Technology Display of the american Helicopter Society International, Montreal, Canada, 11-13 June 2002.

[75] J. Letcher. V-Wings and Diamond-Ring Wings of Minimum Induced Drag. *Journal of Aircraft*, 9(No. 8):605–607, August 1972.

[76] R. Levy and E. Gal. Triangular Shell Element for Large Rotations Analysis. *AIAA Journal*, 41(No. 12):2505–2508, December 2003.

[77] R. Levy and W.R. Spillers. *Analysis of geometrically nonlinear structures*. Number v. 1. Kluwer Academic Publishers, 2003.

[78] G.R. Liu. *Mesh Free Methods: Moving Beyond the Finite Element Method*. Taylor & Francis, 2010.

[79] David Lucia. The sensorcraft configurations: A non-linear aeroservoelastic challenge for aviation. Number AIAA 2005-1943. 46th AIAA/ASME/ASCE/AHS/ASC Structures, Structural Dynamics and Materials Conference, American Institute of Aeronautics and Astronautics, 18-21 April 2005.

[80] A.M. Lyapunov. *General Problem of the Stability Of Motion*. Control Theory and Applications Series. Taylor & Francis, 1992.

[81] C. Michler, S.J. Hulshoff, E.H. van Brummelen, and R. de Borst. A monolithic approach to fluid-structure interaction. *Computers and Fluids*, 33(5):839–848, 2004-06-01T00:00:00.

[82] L. R. Miranda. Boxplane Wing and Aircraft. US Patent 3,834,654, September 1974.

[83] E. H. Moore. On the reciprocal of the general algebraic matrix. *Bulletin of the American Mathematical Society*, 26:394–395.

[84] K.D. Murphy, P.V. Bayly, L.N. Virgin, and J.A. Gottwald. Measuring the stability of periodic attractors using perturbation-induced transients: Applications to two nonlinear oscillators. *Journal of Sound and Vibration*, 172(1):85 – 102, 1994.

[85] Joseba Murua, Rafael Palacios, and J. Michael R. Graham. Applications of the unsteady vortex-lattice method in aircraft aeroelasticity and flight dynamics. *Progress in Aerospace Sciences*, 55(0):46 – 72, 2012.

[86] Ali H. Nayfeh and Balakumar Balachandran. *Applied Nonlinear Dynamics: Analytical, Computational and Experimental Methods*. Wiley Series in Nonlinear Science. Wiley, 2008.

[87] B. Nayroles, G. Touzot, and P. Villon. Generalizing the finite element method: Diffuse approximation and diffuse elements. *Computational Mechanics*, 10:307–318, 1992.

[88] N. M. Newmark. A method of computation for structural dynamics. *Journal of Engineering Mechanics, ASCE*, 85 (EM3):67–94, 1959.

[89] K. C. Park. An improved stiffly stable method for direct integration of nonlinear structural dynamic equations. *Journal of Applied Mechanics*, 42(2):464–470, 1975.

[90] M. J. Patil. Nonlinear Aeroelastic Analysis of Joined-Wing Aircraft. 2003. Presented at the 44$^{\text{th}}$ AIAA/ASME/ASCE/AHS/ASC Structures, Structural Dynamics & Materials Conference, Norfolk, Virginia, April 7-10, 2003.

[91] Jacques E.V. Peter and Richard P. Dwight. Numerical sensitivity analysis for aerodynamic optimization: A survey of approaches. *Computers & Fluids*, 39(3):373 – 391, 2010.

[92] L. Prandtl. Induced drag of multiplanes. Technical Report TN 182, NACA, March 1924.

[93] S. Preidikman and D. Mook. Time-domain simulations of linear and nonlinear aeroelastic behavior. *Journal of Vibration and Control*, 6:1135–1175, 2000.

[94] Giuseppe Quaranta, Paolo Mantegazza, and Pierangelo Masarati. Assessing the local stability of periodic motions for large multibody nonlinear systems using pod. *Journal of Sound and Vibration*, 271:1015–1038, 2003.

[95] Giuseppe Quaranta, Pierangelo Masarati, and Paolo Mantegazza. A conservative mesh-free approach for fluid structure problems in coupled problems. In *International Conference for Coupled Problems in Science and Engineering, Santorini, Greece*, pages 24–27, 23-29 May 2005.

[96] E. Reichenbach, M. Castelluccio, and Sexton B. Joined Wing Sensorcraft Aeroservoelastic Wind Tunnel Test Program. 2011. Presented at the 52nd AIAA/ASME/ASCE/AHS/ASC Structures, Structural Dynamics & Materials Conference, Denver, Colorado, 4-7 April 2011.

[97] E. Reithmeier. *Periodic solutions of nonlinear dynamical systems: numerical computation, stability, bifurcation, and transition to chaos.* Lecture notes in mathematics. Springer-Verlag, 1991.

[98] W. C. Rheinbolt. Numerical analysis of continuation methods for nonlinear structural problems. *Comput. Struct.*, 13:103–113, 1981.

[99] J. Richards, T. Aarons, J. Garnand-Royo, C. Woolsey, and R. Canfield. Airworthiness evaluation of a scaled joined-wing aircraft. Number AIAA-2012-1721. 53rd AIAA/ASME/ASCE/AHS/ASC Structures, Structural Dynamics, and Materials Conference, Honolulu, Hawaii, 23-26 April 2012.

[100] E. Riks. An Incremental Approach to the Solution of Snapping and Buckling Problems. *International Journal of Solids and Structures*, 15(7):529 – 551, 1979.

[101] W. P. Rodden and E. H. Johnson. *User Guide V 68 MSC/NASTRAN Aeroelastic Analysis.* MacNeal-Schwendler Corporation, 1994.

[102] P.B. Ryzhakov, R. Rossi, S.R. Idelsohn, and E. Oate. A monolithic lagrangian approach for fluidstructure interaction problems. *Computational Mechanics*, 46(6):883–899, 2010.

[103] E. T. Schairer and L. A. Hand. Measurements of unsteady aeroelastic model deformation by stereo photogrammetry. *Journal of Aircraft*, 36:1033–1040, 1999.

[104] R. Seydel. *Practical Bifurcation and Stability Analysis.* Interdisciplinary Applied Mathematics. Springer, 2009.

[105] J. C. Simo and N. Tarnow. The discrete energy-momentum method. conserving algorithms for nonlinear elastodynamics. *Zeitschrift fr Angewandte Mathematik und Physik (ZAMP)*, 43:757–792, 1992. 10.1007/BF00913408.

[106] M. J. Smith, D. H. Hodges, and C. E. S. Cesnik. An evaluation of computational algorithms to interface between cfd and csd merhodologies. 1995.

[107] H.B. Squire. The growth of a vortex in turbulent flow. *Aeronautical Quarterly*, pages 302–306, 1965.

[108] Steven H. Strogatz. *Nonlinear Dynamics And Chaos: With Applications To Physics, Biology, Chemistry, And Engineering (Studies in Nonlinearity)*. Studies in nonlinearity. Perseus Books Group, 1 edition, January 1994.

[109] G. Szab and J. Gyrgyi. Three-dimensional fluid-structure interaction analysis for bridge aeroelasticity. World Congress on Engineering and Computer Science.2009, October 20-22, 2009, San Francisco, USA, 20-22 October 2009.

[110] R. van Buskirk and C. Jeffries. Observation of chaotic dynamics of coupled nonlinear oscillators. *hysical Review A - General Physics, 3rd Series*, 31:3332–3357, 1985.

[111] G.H. Vatistas, V. Kozel, and W.C. Mih. A simpler model for concentrated vortices. *Experiments in Fluids*, 11(1):73–76, 1991.

[112] Holger Wendland. Piecewise polynomial, positive definite and compactly supported radial functions of minimal degree. *Advances in Computational Mathematics*, 4:389–396, 1995.

[113] S. Wiggins. *Introduction to Applied Nonlinear Dynamical Systems and Chaos*. Texts in Applied Mathematics. Springer, 2003.

[114] J. Wolkovitch. The Joined Wing Aircraft: an Overview. *Journal of Aircraft*, 23(No. 3):161–178, March 1986.

[115] W. L. Wood, M. Bossak, and O. C. Zienkiewicz. An alpha modification of newmark's method. *International Journal for Numerical Methods in Engineering*, 15(10):1562–1566, 1980.

[116] W. L. Wood and M. E. Oduor. Stability properties of some algorithms for the solution of nonlinear dynamic vibration equations. *Communications in Applied Numerical Methods*, 4(2):205–212, 1988.

[117] Jianming Yang and Elias Balaras. An embedded-boundary formulation for large-eddy simulation of turbulent flows interacting with moving boundaries. *Journal of Computational Physics*, 215(1):12 – 40, 2006.

[118] R. Yurkovich. Status of unsteady aerodynamic prediction for flutter of high-performance aircraft. *AIAA*, 40:832–842, 2003.